ELECTRONIC TRANSITIONS OF MOLECULES BY ELECTRON IMPACT AND MULTIPHOTON IONIZATION SPECTROSCOPY

Thesis by

Ronald Rianda

In Partial Fulfillment of the Requirements

for the Degree of

Doctor of Philosophy

California Institute of Technology

Pasadena, California

1982

(Submitted October 1981)

To my parents

Acknowledgments

I wish to thank my research advisor Professor Aron Kuppermann for his support and encouragement during the course of the studies reported here. Professor Kuppermann provided an environment which allowed a great deal of freedom in choosing project directions and encouraged inventiveness and initiative. In addition, he displayed an uncanny ability to obtain funding for the equipment necessary for the conduct of this research.

I would especially like to thank my predecessor on the electron impact spectrometer, Robert P. Frueholz. Interacting with Bob professionally and socially has been both educational and enjoyable. In addition, it was through his efforts on my behalf that I was able to obtain continued employment in science.

Interacting with fellow subbasement dwellers has proven to be enlightening. I would like to acknowledge Dr. David Edmonson's numerous contributions to the design of the electronics for the EIS III. In spite of our frequent heated scientific arguments, working with Dave was informative and pleasurable. Thanks are also due to Dave Moll for his assistance on the multiphoton ionization studies. I would also like to thank Charles Koerting, Jack Kaye, Dave Moll, and Nancy and Jeff Harvey for their help in transmitting sections of this thesis for typing during my absence from Caltech.

The contribution of Caltech's instrument and electronics shops to this work cannot be overstated. The members of the instrument shop (Bill Schuelke, Tony Stark, Guy Duremberg, Bill Schuelke (the younger),

Ray Garcia, and Delmer Dill)have all assisted in both the design and construction of the apparatus used in this work. Tom Dunn has proven to be a vast storehouse of chip specifications and assisted in the design and repair of the electronics hardware necessary for data acquisition.

I would like to thank Adria McMillan for her assistance in dealing with Caltech's bureaucracy and for typing several of the papers included in this work. I am also indebted to Kathy Lewis for her excellent typing of the bulk of this thesis. Both Kathy and Adria exhibited an amazing ability to read my virtually illegible scrawl.

I am very grateful to my family for their moral and financial support during my graduate studies. I would also like to thank my wife, Belinda, for her encouragement while I was writing this thesis.

Abstract

The experimental work discussed in this thesis is concerned primarily with the detection of electric dipole forbidden transitions of molecules in the gas phase. The thesis is divided into two parts. The first part describes measurements made using the technique of low-energy, variable-angle, electron impact spectroscopy. The second part describes investigations performed using resonance enhanced multiphoton ionization (REMPI) spectroscopy.

The low-energy variable-angle electron impact technique has been used to study the electronic spectroscopy of molecules. Both dipole allowed and dipole forbidden transitions have been investigated. Transitions having excitation energies from 0 eV to 20 eV have been studied using incident electron beam energies ranging from 25 eV to 75 eV and scattering angles from 0^{o} to 80^{o}. Molecules studied included nitric oxide (NO), uranium hexafluoride (UF_6), tungsten hexafluoride (WF_6), nitrogen dioxide (NO_2), hydrogen cyanide (HCN), acetonitrile (CH_3CN), propionitrile (C_2H_5CN), butyronitrile (C_3H_7CN), and malononitrile ($CH_2(CN)_2$).

Weak structure was observed in the spectrum of nitric oxide between 5.22 eV and 5.60 eV. These bands have been assigned as vibronic bands belonging to the $X^2\pi \rightarrow a^4\pi$ transition. Additional structure extending from 5.7 eV to about 7 eV was assigned to the $X^2\pi \rightarrow b^4\Sigma^-$ transition. Several higher lying transitions were observed which have been tentatively assigned as doublet → quartet in nature.

In order to elucidate the electronic structure of uranium hexafluoride

the electron impact spectra at UF_6 and WF_6 were determined. Eleven features were observed in UF_6 with intensity maxima at 3.26, 4.2, 4.7, 5.8, 7.0, 7.86, 9.26, 11.01, 11.75, 12.5 and 13.2 eV. Features were observed in the spectrum at 7.25, 7.9, 8.5, 9.85, 11.75, 12.6 and 13.5 eV. Comparison of the spectra indicate that the primary contribution to transition intensity in UF_6 above 5.8 eV and in WF_6 results form charge transfer excitations from fluorine p orbitals to metal d orbitals. Tentative assignments based on previous theoretical studies are made.

A previously unreported doublet → quartet transition was observed at 4.49 eV in the electron impact spectrum of NO_2, in excellent agreement with theoretical calculations. Doublet → doublet transitions were observed with maxima at 2.95, 5.81, 7.48, 8.64, 9.69, 10.52, 10.68, 10.94 and 11.20 eV in agreement with previous studies.

The series of C≡N containing molecules, hydrogen cyanide, acetonitrile, malononitrile, propionitrile and butyronitrile, have also been studied using the electron impact technique. Results for hydrogen cyanide are in excellent agreement with previous work. Previously undetected singlet → triplet transitions of acetonitrile, propionitrile and butyronitrile are reported. In addition the first study of the electronic spectrum of malononitrile is reported.

Two appendices to Part One are included. The first of these reports the results of generalized valence bond and configuration interaction studies of the low lying states of ammonia. The second appendix discusses an electron impact study of the electronically excited states of 1,3,5-cycloheptatriene.

Part Two of this thesis describes the theory of multiphoton ionization and reports results obtained using this technique. The application of REMPI spectroscopy to the detection of spin forbidden transitions is examined. It is shown in a study of the $X^1\Sigma_g^+ \rightarrow a^3A_2$ state of CS_2 to offer potential for the detection of spin forbidden transitions at high resolution and with great sensitivity.

Finally a preliminary study of the two-photon resonance enhanced multiphoton ionization of p-xylene is reported. Several elements of the $X^1Ag \rightarrow {}^1B_{2u}$ transition observed previously in benzene and p-difluorobenzene are reported.

Table of Contents

Page

Acknowledgments iii

Abstract v

Part I: Electron Impact Spectroscopy 1

1. Introduction 2

2. Experimental 11

2.1 Introduction 11

2.2 Description of the EIS I Spectrometer 12

2.3 Description of the EIS III Spectrometer 16

2.4 EIS III Electronic Hardware 20

2.4.1 EIS III Data Acquisition System 20

2.4.2 Memory Expansion and Interface Board 34

2.4.3 EIS Scan Circuit 49

2.4.4 Deflector Power Supplies 52

2.4.5 Pulse Amplifier and Discriminator 54

2.4.6 PROM Programmer 57

2.5 EIS III Computer System Software 63

2.5.1 Manufacturer Supplied Software 63

2.5.2 Electron Impact Spectrometer Scanning Routine . . . 67

2.5.3 Electron Impact Spectrometer Tuning Routine 71

2.5.4 PROM Programmer Routine 72

2.5.5 General Purpose Routines 74

2.6 Data Handling 85

Table of Contents (continued)

Page

3. Results and Discussion 93

3.1 Paper I: Doublet-Quartet Transitions in Nitric Oxide by Low-Energy, Variable-Angle Electron Scattering. 94

3.2 Paper II: Electronic Spectroscopy of UF_6 and WF_6 by Electron Impact. 121

3.3 Paper III: Doublet → Quartet and Doublet → Doublet Electronic Transitions in NO_2 by Electron Impact. 149

3.4 Paper IV: Singlet → Triplet Transitions in C≡N Containing Molecules by Electron Impact 166

Appendix I: The Low Lying States of Ammonia; Generalized Valence Bond and Configuration Interaction Studies. 201

Appendix II: Excited Electronic States of 1,3,5-Cycloheptatriene . . .219

Part II: Multiphoton Ionization Spectroscopy 234

4. Introduction 235

5. Theory of Multiphoton Ionization 243

5.1 Introduction. 243

5.2 Nonresonant Multiphoton Ionization. 244

5.3 Resonant Multiphoton Ionization 250

5.4 Rate Equation Approach to Multiphoton Ionization. 258

6. Experimental 264

6.1 Introduction. 265

6.2 Description of the Laser System 265

6.3 Detection Apparatus 274

6.4 Digital Data Acquisition System 279

6.4.1 Introduction 279

6.4.2 Commercial Hardware. 279

Table of Contents (continued)

Page

6.4.3 Memory Expansion and Interface Board 292

6.5 MPI Computer System Software 303

6.5.1 Intel SBC 925 Monitor. 304

6.5.2 iCOM Software 304

6.5.3 PROM Resident General Purpose Subroutines 305

6.5.4 Diskette Resident Software 309

6.6 Data Handling 315

7. Results and Discussion 322

7.1 Paper 1: Detection of the $^3A_2$ State of CS_2 by Multiphoton Ionization. 323

7.2 Preliminary Investigation: The Multiphoton Ionization Spectrum of p-Xylene 335

Proposition I 347

Proposition II 357

Proposition III 368

Proposition IV 376

Proposition V 385

Part I: Electron Impact Spectroscopy

1. Introduction

1. Introduction

The collision of an electron with an atom or molecule may result in a number of different outcomes. Included among these are:

1. Transfer of translational energy.
2. Diffraction.
3. Electron exchange.
4. Excitation or de-excitation of internal states of the target.
5. Ionization of the target.
6. Negative ion formation.
7. Fragmentation of the target molecule.

or any combination of these.[1] The studies reported here are concerned with the excitation of target molecules in the gas phase by an energy selected incident electron beam using the technique of low-energy variable-angle electron-impact spectroscopy. This technique is useful not only for investigating transitions which are allowed by electric dipole selection rules but has also been shown to be a very powerful technique for observing and identifying transitions which are forbidden by dipole selection rules.[2 - 5]

The method used for studying the spectroscopy of all the molecular systems reported in this thesis makes use of electron energy loss spectra, the electron impact analog of an optical absorption spectrum. The energy loss spectrum is obtained by directing the energy selected incident electron beam into a scattering chamber containing the target gas. The scattered electron intensity distribution is then measured

as a function of the energy lost relative to the incident electron beam energy. The pressure within the scattering chamber is sufficiently low (usually about 4 mTorr) that a given electron will undergo at most a single collision with the target gas. This ensures that the energy lost by the electron has been transferred to a single target molecule. Therefore, the energy loss spectrum corresponds directly to the excitation energies of the sample gas.

Two significant advantages over optical spectroscopy are provided by electron impact spectroscopy: the capability for measuring an entire energy loss or absorption spectrum from the infrared to the vacuum ultraviolet in a single scan without alteration of the instrument and, most important, the ability to observe transitions which are forbidden by optical selection rules. A typical energy loss spectrum spans a transition energy range of about 10 eV. Thus, a single spectrum may include features which result from low energy excitations, such as vibrational transitions, which would be observed in the infrared region of an optical spectrum as well as features which result from excitations to high lying electronic states which would be observed in the vacuum ultraviolet region of the optical spectrum. In addition, transitions having excitation energies above 10 eV may be as readily observed as those below 10 eV by electron impact spectroscopy. In contrast, the absence of window materials which are transparent above about 12.5 eV make optical spectroscopy very difficult in the high energy region. The resolution of the electron impact spectrum is substantially poorer than that of an optical spectrum at energies below the vacuum ultraviolet.

The resolution of a typical electron impact spectrum is 10 to 100 meV, or about 80 to 800 cm^{-1} versus resolutions on the order of 10^{-6} cm^{-1} in the infrared using a diode laser spectrometer or 10^{-3} cm^{-1} in the visible using a ring dye laser spectrometer. Rotational structure is never resolved and vibrational structure is rarely resolved in an electron impact spectrum. Therefore, rotational analysis and definitive excited state assignments are not possible using only the electron impact spectrum. In spite of this resolution limitation, electron impact spectroscopy may be useful for studying systems possessing very narrow spectral linewidths.[6] Since spectral lines are convoluted with the energy distribution of the incident electron beam, the smallest linewidth presented to the energy analyzer is the energy width of the incident beam. Thus, observed transition intensities may not be distorted as is the case in optical absorption measurements when the spectral linewidth is small relative to the instrumental resolution.[7] In the high energy regions of the spectrum such as the vacuum ultraviolet, the resolutions of the two techniques are comparable. In addition, spectral bandwidths may be quite large for higher-lying excited electronic states since excited state lifetimes are frequently very short and uncertainty principle broadening may result in a 'smearing' of many rovibronic lines into a single broad band. In such cases the resolution of an electron impact spectrometer is quite adequate.

The selection rules for electron impact spectra at high energies (over 100 eV) resemble the optical ones and the excitation cross-sections are related to optical absorption coefficients.[2] The generalized electron impact oscillator strength[8] f_{ei}, given by

$$f_{ei} = \frac{W}{2} \frac{k_o}{k_n} K^2 \frac{d\sigma}{d\Omega}$$

where W is the excitation energy, k_o and k_n are the incident and scattered electron momenta, respectively, K is the change in momentum suffered by the electron as a result of the collision, and $d\sigma/d\Omega$ is the differential cross-section of the transition being measured, approaches the optical oscillator strength, f_{opt}, as K^2 approaches zero.[8] The differential cross-section (DCS) is the rate of change of the total excitation cross-section $\sigma_n(E_o)$ for transition to the n^{th} molecular state as a function of impact energy (E_o), with solid angle $\Omega(\theta,\phi)$. If a spherical polar co-ordinate system is defined such that the z axis lies along the incident beam direction, then θ measures the polar angle of the outgoing electron relative to the incident beam and ϕ is the azimuth. If the target molecules are randomly oriented with respect to the incident beam, as is the case, then the differential cross-section will not depend on ϕ.[1]

At low impact energies (less than 60 eV), optical selection rules are relaxed. In an optical absorption spectrum, spin forbidden transitions ($\Delta S \neq 0$), which occur due to spin-orbit coupling, have oscillator strengths which are five to eight orders of magnitude weaker than those of fully allowed transitions in systems containing only light nuclei.[9] In low energy electron impact spectra, at scattering angles greater than 40^o, spin forbidden transitions are five to ten percent as intense as allowed transitions. Also, at low impact energies the probability for producing symmetry forbidden transitions can be increased by one to three orders of magnitude, typically being 5 to 25% as great as for fully

allowed transitions.[2-5]

The intensity of spin-forbidden transitions in electron impact spectroscopy is enhanced relative to optical intensities through the existence of an alternate mechanism of excitation, for which there is no optical analog, electron exchange.[10] The interaction which gives rise to optically allowed transitions is the relatively long range Coulombic repulsion. However, at low impact energies and small impact parameters, the short range electron exchange process may occur. By this means, the spin of the system is unchanged but the spin multiplicity of the atom or molecule may change.

Symmetry-forbidden but spin-allowed transitions are also more readily detected in electron impact spectroscopy. This may be explained qualitatively by the occurrence of distortion of the electronic wavefunction of the target molecule by the interaction with a low energy incoming electron immediately prior to or during excitation. This distortion perturbs the overall symmetry of the free molecular wavefunction, allowing the mixing of states of different symmetry.[11]

In many cases it is possible to determine the nature of a transition observed in an electron impact spectrum by measuring the differential cross section. The DCS observed for a given transition will, in general, have certain characteristics depending on the nature of the transition.[2-5] Excitations which are fully allowed with respect to dipole selection rules exhibit very strongly forward peaked DCS's. The DCS's of such transitions are generally most intense at 0^{o} scattering angle and decrease by about two orders of magnitude as the scattering angle (θ) is increased from 10^{o}

to 80^{o}. This is because excitation of fully allowed transitions occurs predominantly by means of long range Coulombic interaction, therefore excitation may occur for large impact parameters and small angular deflections. Spin forbidden transitions, on the other hand, exhibit a DCS which is nearly constant, to within a factor of two or three, over a similar angular range. This is a result of the exchange mechanism whereby the scattered electron "forgets" where the incident electron came from, thus yielding a relatively isotropic DCS. Spin-allowed but symmetry-forbidden transitions exhibit an intermediate behavior. The DCS is forward peaked but not so much as that of a fully allowed transiton. Thus, measuring the DCS of a transition may add valuable information as to the type of transition observed.

The author has been actively involved in the study of the electronic spectroscopy of numerous molecular systems using the electron impact technique and has also been responsible for the design of the data acquisition system for use with the new electron impact spectrometer, EISIII, which was recently completed. In Section 3, the results of these studies are discussed in detail. The molecules studied were nitric oxide, uranium hexafluoride, tungsten hexafluoride, nitrogen dioxide, and several C≡N containing compounds. All these experiments were performed in conjunction with Dr. R. P. Frueholz. Two appendices to Section 3 are included. The first consists of a paper describing ab initio calculations on the lower excited states of ammonia performed by Dr. R. P. Frueholz, Professor W. A. Goddard III and myself. These calculations

were initiated at the suggestion of Dr. W. M. Flicker to determine whether low lying features observed in electron impact spectra of ammonia[11] corresponded to triplet transitions in ammonia or to transitions in some impurity. In addition to the electron impact studies mentioned previously, the author, in association with Dr. Frueholz, investigated the electronic spectroscopy of 1,3,5 cycloheptatriene. A description of this study is included as Appendix II.

A description of the apparatus used to obtain the electron impact spectra of the molecular systems reported in this thesis is included in Section 2. Also included in Section 2 is a description of the revised electron optics of EISIII which were designed by Dr. D. A. Edmonson. A description of the data acquisition system which was designed by the author to function with EISIII is also included in Section 2.

References

1. J. K. Rice, PhD Thesis, California Institute of Technology (1969).
2. (a) A. Kuppermann, J. K. Rice and S. Trajmar, J. Phys. Chem. 72 (1968) 3894.
   (b) S. Trajmar, J. K. Rice and A. Kuppermann, Advan. Chem. Phys. 18 (1970) 15.
3. A. Kuppermann, W. M. Flicker and O. A. Mosher, Chem. Rev. 79 (1979) 77.
4. O. A. Mosher, W. M. Flicker and A. Kuppermann, J. Chem. Phys. 59 (1973) 6502.
5. O. A. Mosher, W. M. Flicker and A. Kuppermann, J. Chem. Phys. 62 (1975) 2600.
6. M. Krauss, R. J. Celotta, S. R. Mielczarek and C. E. Kuyatt, Chem. Phys. Lett. 27 (1974) 285.
7. R. E. Huffman, Can. J. Chem. 47 (1969) 1823.
8. E. N. Lassettre, A. Skerbele and N. A. Dillon, J. Chem. Phys. 50 (1969) 1829.
9. S. P. McGlynn, T. Azumi and M. Kinoshita, Molecular Spectroscopy of the Triplet State, (Prentice-Hall Inc., New Jersey, 1969).
10. J. R. Oppenheimer, Phys. Rev. 29 (1927) 433.
11. W. M. Flicker, PhD Thesis, California Institute of Technology (1976).

2. Experimental

2. EXPERIMENTAL

2.1 Introduction

The electron impact spectrometer used to obtain the results presented in this thesis was designed by Rice, Tramar and Kuppermann.[1] This instrument, designated EIS I, was borrowed from the Jet Propulsion Laboratory in order that experimentation might continue while construction of a new spectrometer, designated EIS III, was under way. The spectrometer, which was described in detail in the Ph.D. Thesis of J. K. Rice,[2] was modified in order to improve performance.

This experimental section contains five parts in addition to the Introduction. The second subsection describes the EIS I spectrometer briefly. The third subsection describes the revised electron optics of EIS III while the fourth subsection describes the new computerized data acquisition system. Descriptions of the assembler language software used for data acquisition and of the FORTRAN programs used for data analysis are contained in subsections five and six.

2.2 Description of the EIS I Spectrometer

A schematic drawing of EIS I is shown in figure 1. The instrument consists of an electron gun, two hemispherical electrostatic energy analyzers each with a center radius of 1.00", entrance and exit optics, a flexible bellows scattering chamber, and a detection system. The electron gun used for the experiments reported in this thesis was identical to that of EIS II, which was described in the theses of R. P. Frueholz[3] and O. A. Mosher,[4] and differs from the gun originally used

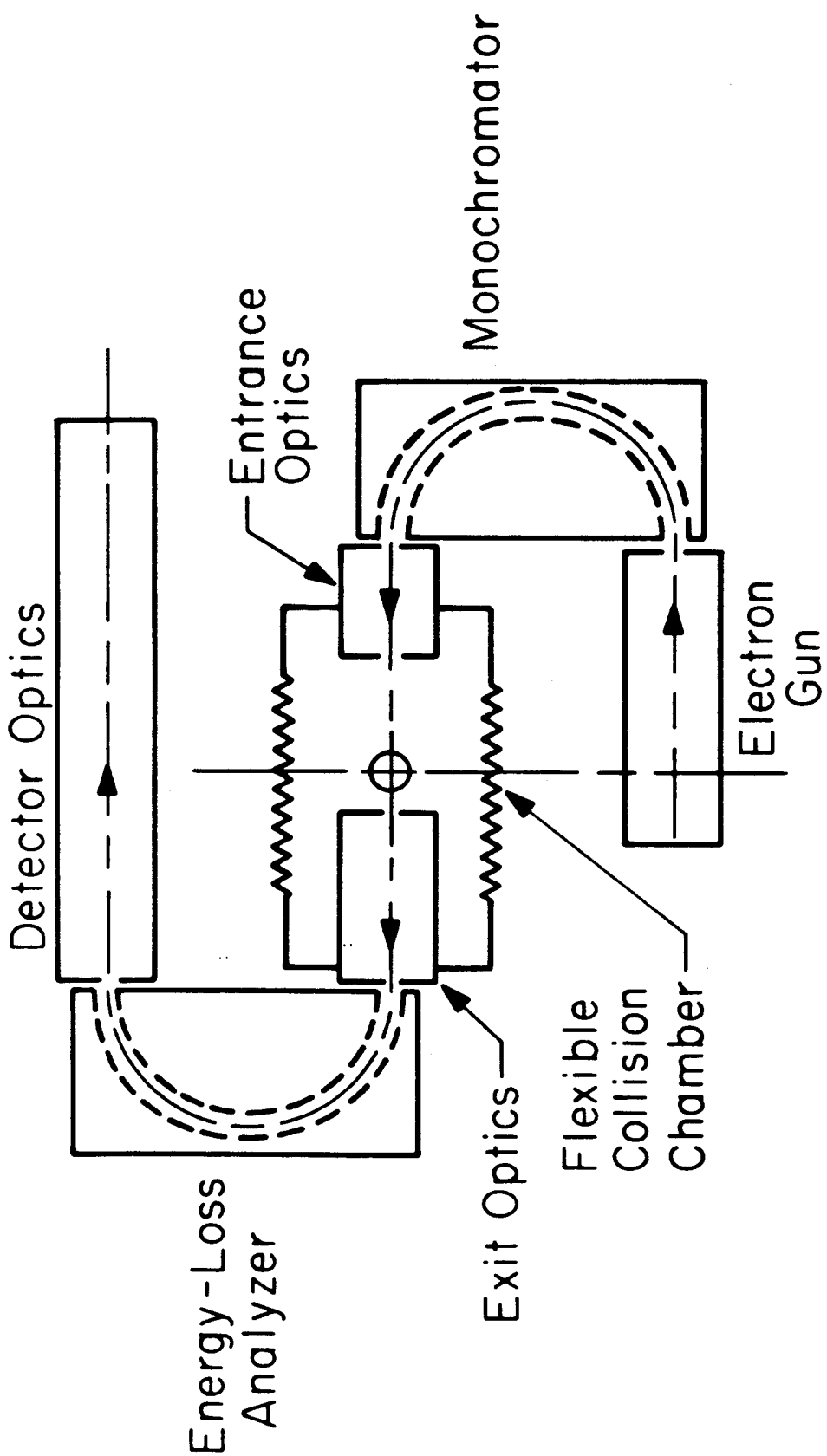

EIS I BLOCK DIAGRAM

Figure 1

with the instrument. All other electron optical components of the spectrometer are identical to those described by Rice,[2] with the following exceptions. All apertures which were originally made of molybdenum were replaced with identically sized apertures made of a platinum/10% iridium alloy. In addition, all lens elements, including the gun lenses except the cathode, have been gold plated. The gold plating and aperture replacement provided relatively inert surfaces within the spectrometer which resist contamination thereby substantially increasing the length of periods between complete disassemblies and cleanings of the instrument when reactive compounds such as UF_6 are studied.

The scattering chamber consists of a double bellows assembly made of 347 stainless steel. The axis of the bellows is positioned at a scattering angle of 30°. The bellows may be bent ±55°, permitting operation at scattering angles from -25° to 85°. Data were typically obtained at scattering angles of 5° and at 10° increments from 10° to 80°. Sample pressures were typically 1 to 10 millitorr.

Energy loss analysis is accomplished by sweeping the potentials of all second half components (optical elements after the scattering chamber) uniformly. Thus, only electrons which have lost energy in collision corresponding to the sweep voltage are transmitted through the analyzer sphere and into the Spiraltron electron multiplier. The sweep voltage was obtained by digital-to-analog conversion of the channel number (0 to 1023) from the Nuclear Data multichannel analyzer. Pulses from the Spiraltron were amplified by a pulse amplifier designed by Q. A. Mosher and D. Mason.[4] The amplified pulses were counted and

stored by the Nuclear Data system. Each channel of the multichannel analyzer corresponds to a specific energy loss. Following completion of data taking, the entire spectrum was punched out on paper tape.

Analysis of data was performed on Caltech's IBM 370/3032 system. Since this system possesses no paper tape handling capability, it was necessary to transfer the data to an IBM compatible magnetic tape. Prior to 1976, this was accomplished utilizing a SCC 4700 computer. When this computer ceased to function, I was forced (in association with Robert Frueholz) to develop a new means of data transfer. This new method required reading the paper tapes onto the PDP 10 through the PDP 8 minicomputer which operates the Multiple Angle Photoelectron Spectrometer. Magnetic tapes written on the PDP 10 system in an IBM compatible format (this required two Macro 10 programs) could then be taken to the 370/3032 for translation from the ASCII and BCD formats used on the paper tapes to IBM compatible EBCDIC (for spectrum headings) and Integer *4 Fortran format (for data). This translation was accomplished through use of the program NDTOMT (not the program previously described by Flicker[5] and Mosher[4]). Another program I wrote, SPEDIT, then transfers data output from several different NDTOMT runs into a single large disk file which is usable by our data analysis programs. Finally, the WRITAPE program copies the disk file onto a data storage magnetic tape (EISDT1 and backup copy EISDT2). Since the entire Nuclear Data based data acquisition system has been replaced by a microcomputer system, no additional documentation of data handling will be included here. Data analysis routines are common to both systems and will be described in section 2.6.

2.3 Description of EIS III

The primary design work for the EIS III spectrometer was performed by Dr. W. M. Flicker and is described in detail in his thesis. Additions and modifications to his design are described in the thesis of Dr. R. P. Frueholz.[3] Construction of the instrument was finally completed in late 1978 and attempts to bring the instrument into operation were begun. The discovery of many problems (no beam current) in the original electron optics of EIS III required that the lens dimensions be revised. Dr. David A. Edmonson designed a new set of optics which were more consistent with other proven designs. I am including a brief description of Dr. Edmonson's optics here since no other discussion is likely to appear in print. Figure 2 shows a diagram of the revised electron optics. With the exceptions of the scattering chamber arrangement (which no longer exists) and the positioning of the beam source and cold trap, the remainder of the instrument is unchanged..

The electron gun lens system is similar to that described by Mosher.[4] Electrons are emitted from a heated tungsten filament (cathode) and are extracted through a .050" aperture in the Pierce element (M9) which is biased at the negative filament lead voltage and are accelerated through a .035" aperture in the anode (M7). The anode, condenser and M3 form a condensing lens of approximate ratio 2:6:1 which translates the anode image to the fixed ratio decelerator and illuminate the entrance window. Two cylindrical plate deflectors in the anode allow trimming of the beam angle for maximum transmission of current through the electron gun stage. Elements M3 and HM1 form a 12:1 fixed ratio decelerator. This lens is

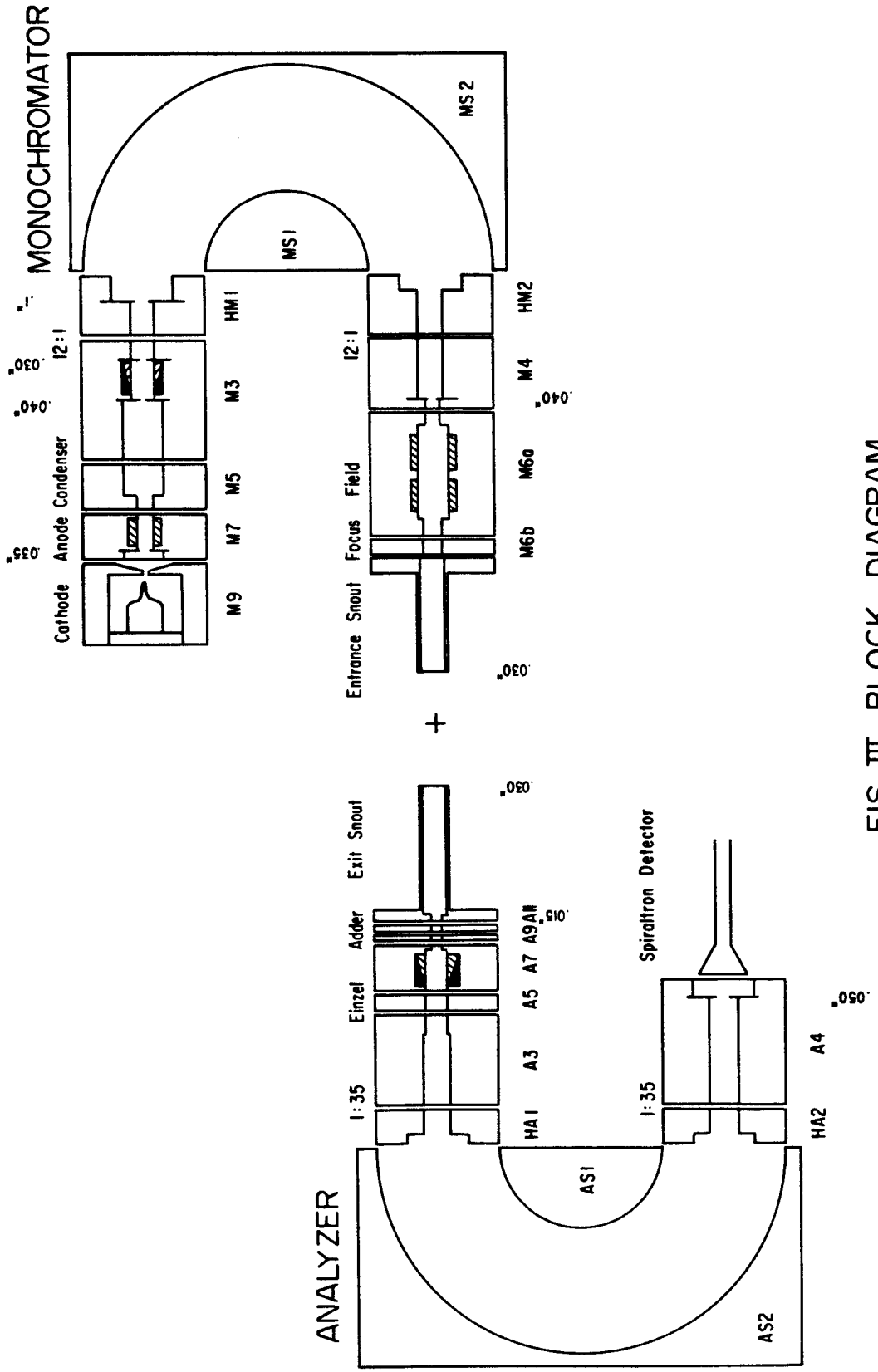

EIS III BLOCK DIAGRAM

Figure 2

the heart of the optics since it sets the image size, pencil angles and energy of the beam as it enters the hemispherical analyzer (monochromator). The window (object, .040") and pupil (.030") located in M3 form the beam angles. The beam itself is imaged onto the focal plane of the hemisphere with a magnification of 1.5 while the final pencil angle is .071 radians. A .1" spatter aperture is located in HM1 to prevent stray electrons from entering the monochromator. Cylindrical plate deflectors are located between the window and pupil apertures and are tuned to maximize current transmission. The monochromator (and analyzer as well) is a spherical section with a center radius of 2.25". The theoretical resolution of the monochromator is 1% $(\frac{\Delta E}{E})$.

Electrons leaving the monochromator are accelerated by the twelve-to-one acceleration system formed by HM2 and M4. The aperture in M4 (the window) is .040". The accelerator is followed by a variable ratio field lens designed to function with 10 - 200 eV electrons. The ratio of the potential at the field lens to that at the focus lens is three-to-one. For 100 eV electrons, the final image size (formed at the end of the entrance snout) is .020". The final beam angle and final pencil angle are .016 radians and .022 radians, respectively.

The acceptance angle of the exit optics is 2°. This is defined by two apertures in a field free region, one at the end of the exit snout (.030") and one between the adder and the snout (.015"). The .015" aperture forms the pupil for the remainder of the electron optical system. The exit beam forming apertures are followed by the adder lens (A11) which adds back the energy lost in collision. This is a weak lens so the focal properties of the beam are unchanged. The focus lens (A9) is designed to

function over a wide voltage range. Lens elements A3, A5 and A7 form a 4:1:4 Einzel lens which forms the image for the 35:1 decelerator made up of A3 and HA1. Two sets of deflector pairs are located in A7. A .045" image is formed at the focal plane of the analyzer sphere by the exit optics.

Electrons which pass through the analyzer sphere are accelerated by the 35:1 accelerator formed by HA2 and A4. The beam passes the final aperture (.050") which serves to eliminate stray electrons and is imaged on the front core of a Spiraltron electron multiplier.

A more thorough discussion of the electron optics may be found in laboratory notebook number 4377. In addition, dimensional specifications and operating lens potentials may be found on page 79 of that notebook.

Initial results obtained using the newly designed optics have been very promising. Lens potentials required to optimize the beam current are very close to those calculated. The instrument tunes rapidly and easily to maximum count rate. However, two serious problems still exist. A substantial magnetic field is possessed by the main flange due to previous attachment of a Vac Ion pump for the chambers containing the electron optics. The mu-metal shielding employed reduces this significantly, however the field in the region of the monochromator is still high enough to warrant concern. Deviations of optimum potentials for the monochromator from those calculated may in part be due to the influence of the magnetic field. In addition, the present vacuum system is insufficient to handle the gas load produced by the capillary array under conditions necessary to obtain a scattered signal. This has

resulted in an extremely short operation time before the optics are contaminated and the instrument ceases to function. Blocking part of the capillary array and adding a diffusion pump for the optics chambers may alleviate this problem.

2.4 EIS III Electronic Hardware

2.4.1 EIS III Data Acquisition System

The Nuclear Data multichannel analyzer system used previously for data acquisition and generation of the voltage ramp for the analyzer optics has been replaced with a Z-80 based microcomputer system. This system consists of a Monolithic Systems Corp. MSC8001 single board computer, an Analog Devices RTI1201 output interface, an ICOM FD3712 dual floppy disk drive and controller, a National Semiconductor RMC660 card-cage and power supply, and a memory expansion and interface board which I have designed.

The MSC8001 is an Intel Multibus compatible single board computer utilizing the Zilog Z-80 processor, an 8-bit microprocessor which is upward compatible with the 8080. The board includes 8K bytes static random access memory (RAM), sockets for the 4K bytes of erasable programmable read only memory, two 8255 parallel peripheral interfaces, a RS232C serial port, an 8253 programmable interval timer and an 8214 eight level interrupt controller.

The Z80 microprocessor operates on a 4 MHz clock, yielding a 1 μs instruction cycle. All 8080 instructions can be executed by the Z-80 without modification, except that the increased clock frequency will alter timing loops. Also, the Z-80 possesses 80 additional instructions, greatly facilitating block transfers and register indirect addressing.

The Z-80 CPU contains eighteen 8-bit registers and four 16-bit registers. These include two sets of six general purpose registers which may be used individually or in pairs as 16-bit registers. The register configuration is shown in figure 3.[6] The Z-80 utilizes a 16-bit address bus. The address bus provides the address for memory (up to 64 K bytes) data exchanges and for I/O data exchanges. I/O addressing uses only the lower 8 address bits to select up to 256 input or 256 output ports. A system memory address map is shown in Table 1. Table 2 shows the system I/O address map. Data transfer occurs through an 8-bit bidirectional data bus.

The MSC8001 includes four PROM sockets which may be configured by jumpers and alteration of the addressing fusible link PROM for 1KX8 EPROMs such as the 2708 or 2758, 2kx8 EPROMS such as the Intel 2716 (Note: The TI TMS2716 is not compatible with the Intel 2716), 4kx8 EPROMS and masked ROMS. The system used with EIS is configured for 2708 EPROMS. Two of the sockets are occupied by PROMs containing the Monolithic System's resident monitor which has been modified substantially by Dr. David Edmonson and myself in order to function with our nonstandard (for Monolithic Systems) memory address map. The third socket contains a PROM extending the monitor. The fourth socket is currently unused.

The MSC 8001 comes with 8K bytes of RAM, consisting of sixteen 4kx1 Zilog 6104-3 static RAMs. The addressing for this block of memory differs from the MSC 8001 standard configuration.

Six 8-bit programmable parallel I/O ports based on a pair of 8255 programmable peripheral interfaces (PPI) are included on the MSC 8001.

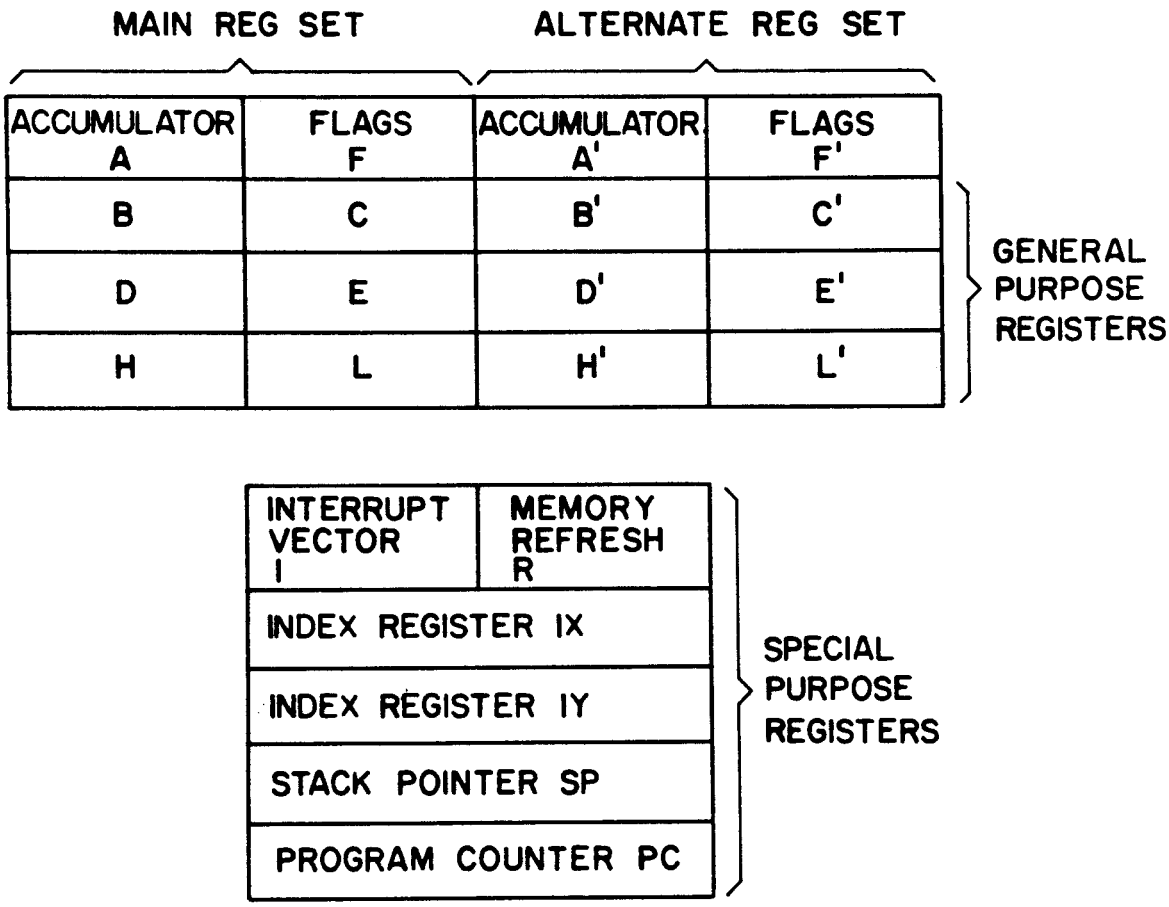

Z-80 CPU REGISTER CONFIGURATION

FIGURE 3

[from Ref. 6]

Table 1

Memory Map for EIS Computer System

0000-0FFF	MSC 8001	PROM (2708's)	
	0000-03FF	MSC monitor PROM No. 1	
	0400-07FF	MSC monitor PROM No. 2	
	0800-0BFF	Monitor extension PROM	
	0C00-0FFF	Currently unused	
1000-1FFF	Prototyped Board		
	1000-13FF	PROM (2708) socket No. 1	
	1400-17FF	PROM socket No. 2	
	1800-1BFF	PROM socket No. 3	
	1C00-1FDF	PROM socket No. 4	
	1FE0-1FE3	USART (8251) No. 2	RS232-C Port
		1FE0 + 1FE2	Data Port
		1FE1 + 1FE3	Control and Status Port
	1FE4-1FE7	Counter Timer Circuit (8253)	
		1FE4	Counter 0
		1FE5	Counter 1
		1FE6	Counter 2
		1FE7	Mode Control
	1FE8-1FEB	Programmable Peripheral Interface (8255)	
		1FE8	Port A
		1FE9	Port B
		1FEA	Port C
		1FEB	Control
	1FEC-1FFF	Decoded but unused	
2000-3FFF	MSC 8001	RAM 8K	
4000-BFFF	Prototyped Board RAM 32K		
E800-EBFF	FDOS RESIDENT PROM		
EC00-EFFF	RTI 1201		
	EC00-EFEF	PROM socket	
	EFF0	DAC 1 data (8-bit)	

Table 1 (continued)

EFF1	DAC 2 data (8-bit)
EFF2	DAC 3 data (8-bit)
EFF3	DAC 4 data (8-bit)
EFF4-EFF5	DAC 1 data (12-bit LSB, MSB)
EFF6-EFF7	DAC 2 data (12-bit)
EFF8-EFF9	DAC 3 data (12-bit)
EFFA-EFFB	DAC 4 data (12-bit)
EFFC	Drivers
EFFD	Reset
EFFE	Unused
EFFF	Card select (unused in our application)

Table 2

I/O Map for EIS Computer System

00-05	Unused
06	Floppy Disk Control Port
07	Floppy Disk Data Port
08-D6	Unused
D7	8214 Priority Interrupt Controller
D8-DB	Unused
DC-DF	Counter Timer Circuit (8253)
	DC Counter 0
	DB Counter 1
	DE Counter 2
	DF Mode Control
E0-E3	Unused
E4-E7	Programmable Peripheral Interface #1 (8253)
	E4 Port A
	E5 Port B
	E6 Port C
	E7 Control
E8-EB	Programmable Peripheral Interface #2 (8255)
	E8 Port A
	E9 Port B
	EA Port C
	EB Control
EC-EF	USART (8251) RS232C Port
	EC + EE Data Port
	ED + EF Control and Status Port
F0-FF	Unused

All three ports of PPI-1 are dedicated to the PROM programmer (discussed in a later section). Only one bit of PPI-2 is currently used, providing gate control for the 8253 programmable interval timer. The PPIs provide enormous flexibility for dealing with parallel data transfer so only the configuration currently in use will be detailed here.

Since all ports of PPI-1 are dedicated for use with the PROM programmer, the hardware configuration is rigidly defined. Port A must be configured for input or output depending on the status of bit 6 of port C (port A drivers are set for output when bit 6 of port C is zero). In addition, inverting bidirectional drivers must be utilized. These requirements are met by jumpering pin 20 to pin 21 and installing DS8835Ns in sockets U5 and U6. Port B must be configured for output using non-inverting drivers. This is accomplished by installing a 74LS240 in socket U1 position B. All lines of port C must be configured for output using inverting drivers. Jumpers between pins 5 and 6, pins 1 and 2, pins 7 and 8, and pins 11 and 12 must be installed. Also, DS8835Ns should be installed in sockets U2 and U3. Writing the appropriate control words to the 8255 allows setting of the PPI under program control, within the constraints of the driver hardware.

PPI-2 is unused at present with the exception of bit 0 of port C which provides gate control for the 8253. All ports are hardware configured for output through inverting drivers. Jumpers are installed between pins 34 and 35, pins 38 and 39, pins 22 and 23, pins 26 and 27, pins 28 and 29, and pins 32 and 33. DS8835's are installed in sockets U8, U9, U11 and U12. A 74LS240 is installed in position B of U7. A

jumper from pin 35A to pin 63 connects bit 0 of port C to the 8253. As only one bit of port C is used currently, the hardware configuration of PPI-2 may be altered without consequence, providing that bit 0 of port C remains configured for output.

An RS232-C serial port is provided by an 8251 universal synchronous/asynchronous receiver/transmitter (USART). The USART accepts data characters from the CPU in parallel format and converts them to a serial data stream for transmission. Simultaneously, the USART can receive serial data and convert them to parallel data for the CPU. The CPU may poll the USART's status register to determine whether a character has been received or whether the USART is ready to accept a character for transmission. In addition, the USART has a set of modem control inputs and outputs which provide for handshaking logic between the computer and the peripheral. The transmitter and receiver clocks are tied to the output of counter 2 of the 8253. Thus, baud rates may be altered by reprogramming the 8253 to generate a different rate. The monitor provided by MSC contains all the software necessary for operation of this serial port, including a baud rate search capability.

The 8253 programmable interval timer is a flexible peripheral which is organized as three independent 16-bit counters each with a count rate up to 2 MHz. Each counter may be programmed to any one of five different modes:

Mode 0: Interrupt on terminal count

Mode 1: Programmable one-shot

Mode 2: Rate generator

Mode 3: Square wave rate generator

Mode 4: Software triggered strobe.

The clock input for counters 0 and 2 is the on-board 2 MHz I/O clock. The gate for counters 0 and 1 is provided by bit 0 of port C of PPI-2. The gate for counter 2 is tied high. Counters 0 and 1 are utilized to generate timing interrupts for the electron impact spectrometer scanning routines. Counter 0 is programmed to mode 3 and divides the 2 MHz clock by 2000 providing a 1 kHz output square wave. The output of counter 0 provides the clock input to counter 1. Counter 1 is set to mode 0 and provides an interrupt 3 after counting down the preset number of milliseconds. Counter 2 is reserved for generation of the transmitter and receiver clocks for the USART. Upon system initialization, the monitor programs the counter to mode 3 and divides the input clock by 13, providing an output of approximtely 153800 Hz (the USART divides this rate by 16, yielding a baud rate of 9600, to within acceptable error). The monitor further divides the baud rate until incoming serial data from the terminal can be read without error, thereby searching out the appropriate rate.

The 8214 priority interrupt control unit can accept eight requesting levels, determine the highest priority, compare this priority to a software controlled status register (individual interrupt levels may be masked), and issue an interrupt to the CPU along with vector information identifying the interrupting device. Currently, only interrupt level three is utilized. When interrupt 3 is received by the 8214, an interrupt is sent to the Z80, assuming the interrupt is not masked. If the interrupt flip-flop within the Z80 is not set, the Z80 generates a special op code fetch cycle. During this cycle, the I/O request signal

becomes active instead of the usual memory request signal. At this time, the 8214 places an 8-bit instruction (RST03) on the data bus. Execution of this instruction follows yielding in effect a Call 0018H. The CPU places the current program counter position onto the stack and jumps to location 0018H and begins execution. Since in our system this location is in PROM only a jump vector to another location in RAM is present. This RAM location (3FE6H) contains another jump instruction, however, in this case the destination address may be altered under program control to the address of the interrupt service routine.

The MSC 8001 interfaces to other boards via the Intel MULTIBUS.[7] The MULTIBUS provides a well-defined bus structure which is capable of multiprocessor configurations and high speed direct memory access (DMA) operations. (The EIS system does not utilize this capability since only the MSC 8001 may operate as a bus master.) The MULTIBUS convention includes 16 address lines, 16 data lines (only the lower 8-bits are used in the EIS system), and 8 interrupt levels. Additional lines provide bus arbitration and control signals. A listing of the MULTIBUS pin assignments appears in table 3. Note that all signals are active low, whereas most signals from the processor and peripherals are active high.

In order to provide analog outputs from the computer system to the analyzer bus of the spectrometer providing energy loss analysis and to provide oscilloscope and X-Y recorder display of data, it is necessary to convert digital signals from the computer to analog outputs. The Analog Devices RTI 1201 provides four 12-bit D/A converters as well as four high current logic drivers. DAC1 provides the voltage ramp to the

Table 3

MULTIBUS PIN ASSIGNMENT

	(COMPONENT SIDE)			(CIRCUIT SIDE)		
	PIN	MNEMONIC	DESCRIPTION	PIN	MNEMONIC	DESCRIPTION
Power Supplies	1	GND	Signal GND	2	GND	Signal GND
	3	+5	+5 VDC	4	+5	+5 VDC
	5	+5	+5 VDC	6	+5	+5 VDC
	7	+12	+12 VDC	8	+12	+12 VDC
	9	-5	-5 VDC	10	-5	-5 VDC
	11	GND	Signal GND	12	GND	Signal GND
Bus Controls	13	BCLK/	Bus Clock	14	INIT/	Initialize
	15	BPRN/	Bus Priority In	16	BPRO/	Bus Priority Out
	17	BUSY/	Bus Busy	18	BREQ/	Bus Request
	19	MRDC/	Memory Read Command	20	MWTC/	Memory Write Command
	21	IORC/	I/O Read Command	22	IOWC/	I/O Write Command
	23	XACK/	XFER Acknowledge	24	INH1/	Inhibit 1 Disable RAM
	25	AACK/	Special Acknowledge	26	INH2/	Inhibit 2 Disable PROM or ROM
	27		Reserved	28		Reserved
	29		Reserved	30		Reserved
	31	CCLK/	Constant Clk	32		Reserved
	33		Reserved	34		Reserved
Interrupts	35	INT6/	Parallel Interrupt Requests	36	INT7/	Parallel Interrupt Requests
	37	INT4/		38	INT5/	
	39	INT2/		40	INT3/	
	41	INT0/		42	INT1/	
Address	43	ADRE/	Address Bus	44	ADRF/	Address Bus
	45	ADRC/		46	ADRD/	
	47	ADRA/		48	ADRB/	
	49	ADR8/		50	ADR9/	
	51	ADR6/		52	ADR7/	
	53	ADR4/		54	ADR5/	
	55	ADR2/		56	ADR3/	
	57	ADR0/		58	ADR1/	
Data	59	DATE/	Data Bus	60	DATF/	Data Bus
	61	DATC/		62	DATD/	
	63	DATA/		64	DATB/	
	65	DAT8/		66	DAT9/	
	67	DAT6/		68	DAT7/	
	69	DAT4/		70	DAT5/	
	71	DAT2/		72	DAT3/	
	73	DAT0/		74	DAT1/	
Power Supplies	75	GND	Signal GND	76	GND	Signal GND
	77	-10*	-10 VDC	78	-10*	-10 VDC
	79	-12	-12 VDC	80	-12	-12 VDC
	81	+5	+5 VDC	82	+5	+5 VDC
	83	+5	+5 VDC	84	+5	+5 VDC
	85	GND	Signal GND	86	GND	Signal GND

*For MDS 800 compatibility.

[from Ref. 7]

analyzer bus. DAC3 and and DAC4 provide the X and Y axes for the oscilloscope and recorder. DAC2 is currently unused. Also, two of the logic drivers are also used. Driver 0 is connected to a relay which switches the X and Y axes outputs between the oscilloscope and the plotter. Driver 1 is connected to another relay which switches in the jump voltage. In addition, the RTI 1201 includes a socket for a 2708 EPROM.

The RTI 1201 interfaces to the CPU as a 1K byte block of memory (see memory map). The first 1008 addresses of the block access the on-board PROM. The remaining 16 addresses are reserved for DAC and driver data. The advantage of utilizing a memory mapped I/O configuration is the increased flexibility of the 8080 instruction set for memory transfer operations. The RTI 1201 is capable of operation in either the third or fourth 1K block of each 4K block of memory. The specific block is set to a base address of EC00H by means of jumpers between pins 5 and 12, pins 6 and 11, pins 7 and 10, and pins 61 and 62. (Note: The RTI 1201 User's Guide has numerous errors regarding address selection. The preceding connections are the correct ones.) The DACs may be configured for any of several different voltage ranges. All four DACs are currently set to operate over the range 0 - 10V. This was accomplished by jumpers between pins 1 and 2, pins 13 and 14, pins 4 and 5, pins 20 and 21, pins 7 and 8, pins 27 and 28, pins 10 and 11, and pins 34 and 35.

Data storage capability is provided by the iCOM FD3712 floppy disk system and interface board. The FD3712 is a dual 8" floppy disk drive for use with IBM 3740 compatible diskettes. The IBM 3740 format specifies that the single-density, single-sided diskettes are organized into 77 concentric circular tracks. Each track is further divided into 26

sectors of 128 bytes each (the number of sectors and the number of bytes per sector are determined when the diskette is formatted not by physical characteristics of the diskette), yielding a storage capacity per diskette of 256K bytes. All formatting and deformatting is done by the controller contained within the dual drive chassis. In addition, this controller performs track seek, and verification as well as cyclic redundancy check generation and verification. The controller contains independent input and output buffers which each hold one sector of data.

The diskette driver and controller connect to the computer via a MULTIBUS compatible interface card. The interface card contains a 2708 EPROM which provides all the software necessary for interaction with the controller. The EPROM occupies memory locations E800H to EBFFH. This software also requires the use of RAM between 3CDFH and 3CEFH. In addition, the interface card occupies I/O addresses 06, for control and status, and 07 for data transfer.

Software contained on the EPROM uses logical-physical techniques for addressing disk. Sectors on the diskettes are contiguous from 1 - 26. In order to avoid time delays which might occur when accessing consecutive logical sectors due to rotation of the diskettes, software translates a requested logical sector into another physical sector. Table 4 shows the correlation between physical and logical sector numbers. Although IBM 3740 format specifies the physical sectoring of the diskettes, the logical-physical translation is not standardized. When attempting to transfer data on diskettes to systems using a different physical-logical translation, the sectors must be reordered. Table 4 also includes the

Table 4

Physical-Logical Sector Number Translation (Hexadecimal)

Physical	Logical-iCOM	Logical-Intel
1	1	1
2	A	4
3	13	7
4	2	A
5	B	D
6	14	10
7	3	13
8	C	16
9	15	19
A	4	2
B	0D	5
C	16	8
D	5	B
E	E	E
F	17	11
10	6	14
11	F	17
12	18	1A
13	7	3
14	10	6
15	19	9
16	8	C
17	11	F
18	1A	12
19	9	15
1A	12	18

Intel physical-logical correlation for comparison. In addition, directory information is not standardized.

2.4.2 Memory Expansion and Interface Board

Capabilities of the computer system in addition to those possessed by the commercial boards described previously were necessary to complete the data acquisition system. The MSC 8001, providing only 8K RAM, lacks the data storage capability for 4096 channels (the resolution of the 16-bit DAC) with up to one million counts per channel (3 bytes per channel). In addition, it is desirable to free the CPU from direct counting so that display and other control functions may be performed without severely limiting the maximum counting rates. This requires counting circuitry which must be then interfaced to the CPU. Also, a second RS232C port was desired for connection to a printer. In order to meet these needs, I designed a memory expansion and interface board. A diagram of the overall board layout is shown in figure 4. Table 5 lists the components utilized. Detailed schematics are shown in Figures 5 through 8.

The board is wired on a Monolithic Systems MSC 8204 Universal Card. The MSC 8204 provides buffering of MULTIBUS address and data lines as well as transfer acknowledge logic. The MSC 8204 also contains its own bus master control system, however for our application the card is configured as a slave.

The prototyped circuitry I have designed may be divided into four sections:

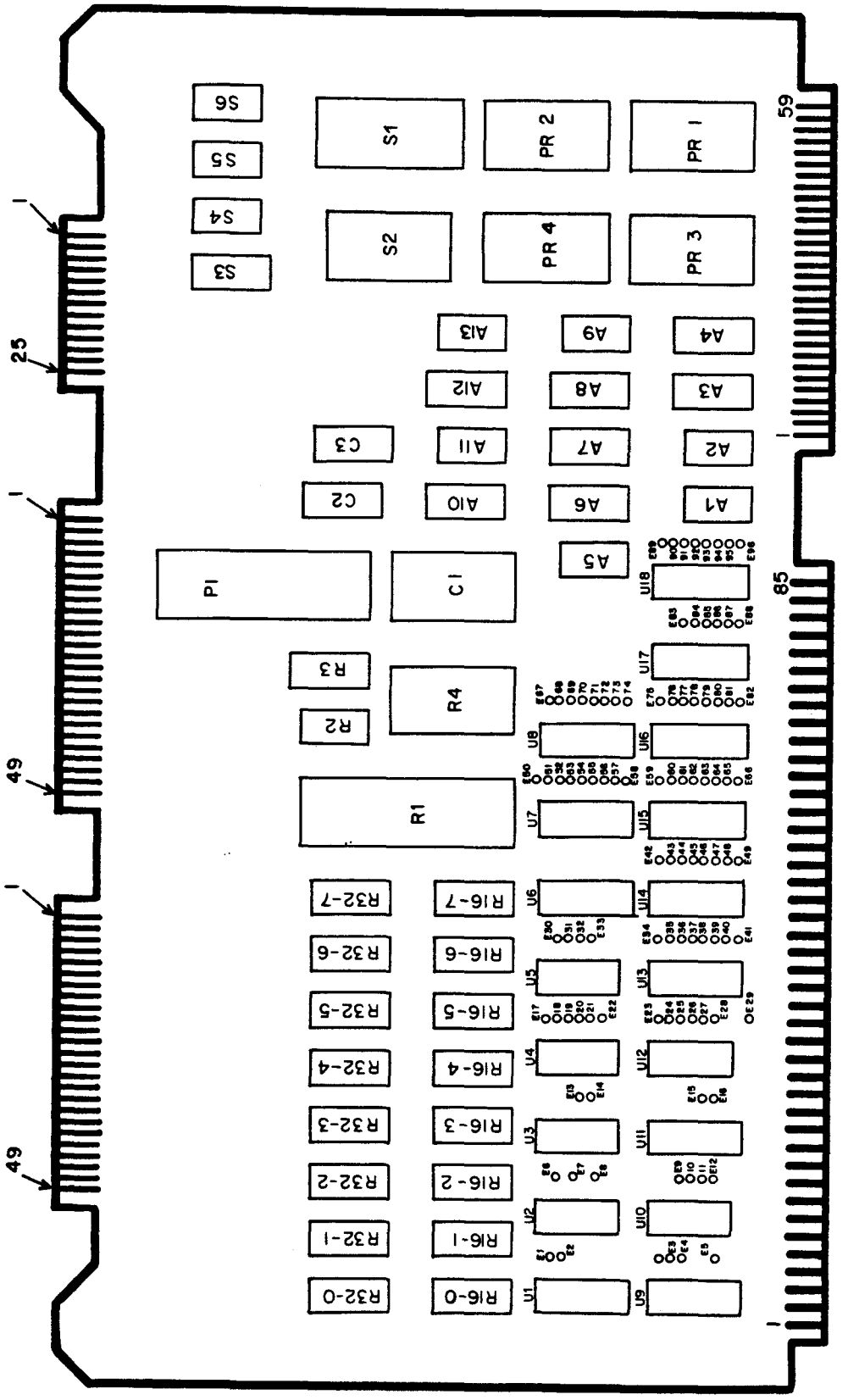

COMPONENT SIDE

MEMORY EXPANSION AND INTERFACE BOARD

Figure 4

Table 5

Memory Expansion and Interface Board Components List

Address Decoding Section

A1	SN7432N
A2	SN7408N
A3	P8205
A4	SN74157N
A5	SN7404N
A6	P8205
A7	16-pin DIP Switch
A8	Beckman 1kΩ Resistor Network
A9	SN74H21
A10	SN74157N
A11	SN7408N
A12	16-pin DIP Switch
A13	SN7400N

16K/32K/48K Ram Section

R1	D8202
R2	Crystek CM2000 20 MHz
R3	SN74157N
R4	P8212
R16-0,7	C2117-4
R32-0,7	D2118-4

4K PROM and RS232C Port

PR1-PR4	Sockets for C2708
S1	P8251A
S2	MC14411P
S3	14-pin DIP switch
S4	Crystek CM2000 1.8432 MHz
S5	MC1489
S6	MC14882

Counter and Parallel Interface

C1	C8253
C2	6N137 and Discrete Components for C3
C3	SN74123
P1	D8255A

Table 5 (continued)

Monolithic Systems Printed Circuitry

U1	SN74S287N
U2	SN74LS04N
U3	DM74LS32N
U4	SN74LS00N
U5	SN74LS164N
U6	Socket for SN74S287
U7	SN74S138N
U8	SN74S138N
U9	SN74LS175N
U10	DM74LS32N
U11	DM8833N
U12	SN7406N
U13 - U18	DS8835N

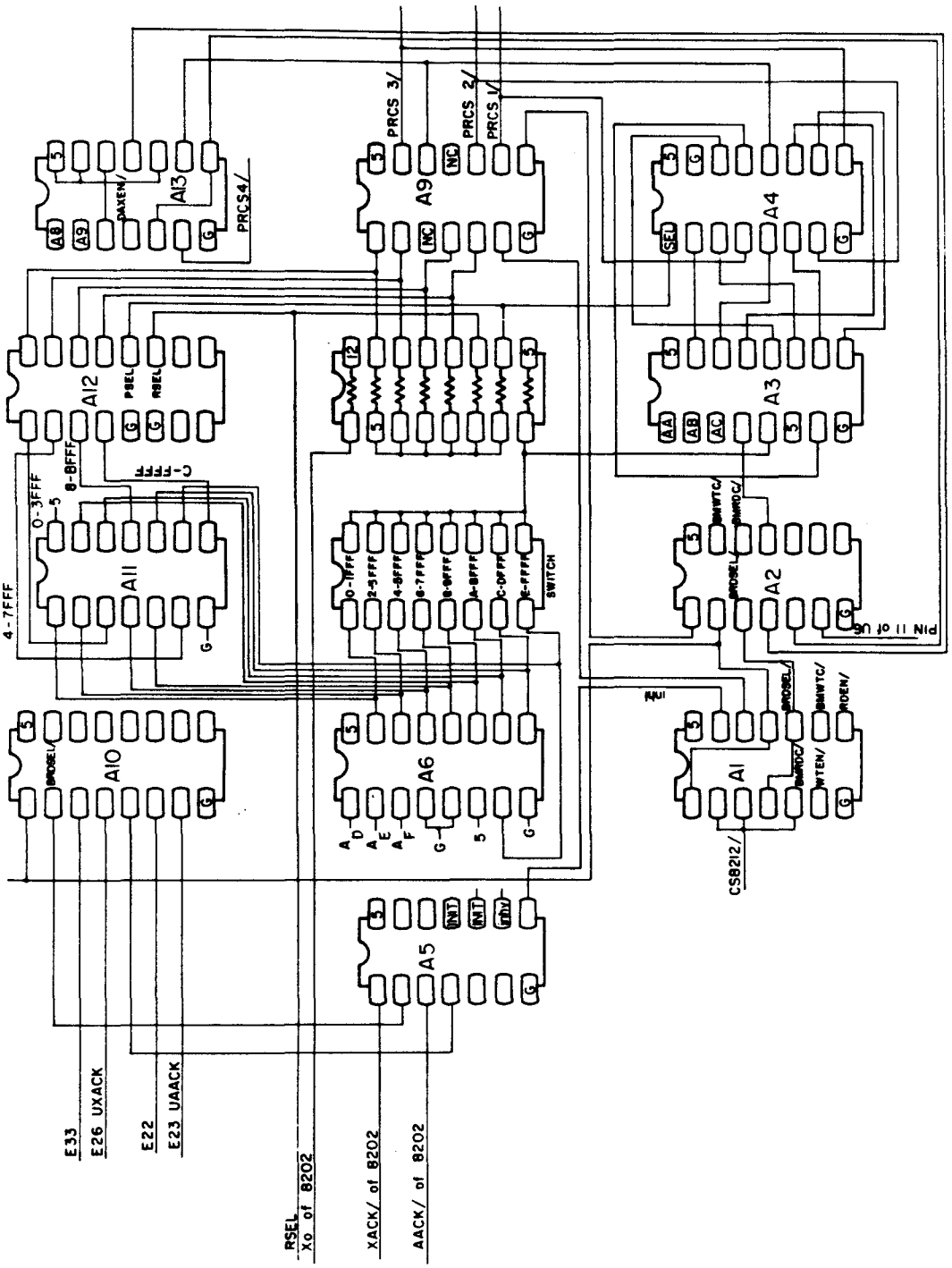

Address Decoding

Figure 5

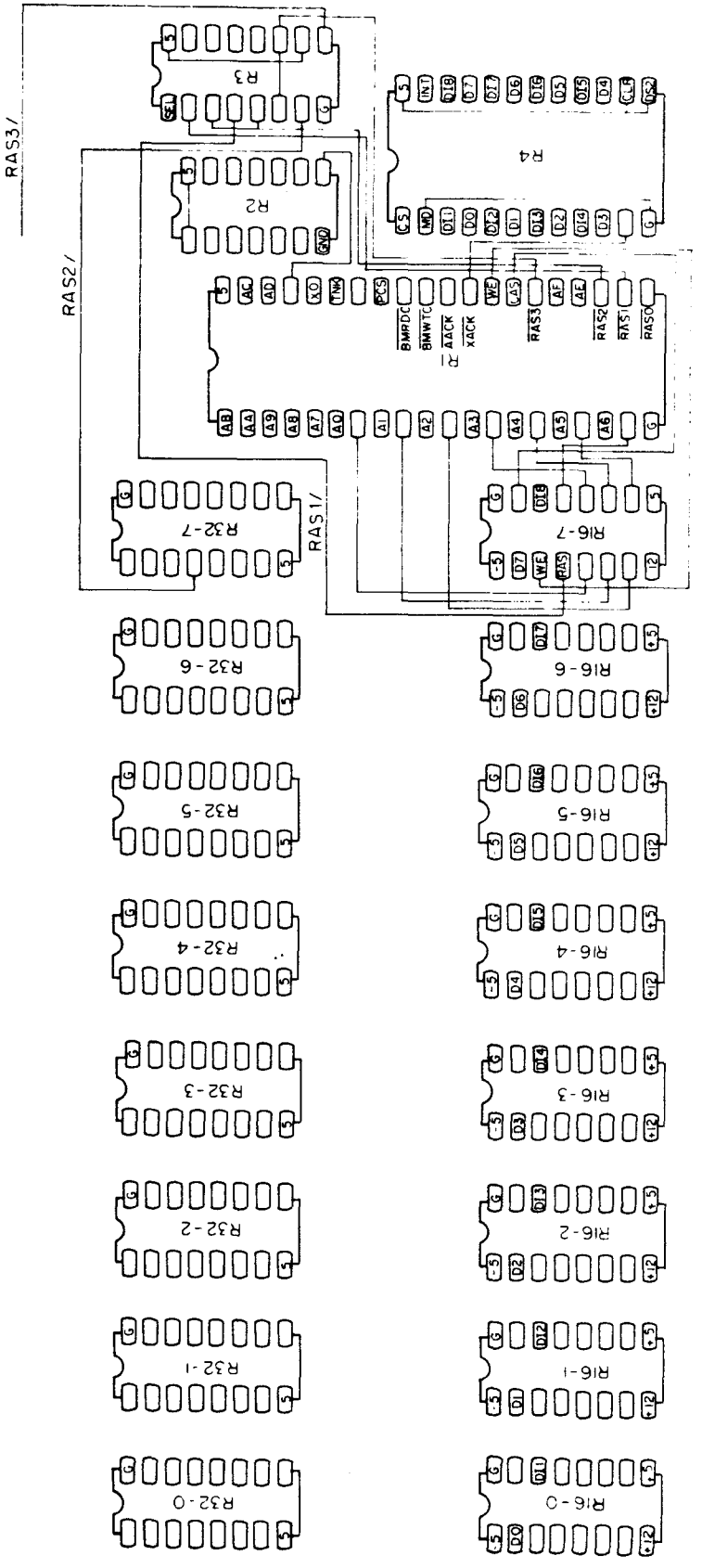

16K-32K RAM

Figure 6

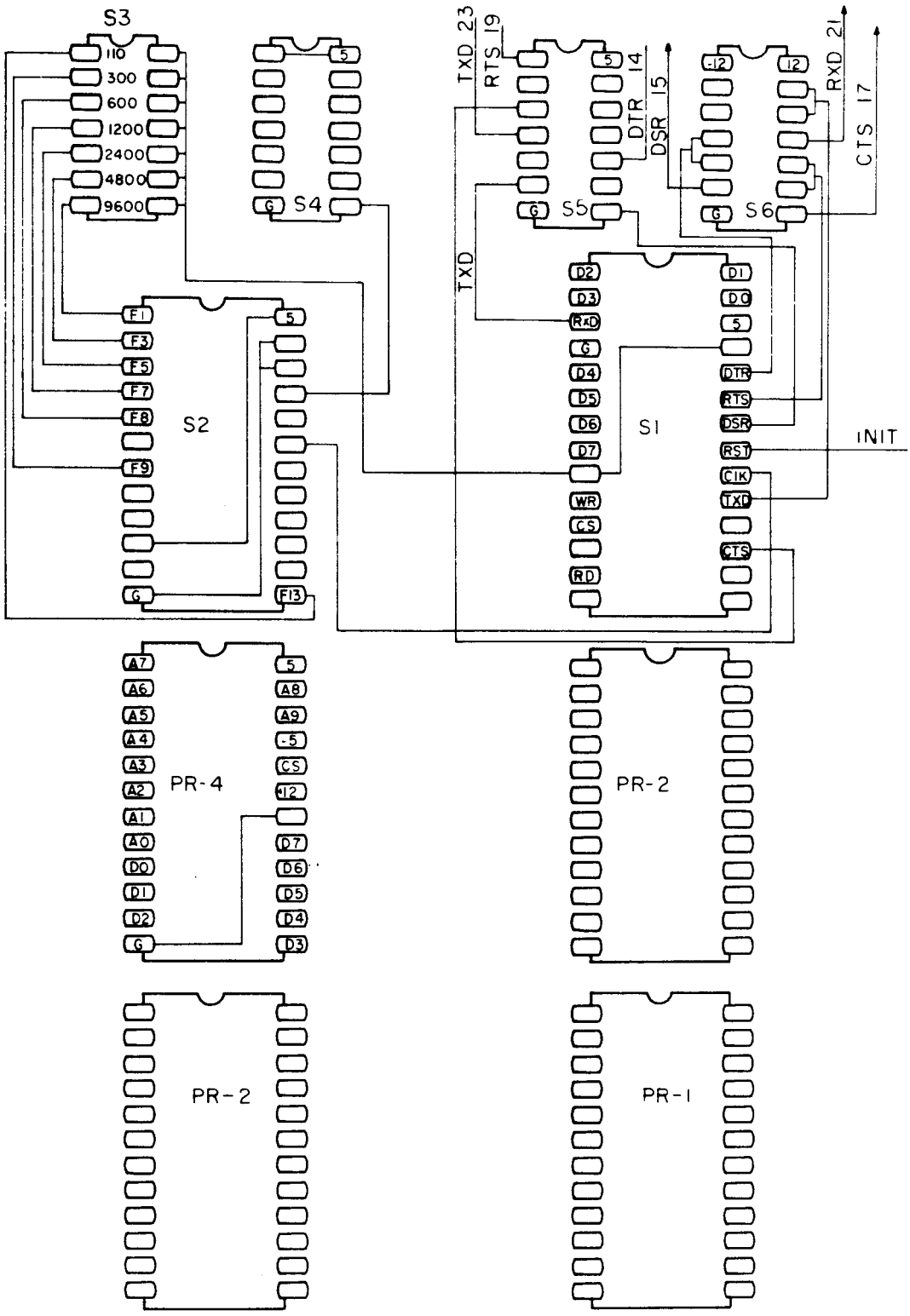

4K PROM and RS232C Port

Fig 7

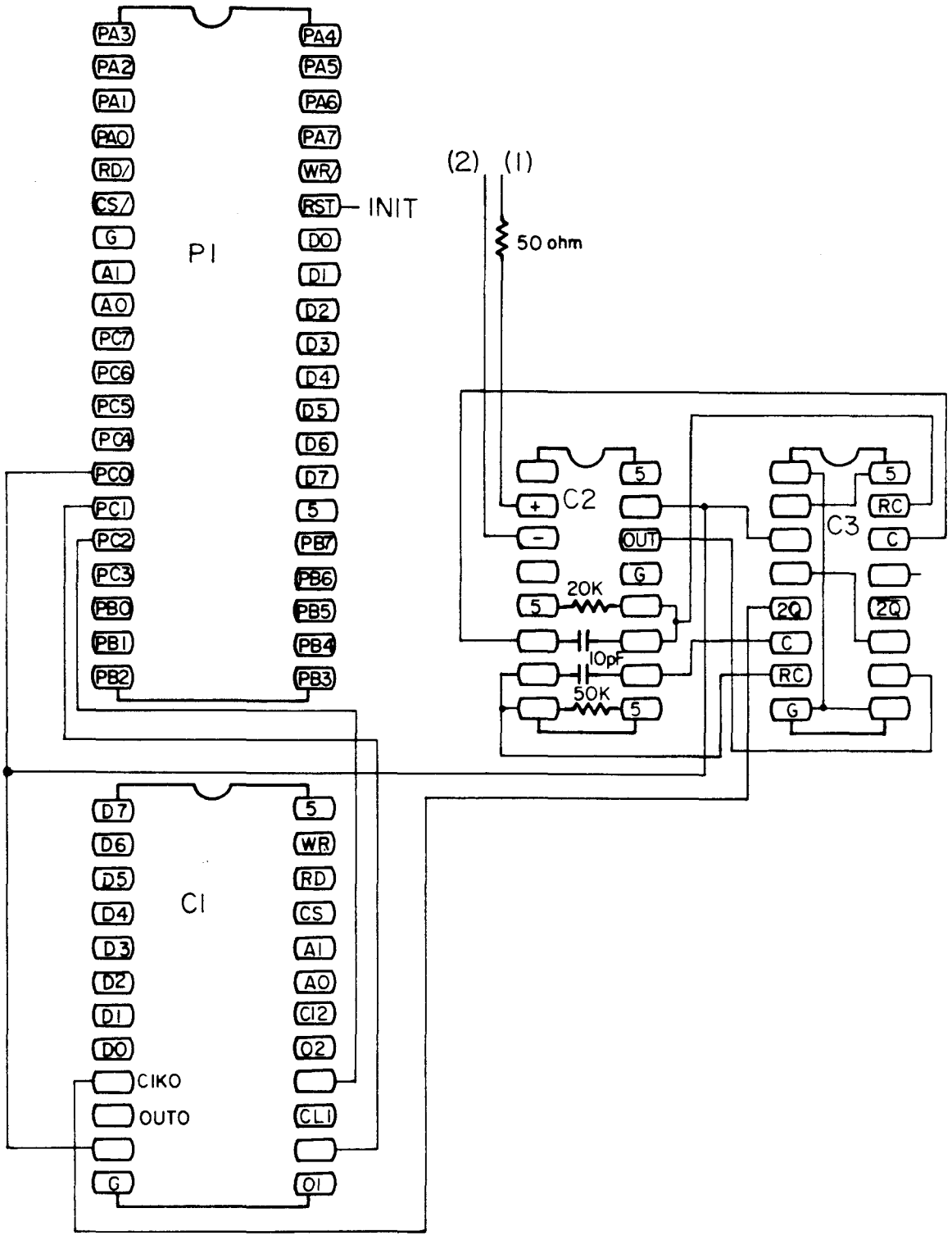

Counter and Parallel Interface

Figure 8

1) Address decoding (figure 5)

2) 16K - 32K RAM (figure 6)

3) 4K PROM and RS232C port (figure 7)

4) Counter and parallel interface (figure 8)

The MSC 8204 provides address decoding circuitry designed for use with 74S287 PROMS, however since we had no facility for programming these PROMS, the MSC 8204 decoding circuitry was left unused. The three high order bits of the 16-bit address (made available by the MSC 8204 circuitry) are connected to an Intel 8205 high speed 1 of 8 binary decoder (A6). The enable inputs (pins 4, 5 and 6) are tied to the appropriate levels such that the chip is always enabled. One of the outputs of the 8205 will be logic level 0 and all other outputs will be logic level 1, depending on the levels of the input address lines. The address is thus decoded into 8K blocks by the 8205. These outputs are connected to a 16-pin DIP switch (A7) which allows selection of the 8K block of memory in which the PROM and memory mapped I/O will lie and also to a 7408 (A11) AND gate which continues the decoding for the RAM. The inputs are connected to the 7408 in pairs of 8K block selects so that outputs of the 7408 select one of four 16K blocks of memory space. These outputs are connected to four levels of a DIP switch (A12) which allows switch selection of the address for RAM. The outputs from the switch are tied through 1KΩ resistors to 5 volts and then are connected to a 7421 (A9) four input AND gate. The outputs of the switch are resistively coupled to 5 volts so that a high level will always appear on the input of the 7421 if a switch is open. However if one or more of the switches are

closed the 7408 will pull the appropriate input of the 7421 low. One switch is closed for each 16K of RAM on the board. The output of the 7421 is OR'ed with the inverted inh1/(RAM inhibit) line on the bus so that a device select to the 8202 dynamic RAM controller occurs when the appropriate address is selected only if the RAM inhibit line remains inactive. (This allows other devices to occupy address space that is overlayed by blocks of RAM.)

The outputs of the PROM addressing DIP switch (A7) are tied together and are connected to 5 volts through a 1KΩ resistor. By closing one of the eight switches, the 8K block of memory that will be occupied by the four PROM sockets and the memory mapped I/O may be chosen. When an address within the 8K block selected appears on the bus, a second 8205 (A3) is enabled. The 8205 decodes the address further yielding device selects for eight 1K blocks of memory. These eight outputs are connected to a 74157 quadruple 2 line-to-1 line data selector/multiplexor (A4). The state of switch five of A12 determines whether the addresses of the four 1K EPROM's will lie in the upper (if switch five is open) or lower 4K of the 8K block selected by A7. Outputs one through three of A4 are connected to inputs of A9 and to the chip selects of PR1 through PR3, respectively. Output four of A4 is connected to A9 and to the 7400 (A13). This level is inverted by the 7400 and is then connected to a 7408 (A2) positive-AND gate where it is ANDed with the inverted NAND of address lines A8 and A9. The associated output of A2 is tied to pin 11 of U6 (part of the MSC 8204 circuitry). This provides the gate input to U7, a 74S138 (equivalent to a P8205), which when gated gives a low output on

one of eight output lines depending on the status of address lines A5, A6 and A7. Output number seven (selected when A5=A6=A7=1) is connected to the gate DAXEN/ of another decoder, U8, by jumpering pins E57 to E50. U8 generates eight device selects each corresponding to four addresses which provide selects for the memory mapped I/O devices. The DAXEN/ line is also NANDed with the inverted output four of A4, yielding the device select for PR4, reserving 32 of the addresses of the 1K block in which PR4 resides for memory mapped I/O. Further decoding of the 32 addresses is accomplished by U8, yielding device selects for S1, C1 and P1.

Chip A1 is used to generate control signals such as BRDSEL/, RDEN/ and WTEN/ used by the MSC 8204 circuitry to switch address and data line buffers among three state, input, or output configurations. Chip A10 is a 74157 multiplexor which determines the source of the bus transfer acknowledge signals XACK/ and AACK/. When RAM is selected, these signals are provided by the 8202 dynamic RAM controller. Otherwise the signals are provided by a shift register U5 which provides AACK/ 800 nanoseconds following the device select and XACK/ 1000 nanoseconds following the device select.

The second section consists of circuitry providing 16K/32K/48K dynamic random access memory. The heart of this section is the Intel 8202 dynamic RAM controller (R1). Dynamic RAM offers significant advantages in terms of reduced power consumption, higher information density, and lower cost. The price for these advantages is that bits are stored on capacitor-type cells which require refreshing periodically

(about every 20 ms). The 8202 performs all the system control support to operate and refresh up to 64K bytes of 2117 or 2118 (16Kx1) dynamic RAM, substantially reducing the complexity of using dynamic RAM. The 8202 provides the address bus multiplexing necessary for 2117's or 2118's, provides all necessary $\overline{CAS}$ (column address strobe), $\overline{RAS}$ (row address strobe, one $\overline{RAS}$ line is provided for each 16K of memory), $\overline{WE}$ (write enable) and $\overline{CS}$ (chip select) signals, provides failsafe refresh, and allows direct interface to the 8080A bus. Timing for the 8202 is provided by a Crystek 20 MHz oscillator (R2).

The dynamic RAM utilized (currently 2117's for the first 16K and 2118's for the second 16K) are organized as 16K x 1 bit so one chip is utilized for each one of the eight bits of the 8080A/Z80 data word for each 16K of memory. (Note: The 2117 and 2118 are pin-to-pin compatible except for power connections.) The 14 address bits are multiplexed into 7 address lines by the 8202. The two 7-bit address words are latched into the RAM chips by the $\overline{RAS}$ and $\overline{CAS}$ signals, also provided by the 8202. Refreshing requires use of the $\overline{RAS}$ signal only. The $\overline{CAS}$ signal controls the output of the RAM. When $\overline{CAS}$ goes low, a datum is latched on the output and remains valid while $\overline{CAS}$ is low (about 250 nsec for our system). Since the data is not valid long enough for transfer to the CPU, the data must be latched onto the MULTIBUS. Latching of output data is provided by an 8212 8-bit input/output port (R4). The 8212 latches the data when the XACK/signal from the 8202 goes low, indicating a valid datum is available from the RAM. The chip select for the 8212 is provided by OR'ing the 8202 chip select with the BMRDC/ (board memory read command) so that the

8212 is selected only during RAM read cycles. Write cycles are accomplished without the need for any additional circuitry.

The 8202 dynamic RAM controller decodes the address and selects a bank of RAM corresponding to that address when the 8202 is selected (i.e. $\overline{RAS0}$ may be utilized for a bank of RAM from 0000H-3FFFH only regardless of what addressing yields a chip select to the 8202). Therefore, in order to allow switch selecting of the RAM address it was necessary to add a 74157 multiplexer (R3) which, depending on the state of switch six of A12, sets the base address of the RAM to either the second or third 16K block of memory. Of course, if the base address is set to the third block of 16K, the maximum dynamic RAM usable is 32K.

The third section consists of 4K EPROM sockets and an RS232C port. The PROM sockets may be used on 2708 UV EPROMS. All 1024 bytes of PROMS PR1, PR2, and PR3 may be read. Only the first 992 bytes of PR4 may be accessed since 32 bytes of that 1K block of memory are reserved for I/O devices.

The RS232C port is provided by an 8251 universal synchronous/asynchronous receiver/transmitter (S1), a MC14411 baud rate generator (S2), a 1.8432 MHz oscillator (S4) which provides the clock for S2, and a DIP switch (S3) which allows selection of the baud rate from one of the following rates: 110, 300, 600, 1200, 2400, 4800 or 9600 baud. Buffering of input and output signals as well as conversion of the 8251 TTL output levels to/from standard EIA levels are accomplished by a MC1489 EIA line receiver (S5) and a MC1488 EIA line driver (S6).

The 8251 is programmed by the CPU to operate using numerous different

serial data transmission techniques. The 8251 accepts 8-bit data from the CPU in parallel format and then converts them into a serial data stream for transmission. Simultaneously, it can receive serial data and convert them into parallel data characters for the CPU. The 8251 also indicates to the CPU when it is ready to accept another character for transmission or when it has received a character for the CPU. In addition, the 8251 provides and accepts all the normally needed RS232C handshaking signals. A list of the RS232C signals normally needed for connection of a CPU to a peripheral such as a terminal or printer (a subset of the full EIA RS232C specification), their direction, and EIA 25-pin D connector pin assignments are given in Table 6.

The remaining section consists of a parallel interface and counting circuitry for obtaining data from the electron impact spectrometer. The parallel interface consists of a 8255A programmable peripheral interface (P1). The 8255A provides 24 I/O pins which may be programmed for many different modes of operation. Currently, only three of the I/O pins are utilized to provide gate control for the 8253 programmable interval timer (C1). All three pins belong to port C, requiring programming the 8255 for output on these lines. No further restrictions on ports A or B or the high order bits of port C currently exists.

The 8253 programmable interval timer (C1) is organized as three independent 16-bit counters, each with a count rate of up to 2 MHz (only counter 0 is currently used). Each counter may be programmed to one of six modes:

Table 6

RS232C Signals

Signal	Direction	Pin #
Protective Ground		1
Transmit Data (TXD)	To CPU	2
Receiver Data (RXD)	From CPU	3
Request to Send (RTS)	To CPU	4
Clear to Send (CTS)	From CPU	5
Data Set Ready (DSR)	From CPU	6
Signal Ground		7
Carrier	From CPU	8
Data Terminal Ready (DTR)	To CPU	20

1. Interrupt on Terminal Count
2. Programmable One Shot
3. Rate Generator
4. Square Wave Rate Generator
5. Software Triggered Strobe
6. Hardware Triggered Strobe

The counters are loaded with an initial count by the CPU. Following enabling,each counter decrements the initial count on each negative going edge of its associated clock. The counters may be used as event counters, as in the present application, by programming an initial count of FFFFH then after a given time the CPU may read the current contents of the count register. The complement of the current count obtained is the number of events which have occurred minus one. A peculiarity of the 8253 is that the first event of a cycle does not decrement the count, making it impossible to distinguish between zero and one counts. This problem is overcome through the use of additional circuitry (C3) which generates one pulse approximately 200 nsec following enabling of counter 0. In addition, C3, a 74123 monostable multivibrator, buffers input pulses which come through a Hewlett Packard 6N137 optical isolator (C2) yielding pulses with faster rise and fall times than C2 gives and all of equal width. Note that the current configuration precludes a count greater than 65,535 so the channel gate time should be judiciously chosen.

2.4.3 EIS Scan Circuit

A 0-10V ramp voltage for the analyzer bus is generated by the

computer through the DAC1 output of the Analog Devices RTI 1201. This output is connected to the scan circuit (Figure 9) which provides switch selectable voltage gain factors from 1 to 16 and optical isolation of the computer output from the remainder of the instrument thereby eliminating ground loops and protecting the computer circuitry from any possible shorts within the instrument.

Isolation and voltage gain by factors of 1, 2, 4 or 8 are provided through the use of a Burr Brown optically coupled linear isolation amplifier model 3650KG. Power for the input side of the amplifier is provided by the ±15 V outputs of a DC/DC converter on the RT1 1201. The 0 - 10 V output from the 12-bit DAC1 (scan input) is connected through a switch selectable input resistance of 125KΩ, 250KΩ, 500KΩ, or 1MΩ to the inverting input of the 3650. Since the effective feedback resistance of the amplifier is 1MΩ, the voltage gain is 8, 4, 2 or 1, respectively. The input offset voltage may be nulled with the 50KΩ trimpot.

The output stage of the isolated amplifier is powered by a Burr Brown model 700 isolated DC-to-DC converter. The model 700 converts a +10-18V DC input to an isolated dual output of the same value. The 100Ω resistors and the 100 μF tantalum capacitors reduce the amount of voltage ripple. The output stage offset of the isolated operational amplifier is nulled with a 10KΩ trimpot to V-. The output of the isolated amplifier varies from 0 to -10V and is completely isolated from ground. (Note: If gain is used at the input stage, the maximum number of channels scanned must be reduced by a corresponding factor in order to avoid saturation of the isolated op amp, i.e. 4096 channels for gain = 1 or 512 channels for gain = 8.)

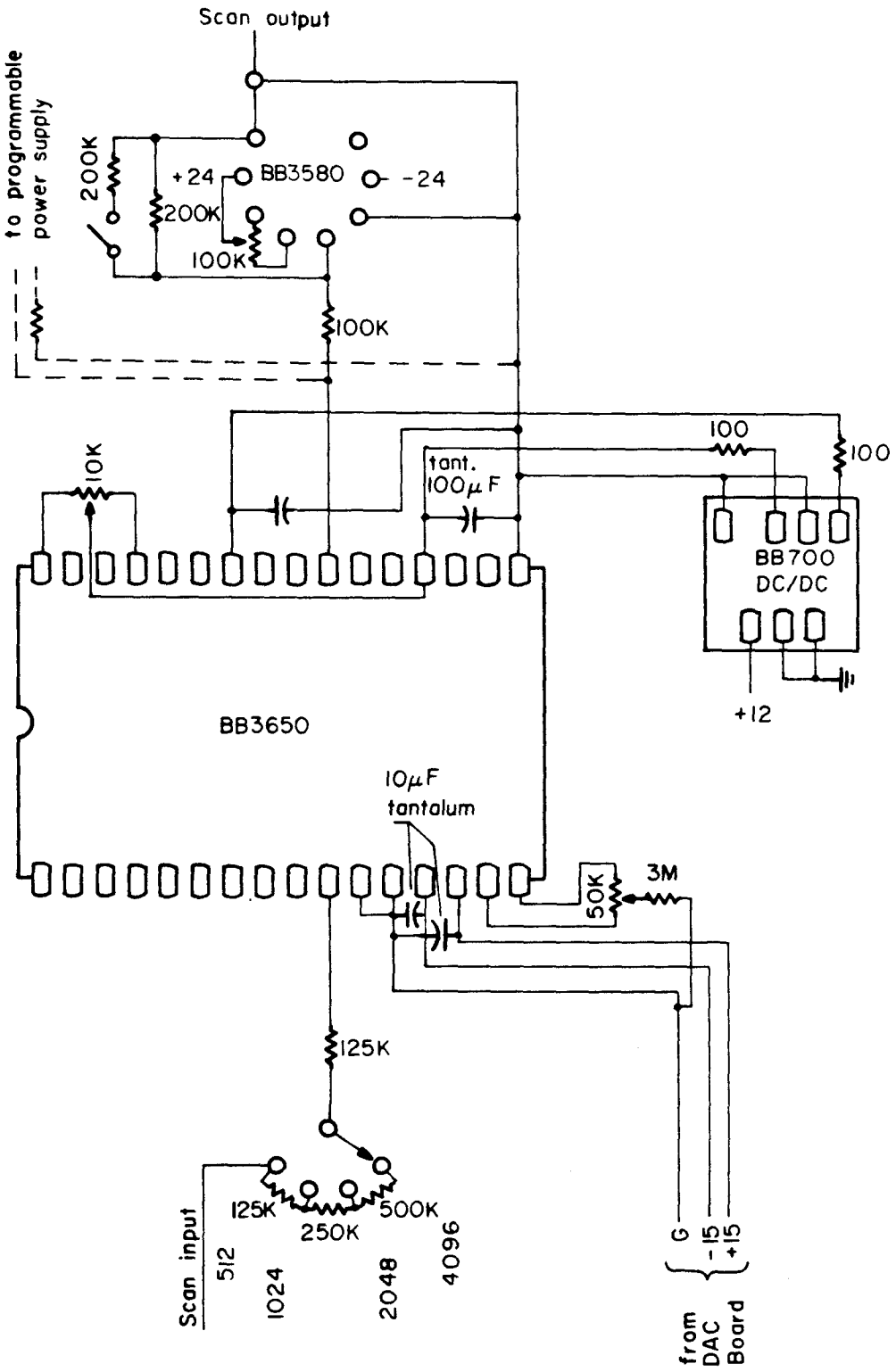

Scan Circuit

Figure 9

The output of the isolation amplifier is then connected to the inverting input of a Burr Brown model 3580J high voltage operational amplifier through a 100K resistor. The feedback resistance for this amplifier is selectable to give a gain of either 1 or 2, yielding an output to the analyzer bus of either 0 - 10V or 0 - 20V. The op amp offset may be nulled using the 100K trimpot connected to +24V DC. The overall function of the scan circuitry then is to provide a voltage ramp of 0 - 10V 2.5 to 20 mV per channel or 0 - 20V at 5 to 40 mV per channel.

2.4.4 Deflector Power Supplies

Bias voltages for two pairs of deflectors within up to four different lens elements are provided by the deflector power supply circuitry. At the heart of the circuit is the Burr Brown model 710 quad isolated DC/DC converter. The model 710 converts +15V DC to four dual isolated outputs of the same value as the input voltage. Short circuit protection for the DC/DC converter is provided by the components on the +15V DC input. Tantalum capacitors on the outputs from the DC/DC converter reduce output ripple. Each dual output powers two identical sets of the circuitry shown on the right-hand side of Figure 10, providing bias voltages for two pairs of deflectors.

The ±15 VDC from the DC/DC converter provides power for a Raytheon RC4194 dual tracking voltage regulator and a Texas Instruments TL022C dual low-power operation amplifier. The RC4194 is set to provide a very stable 10V output with the 25.2KΩ resistor. The regulated 10V DC outputs are connected to a 20KΩ potentiometer so that a potential at the

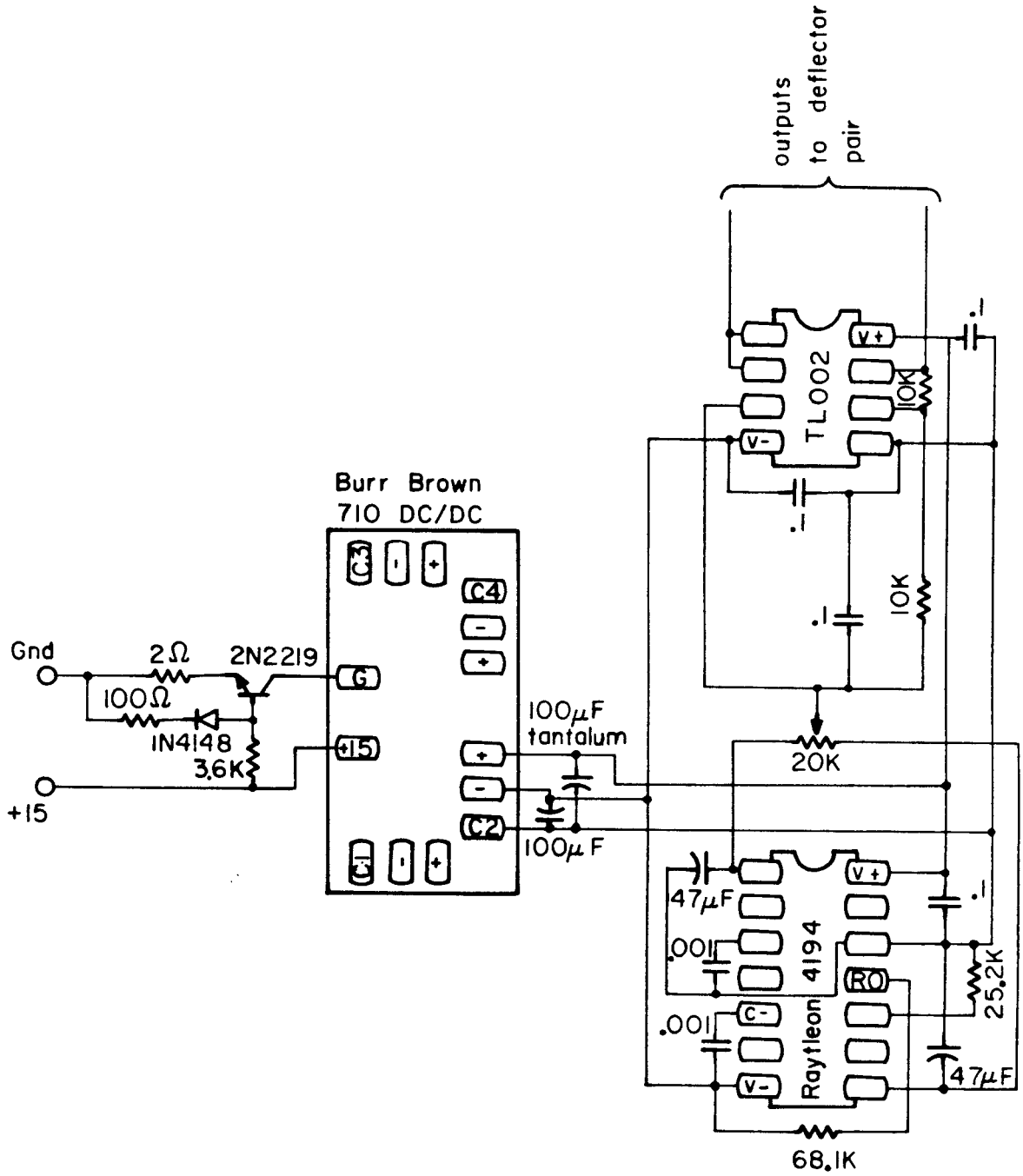

Deflector Supplies

Figure 10

wiper between +10V and -10V may be selected.

The wiper potential is then input into the TL022. The TL022 is configured so that one operational amplifier operates as a voltage follower (gain = +1) and the other amplifier operates as a voltage inverter (gain - -1). Thus, the outputs to a pair of deflectors are +V and -V where $-10 \leq V \leq 10$V DC relative to the lens potential, providing a maximum deflecting potential of 20V DC.

2.4.5 Pulse Amplifier and Discriminator

A new pulse amplifier and descriminator (PAD) was designed to replace the Mosher-Mason design used previously. The new design is significantly less prone to oscillation at low threshold settings. In addition, the reduced bulk enables mounting the PAD on the main flange of the instrument so the device is less susceptible to EMI pickup. The 12V relatively high current output pulses are suitable for driving high speed optical isolators so the computer system may be completely electrically isolated from the instrument. A schematic is shown in Figure 11.

The preamp is an Analog Devices model 528JH high speed, precision, FET-input operational amplifier. This amplifier combines a wide bandwidth (10 MHz) with an extremely low input offset current (5pA). In order to take advantage of the speed of the amplifier, the electron multiplier circuit has also been altered (Figure 12) to reduce the width of spiraltron output pulses. The schematic shows a configuration providing an increased slew rate (100 - 140 V/μsec) and bandwidth (25 MHz) as well as allowing zeroing the very small input offset. These additional

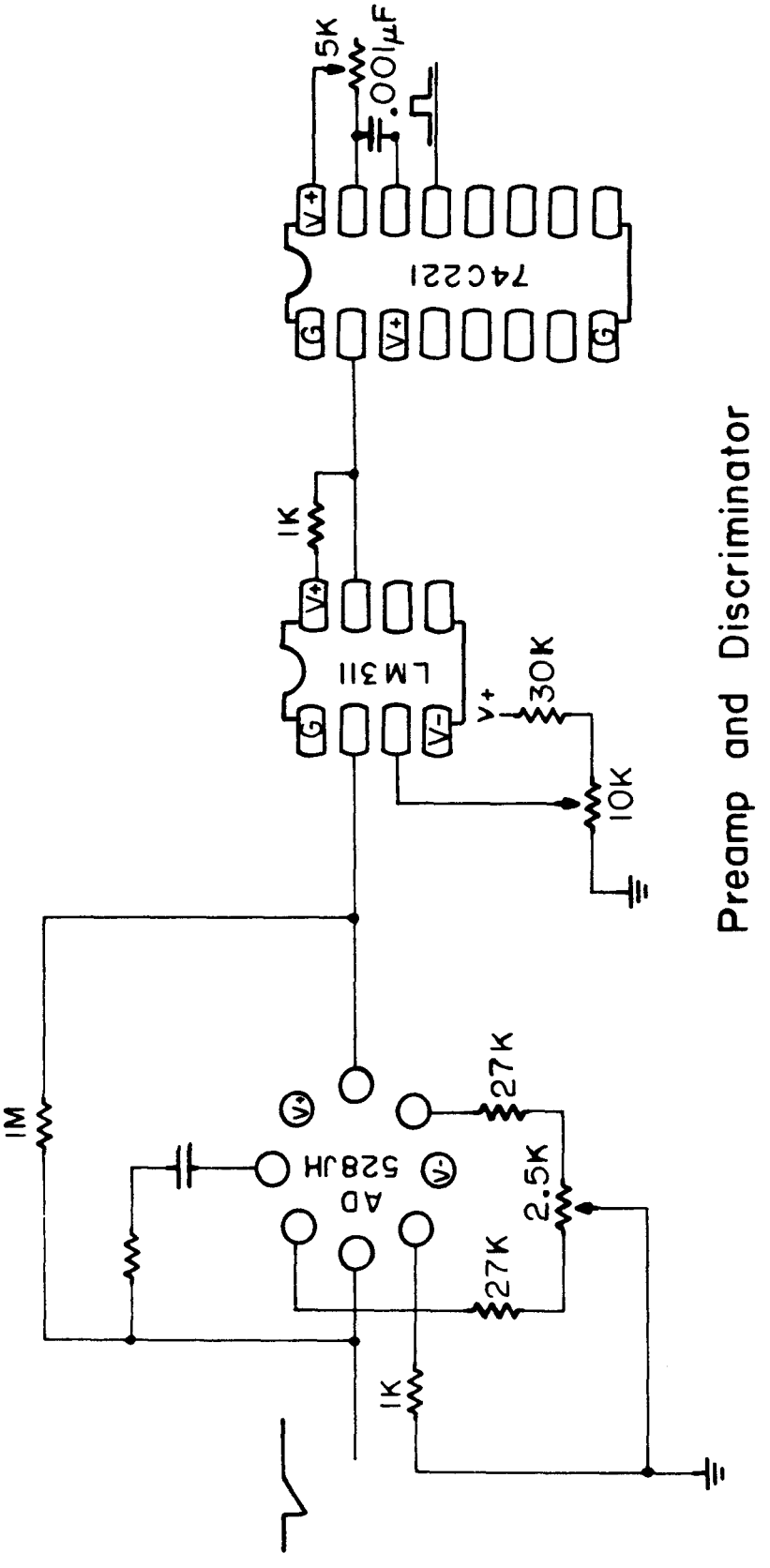

Preamp and Discriminator

Figure 11

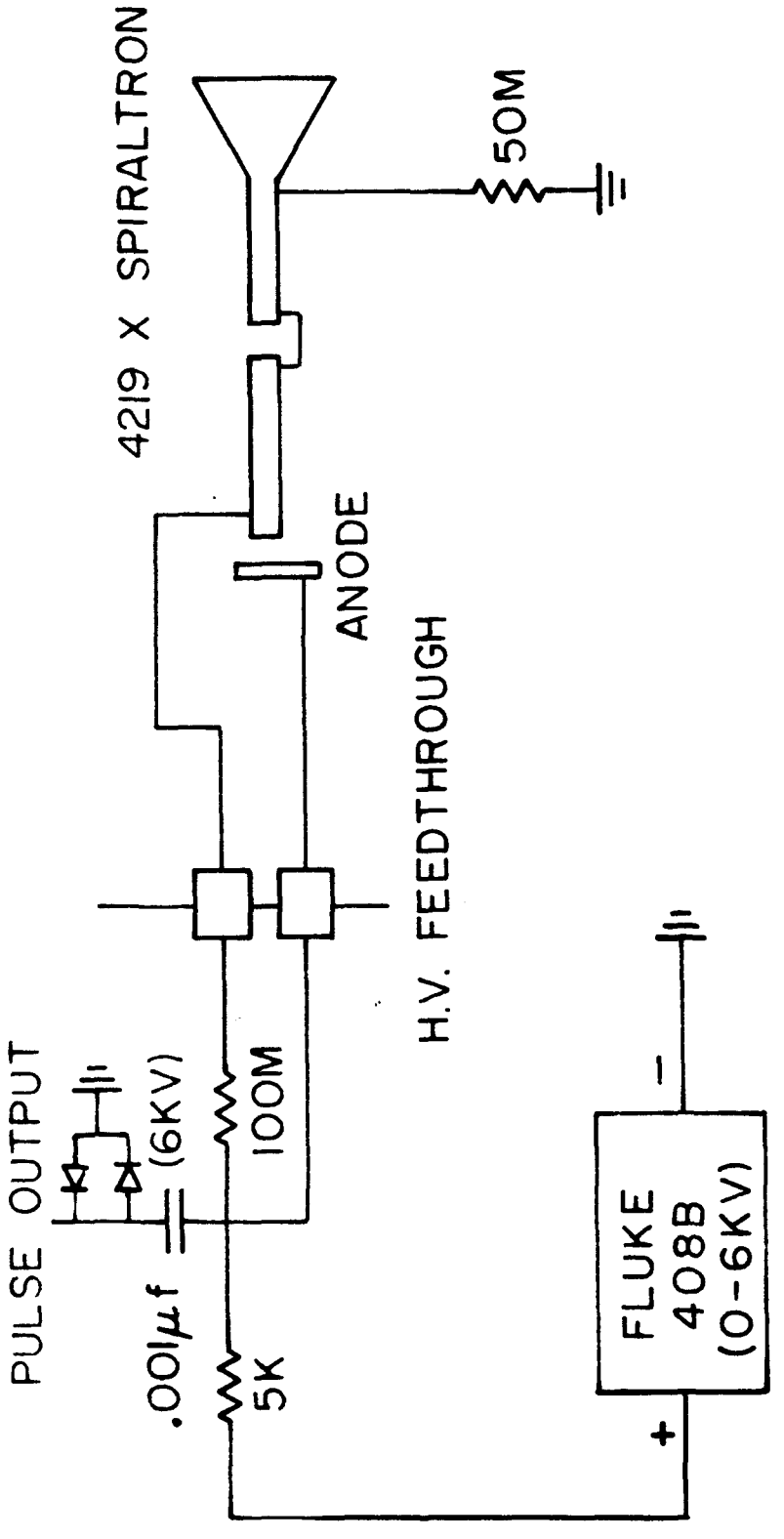

FIGURE 12 ELECTRON MULTIPLIER CIRCUIT

components between pins 2 and 8 and between pins 1 and 5 are optional.

Pulses of about 5 millivolts from the electron multiplier circuit are amplified to 1 - 3 volts by the operational amplifier. Discrimination of pulses is accomplished through the use of the LM311 differential comparator. The threshold is adjusted with a 10KΩ potentiometer.

The variable width pulses from the comparator are input to a MM74C221 monostable multivibrator which provides ∿12V pulses of constant width (adjustable to 5μsec with the 5K trimpot), which may then be transmitted to the data acquisition system with negligible losses or EMI pickup. A printed circuit board for the PAD has been laid out by Dr. David Edmonsen.

2.4.6 PROM Programmer

The microcomputer systems utilized for data acquisition and experimental control for both electron impact spectroscopy and laser spectroscopy each possess a (PROM) resident monitor and reserve memory space for additional PROM resident software. In order to alter the monitor routines or to effectively use memory space, a capability for programming 2708 and 2716 UV erasable PROMs was necessary. I therefore designed a PROM programmer to meet these needs. A schematic is shown in Figure 13.

The PROM programmer makes use of the 8255 parallel peripheral interface number one on the main processing board, the Monolithic Systems MSC8001, for data transfer. Drivers on the MSC8001 for the three 8-bit ports must be installed as follows: inverting drivers for ports A and C and noninverting drivers for port B. Port A is used for address and data transfer between the programmer and the computer. Ports B and C provide control signals to the programmer.

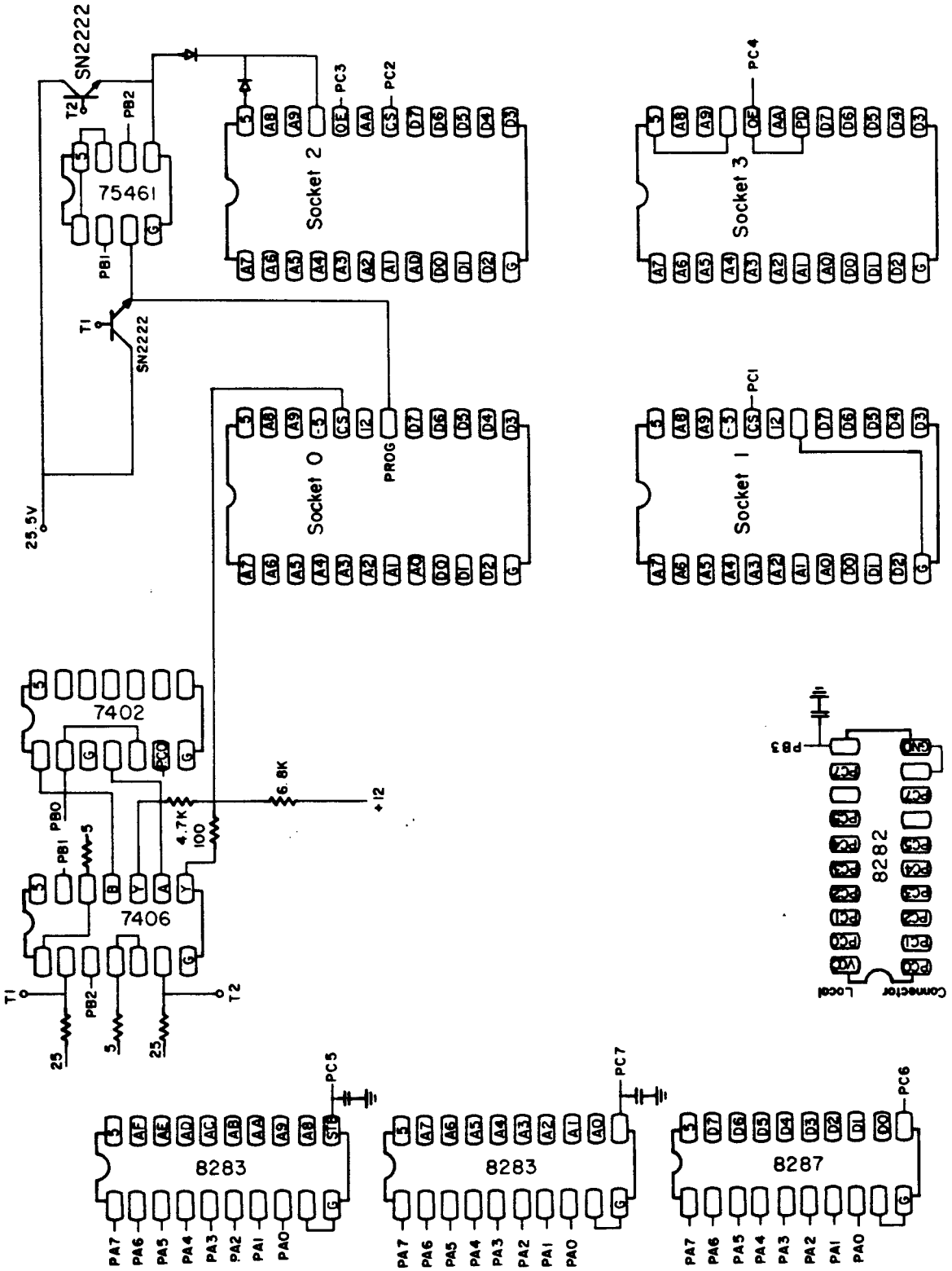

PROM Programmer

Figure 13

Port A signals are connected to two 8283 inverting 8-bit input/output ports on the PPGM which latch signals onto the PPGM address bus when the port C bits are set. A 8287 inverting 8-bit parallel bidirectional bus driver connects port A to the PPGM data bus. The 8287 may be set to either input (for reading) or output (for programming) depending on the level of bit 6 of port C. An 8282 noninverting 8-bit input/output port enables latching of port C bits onto the PPGM. This is necessary to prevent loss of addressing information when the 8255 is reconfigured for reading port A after the address has been set up. The additional logic circuitry enables switching of levels to the programming configuration and is controlled by bits 0 - 2 of port B. Table 7 lists the functions of the various control bits.

The following outline details the steps necessary for operation of the PROM programmer:

A. The 16-bit address is provided to the PROM programmer (PPGM) by the following procedure:
    1. Write a 0 to bit 6 of port C; this configures the port A driver for output.
    2. Write a 0 to bits 5 and 7 of port C releasing the latch on the inverting 8-bit input/output ports 8283A and 8283B.
    3. Write the most significant byte (MSB) of the address to port A.
    4. Write a 1 to bit 5 of port C, latching the MSB onto the PPGM address bus.
    5. Write the least significant byte of the address to port A.
    6. Write a 1 to bit 7 of port C, latching the LSB onto the PPGM address bus.

Table 7

PROM Programmer Interface Lines

Inverting Driver for Port A (Data Input and Output Port)

PA0 - $\overline{D0}$
PA1 - $\overline{D1}$
PA2 - $\overline{D2}$
PA3 - $\overline{D3}$
PA4 - $\overline{D4}$
PA5 - $\overline{D5}$
PA6 - $\overline{D6}$
PA7 - $\overline{D7}$

Noninverting Driver for Port B

PB0 - 2708 programming select
PB1 - 2708 programming pulse
PB2 - 2716 programming select
PB3 - Latch Port C bits
PB4-PB7 - Unused

Inverting Driver for Port C

PC0 - Chip select for socket 0
PC1 - Chip select for socket 1
PC2 - Chip enable for socket 2
PC3 - Output enable for socket 2
PC4 - Chip select for socket 3
PC5 - Latch most significant byte of address
PC6 - Data direction select. PC6 = 1 → Port A output from CPU
PC7 - Latch least significant byte of address

7. Restore bit 6 of port C to original condition.

B. Data are transmitted to the PPGM in the following manner:

1. Configure the 8255 to mode 0; all ports output.
2. Write a 0 to bit 6 of port C.
3. Write data to port A.

C. To program a 2708, the following procedure is observed:

1. Configure the 8255 to mode 0, all ports output.
2. Clear port C.
3. Place an erased 2708 in socket 0 of the PP6M.
4. Turn the programming power on.
5. Write a 09H to port B, bringing pin 20 of socket 0 to 12V and unlatching port C on PPGM.
6. Set up address (0000H-03FFH).
7. Set up data.
8. Write a 1 to bit 1 of port B, raising pin 18 of socket 0 to 25.5V.
9. After .5 msec, clear bit 1 of port B.
10. Loop to step 5 until all addresses have been done 250 times.
11. Clear port B.
12. Turn programming power off.

D. To verify the newly programmed 2708 EPROM:

1. Configure the 8255 to mode 0; all ports output.
2. Write 08H to port B, unlatch bits of port C on PPGM.
3. Set up address.

4. Clear port B, latching port C bits.
5. Configure the 8255 to mode 0, port A input, ports B and C output (Note: Changing the configuration of the 8255 clears all ports).
6. Write E1H to port C.
7. Write 08H to port B.
8. Read port A.
9. Loop to 1 until all addresses are read.
10. Configure 8255 to mode 0; all ports output.
11. Write 08H to port B.
12. Compare data read with desired code.

E. To program a 2716 EPROM:

1. Configure the 8255 to mode 0, all ports output.
2. Place an erased 2716 in socket 2 of the PPGM.
3. Turn the programming power on.
4. Set bit 2 of port C, setting PD/PGM low.
5. Write 0CH to port B, this raises pin 21 of socket 2 to 25V and unlatches port C bits on PPGM.
6. Set up address (0000-07FFH).
7. Clear bit 2 of port C - set PD/PGM high.
8. After 50 msec, set bit 2 of port C.
9. Loop to 6 until all desired addresses are programmed (Note: Not all addresses need to be programmed on a 2716, unlike a 2708 in which all addresses must be programmed).
10. Write 08H to port B.

11. Clear port C.
12. Turn programming power off.

F. To verify the newly programmed 2716:

1. Configure the 8255 mode 0, all ports output.
2. Write 08H to port B.
3. Set up address.
4. Clear port B.
5. Configure the 8255 to mode 0, port A input, ports B and C output.
6. Write ECH to port C.
7. Write 08H to port B.
8. Read port A.
9. Loop to 1 until all addresses are read.
10. Configure 8255 to mode 0 all ports output.
11. Write 08H to port B.
12. Compare data read with desired code.

G. To read a 2708 in socket 1 (read only socket):

1. Follow steps 1 - 11 of D, substituting for step 6; write E2H to port C.

H. To read a 2716 in socket 3 (read only socket):

1. Follow steps 1 - 11 of F, substituting for step 6; write F0H to port C.

2.5 EISIII Computer System Software

2.5.1 Introduction

Software for the EIS III computer system consists of the Monolithic

Systems Z80 Uniform Monitor (MSC 8301), the iCOM Floppy Disk Operating System (FDOS III), iCOM Disk Extended Basic, as well as numerous routines which I have written. The Uniform Monitor is a PROM resident stand alone I/O monitor occupying 2K bytes of memory. The monitor provides commands for examination and alteration of memory as well as transfer of blocks of memory to other locations. The monitor also allows reading and writing of I/O ports. The Uniform Monitor is further documented and listed in the MSC 8301 Program Reference Manual.

In order to make the monitor compatible with our non-Monolithic System Corp. hardware, it has been necessary to modify and extend the Uniform Monitor. The modifications do not alter the function of the monitor in any way. The Uniform Monitor is designed to function utilizing dedicated RAM locations from FF00H to FFFFH. It has been modified to use locations from 3F00H to 3FFFH. In addition, the initialization of the parallel peripheral interface performed by the Uniform Monitor (location 07A6H) has been modified to initialize the interface to a mode compatible with our use of the parallel port. Finally, location 07BEH has been altered to provide for inclusion of a second RS232 C port into the monitor's I/O device table.

The Uniform Monitor provides for extension of the command glossary and initialization routines. The third PROM on the MSC 8001 board contains these extensions of the Uniform Monitor. Storing A5H in memory location 800H (location 0000H of the third PROM) causes the Uniform Monitor to issue a call instruction to location 801H whenever a reset occurs. I have written a subroutine at this location which provides for initialization of parallel port number two, the interrupt controller, and

the second serial port (the printer port). Input and output routines for this second serial port were also stored in the third PROM. I have also added one command, the substitute memory command (SU). This command allows the operator to display a memory location and if desired alter it.

The iCOM Floppy Disk Operating System (FDOS III) provides the software necessary for use of the dual diskette drive. FDOS III consists of the following modules:

Resident Module

Executive

Text Editor

Relocating Assembler

Linker

Library Manager

Copy Program

System I/O Generation

Memory-To-Disk Program .

All modules except the resident module are loaded from diskettes. The resident module is located on a PROM on the floppy disk interface board which occupies memroy locations E800H to EBFFH. Locations E803H to E811H contain jump vectors to terminal and printer I/O routines. These vectors have been changed from those listed in the FDOS III manual in order to make the system computible with the Uniform Monitor. The following are the correct vectors:

Keyboard Input Vector: 0047H

Console Output Vector: 07C7H

Reader Input Vector: 0047H

List Output Vector: 003BH

Punch Output Vector: 07C7H

The diskette resident programs are utilized without alteration with the exception of the Memory-To-Disk Program which was found to be non-functional and has been replaced with MDESS and MTD2S, described later. Detailed documentation of FDOS III software may be found in the FDOS III Operator's Manual.

A diskette containing DEBBI (Disk Extended Basic By iCOM) was recently purchased. DEBBI provides a high level language programming capability. Since DEBBI is an interpretive BASIC (each instruction is individually translated into machine code at the time of execution; no compiled program is created) a substantial price in execution time is paid for the increased programming ease. This fact makes DEBBI unsuitable for most real time experimental control and data acquisition functions. The DEBBI Operator's Manual contains detailed documentation on the use of this program.

The software I have written for the EIS III computer system consists of routines written to perform specific functions related to operation of the spectrometer as well as numerous general purpose routines which provide needed system capabilities such as diskette track/sector examination which are not related to data acquisition and may be used on either the EIS computer system or the laser computer system. All spectrometer operation programs are written in Z-80 assembler language. All the general purpose routines are written in 8080 assembler language, a subset

of the Z80 assembler, so that these routines may be used on either the EIS system or the laser spectroscopy system.

The EIS III only software consists of the 4096 channel scanning routine (the data acquisition program), a tuning routine which facilitates tuning of the instrument for resolution and count rate, and the PROM programmer operation routine. None of these programs may be run on the laser computer system, although subsections of these programs may be 8080 compatible.

2.5.2 Electron Impact Spectrometer Scanning Routine

The scanning routine provides for acquisition, display, and storage of data from the spectrometer. The program occupies memory addresses from 2000H to 3008H and stores data between locations 4000H and 8FFFH. In addition, locations between 3C00H and 3FFFH are also utilized. Upon beginning execution, the program instructs the CPU to initialize the I/O devices required to operate the spectrometer. The operator is then asked to input the number of channels to be scanned. The number of channels must be a nonzero integral power of two less than or equal to 4096. The computer then determines the horizontal scale factor (≤ 32) to be used for data display. Next, the jump channel is requested. This must be an integral power of two less than 4096 or may equal zero if no jump is desired. The dwell time per channel in milliseconds is the next required input. The dwell time must be less than 65535 and must be chosen such that not more than 65535 counts will occur in a channel during the specified dwell time.

The maximum number of scans to be permitted is the next input. In the event of high count rates, this input allows the the operator to initiate a spectrum and leave without fear of overflow of channel data, providing of course that the number chosen is consistent with the count rate. The computer responds following input of this parameter with the message 'RUNNING' and immediately begins scanning. The computer displays the low order 12-bits of each data channel on the oscilloscope while data acquisition is underway. (Only the low order 12-bits of each 24-bit datum are displayed since it is assumed that weak signals or noise levels are of greatest interest.) The display is interrupted briefly at the end of each channel dwell time in order to process the new data.

The computer continues to acquire and display data until the scan limit is reached or until a character is entered from the terminal. When the scan maximum is reached, the message 'SCAN MAXIMUM REACHED, HIT (ESC) appears on the terminal. The oscilloscope display continues until the operator enters an (ESC) from the terminal. If (ESC) is entered while acquiring data, scanning is halted immediately without regard to the current channel number. If any other character is entered, display is immediately halted but the computer continues to acquire data until all channels of the current scan are completed. Once scanning has ceased, a message indicating the number of scans completed will be displayed. The message 'DISPLAY = DATA*2**0' will then appear on the terminal. The oscilloscope display now corresponds to the high order 12-bits of each datum. Each time the operator enters a character other than (ESC), the Y-component of the display is doubled and a message indicating the amplification is typed on the terminal. When an acceptable display is obtained,

the operator enters an (ESC). The message 'RESTART, CONTINUE, XYPLOT, OR SCOPE?' then appears. By entering the first letter of the selected operation, the operator may direct the computer to:

RESTART: Restarts the program resulting in the loss of data from this run.

CONTINUE: Resumes scanning, no data are lost. This command should be used only if the operator has halted scanning by entering a character other than (ESC) from the console. This command allows the operator to interrupt data acquisition in order to view intermediate data or to retune the instrument.

XYPLOT: Produces a plot of data on the X-Y recorder scaled like that on the oscilloscope.

SCOPE: Allows the operator to reenter the oscilloscope display section for a change of scale.

Following the completion of the X-Y recorder plot, the message 'ANOTHER SCALE?' will appear on the terminal. Entering a (Y) will instruct the computer to reenter the oscilloscope display section allowing additional plots at different scale factors. Entering any other character will result in the message 'CONTINUE, WRITE, MNTR, OR PRESENT?' to appear. Entering the first letter of a command causes the computer to:

CONTINUE: Resume scanning, as before.

WRITE: Enters the program section enabling writing data to a floppy disk.

MNTR: Exits to the monitor, terminates the scan routine, all data are lost.

RESTART: Restarts the program.

Following entry of a (W) from the terminal, the message 'FILE:' will appear. The operatory must then enter a filename (FDOS format). The computer will check whether a file with that name may be created. If not, another filename will be requested. Once an acceptable filename has been entered, the computer will request spectrum heading information, requesting each of the following:(formats given are FORTRAN types since subsequent FORTRAN coded programs must access this data):

SPECTRUM NUMBER: Enter the spectrum number I4.

SPECTRUM NAME: Enter the name of the compound run A20.

IMPACT ENERGY: Enter the inpact energy in eV.

ANGLE: Enter the scattering angle.

DATE: Enter the date, format I6 (i.e. 120180).

VSTART: Read and enter the center selector voltage. The computer will set the ramp appropriately for measuring the voltage for this and all other voltage parameters.

VEND: Read and enter the center selector voltage.

VJMP1: Read and enter the center selector voltage (this parameter and VJMP2 are requested only if a jump was used).

VJMP2: Read and enter the center selector voltage.

The computer will then output messages, indicating the number of scans, the dwell time, the number of channels used, and the jump channel (0 if no jump was used). Following these outputs, the computer will output an

electron impact heading in its standard format:

@ES1000@BENZENE,E=50,10D,120180,@2.500, 12.50, 0, 0, 00200,
00100, 01024, 0@/*

The computer will inquire whether the heading is correct. Entering a (Y) from the terminal will cause the computer to write the heading and data (in binary) to floppy disk. Entering any other character will cause the computer to again request heading information so that errors may be corrected.

Once the data file has been written onto a diskette, the computer will respond with 'SCAN, FDOS, OR MNTR?'. Typing the first letter of the command will direct the computer to restart the scan program, load and enter the floppy disk operating system, or exit to the monitor, respectively.

2.5.3 Electron Impact Spectrometer Tuning Routine

The EIS tuning routine is simply a version of the EIS scanning routine that does not provide for either the addition of new channel data to the corresponding old values or the permanent storage of data. The oscilloscope trace displays the most recent value for each data channel only, previous values are erased as new points are obtained. This routine is useful for tuning the spectrometer since a scan of just the elastic peak allows the operator to observe the effects of potential adjustments on both the elastic peak intensity and energy width simultaneously.

Inputs to this routine are identical to the corresponding inputs to the scanning routine. In order to most effectively utilize this routine (i.e. optimize the display quality), it is best to use dwell times of one to five milliseconds and not more than 128 channels. The display is then renewed about two to ten times per second.

Exiting from the program is accomplished in the same manner as from the scanning routine. The computer will respond with 'RESTART, CONTINUE, OR MNTR?'. Entering the first letter of the command will direct the computer to restart the tuning routine, requiring new input parameters; continue using the parameters previously input or exit to the monitor.

2.5.4 PROM Programmer Routine

The PROM programmer routine supports the PROM programmer hardware described previously. The program occupies RAM from 4000H to 4571H and uses additional RAM from 6000H to 67FFH and from 6800H to 6FFFH as the read and write buffers, respectively. In addition, locations between 3C00H and 3FFFH may be altered also. Intel 2708, 2758 and 2716 EPROM's or equivalent may be programmed using this system. (NOTE: Texas Instruments TMS2716 EPROM's are not equivalent and may not be read or programmed with this system.) This routine provides for switching of voltages to the EPROM's and generates all timing necessary in software.

After loading this program is accomplished, the power and programming voltage on the PROM programmer may be switched on. The computer will inquire 'SOCKET:' at which time the operator should enter the number of the socket to be used. Sockets zero and one may be used only for

2708's. Sockets two and three may be used for either 2758's or 2716's. If sockets two or three are selected the computer will respond 'TYPE:' at which time the operator should enter 2758 or 2716. The computer will then inquire 'MNTR, READ, OR WRITE?'. Entering the first letter of the command will direct the computer to exit to the monitor, copy the contents of the PROM in the specified socket into the read buffer and display the data on the terminal, or write the contents of the write buffer into the PROM if sockets zero or two have been specified. The write buffer is not initialized by this program so data may be stored prior to execution of this program and then be written onto the PROM.

If the read operation has been specified, following completion of output to the terminal or entry of (control C) from the terminal, the computer will inquire 'COPY TO WRITE BUFFER?'. If (Y) is entered, the contents of the read buffer will be copied into the write buffer, enabling duplication of PROM's. After copying the data or following entry of any character but (Y), the computer will repeat 'MNTR, READ, OR WRITE?'. At this point the operator may exit to the monitor to alter data in the write buffer before proceeding or by changing the PROM, the operator may proceed directly to a write operation.

Following instruction of the computer to initiate a write operation, the PROM in the specified socket will be read to check for complete erasure of the PROM. If the PROM is not erased, a message so indicating will be typed. The computer will then inquire 'OK TO PROCEED?'. Entering a (N) will cause the computer to restart the program. Entering any other character will cause the PROM to be programmed. After completion of the

programming cycle the contents of the PROM will be compared with the write buffer. Locations of errors, if any, will be typed on the terminal. The computer will once again inquire 'MNTR, READ, OR WRITE?'. If no errors have been detected, the operator may exit to the monitor. If errors have been detected which are unacceptable, the PROM must be erased before another attempt. The only errors which have been thus far observed were the result, apparently, of incomplete erasure of the PROM. Complete erasure of a PROM is not guaranteed by either exposure to UV light for the specified time or examination of the data contained in the PROM. UV exposure times necessary for erasure increase with the number of previous erasures. Also, analog levels within the incompletely erased PROM may be low enough or high enough to appear erased but appear to be altered enough by application of the programming voltage that these locations may not indicate complete erasure following programming with all FFH's. (Erased locations contain FFH, zero's are programmed in.)

2.5.5 General Purpose Routines

EXAMS: Routine to Examine Diskette

This routine allows the operator to dump the contents of any track and sector of a diskette in either drive to the terminal in hexadecimal format. The program also enables alteration of the data within the displayed sector. This program is of great utility for development of additional software for translating diskette formats or for debugging programs which output onto diskettes.

Immediately following loading of the program (EXAMS), the message

'ENABLE CHANGES?' will be typed on the terminal. Entering a (Y) from the terminal will allow the operator to alter data on the diskette. Entering any other character will enable the operator to examine the contents of sectors only. Next, the computer will prompt 'DRIVE:', requesting the operator to input the number (zero or one) of the diskette drive containing the diskette to be read. Similarly, the operator will be prompted to input the track (0 to 76) and sector (1 to 26) to be examined. The numbers input may be in either hexadecimal (i.e. 4DH) or decimal format. Following entry of acceptable track and sector number, the 128 bytes of the selected sector will be displayed on the terminal in hexadecimal format. The first four characters of each line correspond to the relative address of the first byte of each line.

If changes were not enabled, the computer will inquire 'EXAMS, FDOS, OR MNTR?'. Entry of an (F) or (M) will direct the computer to exit to the floppy disk operating system or the monitor, respectively. Entering an (E) will cause the next sector on the diskette to be displayed. An escape (ESC) may be entered to restart the program.

If changes were enabled, the computer will ask 'CHANGE?'. Entry of any character but (Y) will cause the computer to inquire 'EXAMS, FDOS, OR MNTR?' and proceed as when changes are not enabled. Entering a (Y) will result in the message 'LOCATIONS:' being typed on the terminal. Following entry of the relative address of the byte to be changed in either hexadecimal or decimal, the current contents of that location will be displayed. The operator may then enter the new value. The computer will then type 'MORE?'. Entering a (Y) will result in a request for another byte

location. Entry of an (N) will cause the current contents of the sector on diskette to be overwritten with the new values, followed by display of the data now contained in the altered sector. Entry of any character other than (Y) or (N) will result in the contents of the next relative address to be displayed allowing modification of sequential addresses without entering additional addresses. Exit from this section of the program is only possible by an (N) response to the prompt'MORE?'.

DASMS: 8080 Disassembler

This program disassembles 8080 machine code (hexadecimal) stored in memory, yielding the instruction mnemonic corresponding to each byte of machine code. The disassembler is used primarily to disassemble purchased software for which no listing was obtained in order to modify the software or to incorporate it into other programs. This routine is an exapnded and more sophisticated version of Intel's INSITE program AB22.

The disassembler runs in RAM from 4000H to 4A5DH and uses additional RAM locations from 3CE0H to 3FFFH. Therefore, machine code to be disassembled must be moved to memory locations outside this range (unless one desires to disassemble this program itself).

Following loading of the program, the computer will inquire 'MODE:'. The operator may request one of three modes:

Mode 0 — Display on terminal only.

Mode 1 — Display on terminal and printer.

Mode 2 — Display on terminal and write disassembled code to floppy disk.

If mode two has been selected, the computer will request an output filename in the standard FDOS format. Following input of an acceptable filename or if modes zero or one were selected, the computer will type 'START:'. The operator should then input the hexadecimal address (i.e. 7FFFH) at which disassembly is to begin. Next the computer will inquire 'LABEL:'. The operator must then input in hexadecimal the normal starting address of the machine code to be disassembled. (Example: Suppose the machine code to be disassembled normally occupies RAM between 4000H and 5000H. Since the disassembler also runs in this memory space, it is necessary to move the code to be disassembled to another section of memory 6000H to 7000H, for this example. The inputs to the disassembler would then be 'START:' 6000H and 'LABEL:' 4000H.) The 'LABEL:' input will be used to generate actual runtime addresses of instructions on the output.

Following input of the label, the computer will wait until a character other than (ESC) is entered from the keyboard at which time disassembly will begin. The computer will continue disassembly and output to the selected devices until another character is entered. If an (ESC) has been entered, the program will terminate and control will be passed to the monitor. If any other character has been entered, the computer will halt disassembly and will await another character before resuming disassembly. Disassembly will continue until an (ESC) is entered to terminate the program.

If disassembled code has been writted to diskette, FDOSIII commands may be used to examine the file or edit the file so that it will be

acceptable to the FDOS assembler as input. It is, however, very difficult and time-consuming to prepare very long programs (>500 lines) for re-assembly after modification or incorporation into other programs. The program is most useful for disassembly of short programs or subroutines such iCOM's disk handler routines which were not adequately documented for use until they were disassembled.

MDESS: Memory to Disk Program

This program is designed to write data contained between specified limits to diskette or to load a file written previously on diskette into memory. The diskette files are written in Intel Hex-ASCII format (i.e. data byte 27H will be written as the two bytes 32H and 37H, the ASCII representation of the data). The program is derived largely from the iCOM supplied MTDKS which was found to contain many errors and was therefore nonfunctional. The program occupies RAM from 4000H to 47E2H and uses additional RAM from 3C00H to 3FFFH.

Immediately following loading the computer will type 'READ, WRITE, FDOS, OR MONITOR?'. By entering the first letter of the selected operation, the operator may direct the computer to:

READ: Read a file from diskette into memory.

WRITE: Write a section of memory into a diskette file.

FDOS: Exit, load, and begin execution of the floppy disk operating system.

MONITOR: Exit to the monitor.

If 'WRITE' is specified, the computer will request a name for the output file in standard FDOS format. Next, the computer will type 'BYTES PER RECORD'. The operator must then input a number less than 256 in either hexadecimal or decimal which will define the output record format. If a zero is entered, the default value of 32 bytes per record will be used. The format of each record written to disk is:

Byte Number	— Value.
1	— ASCII colon 3AH.
2,3	— Hex ASCII representation of the number of bytes per record (BPR).
4,5,6,7	— Hex ASCII representation of the starting address in memory of this record.
8,9	— Hex ASCII representation of 00H.
10-N	— Hex ASCII representations of the data in memory. There will be two bytes of data written to disk for each byte of data in memory. The number of bytes per record refers to bytes in memory. N = (2*BPR) + 10.
N+1, N+2	— Checksum: The Hex ASCII representation of the number obtained by adding the values of all the bytes in memory of this record and subtracting from zero.
N+3	— ASCII line feed 0AH.
N+4	— ASCII carriage return 0DH.

Record lengths do not necessarily correspond to sector lengths, and a single sector may contain several records. Conversely, a single record may span several sectors. Diskette space utilization is most efficient

when large record lengths are specified.

After the record length has been specified, the computer will type 'ENTER LOW MEMORY ADDR'. The operator should then enter the address of the first byte in memory to be written to diskette. Following the entry of this address the computer will respond with 'ENTER HI MEMORY ADDR'. The operator should then enter the address of the last byte in memory to be output. (Note: All numeric inputs to this program may be either hexadecimal or decimal. Hexadecimal numbers are denoted with an H suffix.) The computer will then write the block of memory specified to disk. Following completion of diskette output the computer is directed to restart the MDESS program.

If 'READ' is specified, the computer will request the name of the file to be read. Once the file has been opened for reading, the computer will type 'OFFSET'. The number entered is added to the memory address of each record stored on diskette and the records are read into memory locations given by those sums. The hex ASCII data on the diskette are restored to hexadecimal before storage in memory. When reading of the diskette file is completed, the program is restarted.

INTLS: Routine to Translate Diskettes in Intel or ISC Format to FDOS Format

This program translates diskettes written utilizing Intel's or ISC's physical-logical sector correspondence into diskettes which use the iCOM FDOSIII physical-logical sector correlation. (See earlier description of diskette drive hardware for discussion of physical vs. logical sectoring.) This program enables the use of program source or machine code

on diskettes from other sources, such as Intel's Insite Library, which are written in a format different from that used on the iCOM system. The INTLS machine code occupies RAM from 4000H to 4915H and uses RAM between 3C00H and 3FFFH.

Following loading of the program the computer will request the name of the diskette file to be created. The computer will then type 'START', indicating that the parameter inputs to follow refer to the beginning of the Intel format file. The computer next requests the number of the drive containing the Intel format diskette. (Note: This program requires the use of two different diskettes, one for input and another for output.) The operator will be prompted to enter the track and sector numbers (Intel logical number) of the beginning of the input file. After this information is input, the computer will type 'MODE:'. The operator may choose one of the two modes

Mode 0: The computer will copy sectors from the input file into the output file sequentially until the ending track and sector is reached displaying only the contents of sectors which do not appear to contain valid ASCII characters. Displayed sectors may be deleted or written to the output file. This check for non-ASCII characters is necessitated by the fact that diskette drive controllers differ in the means of marking bad sectors. A controller will write data to a sector and then recheck it. If an error is detected, the controller will attempt to write the data again. If after several tries (the number varies among controllers)

errors are still detected, the controller will write a code onto the diskette indicating that this is a 'bad' sector and will then skip to the next sector and write the data. Controllers do not necessarily recognize 'bad' sector designations of other manufacturers' controllers. Therefore, when translating files, these 'bad' sectors must not be transferred to the new diskette since they do not contain valid data. This mode is very useful when translating long source programs since only sectors with a high probability of erroneous data are displayed.

Mode 1: The computer will display every sector before writing it to the output file. The displayed sector will be written to the output file if any character but (S) or (ESC) is typed and the next sector will be displayed. If (S) is typed, the next sector will be displayed without writing anything to disk. If (ESC) is entered, the program closes the output file and exits to the monitor.

If mode 1 has been selected, the contents of a sector will be displayed immediately. If mode 0 has been selected, the computer will type 'END' and request the track and sector numbers at which translation is to be stopped. The computer will then begin translation of the diskette. If a potentially bad sector is displayed, operator action is the same as given for mode 1. When the ending track and sector are reached, the output file will be closed and the message 'FINIS' will be displayed.

FINTS: Routine to Translate an FDOS Diskette File into an Intel Compatible File

This routine copies a file on a diskette in drive zero written using the iCOM FDOSIII physical-logical sector correlation into a file on a diskette in drive one written using the Intel ISIS physical-logical sector correspondence. The output diskette, which may not initially contain any files, will also contain an ISIS directory entry. This program was written in order to make use of the Intel Microcomputer Development System, especially the PROM programmer, owned by Caltech's electrical engineering department. Dr. David Edmonson and I subsequently designed and built our own PROM programmer, rendering this program unnecessary. It is included solely for the sake of completeness.

The FINTS code occupies RAM from 4000H to 46FEH and uses RAM between 3C00H and 3FFFH. The program begins execution by requesting the name of the input file in FDOS format. Upon receipt of the input filename (the file must be on drive zero), the program begins copying the file onto the diskette in drive one. An ISIS compatible directory entry FDOS.OBJ will also be written on the output diskette. When file copying is completed, the computer will type 'FINIS' on the console and will exit to the monitor immediately.

FISCS: Routine to Translate an FDOS Diskette File into an Intelligent Systems Corporation Compatible File

This routine copies a file on a diskette in drive zero written using the iCOM FDOSIII physical-logical sector correlation into a file on a diskette in drive one written using the ISC physical-logical sector

correspondence utilized on computer systems possessed by the Kuppermann and Janda groups. This program is very similar to FINTS since the Intel and ISC sector correlations are identical for the IBM 3740 compatible sectors 1-26. However, an unmodified ISC system adds a sector zero and sectors 27-29. These additional sectors are not accessible to the iCOM controller so the output diskette will require substantial preprocessing before this routine is run and further processing following file translation if the diskette is to be compatible with an unmodified ISC system. (The Janda group ISC 8053 has been modified by David Brinza to IBM 3740 compatible format.) In addition, no directory entry is made by this program. The FISCS code occupies RAM from 4000H to 46CCH and uses RAM between 3C00H and 3FFFH.

Prior to running this program, an output diskette must be prepared. This diskette should be formatted on the ISC system and initialized reserving all of track 0, ISC blocks zeroto twenty-nine if the system is unmodified or blocks one to twenty-six if the system has been modified. Next, ISC BASIC may be used to open a file with length in blocks equal to that of the FDOS file in sectors if the system has been modified. For the unmodified system, the length in blocks must be determined by adding the length of the input file in sector to the number of unusable (by FDOS) blocks which will be spanned by the file. For example, if the input file is forty sectors long, five unusable blocks will be spanned, sectors 0, 27, 28 and 29 of track one and sector zero of track two, thus the length specification must be forty-five blocks. These unusable blocks must be loaded with ASCII characters prior to running FISCS.

Once the output diskette has been prepared, FICS may be run. The computer will request an FDOS compatible input filename and will begin copying immediately upon receipt of an acceptable filename. Upon completion, the program will type 'FINIS' and exit to the monitor. The output diskette may then be edited using the ISC scrolling text editor to eliminate the extraneous characters written in the FDOS inaccessible blocks if this was necessary.

2.6 Data Handling

Data obtained using the EIS III computer system are stored on diskettes (see Section 2.5.2). Since the IBM 370/3032 has no facility for retrieval of data directly from diskettes, it is necessary to transfer the data to an IBM compatible magnetic tape as it was with the previously used paper tapes. Fortunately, a much simpler system exists for handling diskettes. The diskette containing data to be transferred and a magnetic tape are given to a 370/3032 operator with a card requesting transfer of tracks 1-76 (track 0 contains directory information and should not be transferred) to the magnetic tape. The magnetic tape upon return will contain an image of all the data on the diskette. The tape format is 9 track, 1600 bytes per inch with a blocksize of 3328 bytes and record format F. The data now contained on magnetic tape are written in ASCII and binary and must be processed prior to use by data analysis programs. I have written a program, ESTOMT, which is designed to perform the necessary translation of data to a format compatible with existing data analysis programs. Since no data have ever been obtained from EIS III, this program has never

been tested. It is, however, based on the working programs NDTOMT (which translated EIS I paper tapes) and FLOPPY (which translates laser spectra on diskettes) and should therefore require few, if any, changes prior to successful operation.

ESTOMT is very similar to the NDTOMT program I wrote to perform data translation for the EIS I paper tape based data sets. Data stored on the magnetic tape are read one block (which corresponds to one track on a diskette) at a time using the system subroutine READSP. READSP converts 8-bit byte in the 3328 byte block into a 16-bit word of the form ZOOFF (Z indicates hexadecimal) by filling the 8 most significant bits of the 16-bit word with zeroes. In this manner, READSP fills the integer *2 array DATAST with the data contained in one magnetic tape block. Unfortunately, the floppy disk system used by the computer center does not use the same physical-logical sector correlation as does iCOM (see Section 2.4.1 and Table 4). Therefore, the data now stored in the array DATAST are not ordered properly. Subroutine TRKRD, which calls READSP in this program, restores the data to its proper sequence prior to returning to Main. Five tracks of data are stored in the DATAST matrix in order that a complete 4096 channel data set may be stored. If the beginning of a data set is located beyond the 3328^{th} element of DATAST, the matrix is rotated such that the first 3328 words are deleted, the addresses of subsequent elements are decremented by 3328, and another track full of data is read.

A data set is located by searching for the sequence @ES (in ASCII) in the data matrix. In order to reduce the probability that a particular

set of digital data, containing binary equivalent of @ES, would be mistaken for the beginning of a data set, the program requires that the words immediately following be ASCII numerals followed by a comma. If this is not true, a search for another @ES is initiated. The probability that a particular sequence of data bytes might be mistaken for a data heading is also made virtually nil by the fact that the first occurrence of @ES will be at the beginning of the tape. The heading that follows informs the program of how many data words should follow. The computer does not seek another heading until the necessary data words have been obtained. Therefore, only sector-filling zeroes should be found between a data set and the next @ES. Subroutine NUMBER converts the ASCII representation of numbers in the heading (the heading format was described in Section 2.5.2) into FORTRAN real numbers. The presence of an * following a heading indicates the beginning of a data set. The data are translated three integer *2 words at a time (the least significant bytes are first) into a single integer *4 variable. This process continues until the newly formed data matrix contains the number of channels that was specified in the heading. The heading is printed out and the entire data set is written to disk. The program then loops back and searches for another data set, continuing until an end of file is reached. The disk file produced by ESTOMT is not compatible with the ANDATA series of programs which perform data analysis. The program SPEDIT will read the output of several different ESTOMT runs and combine them into the format required for data analysis. It should also be noted that ESTOMT is the only current FORTRAN program which is capable of handling spectra with more than 1024 channels. (The EIS III computer

system can produce up to 4096 channel spectra.) All other FORTRAN programs are designed for the 1024 channel maximum data sets produced by the Nuclear Data system. Redimensioning of all the data matrices will be necessary before data analysis may be performed on spectra containing more than 1024 channels of data. In addition to redimensioning arrays, the format of data storage tapes and disk files will also need to be changed to a more efficient variable block size format such as that used by ESTOMT from the present fixed 6244 byte blocks. This will also require rewriting the sections of the programs which acquire data from the tape.

The program SPEDIT is unchanged from that described previously in Section 2.6.2 and in the thesis of R. P. Fureholz. The sole function of SPEDIT is to read the output(s) of ESTOMT or NDTOMT, allow corrections to headings or data sets obtaining the data sets from one or more disk files (produced by NDTOMT or ESTOMT), and write the corrected spectra to disk in the format required by the data analysis programs. When I wrote this program, data were still being obtained on paper tape using the Nuclear Data system. Numerous errors occurred when transferring the data on paper tape to the PDP10 due to problems with hole spacings, read errors, etc. SPEDIT allowed correction of these errors and for rereading a spectrum in the middle of a paper tape and insertion for the proper sequence into the disk data file. My experience with the computer system I designed and built for the laser spectroscopy laboratory indicates that no such errors will occur when using diskettes. Therefore, the EIS III computer system renders SPEDIT obsolete. Once the data analysis programs have been altered to use the superior data storage format used by ESTOMT, the SPEDIT step may be deleted.

The programs SPEDIT and ESTOMT output data sets to 370/3032 disk storage. Subsequent data analysis programs may operate using the data sets stored on disk as input. In fact, a substantial cost and time savings may be realized by utilizing the disk data sets instead of magnetic tapes. Permanent storage of data is accomplished by copying the new data set stored on disk onto the magnetic tapes EISDT1 and EISDT2 (the backup tape) using the program WRITAPE. The format used for these tapes, which contain all the spectra ever obtained digitally in this laboratory, is 9 tracks, 1600 bpi, blocksize 6244 bytes and record format F (note: this has been changed from the format used previously) WRITAPE appends the data to the most recent tape file or creates a new file then checks the tape by reading and printing all the spectrum headings contained in the current file. The tapes are divided into seven different files so that I/O is reduced when searching for a particular spectrum. The current contents of the seven files are:

File 1	Spectra	1053-2188
File 2		2189-2404
File 3		2405-2518
File 4		2520-2700
File 5		2701-2823
File 6		2824-2974
File 7		2975-

The ANDATA series of programs have been described previously in the theses of W. M. Flicker and R. P. Frueholz. There have been several changes made in these routines. The programs ANDATA1 and ANDATA2 have

been reorganized into more efficient code. The smoothing routine used originally in these programs (a simple running average) has been replaced by a cubic quadratic polynomial convolution. The previous routine could produce spurious peaks or shift peaks under certain conditions. Also, the noise spike removal routine has also been replaced with one I wrote which has proven to be much more reliable. In addition, the section of ANDATA2 which provides for subtraction of a high angle spectrum from a low angle spectrum was found to be incorrect. The flow of the program is extremely convoluted, making correction very difficult so I wrote a new program, ESSUBTR, which correctly performs spectrum subtractions. Only the peak area section of ANDATA2 may be considered reliable. Programs ANDATA1B and ANDATA1C are no longer used having been replaced with my new program ESDATA. ANDATA3, used to plot DCS and ratio curves using the punched integrated area outputs of ANDATA2, has not been changed.

ESSUBTR was written in order to perform subtractions of low angle spectra (appropriately normalized) from high angle spectra. This program was extensively and successfully used for the analysis of nitric oxide data. A single standard (i.e. low angle) spectrum may be normalized to each of several different high angle spectra at some channel where little contribution to the intensity is believed to result from spin-forbidden transitions. The energy loss axis of the standard spectrum may also be shifted so that it may be made coincident with that of the higher angle spectrum. The resulting normalized and, if necessary, shifted low angle spectrum is subtracted from the high angle spectra. The subtraction result is then presumed to be due primarily to spin-forbidden transitions.

The subtraction spectrum is plotted with a vertical scale equal to the relative intensity contribution of the subtraction result to the original high angle spectrum. The subtraction result should represent an increasing relative intensity as the scattering angle is increased.

I originally wrote the progam ESDATA to perform least squares fitting of Gaussians to electron impact spectra. The program will fit up to eight Gaussians to a spectrum or some section of a spectrum. Since our spectra are generally over-determined in that instrumental resolution is equivalent to seven to ten data channels, ESDATA may be programmed to fit a subset of the spectrum data such as every fifth data point. Once the required convergence criterion is met, the calculated peak positions, width, and areas are output. Unfortunately, spectra frequently contain highly overlapped peaks with a substantial noise background, especially at high angles. This results in very slow convergence and therefore an unreasonably large amount of computer time is required. The utility of the Gaussian fitting of spectra is unfortunately limited. However, ESDATA also contains the best plotting routine of the data analysis programs and is used primarily without any curve fitting for plotting spectra for publication.

References

1. (a) A. Kuppermann, J. K. Rice and S. Trajmar, J. Phys. Chem. 72, 3894 (1968);

   (b) S. Trajmar, J. K. Rice and A. Kuppermann, Advan. Chem. Phys. 18, 15 (1970).

2. J. K. Rice, PhD Thesis, California Institute of Technology, 1969.

3. R. P. Frueholz, PhD Thesis, California Institute of Technology, 1978.

4. O. A. Mosher, PhD Thesis, California Institute of Technology, 1973.

5. W. M. Flicker, PhD Thesis, California Institute of Technology, 1976.

6. Z80-CPU, Z80A-CPU Technical Manual, Zilog, Inc., 1977.

7. T. Rolander, Intel MULTIBUS Interfacing, Application Note AP28, Intel Corporation.

3. RESULTS AND DISCUSSION

3.1. Paper 1: Doublet-Quartet Transitions in Nitric Oxide by Low-Energy, Variable-Angle Electron Scattering

Doublet-Quartet Transitions in Nitric Oxide by Low-Energy, Variable-Angle Electron Scattering[a)]

Robert P. Frueholz, Ronald Rianda[b)] and Aron Kuppermann

Arthur Amos Noyes Laboratory of Chemical Physics[c)]
California Institute of Technology
Pasadena, California 91125

Abstract

The electron impact spectrum of nitric oxide between 4 eV and 10 eV energy loss has been studied in detail at impact energies of 25, 35 and 50 eV and at scattering angles between 5^{o} and 80^{o}. Weak structure occurring between 5.22 eV and 5.60 eV has been assigned as vibronic bands belonging to the $X\ ^{2}\pi \rightarrow a^{4}\pi$ transition. Structure with an apparent Franck-Condon envelope extending from 5.70 eV to approximately 7 eV with intensity maximum at 6.29 eV was assigned to the $X\ ^{2}\pi \rightarrow b^{4}\Sigma^{-}$ transition. Additional higher lying transitions have been tentatively assigned as doublet → quartet in nature. These represent the first direct observation of doublet → quartet excitations in the gas phase. Several previously unobserved doublet → doublet transitions occuring near 10 eV energy are also reported.

a)This work was supported in part by a contract (No. EY-76-S-03-767) from the Department of Energy. Report Code: CALT-767P4-153.

b)Work done in partial fulfillment of the requirements for the Degree of Doctor of Philosophy in Chemistry.

c)Contribution No. 5705.

I. Introduction

For over 50 years the electronic spectroscopy of nitric oxide has been studied intensively.[1-5] These investigations have been spurred by the inherent interest of this relatively simple diatomic molecule which possesses a doublet ground state. More recently, nitric oxide has been observed in auroral arcs[6,7] and has been found to play an important role in the atmospheric chemistry of ozone.[8-10] While the doublet excited state spectrum is rather well understood, information on the doublet quartet transitions is scarce. Prior to the present investigation, no direct doublet quartet excitations were observed in the nitric oxide spectrum. Indeed, to our knowledge, no direct gas phase doublet → quartet transitions have been observed previously in any molecule.

The objective of our study was to locate doublet → quartet transitions in the electronic spectrum of nitric oxide. The method of low-energy, variable-angle, electron-impact spectroscopy is well suited for the investigation of both spin- and symmetry-forbidden transitions.[11-13] With regard to spin-forbidden excitations, the most important feature of the electron impact technique is the sensitivity of the shape of the differential cross-section (DCS) versus scattering angle curve to the change in spin quantum number of the target molecule. Optically-allowed processes have sharply forward-peaked DCS's for impact energies, E_o, 15 eV or more above the excitation threshold. In contrast, singlet → triplet[11,12] and triplet → singlet[13] transitions have a more nearly isotropic DCS over the angular range 10^o to 80^o. Such transitions occur by the mechanism of electron exchange.[14] For this reason, the ratio of

the intensity of a spin-forbidden excitation to that of an optically-allowed one is found to increase by about two orders of magnitude as the scattering angle, θ, increases from 10^{o} to 80^{o}.[11,12] Moreover, this ratio is usually found to be larger at low impact energies than at high ones.[12] On firm theoretical grounds, this behavior should characterize any transition involving a change of unit in the spin-multiplicity, as would be the case for doublet → quartet excitations, although heretofore no such processes have been observed. In addition, the ratio of intensities of two electric dipole-allowed transitions is nearly independent of angle, usually varying by less than a factor of three over the angular range 10^{o} to 80^{o}.[11-13] Finally, spin-allowed but symmetry-forbidden transitions may display somewhat less forward-peaked DCS's than fully-allowed excitations. Consequently, the ratios of their intensities to those of fully-allowed excitations may increase by factors from three to about eight as the scattering angle increases from 10^{o} to 80^{o}.[12]

II. Electronic Structure of Nitric Oxide

The electronic configuration of the $X\ ^2\Pi$ ground state of nitric oxide is[15] $(KK)^4(\sigma_{2s})^2(\sigma^*_{2s})^2(\sigma_{2p})^2(\pi_{2p})^4(\pi^*_{2p})^1$. The electronically excited states of nitric oxide consist of two different classes of excitation. Rydberg transitions involve the excitation of an electron into a Rydberg-like orbital. Miescher[4] has assigned the first few excited states as excitations from the π^*_{2p} orbital to the Rydberg orbitals $3s\sigma$ ($X\ ^2\Pi \rightarrow A\ ^2\Sigma^+,\gamma$ bands), $3p\pi$ ($X\ ^2\Pi \rightarrow C\ ^2\Pi,\sigma$ bands), $3d\sigma$ ($X\ ^2\Pi \rightarrow D\ ^2\Sigma^+,\varepsilon$ bands), and $4s\sigma$ ($X\ ^2\Pi \rightarrow E\ ^2\Sigma^+,\gamma'$ bands). Rydberg

excitations involving transitions from the π^*_{2p} orbital can only result in doublet excited states. As would be expected for excitations from an antibonding orbital to a nonbonding orbital, the vibrational spacings for these lower lying Rydberg states are larger ($\sim$2350 cm^{-1}) than those of the ground state ($\sim$1900 cm^{-1}).[16] Both doublet and quartet Rydberg states may result from excitations from orbitals other than the π^*_{2p}.

The second category of excitations is comprised of transitions to valence excited states. These are of particular interest in the present study because their doublet-quartet splittings are expected to be larger than those for Rydberg excitations, leading to easier resolution of quartet states from doublet states. The valence excited configuration $(KK)^4(\sigma_{2s})^2(\sigma^*_{2s})^2(\sigma_{2p})^2(\pi_{2p})^3(\pi^*_{2p})^2$ yields one $^4\Pi$ and several $^2\Pi$ excited states. The $X\ ^2\Pi \rightarrow B\ ^2\Pi$ transitions (β bands) are believed to result from excitation to one of these $^2\Pi$ states.[17] The configuration $(KK)^4(\sigma_{2s})^2(\sigma^*_{2s})^2(\sigma_{2p})^1(\pi_{2p})^4(\pi^*_{2p})^2$ yields term symbols $^4\Sigma^-$, $^2\Delta$, $^2\Sigma^-$, and $^2\Sigma^+$. It is believed that the β' bands ($X\ ^2\Pi \rightarrow B'\ ^2\Delta$) result from excitation to this $^2\Delta$ state.[2,18] Excitations to these valence states weaken the internuclear bond, resulting in vibrational frequencies of approximately 1100 cm^{-1}.[4]

III. Experimental

The experimental apparatus used in this study was similar to that described by Kuppermann et al.[11] The spectrometer consists basically of a multistage electron gun, a hemispherical electrostatic energy monochromator, a flexible bellows scattering chamber which contains the

target gas, an energy-loss analyzer identical to the monochromator, and a Spiraltron electron multiplier. Pulses from the multiplier are amplified and shaped, and then counted with a 1024 channel scaler. In a typical experiment, the incident electron energy and scattering angle of detection are both fixed, and the energy-loss spectrum is scanned repeatedly, usually for a period of four to eight hours, corresponding to an accumulation time per channel of approximately 20 sec to 30 sec. However, in these studies, in order to obtain the desired signal-to-noise ratios, accumulation times per channel were increased to 150 - 190 sec.

In the present experiments, the electron-impact spectrum of nitric oxide in the energy-loss region 4 to 10 eV was studied at impact energies of 25, 35 and 50 eV, over scattering angles from 5^{o} to 80^{o}. Sample pressures in the scattering chamber were typically 1.8 mTorr as indicated by an uncalibrated Schulz-Phelps ionization gauge, while the incident electron beam current was approximately 70 nA. The energy resolution, as measured by the full width at half maximum (FWHM) of the elastic peak was set electron-optically at about 0.085 eV. The nitric oxide sample was obtained from Matheson Gas products with a stated minimum purity of 99.0%. Our samples were further purified by trap-to-trap distillation at liquid nitrogen temperature. No indication of impurity was observed in any spectrum.

IV. Results and Discussion

A. Doublet Excited States

Figures 1 and 2a show the spectrum of nitric oxide at low scattering

angles. These spectra result from predominantly doublet → doublet excitations. The transition energies are in good agreement with previous optical studies and are summarized in Table I. The doublet → doublet spectrum in the energy region studied has been well characterized by previous optical studies.[1-5] In our spectra we have detected several spin-allowed transitions near 10 eV that do not appear to have been previously observed. Their excitation energies are listed in Table I. Considering our relatively limited resolution, further discussion of doublet → doublet transitions in this energy-loss region is not warranted.

B. Subtraction Techniques

As discussed in the Introduction, the ratio of the intensities of spin-forbidden to spin-allowed transitions increases significantly as the scattering angle is increased. We may make use of this fact to nearly eliminate the contribution of spin-allowed transitions to the high angle spectra by subtracting from the latter, after appropriate scaling, the low-angle spectra. The resulting difference spectrum is believed to be due primarily to spin-forbidden transitions. This technique has been used previously.[12a,19] Its validity rests upon the assumptions that (a) relative intensities of different vibronic elements of the same electronic transition remain constant with varying scattering angle (i.e. Franck-Condon factors are independent of scattering angle), and (b) relative intensity changes as a function of scattering angle between spin-allowed transitions resulting from excitations to different electronically excited states will be much smaller than the corresponding

relative intensity changes between spin-allowed and spin-forbidden excitations over the same angular regions. Experimental observatiions indicate that these assumptions are well-founded.[11,20]

Spectra taken at 20^{0} are used as low-angle standards in all subtractions reported for reasons discussed below. In this subtraction technique it is desirable to use as a low-angle standard spectrum one that has minimal contribution from spin-forbidden transitions while simultaneously possessing spin-allowed structure for which relative intensities among different doublet → doublet electronic excitations change as little as possible in going from the selected low scattering angle to high scattering angles. Relatively large spin-allowed transition intensity variations among such electronic states are frequently observed between high-angle spectra and spectra obtained at angles of 5^{0} or 10^{0} when compared with the differences between 20^{0} spectra and high-angle spectra. In addition, the relative contribution of spin-forbidden transitions to the spectrum increases rapidly as the scattering angle is increased beyond 20^{0}.

In preparation for subtraction, both the high- and low-angle spectra are corrected for background noise contributions. Intensity scaling is accomplished by multiplying the low-angle spectrum by a factor that makes the intensity of a selected spin-allowed vibronic peak (hereafter called the scaling peak) equal to the intensity of the corresponding peak in the high-angle spectrum. It is important that the peaks used for scaling have minimal underlying spin-forbidden structure. Subtraction is performed channel by channel after appropriate energy scale calibration, and the intensities of the features in the resulting difference spectrum are

expressed as fractions of the intensity of the strongest feature in the original high-angle spectrum. This normalization gives a clear representation of the fractional contribution of the spin-forbidden transitions to the high-angle spectra.

We have performed extensive tests to guarantee that the difference spectra obtained in this manner are not simply artifacts of the subtraction technique. Instrumental background is usually affected by the presence of the sample in the apparatus and is determined with sample present using the energy-loss regions between non-overlapping transitions, such as the region below 5 eV in nitric oxide. Above 7 eV, such a region does not exist in NO, preventing an accurate determination of the noise background. We assumed that it was the same as below 5 eV but varied it significantly (±50%); we found that the difference spectra were essentially unchanged. An examination of the widths of the elastic peaks indicates that the difference in resolution between our high- and low-angle spectra is no larger than 5 meV. In order to test the effects of this possible resolution variation on the structure of the difference spectra, we convoluted gaussian peaks of FWHM varying between 10 meV and 40 meV into a low-angle spectrum yielding resolutions as much as 10 meV worse than in the unconvoluted spectrum. After subtracting the unconvoluted spectrum from the convoluted ones, the resulting difference spectra were found to have residual structural features with a maximum relative intensity no greater than 6% of the strongest feature of the convoluted spectra for a 10 meV resolution deterioration and 3% for a 5 meV resolution worsening. This is a small effect compared with most of our observed difference spectra.

These spectra, resulting from experimental data, also meet the following criteria. The general features are unchanged upon changing the angle of the high-angle spectrum used in the subtraction and the impact energy used for both the high- and low-angle spectra. In addition, intensities of the peaks in the difference spectrum relative to the spin-allowed contributions at the same angle increased as the high-angle spectrum angle was increased. This behavior is consistent with that expected for a spin-forbidden transition.

C. Doublet → Quartet Transitions

Figure 2 shows the energy-loss spectrum of nitric oxide at 20^{o} and 80^{o} scattering angles over the energy-loss region 5 eV to 10 eV. Significant changes between the high- and low-angle spectra are observed. The new vibronic peaks at 5.86 and 6.14 eV, never observed previously, are seen in the high-angle spectrum. In addition, the relative intensities of the other peaks are very different in the two spectra, and close inspection reveals small shifts in energy of the intensity maxima of several vibronic peaks. This change is due to the increase in the relative intensity of doublet → quartet transitions (with respect to doublet→ doublet excitations) in going from 20^{o} to 80^{o}. To facilitate discussion of the spectra, we will consider various energy-loss regions separately.

1. $X\ ^{2}\Pi \rightarrow a\ ^{4}\Pi$ Excitations (5.0 to 5.7 eV)

The lowest energy spin-forbidden transition in nitric oxide is predicted by a semi-empirical calculation to be the $X\ ^{2}\Pi \rightarrow a\ ^{4}\Pi$ excitation.[18]

Broida and Peyron[21] and Frosch and Robinson[22] have observed emission bands from NO in rare gas matrices which they assign as a $^4\Pi$ v' = 0 → X $^2\Pi$ v" = n transitions (M bands). Ogawa[23] and Brook and Kaplan[24] have observed emission bands in the infrared which Ogawa suggested were the result of $^4\Sigma^-$ → $^4\Pi$ fluorescence. Frosch and Robinson, using vibrational data derived from these results and their own estimation of the gas phase X $^2\Pi$ v" = 0 → a $^4\Pi$ v' = 0 transition energy, predicted the positions of the vibronic elements of this transition as shown in Table II. There has been no previous direct observation of the X $^2\Pi$ → a $^4\Pi$ excitations in spite of attempts by Bernstein and Herzberg[25] using a 28 m atm path.

In Fig. 3b and the low energy-loss region of Fig. 4d, we observe very weak structure at 5.22, 5.31, 5.41 and 5.60 eV. The intensities of these peaks relative to that of the γ(0-0) at 5.47 eV increases by more than one order of magnitude as the scattering angle increases from 20° to 80°. This behavior is indicative of a spin-forbidden transition. Using this angular behavior and the predictions of Frosch and Robinson,[22] we assign these excitations to the X $^2\Pi$ v" = 0 → a $^4\Pi$ v' = 4,5,6 and 8 transitions. The 5.41 eV feature is only distinguishable in the difference spectra (using the γ(0,0) feature at 5.47 eV as the scaling peak) shown in Figs. 3c, 4e, f and g; however, a noticeable broadening of the γ(0,0) transition is observed at the high-angles. The peak occurring at 5.55 eV in the difference spectra is most likely the v' = 7 member of the X $^2\Pi$ → a $^4\Pi$ vibrational series. However, the exact location of the transition corresponding to the 5.55 eV feature in the difference spectrum is uncertain because of its closeness to the scaling peak. Although the

peak observed at 5.70 eV corresponds exactly to the predicted location of the v' = 9 transition, its significantly increased intensity relative to the other vibrational members of this transition contradicts the Franck-Condon factors predicted by Frosch and Robinson.[22] For this reason, it seems more reasonable to attribute this 5.70 eV feature predominantly to another doublet → quartet transition.

2. $X\ ^2\Pi \rightarrow b\ ^4\Sigma^-$ Excitations (5.7 to 7.3 eV)

Figure 4 shows the 5 eV to 7.4 eV region in great detail. Spectra taken at 20^o, 40^o, 60^o and 80^o and the results of subtracting the 20^o spectrum from the other three spectra are shown in this figure. In addition to the peaks discussed previously, a new series of vibronic bands is observed beginning with the feature at 5.70 eV in the difference spectra (Fig. 4e, f and g). The new transitions at 5.86 and 6.14 eV, clearly distinguishable, even in the high angle original spectra, increase in intensity by nearly two orders of magnitude relative to the $\gamma(0,0)$ intensity as the scattering angle increases from 20^o to 80^o. The other peaks observed in the difference spectra maintain a nearly constant intensity relative to the transitions at 5.86 eV and 6.14 eV. This constancy indicates that the transitions which are distinguishable only in the difference spectra undergo an increase in intensity relative to doublet → doublet transitions similar to that of the 5.86 and 6.14 eV transitions, allowing us to assign these transitions as doublet → quartet in nature.

Semi-empirical calculations[18] suggest that the second quartet excited

state should be the b $^4\Sigma^-$ resulting from an excitation of a σ_{2p} electron to the π^*_{2p} orbital. Using the infrared emission results of Ogawa[23] and Brook and Kaplan,[24] which were suggested to be due to b $^4\Sigma^- \rightarrow a\,^4\Pi$ transitions, and the X $^2\Pi v'' = 0 \rightarrow a\ ^4\Pi\ v' = 0$ excitation energy of Frosch and Robinson,[22] the following excitation energies for vibronic members of the X $^2\Pi \rightarrow$ b $^4\Sigma^-$ transition may be predicted: 5.99, 6.15, 6.28 and 6.43 eV. In our difference spectra, the corresponding transitions are observed at 6.00, 6.14, 6.29 and 6.43 eV. This agreement allows definite assignment of the infrared transitions[23,24] to a b $^4\Sigma^- \rightarrow$ a $^4\Pi$ emission. However, the presence of peaks in our spectrum at 5.70 and 5.86 eV, which we tentatively assign to the X $^2\Pi$ v" = 0 $\rightarrow$ b $^4\Sigma^-$v' = 0, 1 transitions, indicates that previous vibrational assignments of the emission spectrum were incorrect due apparently to the lack of observation of emission from b $^4\Sigma^-$v' = 0,1. We assign the transitions in the difference spectra from 5.70 to 7.24 eV to the X $^2\Pi$ v" = 0 $\rightarrow$ b $^4\Sigma^-$v' = 0 $\rightarrow$ 11 transitions. Our specific assignment of the vibration quantum numbers for elements of b $^4\Sigma^-$ is not, however, definitive since experimental resolution precludes rotational analysis. The possibility exists that the true v' = 0 lies at a lower excitation energy than 5.70 eV. This preliminary assignment is based on the inability to detect transitions below 5.70 eV which have intensity sufficient, in our opinion, to belong to the b $^4\Sigma^-$ progression. We do feel that if our assignment of vibronic quantum number, v', is in error, this would shift our assignments by no more than unity, in which case the 5.70 eV feature would correspond to v' = 1. The transition energies are summarized in Table II. Peaks at 6.70 eV and 6.97 eV have

intensities which are greater than would be expected for consistency with the remainder of the Franck-Condon envelope. This behavior may result from the presence of an additional underlying doublet → quartet transition or to a vibrational perturbation[26] resulting from an avoided potential crossing with another electronic state.[26-29]

3. Higher Energy Quartet Transitions (7.3 to 10.0 eV)

Figure 5 shows the nitric oxide spectrum at 20^{o} and 80^{o} between 6.5 and 9.0 eV and the resulting difference spectrum. The low-angle spectrum was normalized to the 8.36 eV feature of the high-angle spectrum. While relative peak intensities in the difference spectrum vary somewhat depending on the peak used for such scaling, peak locations are independent of the choice of scaling peak. The ratios of the intensities of the difference peaks observed above 7 eV to those between 5.0 and 7.0 eV, which we assigned previously as doublet → quartet transitions, remain relatively constant over the angular region we have studied. The behavior suggests a doublet → quartet assignment for these bands. However, the presence of over 20 previously identified doublet excited states in this enregy-loss region[2] might result in a significant contribution to the difference spectrum from relative doublet → doublet transition intensity variations with angle. We do not believe, though, this to be the case for the following reasons. (a) Essentially the same spectrum is observed regardless of the peak chosen for scaling. Since each of the scaling peaks corresponds to a different doublet excited state, changes in the relative intensities in resulting difference spectra would be expected

to appear if relative changes in doublet → doublet transition intensities with angle were significant. (b) We are unable to correlate any more than two or three difference features out of the 17 observed to known vibronic elements of any given doublet → doublet transition. Since vibronic envelopes are independent of scattering angle, if one element of the envelope is observed, then the remaining elements of comparable intensity should be observed also. (c) Finally, the angular behavior of the intensities of the features observed in the difference spectrum appears to be consistent with their assignment as doublet → quartet transitions.

The appearance of the difference spectrum above 7 V suggests the overlapping of several different quartet states. At the present time we are unable to assign these features to specific transitions. Excitation of a σ^*_{2s} electron to a π^*_{2p} orbital will result in a higher lying $^4\Sigma^-$ state. Also, excitation from orbitals lying below the π^*_{2p} to Rydberg orbitals will lead to quartet excited states. In light of our present experimental results, we feel that further theoretical investigations are warranted.

V. Summary and Conclusions

In summary, using the technique of low-energy, variable-angle, electron-impact spectroscopy, we have studied the 4 to 10 eV region of the nitric oxide electronic spectrum in detail and have observed the first doublet → quartet transitions in the gas phase. We have located and assigned two doublet → quartet transitions, $X\ ^2\Pi \rightarrow a\ ^4\Pi$ and $X\ ^2\Pi \rightarrow b\ ^4\Sigma^-$.

These assignments allow reinterpretation of previously observed infrared emission bands of nitric oxide. In addition, transitions above 7 eV energy-loss have been tentatively assigned as doublet → quartet in nature, though specific electronic state assignments were not possible. Finally, we have observed several doublet → doublet transitions near 10 eV energy which have not been reported previously.

Acknowledgment

The authors would like to thank Dr. R. H. Reiner for helpful suggestions.

Table I. Observed features in the nitric oxide spectrum in the 5-10 eV region attributable to doublet → doublet excitations.

Present Results (eV ± 0.02 eV)	Liefson[a] (eV ± 0.001 eV)	Present Results (eV ± 0.02 eV)	Liefson[a] (eV ± 0.001 eV)
5.47	5.475		7.752
5.75	5.765		7.780
	5.873	7.84	7.842
	5.998	7.97	7.965
6.04	6.052		7.989
	6.119	8.10	8.116
	6.241	8.24	8.254
6.33	6.335		8.282
	6.357	8.36	8.309
6.48	6.490		8.440
6.59	6.605	8.51	8.536
	6.712	8.56	8.563
6.76	6.779	8.67	8.590
6.88	6.890		8.713
	6.929	8.78	8.808
7.04	7.029	8.88	8.915
	7.072	8.98	9.007
7.14	7.126	9.08	9.098
	7.168	9.26[b]	
	7.254	9.54	9.564
7.33	7.336	9.62[b]	
7.41	7.391	9.72[b]	
	7.440	9.84[b]	
7.56	7.550		
	7.649		
7.70	7.699		
	7.723		

[a]Reference 1.

[b]Previously unreported.

Table II. X $^2\Pi$ v" = 0 → quartet excitation energies in the 5 to 10 eV region.

Excitation Energy (eV)		Present Quartet Assignment	Excitation Energy (eV)		Present Quartet Assignment
Present Observations (±0.02 eV)	Estimations from Optical Data		Present Observations (±0.02 eV)	Estimations from Optical Data	
5.22	5.19[a]	a $^4\Pi$ v' = 4	7.24		b $^4\Sigma^-$ b' = 11[e]
5.31	5.30[a]	5	7.36		
5.41	5.41[a]	6	7.48		
5.55[b]	5.51[a]	7	7.64		
5.60	5.60[a]	8	7.77		
5.70	5.70	b $^4\Sigma^-$ v' = 0[c]	7.91		
5.86		1	8.05		
6.00	5.99[d]	2	8.17		
6.14	6.15[d]	3	8.31		
6.29	6.28[d]	4	8.43		
6.43	6.43[d]	5	8.53		
6.57		6	8.63		
6.70		7	8.74		
6.83		8	8.85		
6.97		9	8.95		
7.12		10[e]	9.05		

[a] Estimated transition energies based on rare gas matrix optical emission data; Ref. 22.

[b] Energy uncertainty ±0.05 eV; see text.

[c] The upper state is predominantly b $^4\Sigma^-$ v' = 0 with a small a $^4\Pi$ v' = 9 contribution. the latter is also estimated in Ref. 22 to occur at 5.70 eV.

[d] Present paper's transition energy estimates using data in Refs. 22 and 23; see text.

[e] Assignment uncertain.

References

1. S. Leifson, Astrophys. J. 63, 73 (1926).
2. L. Wallace, Astrophys. J. Suppl. Ser. 7, 165 (1962).
3. H. W. Thompson and B. A. Green, Spectrochim. Acta 8, 129 (1956).
4. E. Miescher, J. Quant. Spectrosc. Radiat. Transfer 2, 421 (1962).
5. K. P. Huber and E. Miescher, Helv. Phys. Acta 36, 257 (1963).
6. T. M. Donahue, E. C. Zipf, Jr. and T. D. Parkinson, Planet. Space Sci. 18, 171 (1970).
7. E. C. Zipf, W. L. Borst and T. M. Donahue, J. Geophys. Res. 75, 6371 (1970).
8. H. S. Johnston, Acta Astronautica 1, 135 (1974).
9. J. London and J. H. Park, Can. J. Chem. 52, 1599 (1974).
10. H. Levy II, Adv. Photochem. 9, 369 (1973).
11. (a) A. Kuppermann, J. K. Rice and S. Trajmar, J. Phys. Chem. 72, 3894 (1968);
    (b) S. Trajmar, J. K. Rice and A. Kuppermann, Adv. Chem. Phys. 18, 15 (1970).
12. (a) O. A. Mosher, W. M. Flicker and A. Kuppermann, J. Chem. Phys. 59, 6502 (1973);
    (b) idem, ibid. 62, 2600 (1975).
13. S. Trajmar, W. Williams and A. Kuppermann, J. Chem. Phys. 56, 3759 (1972).
14. J. R. Oppenheimer, Phys. Rev. 29, 433 (1927).
15. G. Herzberg, Spectra of Diatomic Molecules (D. Van Nostrand and Reinhold, New York, 1950), p. 343.

16. Ref. 15, p. 558.

17. L. H. Suttcliff and A. D. Walsh, Proc. Phys. Soc. Lond. A 66, 209 (1953).

18. P. Carsky, J. Kuh and R. Sahradnik, J. Mol. Spectrosc. 55, 131 (1975).

19. K. E. Johnson and S. Lipsky, J. Chem. Phys. 66, 4719 (1977).

20. E. N. Lassettre, A. Skerbele, M. A. Dillon and K. J. Ross, J. Chem. Phys. 48, 5066 (1968).

21. H. P. Broida and M. Peyron, J. Chem. Phys. 32, 1068 (1960).

22. R. P. Frosch and G. W. Robinson, J. Chem. Phys. 41, 367 (1964).

23. M. Ogawa, Science of Light 3, 39 (1954).

24. M. Brook and J. Kaplan, Phys. Rev. 96, 1540 (1954).

25. H. J. Bernstein and G. Herzberg, J. Chem. Phys. 15, 77 (1947).

26. Ref. 15, pp. 280-295.

27. (a) I. Kovacs, Can. J. Phys. 36, 309 (1958).
(b) idem, ibid., 329 (1958).

28. R. W. Field, J. Chem. Phys. 60, 2400 (1974).

29. R. W. Field, C. R. Jones and H. P. Broida, J. Chem. Phys. 60, 4377 (1974).

Figure Captions

Fig. 1. Electron energy-loss spectrum of nitric oxide at a scattering angle of 10^{o} and impact energy of 35 eV; channel width 10 meV; accumulation time per channel 16 sec.

Fig. 2. Electron energy-loss spectrum of nitric oxide at a scattering angle of (a) 20^{o}, and (b) 80^{o}; 25 eV incident electron energy; channel width 10 meV; accumulation time per channel (a) 12 sec, and (b) 45 sec.

Fig. 3. Electron energy-loss spectrum of nitric oxide at scattering angles (a) 20^{o}, and (b) 60^{o}, at an impact energy of 25 eV and channel width fo 5 meV. (c) shows the resulting difference spectrum of (b) minus (a) as a fraction of the most intense feature of (b); accumulation time per channel (a) 329 sec and (b) 990 sec. See Section IV.B for details of calculation of difference spectrum. In panel (a), the bands designated γ belong to the $X\ ^{2}\Pi \rightarrow A\ ^{2}\Sigma^{+}$ transition and the two numbers in parentheses designate final and initial vibrational states, in that order.

Fig. 4. Electron energy-loss spectra of nitric oxide at scattering angles of (a) 20^{o}, (b) 40^{o}, (c) 60^{o} and (d) 80^{o} at an impact energy of 25 eV and channel width of 10 meV. The energy resolution is 0.085 (fwhm). (e) to (g) are difference spectra resulting, respectively, from (b) minus (a), (c) minus (a), and (d) minus (a), each expressed as a fraction of the most intense feature of the corresponding higher-angle spectrum; average accumulation time per channel 150 sec. See Section IV.B for details of calculation

of difference spectra. In panel (a), the bands designated γ, δ and ϵ belong to transitions $X\ ^2\Pi \rightarrow A\ ^2\Sigma^+$, $C\ ^2\Pi$ and $D\ ^2\Sigma^+$, respectively, and the two numbers in parentheses designate the final and initial vibrational states, in that order. The assignment of the vibrational levels of the $b\ ^4\Sigma^-$ state indicated in panel (g) are those proposed in the present work (see Section IV.C.2).

Fig. 5. Electron energy-loss spectrum of nitric oxide at scattering angles of (a) 20^o and (b) 80^o at an impact energy of 25 eV and channel width of 10 meV. (c) shows the resulting difference spectrum (b) minus (a) expressed as a fraction of the most intense feature of (b); accumulation time per channel (a) 64 sec and (b) 360 sec. See Section IV.B for details of calculation of difference spectrum.

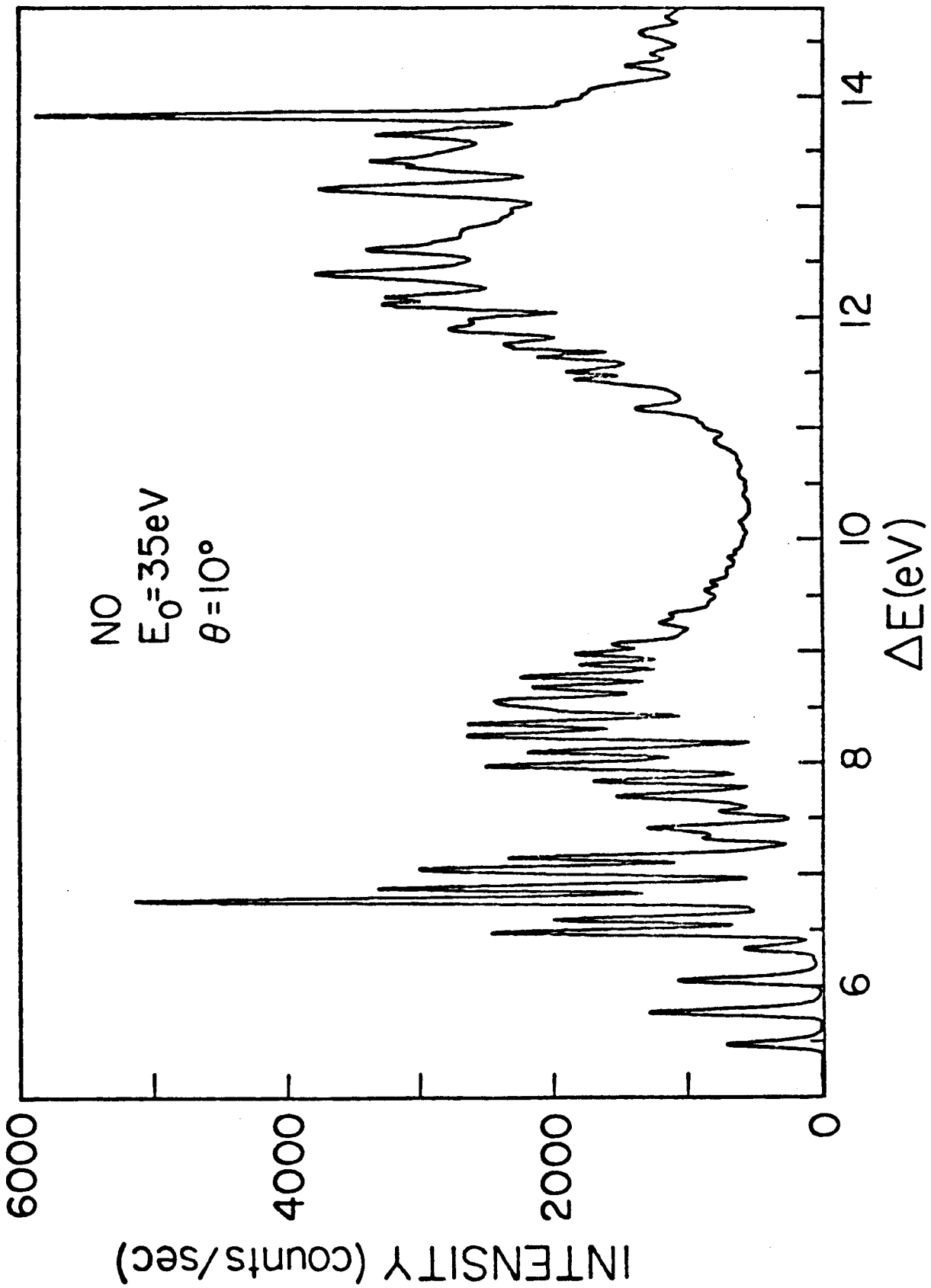
NO
E_0=35eV
θ=10°
INTENSITY (counts/sec)
6000
4000
2000
0
6
8
10
12
14
ΔE(eV)

Figure 1.

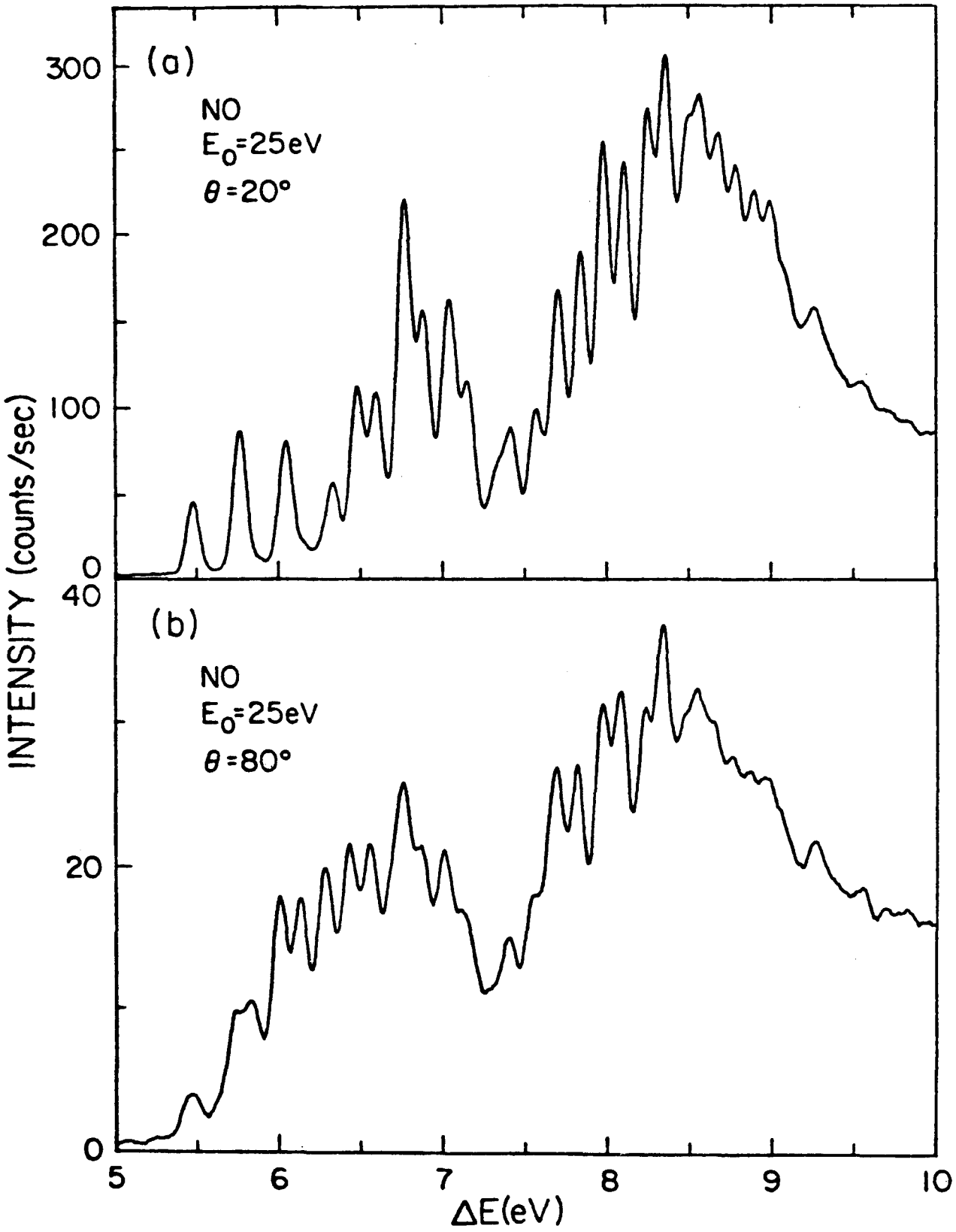
(a)
NO
E_0=25eV
θ=20°
300
200
100
0
(b)
NO
E_0=25eV
θ=80°
40
20
0
INTENSITY (counts/sec)
5
6
7
8
9
10
ΔE(eV)

Figure 2.

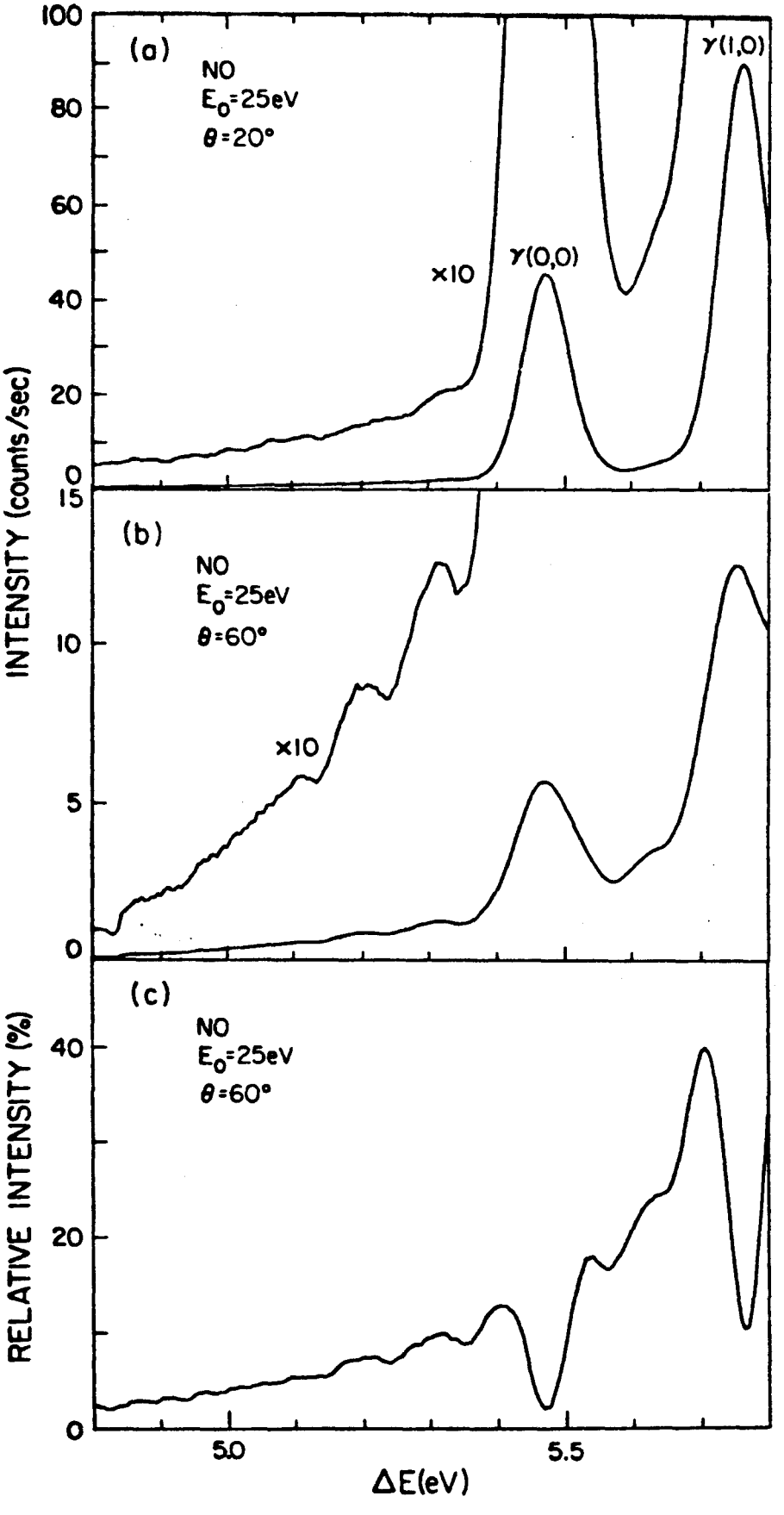
(a)
NO
E_0=25eV
θ=20°
γ(1,0)
γ(0,0)
×10
(b)
NO
E_0=25eV
θ=60°
×10
(c)
NO
E_0=25eV
θ=60°
INTENSITY (counts/sec)
RELATIVE INTENSITY (%)
ΔE(eV)
100
80
60
40
20
0
15
10
5
0
40
20
0
5.0
5.5

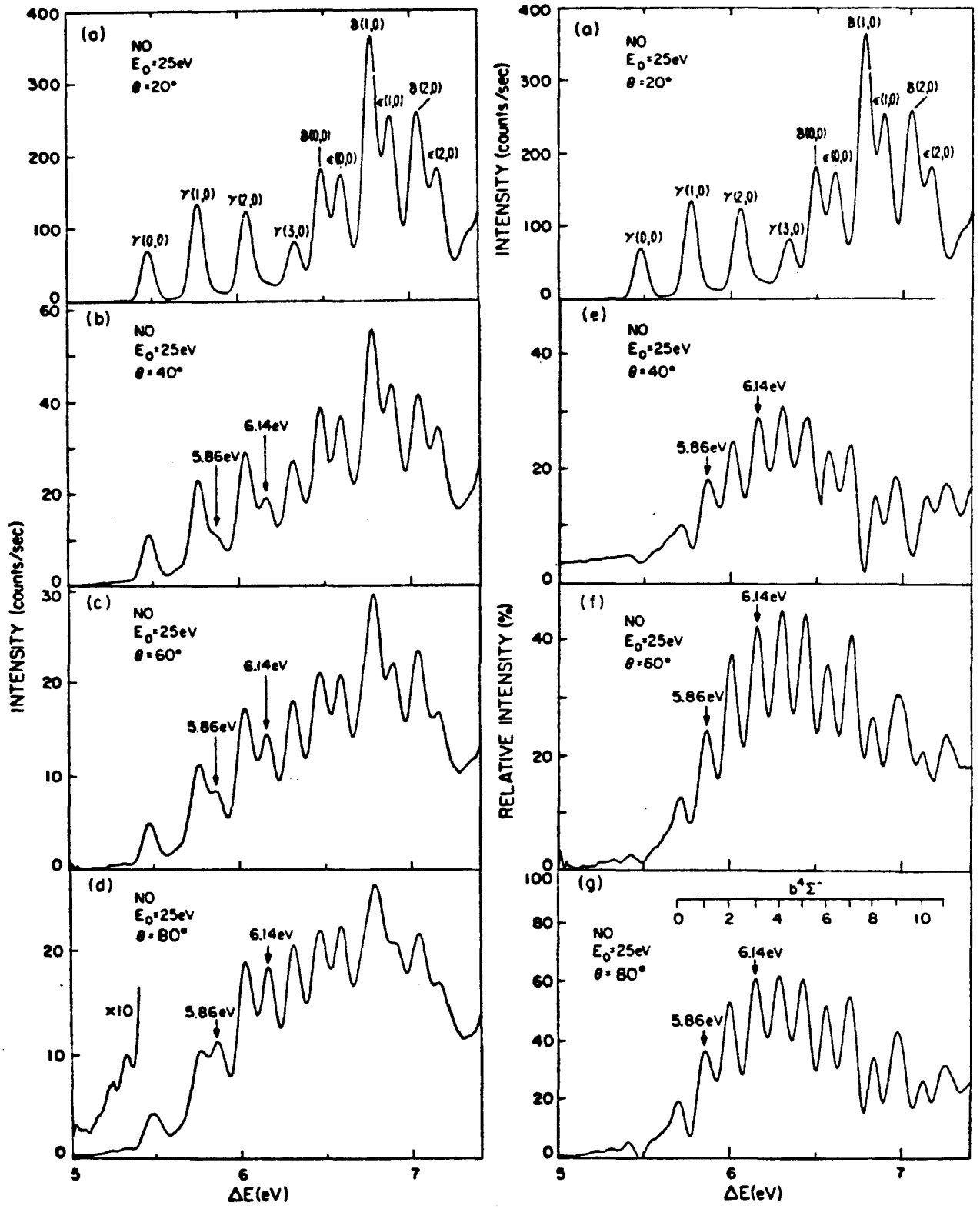
(a)
NO
E0=25eV
θ=20°
γ(0,0)
γ(1,0)
γ(2,0)
γ(3,0)
δ(0,0)
ε(0,0)
δ(1,0)
ε(1,0)
δ(2,0)
ε(2,0)
(b)
NO
E0=25eV
θ=40°
5.86eV
6.14eV
(c)
NO
E0=25eV
θ=60°
5.86eV
6.14eV
(d)
NO
E0=25eV
θ=80°
×10
5.86eV
6.14eV
INTENSITY (counts/sec)
ΔE(eV)
(e)
NO
E0=25eV
θ=40°
5.86eV
6.14eV
(f)
NO
E0=25eV
θ=60°
5.86eV
6.14eV
(g)
b⁴Σ⁻
NO
E0=25eV
θ=80°
5.86eV
6.14eV
RELATIVE INTENSITY (%)
ΔE(eV)

Figure 4.

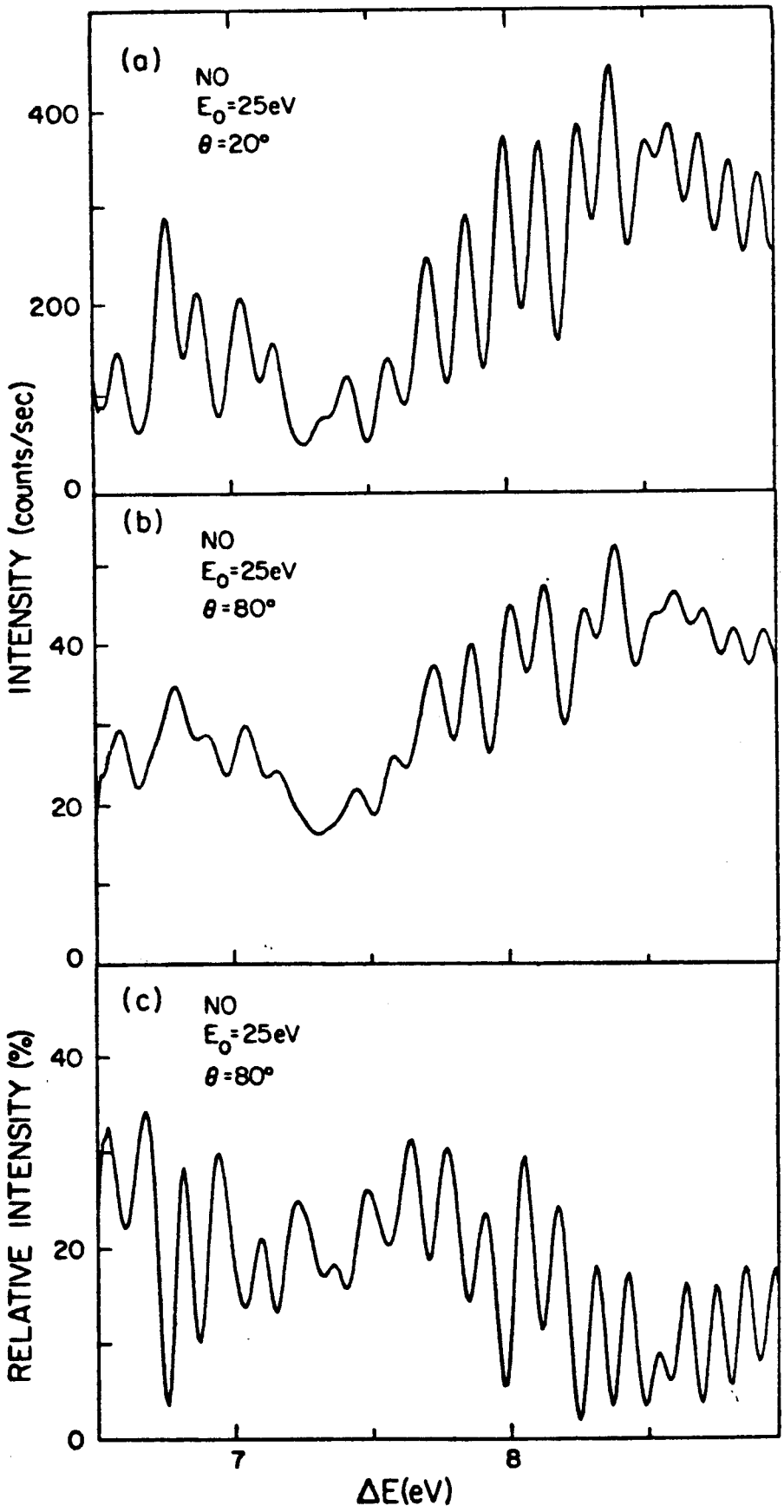
(a)
NO
E_0=25eV
θ=20°
400
200
0
(b)
NO
E_0=25eV
θ=80°
40
20
0
INTENSITY (counts/sec)
(c)
NO
E_0=25eV
θ=80°
40
20
0
RELATIVE INTENSITY (%)
7
8
ΔE(eV)

3.2. Paper II: Electronic Spectroscopy of UF_6 and WF_6 by Electron Impact

Electronic spectroscopy of UF_6 and WF_6 by electron impact[a)]

Ronald Rianda,[b)] Robert P. Frueholz, and Aron Kuppermann

Arthur Amos Noyes Laboratory of Chemical Physics,[c)]
California Institute of Technology, Pasadena, California 91125

(Received 21 March 1978)

The electron-impact excitation spectra of uranium hexafluoride (UF_6) and tungsten hexafluoride (WF_6) have been studied experimentally at impact energies of 30, 50, and 75 eV and at scattering angles from 5° to 80°. Eleven features in UF_6 are observed with maxima at 3.26, 4.2, ~4.7, 5.8, 7.0, 7.86, 9.26, 11.01, 11.75, 12.5, and 13.2 eV. Four features in WF_6 are observed with maximum intensity at 7.25, 7.9, 8.5, and 9.85, in good agreement with optical work. In addition three previously unobserved features in WF_6 at 11.75, 12.6, and 13.5 eV are reported. Similarity between the spectra of UF_6 and WF_6 suggests that the primary contribution to the absorption intensity in UF_6 above 5.8 eV and in WF_6 results from charge transfer transitions from fluorine p orbitals to metal d orbitals. Tentative assignments based in part on recent theoretical studies are made.

---

a) This work was supported in part by the Department of Energy (Contract No. EX-76-G-03-1205).

b) Work completed in partial fulfillment of the requirements for the PhD in chemistry at the California Institute of Technology.

c) Contribution No. 5753.

I. INTRODUCTION

A potential uranium isotope separation scheme involves isotopically specific vibrational excitation of the ν_3 mode of $^{235}UF_6$ followed by the electronic excitation of the vibrationally excited species by one or two ultraviolet photons to a dissociative or predissociative state. In order to determine the positions and nature of the electronically excited states which might prove important to such a scheme the electron-impact spectrum of UF_6 has been studied. As an aid to assignment of the spectrum of UF_6 the electron impact spectrum of WF_6 has also been determined.

In previous studies the technique of low-energy variable-angle electron-impact spectroscopy has been primarily applied to molecules composed of light nuclei (first and second row elements) with principal emphasis on the detection of spin-forbidden transitions.[1-4] In these systems the differential cross section (DCS) as a function of angle is a sensitive probe of the spin-forbiddenness or allowedness of a transition. Typically, the DCS for an optically allowed transition decreases by approximately two orders of magnitude as the scattering angle is increased from 10° to 80°. In contrast the DCS for a spin-forbidden excitation (one in which the spin quantum number changes by unity) remains relatively constant, within a factor of 2 or 3, over a similar angular range. Electron impact spectroscopy is also suitable for studying molecules containing heavy nuclei[5-7] such as UF_6 and WF_6, but in these systems spin-orbit coupling may be significant. The

resultant mixing of states of different spin multiplicities causes the correlation between the angular behavior of the DCS and the spin nature of the transition to become less clear.[5]

Both UF_6 and WF_6 possess O_h symmetry.[8] From the viewpoint of ligand field theory the valence electrons of the central metal atom (the 5f, 6d, and 7s electrons of uranium and the 5d and 6s electrons of tungsten) are assumed to be transferred to the fluorine atoms yielding a complex of the form $M^{6+} F_6^{6-}$. This is a crude approximation which nevertheless is helpful in explaining the observed spectra. In this model,transitions correspond to charge transfer from ligand fluorine atom orbitals to the 5f, 6d, and 7s orbitals of uranium and the 5d and 6s orbitals of tungsten.

Previous theoretical studies on UF_6 have considered only transitions from ligand orbitals to uranium 5f orbitals and therefore assignment of only the low energy portion of the spectrum was attempted.[9-11] The most reliable calculation to date is that of Koelling, Ellis, and Bartlett[11] using the relativistic,self-consistent, Dirac-Slater model. They have obtained one-electron energy levels, charge distributions, ligand-to-uranium 5f orbital transitions energies, and ionization potentials which agree well with experiment. Figure 1 shows the orbital energy diagram obtained for UF_6 based in part on their calculations. There have been no theoretical studies of the electronic structure of WF_6 to date.

Prior to our investigation numerous optical absorption studies of UF_6 in the region below 6 eV have been performed.[12-16] Agreement

between these previous experimental results and the theoretical calculations is fair. However, considering the density of predicted transitions, any apparent agreement may be fortuitous. McDiarmid has performed the only optical studies of UF_6 and WF_6 above 6 eV.[17,18] In addition to the optical work, previous electron-impact studies of UF_6 have been performed by Chutjian et al.[6] and Srivastava et al.[7] from which photoabsorption cross sections were obtained. Attempts at interpreting the observed spectra were limited.

II. EXPERIMENTAL

The electron-impact spectrometer used in this study was that reported by Kuppermann et al.[1] with the surfaces of all electron optical elements having been goldplated. With unplated surfaces (oxygen-free, high-purity copper lenses and hemispherical analyzers and molybdenum apertures) operation of the instrument was limited to periods of one to two hours before complete disassembly and cleaning of the electron optics was required, due to the reactivity of the hexafluorides. After goldplating continuous operation for periods up to one week was possible.

Spectra of UF_6 and WF_6 in the energy-loss region 0-18 eV were taken at impact energies of 30, 50, and 75 eV at scattering angles from 5° to 80°. The sample chamber pressure was typically 2 mTorr as indicated by an uncalibrated Schulz-Phelps ionization gauge, while the incident electron beam current was approximately 40 nA. Instrumental resolution was electron-optically set at approximately 0.18 eV. Accumulation times for typical spectra ranged from 3 hours for a 10° spectrum to about 12 hours for an 80° spectrum. This corresponds to a 10 meV channel width accumulation time of between 10 sec and 40 sec. Spectra presented in Figs. 2 through 5 were digitally smoothed using an 11 to 19 channel least-squares cubic polynomial convolution. Before smoothing, typical signal-to-noise ranged from about 3 : 1 on weak features in high-angle spectra to approximately 100 : 1 for strong features in low-angle spectra.

The UF_6 was supplied by Varlacoid Chemical Co.[19] with a stated purity of 99.9%. The WF_6 was obtained from PCR Inc.[20] with a stated purity of 99%. Both samples were used without further purification.

III. RESULTS

Figures 2 and 3 show the electron-impact spectrum of UF_6 and WF_6 at an impact energy of 50 eV and scattering angles of 10° and 70°. The higher energy-loss regions of both UF_6 and WF_6 are shown in greater detail at 75 eV impact energy in Figs. 4 and 5. The ratios of DCS's of several features in the spectrum of UF_6 at 50 eV to the DCS of the 5.8 eV feature are shown in Fig. 6. Similarly, for WF_6 DCS ratios with respect to the 8.5 eV feature are shown in Fig. 7.

The most significant changes with angle in the spectra of UF_6 occur in the 3-5 eV region and at the 11.01 eV feature. At an impact energy of 50 eV the integrated intensity under the 3.26 eV feature increases by about an order of magnitude relative to that under the feature at 5.8 eV as the scattering angle is increased from 10° to 80°. The major portion of this change occurs between scattering angles of 10° and 20°. Chutjian et al.[6] found a change in this ratio by a factor of about 3.5 in going from 20° to 135°, at an impact energy of 20 eV. There is no inconsistency between these two observations. For molecules with light nuclei, such behavior would be consistent with three possible interpretations: a) this feature is due to a spin-forbidden transition; b) it is due to a spin-allowed but symmetry-forbidden transition; and c) it results from a spin-allowed transition with an underlying spin-forbidden transition, a possibility that would have been considered to be the most likely.

However, the relationship of the variation of the DCS with scattering angle and the spin-allowedness of a transition is ambiguous for molecules such as UF_6 and WF_6 which contain heavy nuclei. In these systems the "goodness" of the orbital and spin angular momentum quantum numbers L and S is questionable. Both theoretical and experi-

mental information regarding the spin-orbit interaction as applied to the spin nature of the wavefunction is lacking. Similarly, attempts at correlating the electron impact DCS with the magnitude of the spin-orbit interaction have been limited to a study of Xe by Williams, Trajmar, and Kuppermann.[5] The results of this study indicate that for atoms with significant spin-orbit interactions DCS variations with angle may no longer be used with reliability to assign the spin nature of a transition. In molecular systems containing a heavy central atom in a strong ligand field provided by surrounding atoms, the influence of that field on the central atom orbitals may predominate over the spin-orbit interaction.[21-23] However, the implication of this regarding DCS variations is unknown.

In the 4 to 5 eV region the low-angle spectrum shows an unresolved feature with an apparent (deconvoluted) intensity maximum at approximately 4.7 eV, while the high-angle spectrum shows a feature with a distinct maximum at 4.2 eV. This observed shift in position indicates the overlap of at least two electronic transitions. In the previous electron-impact study of UF_6,[6] these features were also observed at 4.2 and 4.8 eV. The former was attributed to an optically forbidden transition and the latter to a weak dipole-allowed transition. However, Koelling et al.,[11] on the basis of the relativistic SCF $X\alpha$ calculations, assign both as dipole-allowed transitions. Optically, a feature is observed at 4.77 eV as well as two much weaker transitions at 4.13 and 3.87 eV.[15] The intensity under the 11.01 eV feature increases by a factor of 5 relative to that under the 5.8 eV one as the scattering angle is increased from 10° to 80°. This increase is significant and will be used in discussing the assignment of the 11.01 eV transition in Sec. IV.

In the spectrum of WF_6 there is no detectable absorption below 5.5 eV. The only significant change with angle in the spectrum of this molecule occurs at 11.75 eV. The integrated intensity under this feature increases by a factor of about 7 relative to that under the 8.5 eV one as the scattering angle is increased from 10° to 80°.

The similarities between the spectra of UF_6 and WF_6 are quite apparent from comparison of Figs. 2-5. In addition to the absence of the low-lying absorptions in WF_6, the principal difference is that the WF_6 spectrum is shifted to higher energy by about 1 eV with respect to the UF_6 spectrum. Table I summarizes our results for UF_6 and WF_6, respectively.

V. DISCUSSION

In order to assign the bands in the UF_6 spectrum it is worthwhile to make use of the similarities between it and the WF_6 spectrum. Since WF_6 does not possess low-lying unoccupied f valence orbitals we believe all transitions observed below 14 eV in this molecule correspond to a valence charge transfer from fluorine ligand σ and π orbitals to tungsten 5d orbitals. The possibility exists that features observed in the region of the spectrum above approximately 10 eV are due to Rydberg excitations. We do not think this to be a correct assignment for the features at 12.6 and 13.5 eV for the following reason. The intensities of these transitions are significantly greater than would be expected for Rydberg excitations. The oscillator strength for the transition at 13.5 eV in WF_6 may be estimated in the following manner. The generalized electron impact oscillator strength,[24] f_{ei}, is given by

$$f_{ei} = \frac{W}{2} \frac{k_0}{k_n} K^2 \sigma \quad ,$$

where W is the excitation energy, k_0 and k_n are the incident and scattered electron momenta, respectively, K is the change in momentum suffered by the electron as a result of the collision, and σ is the differential cross section for the transition being considered. Since we have not obtained absolute DCS's we are only able to estimate ratios of f_{ei}. Lassettre et al.[24] have shown that as K^2 approaches zero, f_{ei} approaches the optical oscillator strength f_{opt}. From the optical data of R. McDiarmid[17] we estimate f_{opt} of the 8.5 eV feature to be 0.3.[25]

Using our 50 eV incident energy spectra, and extrapolating the f_{ei} versus K^2 curve monotonically to $K^2 = 0$, we obtained an unnormalized f_{opt} for the 8.5 eV transition.[26] Since this must correspond to the value of f_{opt} (absolute) obtained from the data of ref. 17, we are able to calculate the normalization factor which makes our measurements absolute. This factor is independent of the transition being considered and is, hence, the same for the 13.5 eV feature. The resulting absolute value of f_{opt} for this transition (obtained from a similar extrapolation[26] to $K^2 = 0$ of the corresponding f_{ei}) is about 0.8, which is roughly three times greater than the maximum oscillator strength expected for a Rydberg excitation.[27] The transition at 11.75 eV in WF_6 is significantly weaker than that at 13.5 eV, making differentiation between valence or Rydberg states unclear.

The similarity of the UF_6 spectrum above 5 eV energy loss to that of WF_6 suggests that the primary contribution to the spectrum in this region is also due to transitions from fluorine ligand σ and π orbitals to uranium 6d orbitals, although the apparently increased intensity of the features at 5.8 and 7.86 eV in UF_6 relative to the corresponding features in WF_6 may indicate an additional contribution in UF_6 from ligand to 5f orbital excitations.

Use of the orbital energy ordering for UF_6 as well as excitation energies calculated by Koelling et al.[11] (orbital energy diagram shown in Fig. 1) allows a more specific assignment of some of the transitions. Orbital designations are those appropriate for the O_h' double group[28] re-

quired by the spin-orbit interactions in these systems. Since no electronic structure calculations have been reported for WF_6, we assume in our analysis that the orbital ordering in that molecule is the same as for the corresponding orbitals in UF_6. Transitions below 5.8 eV in UF_6 have been assigned by Koelling et al. as ligand to 5f orbital excitations.[11] These assignments are consistent with our results and are summarized in Table 1. The 5.8 eV feature in UF_6 has been assigned as a ligand to 5f transition for which the calculated excitation energy is 6.31 eV. However, comparison with our WF_6 results indicates that a significant fraction of the intensity of this feature is due to excitation to the uranium 6d ($4\gamma_{8g}$, $2\gamma_{7g}$) orbitals (see Fig. 1). Therefore, the most reasonable explanation would be that this UF_6 feature results from a superposition of at least the $3\gamma_{8g} \rightarrow 5\gamma_{8u}$ and $3\gamma_{8u} \rightarrow 4\gamma_{8g}$, $2\gamma_{7g}$ one-electron excitations. Analogously, the 7.25 eV feature in WF_6 is assigned to the $3\gamma_{8u} \rightarrow 4\gamma_{8g}$, $2\gamma_{7g}$ transitions. The next two excitations in UF_6 at 7.0 and 7.86 and in WF_6 at 7.9 and 8.5 eV are assigned as the $2\gamma_{6u} \rightarrow 4\gamma_{8g}$, $2\gamma_{7g}$ and $2\gamma_{8u}$, $1\gamma_{7u} \rightarrow 4\gamma_{8g}$, $2\gamma_{7g}$ one-electron transitions, respectively. In the ligand field theory approach, using O_h symmetry, among the most intense transitions is expected to be the transition from the fluorine $p\sigma$ (t_{2u}) orbital to the metal e_g-orbital (from spatial overlap considerations). Therefore we assign the intense features at 13.5 eV in WF_6 and 13.2 eV in UF_6 as the $1\gamma_{6u}$, $1\gamma_{8u} \rightarrow 5\gamma_{8g}$ transitions. In UF_6 the nearly degenerate $1\gamma_{7u}$ and $2\gamma_{8u}$ orbitals are calculated to lie approximately 0.6 eV higher in energy than the $1\gamma_{6u}$ and $1\gamma_{8u}$ orbitals. Excitation from these orbitals is allowed and

is expected to be about 0.6 eV below the $1\gamma_{6u}$, $1\gamma_{8u} \rightarrow 5\gamma_{8g}$ transition. Therefore we tentatively assign the 12.5 eV feature in UF_6 and the 12.6 eV feature in WF_6 to the $1\gamma_{7u}$, $2\gamma_{8u} \rightarrow 5\gamma_{8g}$ excitations. The angular behavior of the features at 3.26 and 11.01 eV in UF_6 and at 11.75 eV in WF_6 is distinctly different from that of the other features in the spectra. Figure 6 displays the ratios of integrated intensities of some bands of UF_6 relative to the 5.8 eV feature. Figure 7 shows the corresponding ratios for features of WF_6 relative to the integrated intensity of the 8.5 eV band. The ratios demonstrate that the features at 3.26 and 11.01 in UF_6 and at 11.75 eV in WF_6 display a significant increase in relative intensity as the scattering angle is increased. While the concept of singlet and triplet states is not well defined for these molecules (see Section I), this angular behavior is very similar to that displayed by transitions which have been definitively assigned as singlet → triplet in systems containing only light nuclei.[1-4] A possible explanation for the angular behavior of the 11.01 eV feature in UF_6 and the 11.75 eV feature in WF_6 is that these transitions contain significant singlet → triplet contributions. It is possible that the ligand-field interaction is sufficiently strong to predominate over the spin-orbit interaction yielding states which are either primarily singlet or primarily triplet in nature.[21-23] In addition to the feature at 11.01 eV in UF_6 there is also a transition at 11.75 eV which appears to display similar angular behavior, suggesting that it too may be due to a singlet → triplet transition. Unfortunately, this transition is heavily overlapped with the 12.5 eV feature and reliable integrated intensity ratios were not obtainable.

The feature at 3.26 eV in UF_6 has been previously assigned to overlapping singlet → singlet and singlet → triplet transitions.[16] This transition is presumably due exclusively to a ligand to uranium 5f orbital excitation, and consequently care must be taken when attempting to assign it using an LS coupling scheme. This is due to the fact that the ligand field interaction for the 5f orbitals is significantly weaker than that for the 6d orbitals and is expected to be of the same order as the spin orbit interaction, weakening the argument in behalf of an LS coupling scheme.[21-23]

Three additional optically allowed excitations, $1\gamma_{6u}$, $1\gamma_{8u} \rightarrow 4\gamma_{8g}$, $2\gamma_{7g}$, $3\gamma_{8u} \rightarrow 5\gamma_{8g}$ and $2\gamma_{6u} \rightarrow 5\gamma_{8g}$ are predicted by the ordering scheme of Fig. 1. They may lie in the 8-11 eV region where only one feature is apparent in our spectra: the 9.26 eV feature in UF_6 and the 9.85 feature in WF_6. Several higher lying transitions are also observed in both WF_6 and UF_6 above 14 eV which we tentatively assign to Rydberg excitations.

VI. CONCLUSIONS AND SUMMARY

We have obtained electron impact spectra of UF_6 and WF_6 at several different impact energies and scattering angles from 5° to 80°. Our measurements for UF_6 are in good agreement with previous ones. For WF_6 the results of our experiments are also in good agreement with previous limited optical studies. We have reported several previously unobserved transitions at higher energy losses. Assignments of the spectra of both UF_6 and WF_6 are proposed using the theoretical results of Koelling et al.[11] and relying heavily upon similarities in the UF_6 and WF_6 spectra. Below 14 eV we assign all transitions in WF_6 as ligand to tungsten 5d orbital charge transfer excitations, with the exception of the feature at 11.75 eV, the possible Rydberg nature of which cannot be excluded. The spectrum of UF_6 between 5 and 14 eV is very similar to that of WF_6, and the primary contribution to this region is similarly assigned to ligand-to-uranium 6d orbital excitations. Correspondingly, transitions in UF_6 below 5 eV are assigned exclusively to ligand-to-5f excitations.

ACKNOWLEDGMENT

The authors express their appreciation to Professor H. B. Gray for useful discussions.

TABLE I. Energy-loss features in UF_6 and WF_6.[a, b]

Transition	UF_6	WF_6
$3\gamma_{8u} \rightarrow 2\gamma_{7u}, 4\gamma_{8u}, 3\gamma_{7u}$	3.26	
$3\gamma_{8g} \rightarrow 2\gamma_{7u}$	4.2	
$3\gamma_{8g} \rightarrow 4\gamma_{8u}$	~4.7	
$3\gamma_{8u} \rightarrow 4\gamma_{8g}, 2\gamma_{7g}$	5.8[c]	7.25
$2\gamma_{6u} \rightarrow 4\gamma_{8g}, 2\gamma_{7g}$	7.0[c]	7.9
$2\gamma_{8u}, 1\gamma_{7u} \rightarrow 4\gamma_{8g}, 2\gamma_{7g}$	7.86[c]	8.5
	9.26	9.85
	11.01	
	11.75	11.75
$2\gamma_{8u}, 1\gamma_{7u} \rightarrow 5\gamma_{8g}$	12.5	12.6
$1\gamma_{6u}, 1\gamma_{8u} \rightarrow 5\gamma_{8g}$	13.2	13.5

[a]The energy losses are in eV and have an accuracy of ± 0.05 eV.

[b]The assignments in this table are based in part on the calculations of ref. 11; the energy losses are those of the present experiments.

[c]There may also be contribution to these features from ligand-to-5f transitions.

References

[1](a) A. Kuppermann, J. K. Rice and S. Trajmar, J. Phys. Chem. 72, 3894 (1965); (b) J. K. Rice, Ph.D. Thesis, California Institute of Technology, Pasadena, California (1969).

[2]S. Trajmar, J. K. Rice and A. Kuppermann, Advan. Chem. Phys. 78, 15 (1970).

[3](a) O. A. Mosher, W. M. Flicker and A. Kuppermann, J. Chem. Phys. 59, 6502 (1973); (b) O. A. Mosher, W. M. Flicker and A. Kuppermann, J. Chem. Phys. 62, 2600 (1975).

[4]R. P. Frueholz, W. M. Flicker, O. A. Mosher and A. Kuppermann, Chem. Phys. Lett. 52, 86 (1977).

[5]W. Williams, S. Trajmar and A. Kuppermann, J. Chem. Phys. 62, 3031 (1975).

[6]A. Chutjian, S. K. Srivastava, S. Trajmar, W. Williams and D. C. Cartwright, J. Chem. Phys. 64, 4791 (1976).

[7]S. K. Srivastava, D. C. Cartwright, S. Trajmar, A. Chutjian and W. X. Williams, J. Chem. Phys. 65, 208 (1976).

[8]R. S. McDowell, L. B. Asprey and R. T. Paine, J. Chem. Phys. 61, 3571 (1974).

[9]D. H. Maylotte, R. L. St. Peters and R. P. Messmer, Chem. Phys. Lett. 38, 181 (1976).

[10]M. Boring and J. W. Moskowitz, Chem. Phys. Lett. 38, 185 (1976).

[11]D. D. Koelling, D. E. Ellis, and R. J. Bartlett, J. Chem. Phys. 65, 3331 (1976).

[12]G. H. Dieke and A. B. F. Duncan, Spectroscopic Properties of Uranium Compounds, (McGraw-Hill, Inc., New York, 1949).

[13] G. P. Sheretmet'ev, Optika i Spektroskopiya 1, 181 (1956).

[14] H. J. Hurst and P. W. Wilson, Spectr. Lett. 5, 275 (1972).

[15] G. L. De Poorter and C. K. Rofer-De Poorter, Spectr. Lett. 8, 521 (1975).

[16] W. B. Lewis, L. B. Asprey, L. H. Jones, R. S. McDowell, S. W. Rabideau, A. H. Zeltmann and R. T. Paine, J. Chem. Phys. 65, 2707 (1976).

[17] R. McDiarmid, J. Chem. Phys. 65, 168 (1976).

[18] R. McDiarmid, J. Chem. Phys. 61, 3333 (1974).

[19] Varlacoid Chemical Co., 666 S. Front St., Elizabeth, NJ 07202.

[20] PCR Inc., Research Chemicals Division, P.O. Box 1466, Gainesville, FL 32602.

[21] W. Moffitt, G. L. Goodman, M. Fred and B. Weinstock, Mol. Phys. 2, 109 (1959).

[22] N. J. Reisfeld and G. A. Crosby, Inorg. Chem. 4, 65 (1965).

[23] G. C. Allen and K. D. Warren, Coord. Chem. Rev. 16, 227 (1975).

[24] E. N. Lassettre, A. Skerbele and N. A. Dillon, J. Chem. Phys. 50, 1829 (1969).

[25] Value of f_{opt} obtained using data of ref. 17 and a path length of 10 cm (personal communication, R. McDiarmid).

[26] The values of K^2 ranged from about 0.15 to about 2.4, over which range the unnormalized f_{ei} increased by a factor of only about 2.1 for the 8.5 eV transition and about 1.6 for the 13.5 eV feature. Therefore, the extrapolations to $K^2 = 0$, although approximate, should be adequate[24] for the present purposes.

[27] M. B. Robin, Higher Excited States of Polyatomic Molecules, Vol. I, (Academic Press, New York, 1974) p. 30.

[28] N. Tinkham, Group Theory and Quantum Mechanics, (McGraw-Hill, Inc., New York, 1964) pp. 75-80.

Figure Captions

Figure 1. Valence orbital energy ordering for UF_6. Symmetry designations listed under O_h are those appropriate for the octahedral point group, while those beneath O_h' are appropriate for the octahedral double point group. The $5\gamma_{sg}$ is about 13.2 eV above the $1\gamma_{su}$. The location of the others is approximate. The levels $3\gamma_{su}$ and below represent fully occupied valence orbitals involved in the U–F bonding.

Figure 2. Electron energy loss spectrum of UF_6 at (1) 10° and (b) 70°; 50 eV incident electron energy; 4×10^{-8} A incident beam current; 2 mTorr sample pressure reading from an uncalibrated Schulz-Phelps gauge; resolution approximately 0.18 eV (fwhm).

Figure 3. Electron energy loss spectrum of WF_6 at (a) 10° and (b) 70°; 50 eV incident electron energy; 7×10^{-8} A incident beam current; 1 mTorr sample pressure reading from an uncalibrated Schulz-Phelps gauge; resolution approximately 0.18 eV (fwhm). No absorption is observed for ΔE below 5.5 eV.

Figure 4. Electron energy loss spectrum of UF_6 at 5°; 75 eV incident electron energy; other experimental parameters are similar to those in Fig. 2.

Figure 5. Electron energy loss spectrum of WF_6 at 5°; 75 eV incident electron energy; other experimental parameters are similar to those in Fig. 3.

Figure 6. Integrated intensities of several electronic transitions in UF_6 divided by the integrated intensity of the 5.8 eV feature as a function of scattering angle θ at an incident electron-energy of 50 eV; the transition energies for each of the curves are indicated. The scale factors in parentheses indicate the coefficients by which the intensity ratios were multiplied before being plotted.

Figure 7. Integrated intensities of several electronic transitions in WF_6 divided by the integrated intensity of the 8.5 eV feature as a function of θ at an incident electron energy of 50 eV; the transition energies for each of the curves are indicated. The intensity ratio for the 11.01 eV transition was multiplied by 0.01 before plotting.

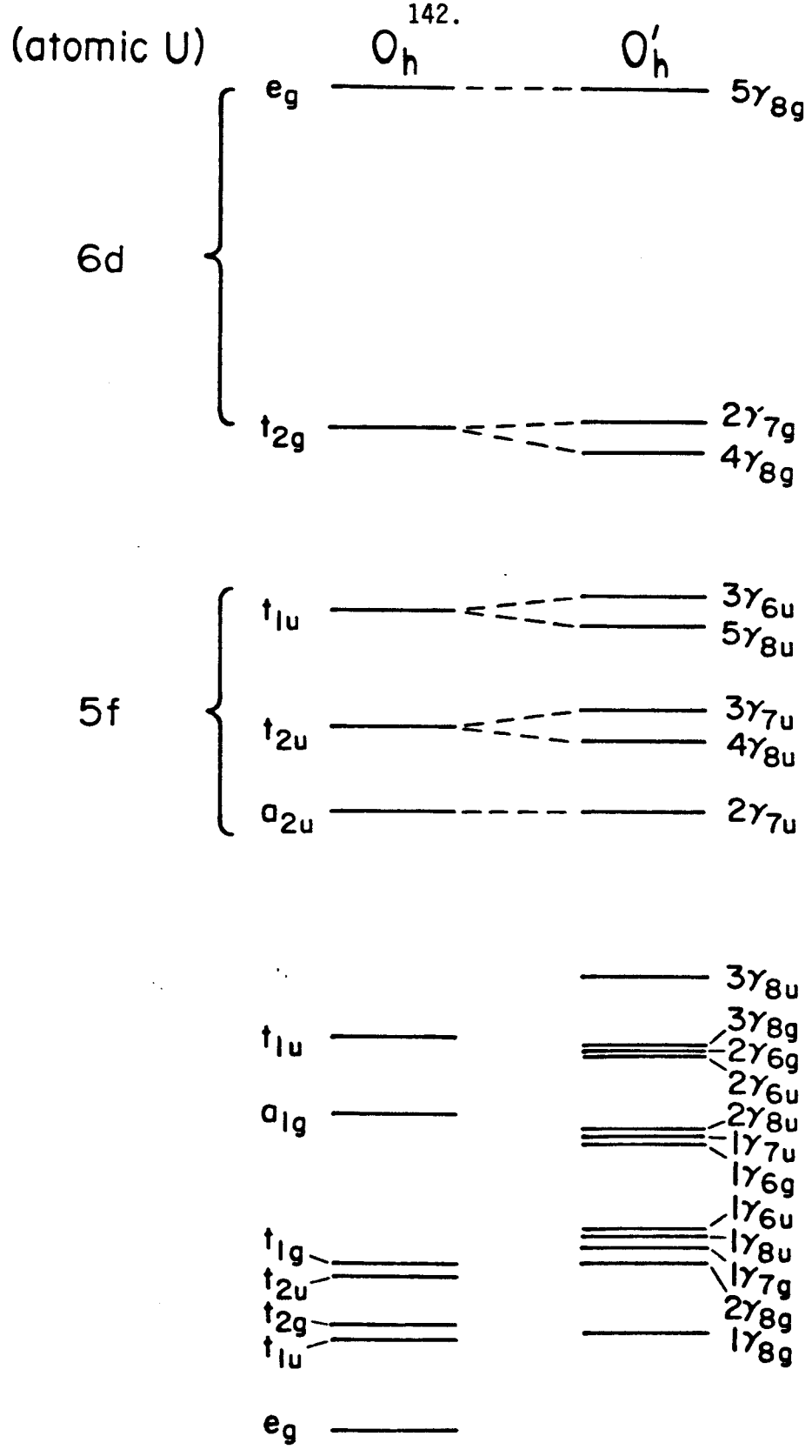
(atomic U)
O_h
O_h'
e_g
$5\gamma_{8g}$
6d
t_{2g}
$2\gamma_{7g}$
$4\gamma_{8g}$
t_{1u}
$3\gamma_{6u}$
$5\gamma_{8u}$
5f
t_{2u}
$3\gamma_{7u}$
$4\gamma_{8u}$
a_{2u}
$2\gamma_{7u}$
$3\gamma_{8u}$
t_{1u}
$3\gamma_{8g}$
$2\gamma_{6g}$
$2\gamma_{6u}$
a_{1g}
$2\gamma_{8u}$
$1\gamma_{7u}$
$1\gamma_{6g}$
$1\gamma_{6u}$
t_{1g}
$1\gamma_{8u}$
t_{2u}
$1\gamma_{7g}$
t_{2g}
$2\gamma_{8g}$
t_{1u}
$1\gamma_{8g}$
e_g

Figure 1.

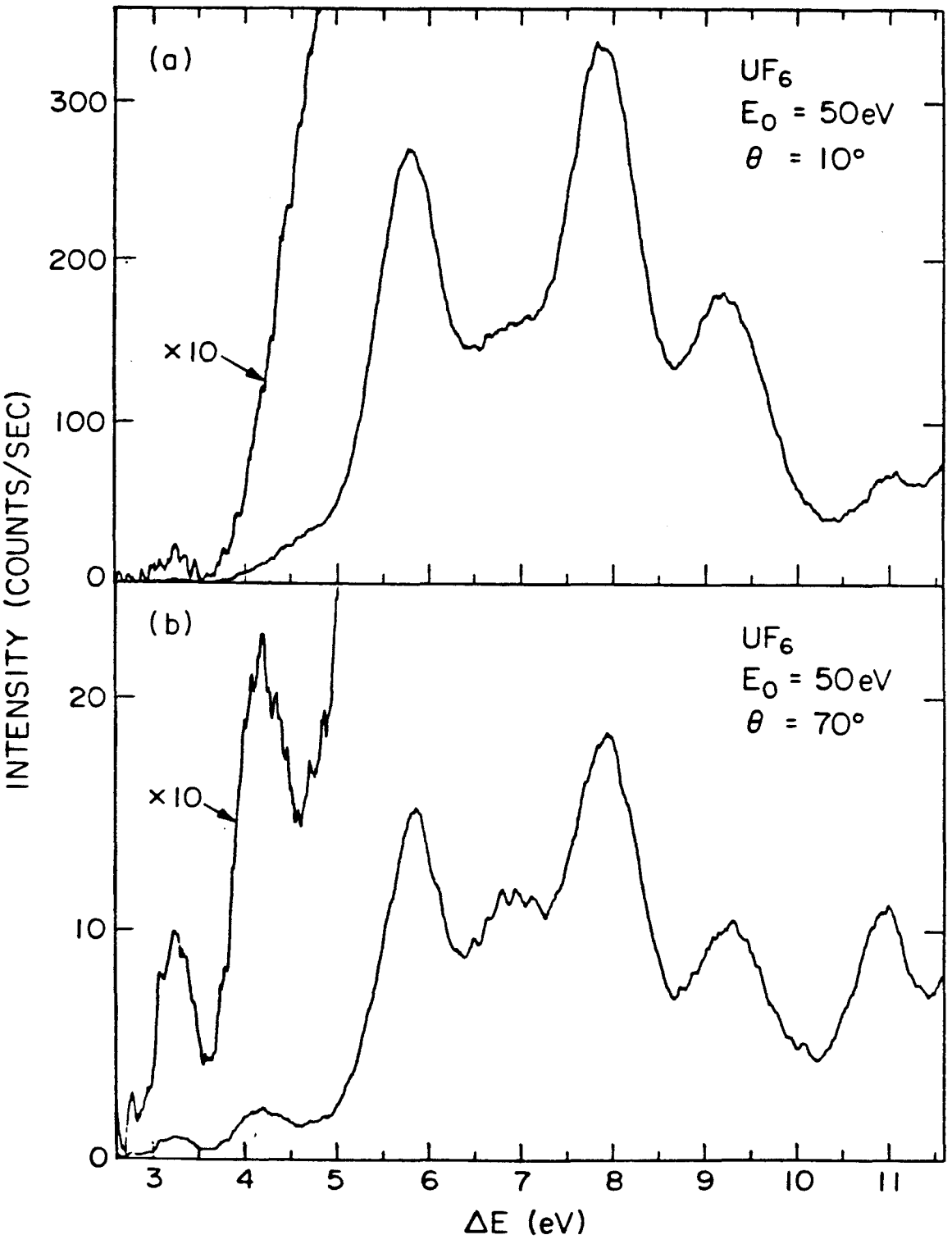
(a)
UF6
E0 = 50eV
θ = 10°
×10
300
200
100
0
(b)
UF6
E0 = 50eV
θ = 70°
×10
20
10
0
INTENSITY (COUNTS/SEC)
3
4
5
6
7
8
9
10
11
ΔE (eV)

Figure 2.

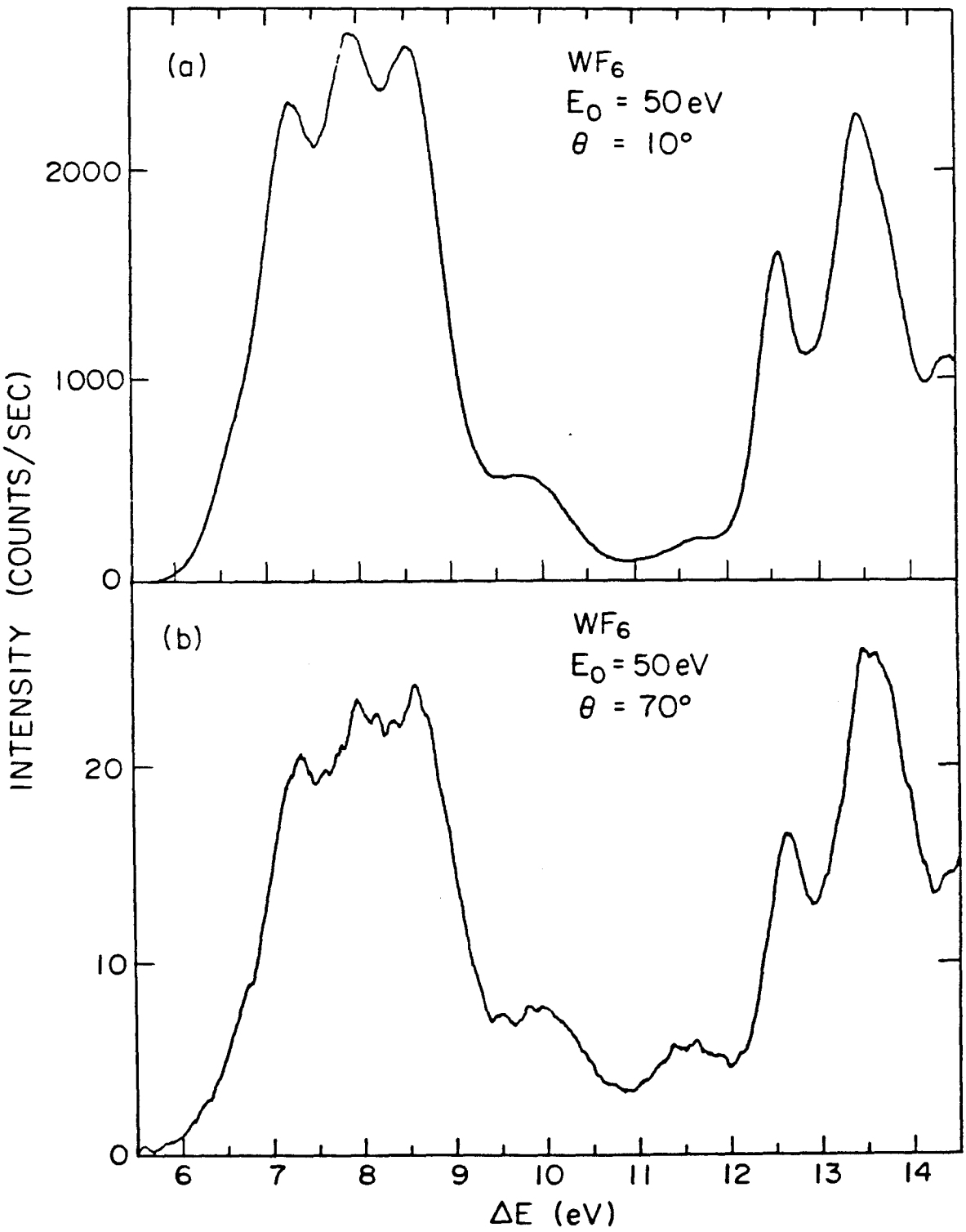
(a)
WF6
E0 = 50 eV
θ = 10°
2000
1000
0
(b)
WF6
E0 = 50 eV
θ = 70°
20
10
0
INTENSITY (COUNTS/SEC)
6
7
8
9
10
11
12
13
14
ΔE (eV)

Figure 3.

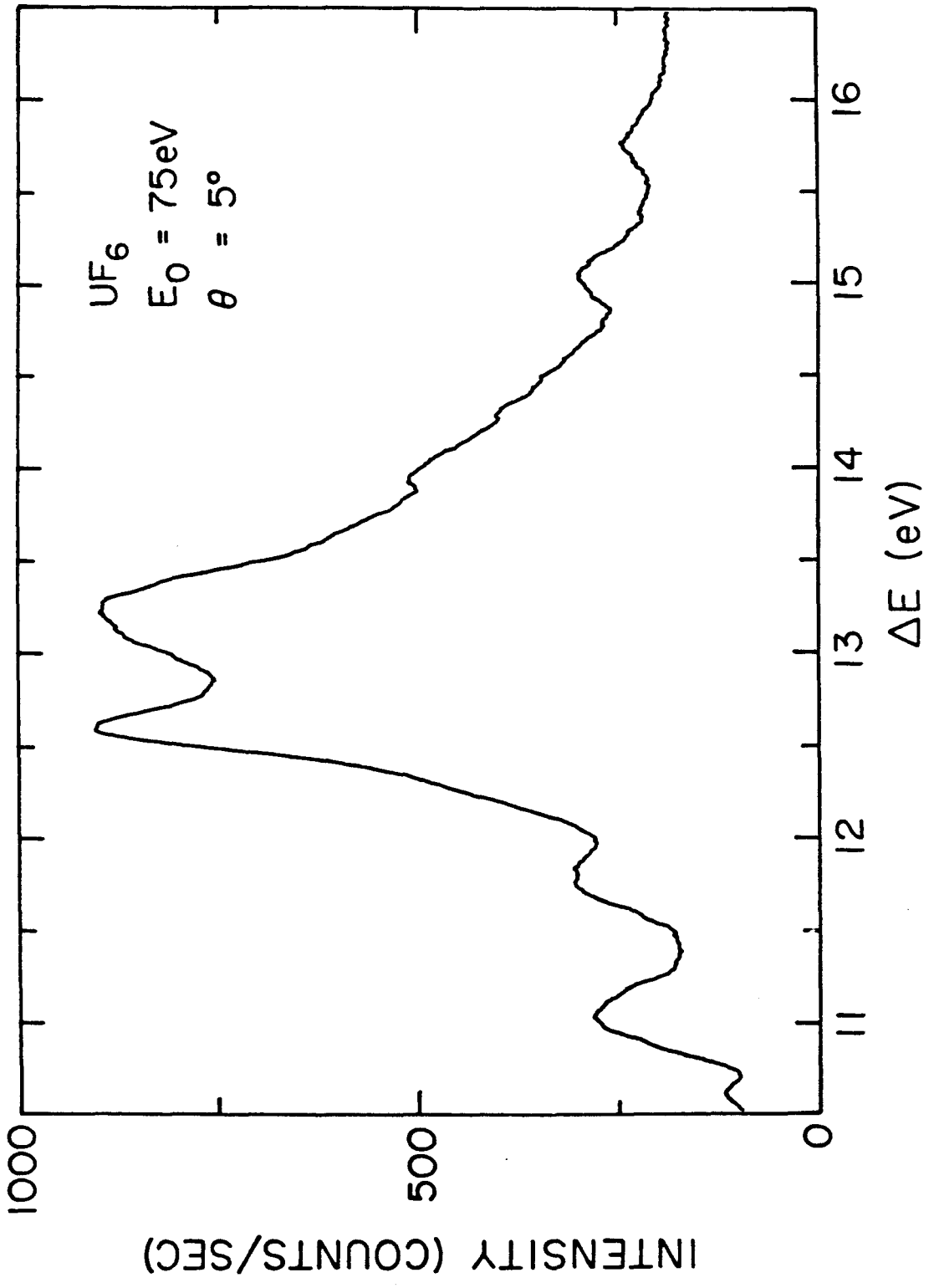
UF6
E0 = 75eV
θ = 5°
INTENSITY (COUNTS/SEC)
1000
500
0
11
12
13
14
15
16
ΔE (eV)

Figure 4.

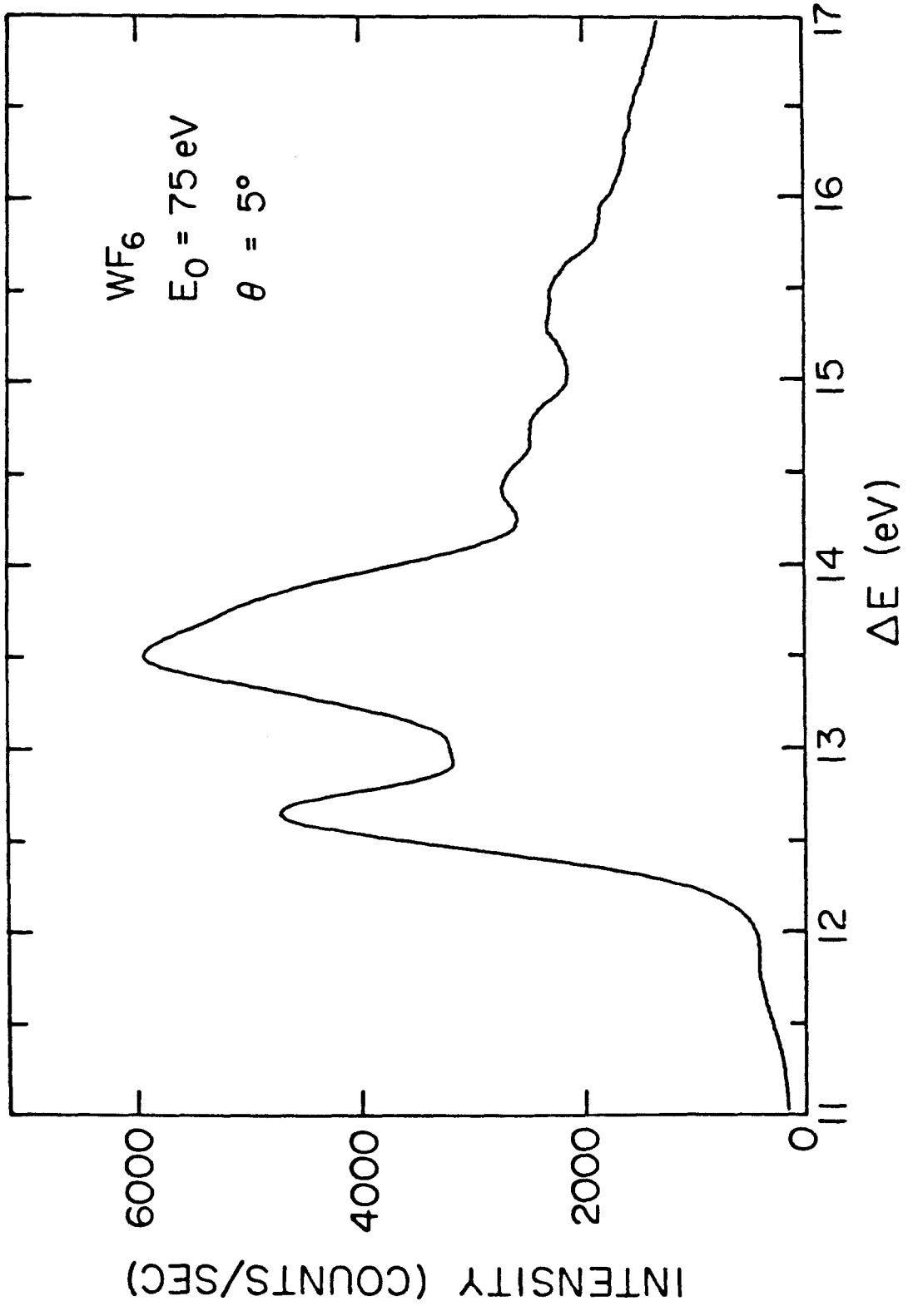
WF6
E0 = 75 eV
θ = 5°
INTENSITY (COUNTS/SEC)
0
2000
4000
6000
11
12
13
14
15
16
17
ΔE (eV)

Figure 5.

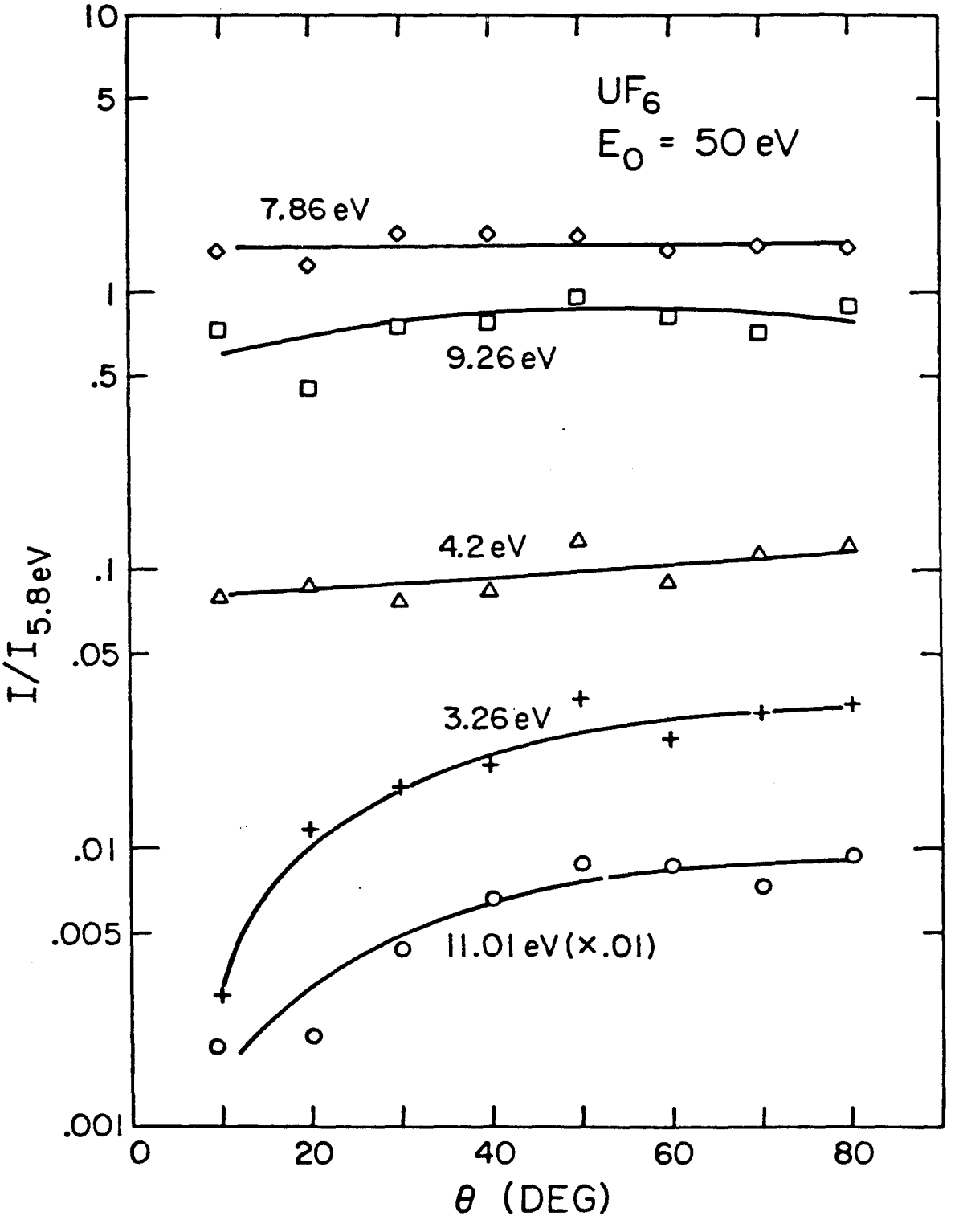
UF6
E0 = 50 eV
7.86 eV
9.26 eV
4.2 eV
3.26 eV
11.01 eV (×.01)
I/I5.8eV
θ (DEG)
10
5
1
.5
.1
.05
.01
.005
.001
0
20
40
60
80

Figure 6.

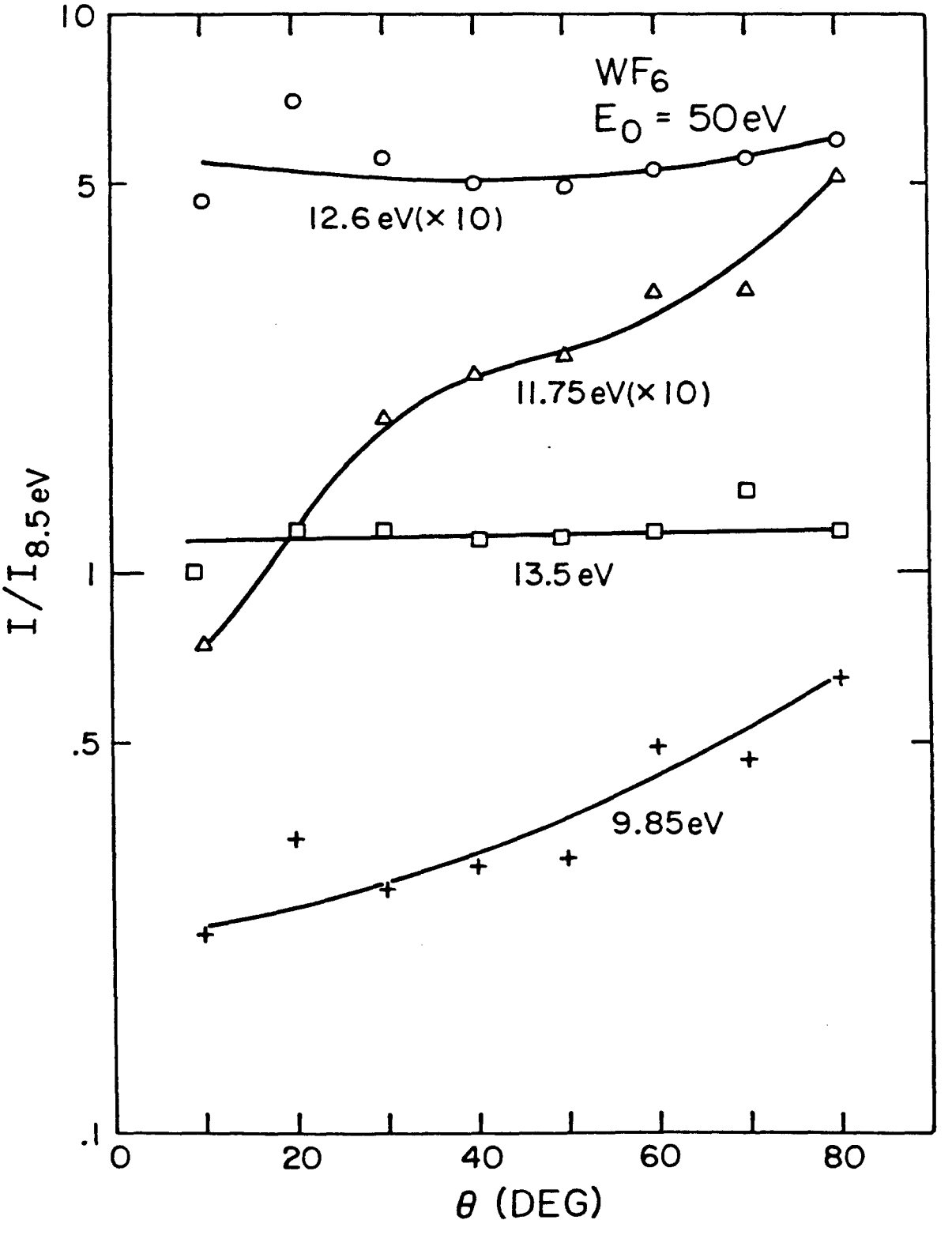
WF6
E0 = 50eV
12.6 eV(× 10)
11.75eV(× 10)
13.5 eV
9.85eV
I/I8.5eV
θ (DEG)
10
5
1
.5
.1
0
20
40
60
80

Figure 7.

3.3. Paper III: Doublet → Quartet Transitions and Doublet → Doublet Electronic Transitions in NO_2 by Electron Impact

Doublet → Quartet and Doublet → Doublet Electronic Transitions in NO_2 by Electron Impact[†]

R. Rianda,[‡] R. P. Frueholz[§] and A. Kuppermann

Arthur Amos Noyes Laboratory of Chemical Physics
California Institute of Technology
Pasadena, California 91125 USA

The electron-impact energy-loss spectrum of nitrogen dioxide (NO_2) has been measured at impact energies of 25, 50 and 75 eV, and scattering angles varying from 5^o to 80^o. A previously unreported spin-forbidden doublet → quartet transition was observed at 4.49 eV, in excellent agreement with theoretical calculations. Doublet → doublet transitions were observed at 2.95, 5.81, 7.48, 8.64, 9.69, 10.52, 10.68, 10.94 and 11.20 eV in agreement with previous experimental and theoretical work. In addition, numerous doublet → doublet transitions to super-excited states were also observed.

[†]This work was supported by a contract

[‡]Work performed in partial fulfillment of the requirements for the PhD degree in Chemistry at the California Institute of Technology.

[§]Present address: The Aerospace Corporation, P.O. Box 92957, Los Angeles, CA 90009.

Introduction

The electronic structure of NO_2 has been the subject of extensive experimental[1-14] and theoretical investigations.[15-26] Agreement between calculated and experimental doublet → doublet excitation energies has been quite good; however, prior to the present investigation, no experimental confirmation of calculated doublet → quartet transition energies was available. In order to further elucidate the electronic structure of NO_2 with particular emphasis on the low lying quartet states, we have applied the technique of low-energy variable-angle electron-impact spectroscopy to this molecule.

Electron impact spectroscopy has been shown to be a very powerful tool for the investigation of both spin and symmetry forbidden transitions.[27-30] The shape of the differential cross section (DCS) versus scattering angle curve is a sensitive indicator of the forbiddeness or allowedness of a transition. Optically allowed processes have very sharply forward peaked DCS's for impact energies 15 eV or more above the excitation threshold. In contrast, spin forbidden transitions (ones in which the spin quantum number changes by unity) have a nearly isotropic DCS over the angular range 10^o to 80^o. Such transitions occur by the mechanism of electron exchange.[31] Consequently, the ratio of the intensity of a spin forbidden transition to that of a fully allowed transition increases by one to two orders of magnitude as the scattering angle increases from 10^o to 80^o.

The configuration of the $\tilde{X}^2A$ ground state of NO_2 is $(1a_1)^2$ $(1b_2)^2$ $(2a_1)^2$ $(3a_1)^2$ $(2b_2)^2$ $(4a_1)^2$ $(5a_1)^2$ $(3b_2)^2$ $(1b_1)^2$ $(4b_2)^2$ $(1a_2)^2$ $(6a_1)^1$.[26]

Transitions may occur to either valence or Rydberg-like orbitals. Single valence or Rydberg excitations from the $6a_1$ orbital may only result in doublet excited states. In addition, valence transitions from lower lying orbitals to the $6a_1$ may also only result in doublet excited states. All other transitions will result in both doublet and quartet excited states. The excitations to valence excited states are of particular interest in this study since, because of orbital overlap considerations, the doublet-quartet splittings are expected to be larger than those for Rydberg excitations, leading to easier resolution of quartet states from doublet states.

Experimental

The electron spectrometer used in this study was that described by Kuppermann et al.[27] Spectra of NO_2 in the energy loss range 0 → 20 eV were obtained at impact energies of 25, 50 and 75 eV and scattering angles from 5^o to 80^o. Sample pressures in the scattering chamber were typically 4 mTorr as indicated by an uncalibrated Schulz-Phelps ionization gauge while the incident electron beam current was approximately 80 nAmps. The energy resolution was electron optically set to 120 meV (FWHM). The NO_2 sample was obtained from Matheson Gas Products with a stated purity of 99.5% and was subjected to several freeze-pump-thaw cycles before use.

Discussion

Figure 1 shows the electron impact spectrum of NO_2 from 1.6 to 9.6 eV energy loss at an impact energy of 50 eV and scattering angles of 10^o

and 80°. Relatively intense features appear in both spectra at 2.95, 5.81, 7.48 and 8.64 eV. No inelastic electronic features are observed below 1.6 eV. Two electric dipole allowed transitions, the $\tilde{X}^2A_1 \rightarrow \tilde{A}^2B_1$ and the $\tilde{X}^2A_1 \rightarrow 1^2B_2$, are predicted to lie near 3 eV energy loss.[18-24,26] Krauss et al.,[13] on the basis of a long vibrational progression observed in their 100 eV, 0° electron impact spectrum, have assigned the feature with an intensity maximum at about 2.96 eV in their spectrum to the $\tilde{X}^2A_1 \rightarrow 1^2B_2$ valence transition. Our observed transition energy of 2.95 eV is in excellent agreement with theirs and we assign this feature to that same transition.

A transition with an intensity maximum at about 2167Å (5.72 eV) has been observed in the optical spectrum of Nakayama et al.[5] In our spectra, a feature is observed with an intensity maximum at 5.81 eV in very good agreement with the results of Nakayama et al.[5] This transition has been tentatively identified as the $\tilde{X}^2A_1 \rightarrow \tilde{C}$ transition by Herzberg[9] (no symmetry designation has been given); however, it has been suggested that the progression observed between 2000 and 2350Å (8.62 → 5.28 eV) may be part of the $\tilde{X}^2A_1 \rightarrow \tilde{B}^2B_2$ system.[9] The CI calculations of Shih et al.[23] indicate only one transition in the 5.5 to 6 eV range, the $\tilde{X}^2A_1 \rightarrow \tilde{B}^2B_2$ at 5.51 eV. Additional optical studies by Coon et al.[11] have indicated a transition with an intensity maximum at 5.22 eV which has been assigned to the $\tilde{X}^2A_1 \rightarrow \tilde{B}^2B_2$. Shih et al.[23] have suggested that the true vertical excitation energy may be higher than that of the most probable vibrational transition. In addition, previous electron impact studies[10] have observed only one transition in this region, at about 5.7 eV. It is

therefore not clear from our results whether the 5.81 eV feature may be assigned as the $\tilde{X}^2A_1 \rightarrow \tilde{B}^2B_2$ or whether the $\tilde{X} \rightarrow \tilde{B}$ transition, which is quite weak (the absorption coefficient is roughly 20% of that of the $\tilde{X} \rightarrow \tilde{C}$ transition[5]), is simply not resolved from an $\tilde{X}^2A_1 \rightarrow \tilde{C}$ transition of unknown symmetry.

The transition which we observe with an intensity maximum at 7.48 eV has been reported previously as a broad maximum between 1750Å and 1600Å (7.1 and 7.75 eV) in the optical work of Nakayama et al.[5] and as an intense peak at 7.5 eV in the electron impact results of Edqvist et al.[10] This feature has been assigned as the $\tilde{X}^2A_1 \rightarrow \tilde{D}^2A_1$ transition corresponding to the Rydberg excitation $6a_1 \rightarrow 3s$. Shih et al.[23] have calculated an excitation energy of 7.71 eV for this transition in good agreement with experimental results.

The transition which we observe with a maximum at 8.64 eV has been reported previously by Price and Simpson[1] at 1450A (8.55 eV) and by Edqvist et al.[10] at 8.6 eV. This transition has been assigned as due to excitation from the $6a_1$ orbital to the $3p_{x,y,z}$ orbital. The calculated energies for excitation to the $3p_x$, $3p_y$ and $3p_z$ orbitals are 8.84, 8.62 and 8.73 eV, respectively[23] and are in excellent agreement with the experimental work.

In addition to these previously reported doublet → doublet transitions, we observe a feature at 4.49 eV in the 80^o spectrum which is not observed in the 10^o spectrum and has not been reported previously. The DCS's for this feature and several other features are shown in Figure 2. The method used for obtaining DCS curves has been described previously.[29]

The DCS for the 4.49 eV feature is constant to within a factor of about 2 over the angular range 10^{o} to 80^{o}. This behavior is exactly as is expected for a spin forbidden transition, so the feature may be definitively assigned as doublet → quartet in nature. Two doublet-to-quartet transitions have been theoretically predicted to lie in this region, the $\tilde{X}^2A_1 \rightarrow {}^4B_2$ $(1a_2 \rightarrow 2b_1)$ and the $\tilde{X}^2A_1 \rightarrow {}^4A_2$ $(4b_2 \rightarrow 2b_1)$.[18-20,22-26] Due to resolution limitations, we are unable to determine which of these transitions is the primary contributor to the 4.49 eV feature we observe.

Figure 3 shows the spectrum of NO_2 at an impact energy of 75 eV and a scattering angle of 5^{o} in the energy loss region 9.5 to 19.5 eV. The excitation energies of the numerous transitions which appear in this spectrum are listed in Table 1. Edqvist *et al.*,[10] also using the electron impact technqiue, have assigned the features in this energy loss region to various Rydberg series. Our results are in excellent agreement with those of Edqvist *et al.*[10] In addition to the features which may be correlated with previously identified transitions, we observe several weak transitions between 12.5 and 14 eV and between 15.5 and 16 eV energy loss, including one fairly intense feature at 13.86 eV which appears at excitation energies which exactly correspond to intense transitions of nitric oxide.[30] We therefore believe that these features are due to a small nitric oxide impurity.

In summary, we have used the technique of low-energy, variable-angle, electron impact spectroscopy to investigate the excited states of NO_2. We have observed a previously unreported doublet → quartet transition at 4.49 eV. In addition, doublet → doublet transitions were

observed at excitation energies which were in good agreement with previous experimental and theoretical work.

Table 1

Transition Energies for NO_2

State	Excitation	Theoretical (eV)	Previous Experimental (eV)	This Work (eV)
$\tilde{X}^2A_1$	Ground State	0	0	0
$\tilde{A}^2B_1$	$6a_1 \rightarrow 2b_1$	2.13[a], 2.58[b], 1.75[d], 2.45[e] 2.8[f], 2.46[g], 2.79[h], 2.93[i] 2.97[k]	2.81 - 2.84[m]	
$^2B_2$	$4b_2 \rightarrow 6a_1$	3.15[c], 3.33[d], 3.03[e] 3.4[f], 2.43[g], 3.22[h] 3.40[i], 3.59[k]	~3.0[m], 2.96[q], 3.0[p]	2.95
$^2A_2$	$1a_2 \rightarrow 6a_1$	2.46[b], 1.68[c], 4.13[d] 3.09[e], 3.4[f], 2.15[g] 3.25[h], 3.61[i], 3.63[k]		
$^4B_2$	$1a_2 \rightarrow 2b_1$	3.38[d], 3.80[e], 4.6[f] 2.88[g], 4.04[h], 4.85[i] 4.47[j], 4.53[k]		4.49
$^4A_2$	$4b_2 \rightarrow 2b_1$	3.43[d], 3.81[e], 4.7[f] 3.10[g], 4.09[h], 4.72[i] 4.30[j], 4.37[k]		

Table 1 (continued)

State	Excitation	Theoretical (eV)	Previous Experimental (eV)	This Work (eV)
$^2A_2$	$4b_2 \rightarrow 2b_1$	4.82[e], 5.04[f]		
$\tilde{B}^2B_2$	$1a_2 \rightarrow 2b_1$	3.95[a], 3.73[b], 5.18[e], 5.51[h]	5.22[p]	
			5.72[n], 5.7[p]	5.81
$^2A_2$	$4b_2 \rightarrow 2b_1$	6.5[e], 6.76[h]		
$\tilde{D}^2A_1$	$6a_1 \rightarrow 3s$	7.0[a], 9.87[b], 7.71[h]	7.1 - 7.75[n], 7.5[p]	7.48
$^2B_1$	$6a_1 \rightarrow 3p_y$	8.62[h]		
$^2A_1$	$6a_1 \rightarrow 3p_z$	8.73[h]	8.55,[l] 8.65[n], 8.6[p]	8.64
$^2B_2$	$6a_1 \rightarrow 3p_x$	8.84[h]		
$^2B_2$	$1a_2 \rightarrow 2b_1$	9.07[h]		
$^4B_2$	$4b_2 \rightarrow 3s$	9.20[h]		
$^2B_2$	$6a_1, 4b_2 \rightarrow 2b_1^2$	9.33[h]		
$^4A_2$	$1a_2 \rightarrow 3s$	9.62[h]		
$^2B_2$	$4b_2 \rightarrow 3s$	9.70	9.66[p]	9.69
$^2A_2$	$1a_2 \rightarrow 3s$	9.86		
$^2A_1$	$4b_2 \rightarrow 3p_\sigma$		10.46[p]	10.52

Table 1 (continued)

State	Excitation	Theoretical (eV)	Previous Experimental (eV)	This Work (eV)
$^2A_2$	$1a_2 \rightarrow 3s$	10.9		
$^2B_1$	$1a_2 \rightarrow 2p_\sigma$		10.85	10.94
$^2B_2$	$4b_2 \rightarrow 3s$		11.12	11.20
$^2B_2$	$4b_2 \rightarrow 4s$		11.55	11.61
$^2B_2$	$4b_2 \rightarrow 5s$		12.11	12.20
$^2B_2$	$4b_2 \rightarrow 6s$		12.40 14.7	12.46 14.62
$^2B_2$	$3b_2 \rightarrow 3s$		15.38	15.36
$^2A_2, ^2B_2$	$3b_2 \rightarrow 3p_\pi$		16.35	16.37
$^2A_1, ^2B_1$	$3b_2 \rightarrow 3d_\pi$		17.22	17.23
$^2B_2$	$3b_2 \rightarrow 4s$		17.34	17.35
$^2A_2, ^2B_2$	$3b_2 \rightarrow 4p_\pi$		17.63	17.69
$^2B_2$	$3b_2 \rightarrow 5s$		18.01	18.03
$^2B_2$	$3b_2 \rightarrow 6s$		18.32	18.33
$^2B_2$	$3b_2 \rightarrow 7s$		18.49	18.5
$^2B_2$	$4a_1 \rightarrow 3p_\sigma$		18.63	18.65

[a]Ref. 15, [b]Ref. 16, [c]Ref. 17, [d]Ref. 18, [e]Ref. 19, [f]Ref. 20, [g]Ref. 22, [h]Ref. 23, [i]Ref. 24, [j]Ref. 25, [k]Ref. 26, [l]Ref. 1, [m]Ref. 2, [n]Ref. 5, [o]Ref. 9, [p]Ref. 11, [q]Ref. 13.

References and Notes

1. W. C. Price and D. M. Simpson, Trans. Far. Soc., 37, 106 (1941).
2. T. C. Hall, Jr. and F. E. Blacet, J. Chem. Phys., 20, 1745 (1952).
3. K. Mori, Sci. of Light, 3, 62 (1954).
4. K. Mori, Sci. of Light, 4, 130 (1955).
5. T. Nakayama, M. Y. Kitamura and K. Watanabe, J. Chem. Phys., 30, 1180 (1959).
6. R. K. Ritchie and A. D. Walsh, Proc. Roy. Soc., 267A, 395 (1962).
7. Y. Tanaka and A. S. Jursa, J. Chem. Phys., 36, 2493 (1962).
8. A. E. Douglas and K. P. Huber, Can. J. Phys., 43, 74 (1965).
9. G. Herzberg, Electronic Spectra of Polyatomic Molecules, (Van Nostrand, Princeotn, NJ, 1966), p. 507-509.
10. O. Edqvist, E. Lindholm, L. E. Selin, L. Asbrink, C. E. Kuyatt, S. R. Mielczarek, J. A. Simpson and I. Fischer-Hjalmars, Physica Scripta, 1, 172 (1970).
11. J.-B. Coon, F. A. Cesani and F. P. Huberman, J. Chem. Phys., 52, 1647 (1970).
12. J. L. Hardwick and J. C. D. Brand, Chem. Phys. Lett., 21, 458 (1973).
13. M. Krauss, R. J. Celotta, S. R. Mielczarek and C. E. Kuyatt, Chem. Phys. Lett., 27, 285 (1974).
14. R. J. Pirkle and V. T. Jones, J. Mol. Spect., 54, 375 (1975).
15. W. H. Fink, J. Chem. Phys., 49, 5054 (1968).
16. W. H. Fink, J. Chem. Phys., 54, 2911 (1971).
17. J. E. Del Bene, J. Chem. Phys., 54, 3487 (1971).
18. R. A. Gangi and L. Burnelle, J. Chem. Phys., 55, 851 (1971).

19. P. J. Hay, J. Chem. Phys., 58, 4706 (1973).

20. G. D. Gillespie, A. U. Khan, A. C. Wahl, R. P. Hosteny and M. Krauss, J. Chem. Phys., 63, 3425 (1975).

21. G. D. Gillespie and A. U. Khan, J. Chem. Phys., 65, 1624 (1976).

22. C. F. Jackels and E. R. Davidson, J. Chem. Phys., 65, 2941 (1976).

23. S.-K. Shih, S. D. Peyerimhoff and R. J. Buenker, Chem. Phys. Lett., 46, 201 (1977).

24. P. A. Benioff, J. Chem. Phys., 68, 3405 (1978).

25. C. F. Jackels, J. Chem. Phys., 70, 4664 (1979).

26. N. C. Handy, J. D. Goddard and H. F. Schaefer III, J. Chem. Phys., 71, 426 (1979).

27. (a) A. Kuppermann, J. K. Rice and S. Trajmar, J. Phys. Chem., 72, 3894 (1968).

(b) S. Trajmar, J. K. Rice and A. Kuppermann, Advan. Chem. Phys., 18, 15 (1970).

(c) A. Kuppermann, W. M. Flicker and O. A. Mosher, Chem. Rev., 79, 77 (1979).

28. O. A. Mosher, W. M. Flicker and A. Kuppermann, J. Chem. Phys., 59, 6502 (1973).

29. O. A. Mosher, W. M. Flicker and A. Kuppermann, J. Chem. Phys., 62, 2600 (1975).

30. R. P. Frueholz, R. Rianda and A. Kuppermann, Chem. Phys., 31, 315 (1978).

31. J. R. Oppenheimer, Phys. Rev., 29, 433 (1927).

Figure Captions

Fig. 1: Electron energy-loss spectrum of NO_2 at a scattering angle of (a) 10^o, and (b) 80^o; 50 eV impact energy; 8×10^{-8} A incident beam current; 5 mTorr sample pressure reading from an uncalibrated Shulz-Phelps gauge; resolution approximately 0.12 eV (FWHM).

Fig. 2: Differential cross-sections of NO_2 as a function of scattering angle at an incident electron energy of 50 eV; for elastic scattering (+) and for excited states: $D_{2.95}$ (○), $Q_{4.49}$(□), $D_{5.81}$ (◇), and $D_{7.48}$ (△). The elastic peak DCS was multiplied by 0.1 before plotting. The letters D and Q stand for doublet and quartet upper states, respectively, and the index represents the corresponding transition energy.

Fig. 3: Electron energy-loss spectrum of NO_2 at a scattering angle of 5^o, 75 eV incident electron energy; 8×10^{-8} A incident beam current; 3 mTorr sample pressure measured by an uncalibrated Schulz Phelps gauge.

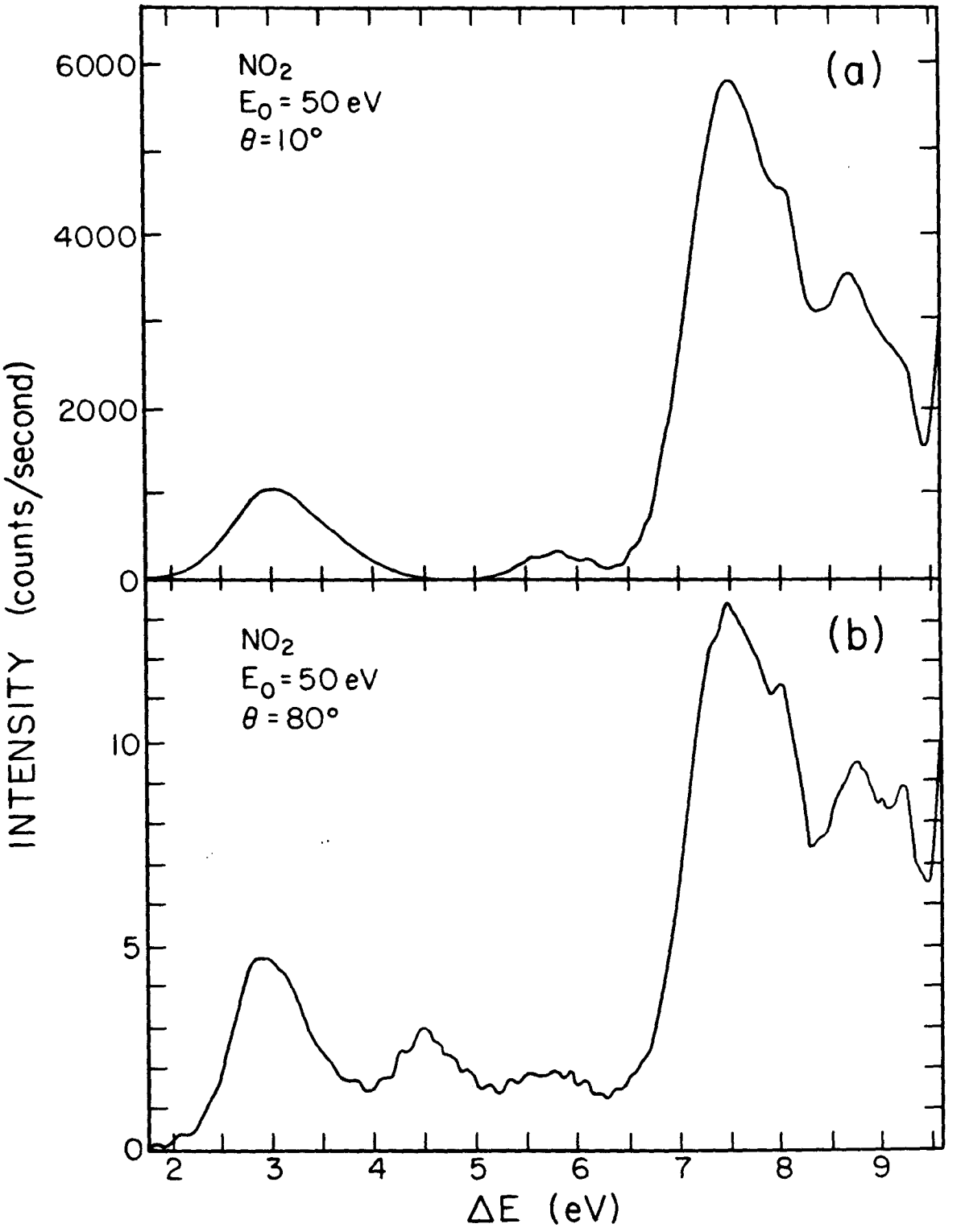
NO2
E0 = 50 eV
θ = 10°
(a)
NO2
E0 = 50 eV
θ = 80°
(b)
INTENSITY (counts/second)
6000
4000
2000
0
10
5
0
2
3
4
5
6
7
8
9
ΔE (eV)

Figure 1

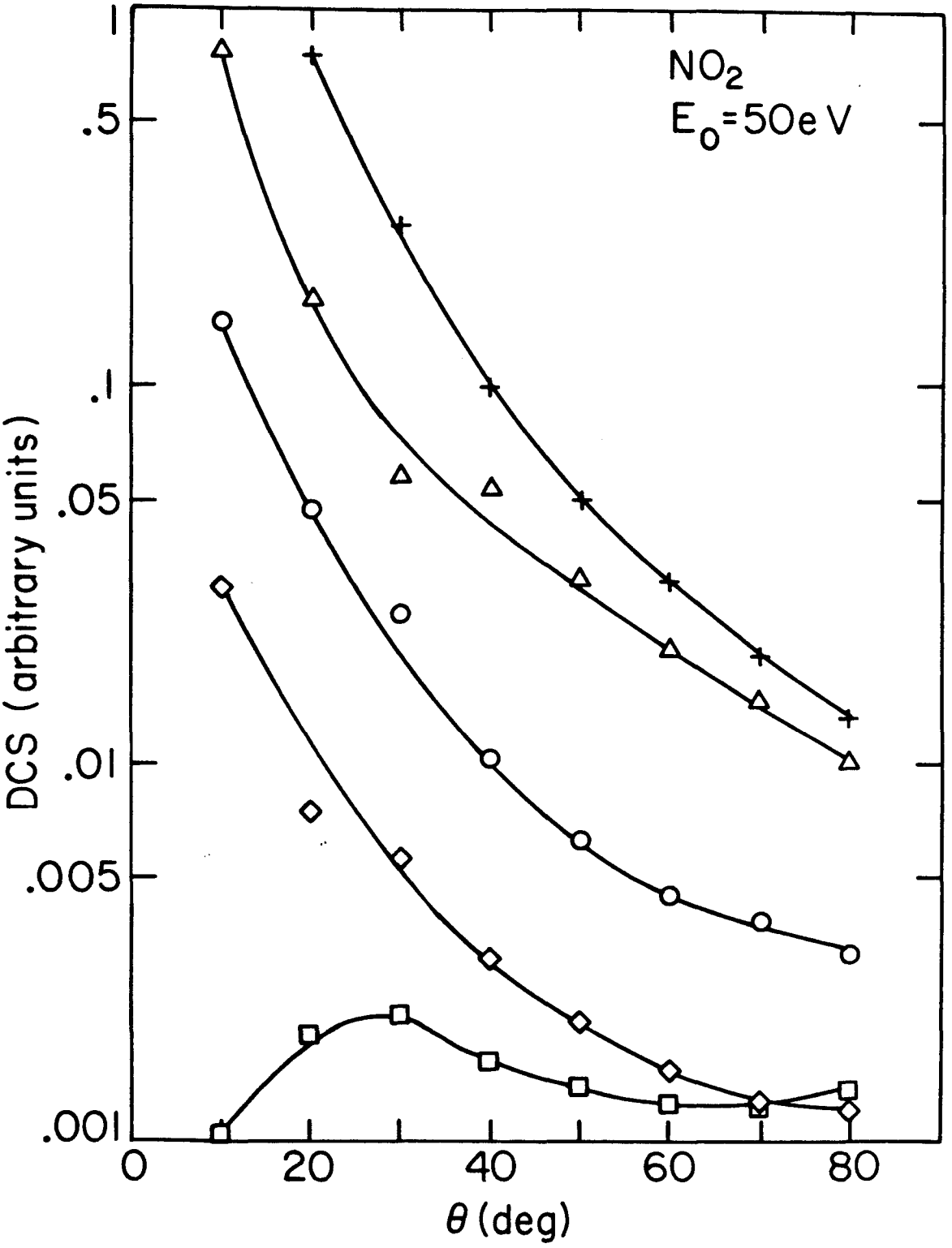
NO2
E0=50eV
DCS (arbitrary units)
1
.5
.1
.05
.01
.005
.001
0
20
40
60
80
θ (deg)

Figure 2

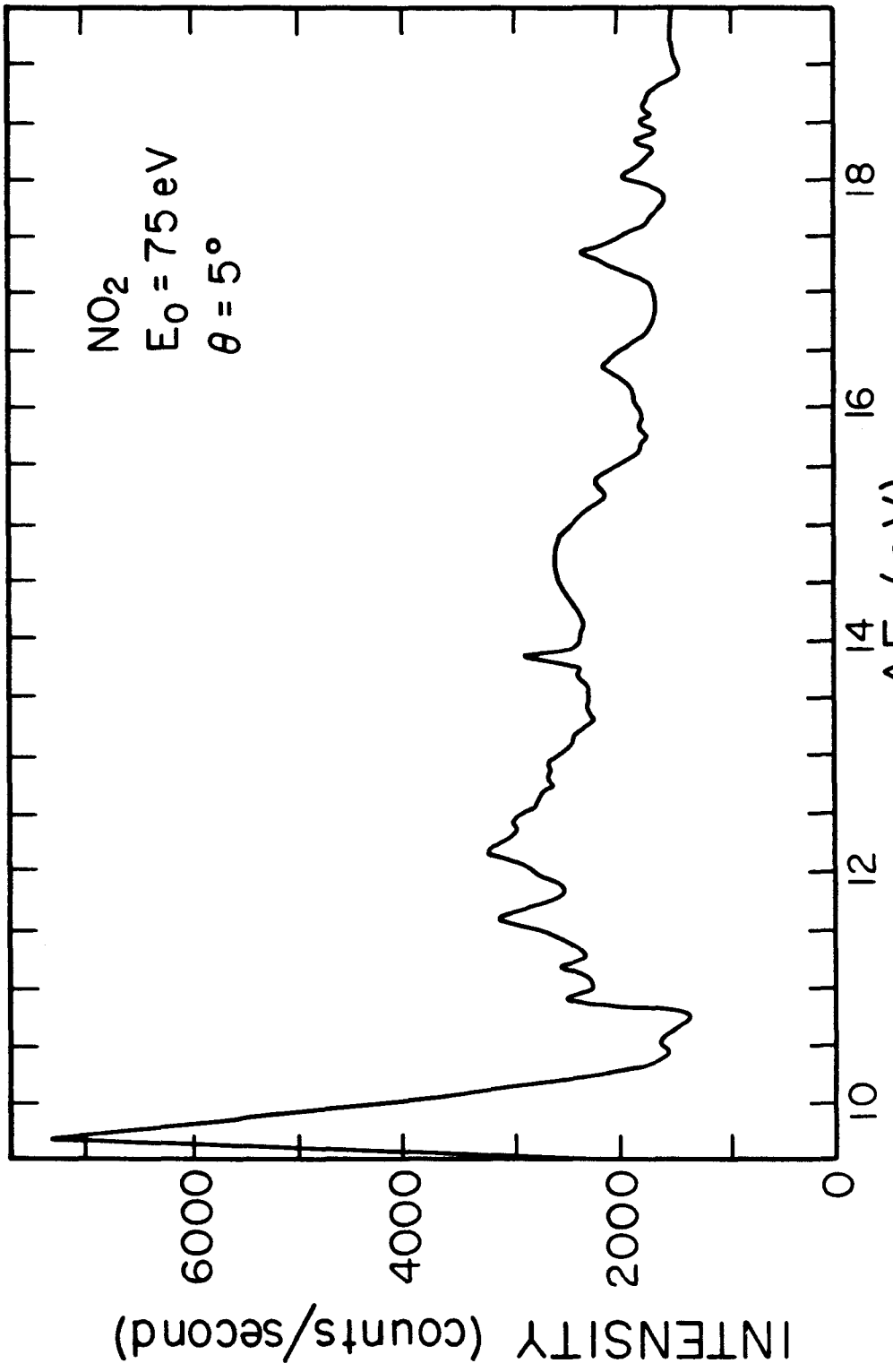
NO2
E0 = 75 eV
θ = 5°
INTENSITY (counts/second)
6000
4000
2000
0
10
12
14
16
18
ΔE (eV)

Figure 3

3.4 Paper IV: Singlet → Triplet Transitions in C≡N Containing Molecules by Electron Impact.

Singlet → Triplet Transitions in C≡N Containing Molecules by Electron Impact

Ronald Rianda, Robert P. Frueholz, and Aron Kuppermann
Arthur Amos Noyes Laboratory of Chemical Physics
California Institute of Technology
Pasadena, California 91125

The electron-impact excitation spectra of hydrogen cyanide (HCN), acetonitrile (CH_3CN), malononitrile ($CH_2(CN)_2$), propionitrile (C_2H_5CN), and butyronitrile (C_3H_7CN) have been studied experimentally at impact energies of 25, 50 and 75 eV and at scattering angles from 5° to 80°. Results for hydrogen cyanide are in excellent agreement with previous work. Previously unobserved singlet → triplet transitions of acetonitrile, propionitrile and butyronitrile are reported. Also, the first study of the electronic spectrum of malononitrile is reported. Tentative assignments for transitions observed are reported.

Introduction

Although much has been published on the electronic spectroscopy of C≡N containing molecular systems, especially hydrogen cyanide, the assignments of transitions observed are still very much in question.[1-16] In order to resolve some of these questions, we have applied the technique of low-energy, variable-angle, electron-impact spectroscopy to hydrogen cyanide, acetonitrile, malononitrile, propionitrile and butyronitrile.

Electron impact spectroscopy has proven to be a very powerful technique for studying the electronic structure of molecules.[17-20] The shape of the differential cross-section (DCS) versus scattering angle curve is a great aid in the identification of the nature of a transition. Excitations which are fully allowed with respect to dipole selection rules exhibit very strongly forward peaked DCS's. The DCS's of such transitions are most intense at 0° scattering angle and decrease by about two orders of magnitude as the scattering angle (θ) is increased from 10° to 80°. Spin forbidden transitions exhibit DCS's which are nearly constant, to within a factor of two or three, over a similar angular range. Spin-allowed but symmetry-forbidden transitions display an intermediate behavior. The DCS is forward peaked but not so much as that of a fully allowed transition. Thus, measuring the DCS of a transition may add valuable information as to the type of transition observed. The lower energy region of the spectra of CN containing molecules is expected to be dominated by $\pi \rightarrow \pi^*$ and $n \rightarrow \pi^*$ transitions

within the C≡N group. Therefore, hydrogen cyanide, the simplest and most thoroughly studied member of this group, will serve as a model to assist in assigning transitions in the remainder of the group. Hydrogen cyanide is linear in its ground state and thus belongs to the C∞v point group The electronic configuration in the ground state is $1\sigma^2\ 2\sigma^2\ 3\sigma^2\ 4\sigma^2\ 5\sigma^2\ 1\pi^4$ yielding the ground state symmetry of $^1\Sigma^+$.[5,6] The higher energy regions of the spectra are expected to be dominated by Rydberg transitions.

Hydrogen cyanide is bent in many of its excited states and in these cases and possessés C_s symmetry.[3] This results in a splitting of the π orbitals into a' and a" components. In C_s symmetry, the ground state is $1a'^2\ 2a'^2\ 3a'^2\ 4a'^2\ 5a'^2\ 6a'^2\ 1a''^2$ ($^1A''$).[5,6] Assignments for transitions of the alkyl cyanides will be listed in accordance with the $C_{\infty v}$ symmetry of the C≡N group only.

Experimental

The electron spectrometer used in this study was that described by Kuppermann et al.[17] . Spectra of hydrogen cyanide, acetonitrile, propionitrile, butyronitrile and malononitrile in the energy loss range 0 → 17 eV were obtained at impact energies of 25, 50 and 75 eV and scattering angles from 5° to 80°. Sample pressures in the scattering chamber were typically 2 - 4 mTorr, as indicated by an uncalibrated Schulz-Phelps ionization gauge while the incident electron beam current varied from 10 to 100 nAmps. The samples of hydrogen cyanide (99.5%), acetonitrile (99+%), propionitrile (98+%), butyronitrile, and malononitrile (99+%) were obtained from Fumico Inc., Aldrich Chemical Co., Inc., Eastman Kodak Co., Matheson, Coleman and Bell, and Aldrich Chemical Co., Inc.,

respectively. The minimum stated purity, when available, is given in parentheses. All samples were subjected to several trap-to-trap distillations (HCN) or freeze-pump thaw cycles before use. No indication of impurity was observed in any spectrum.

Results and Discussion

Figure 1 shows the electron impact spectra of hydrogen cyanide (HCN), acetonitrile (CH_3CN), malononitrile ($CH_2(CN)_2$), propionitrile (C_2H_5CN) and butyronitrile (C_3H_7CN) from 4.6 to 11.6 eV energy loss at an impact energy of 25 eV and scattering angles of 10° and 80° (70° for HCN). The spectra of hydrogen cyanide at 10° and 70° scattering angles are repeated in figure 2 so that the vibrational structure we report may be more readily observed. Differential cross-section versus scattering angle curves for several of the features appearing in this energy loss region in hydrogen cyanide, acetonitrile and malononitrile are shown in figures 3, 4 and 5, respectively. The features in the spectra of propionitrile and butyronitrile are so heavily overlapped that differential cross-sections could not be obtained. Figure 6 shows the spectra of hydrogen cyanide, acetonitrile, malononitrile propionitrile and butyronitrile from 10 to 17 eV energy loss at an impact energy of 75 eV and a scattering angle of 5°.

Hydrogen Cyanide

Intense features are observed with intensity maxima at 8.75, 10.17, 10.41, 10.70, 10.86, 11.03, 11.30 and 11.50 eV in the 10° spectrum of hydrogen cyanide. A considerable amount of vibrational structure is evident on the 8.75 eV feature. In addition to these intense features much weaker features with apparent intensity maxima at about 6.4 eV and 7.8 eV are observed. The feature at 6.4 eV has been previously observed in both electron impact[10] and optical spectra[3] and has been attributed to the $\tilde{X}\ ^1\Sigma^+ \rightarrow \tilde{A}^1A''$ ($\pi \rightarrow \pi^*$) excitation. The theoretical calculations of Schwenzer et al.[6] indicate that this transition is the lowest lying singlet → singlet excitation. They have adjusted their calculated transition energies to match the observed value of 6.48 eV. The $\tilde{X}\ ^1\Sigma^+ \rightarrow \tilde{A}\ ^1A''$ transition is forbidden in the linear configuration (the excited state bond angle is 125.0°) so the intensity is expected to be low. The second feature in the low angle spectrum of hydrogen cyanide occurs between 7.5 and 8.0 eV. This transition has also been previously observed at 7.5 eV in the electron impact spectra of Chutjian et al.[10] Schwenzer et al.[6] predict the $\tilde{X}\ ^1\Sigma^+ \rightarrow \tilde{B}\ ^1A''$ transition, which is also forbidden in the linear configuration, to occur at 7.52 eV. However, Asbrink et al.,[11] on the basis of HAM/3 calculations have suggested that the transitions observed at 6.48 eV and 7.5 eV in both the optical and electron impact spectra result from transitions to triplet excited states and that due to low intensities the $\tilde{X}\ ^1\Sigma^+ \rightarrow 1\ ^1A''$ and $\tilde{X}\ ^1\Sigma^+ \rightarrow 2\ ^1A''$ transitions are not observed. In our 25 eV, 70° spectrum (figure 2b), we observe a broad feature between 5.5 and 7.25 eV and another feature at 7.86 eV

which on the basis of the DCS's measured (shown in figure 3) may be assigned as singlet → triplet transitions. Vibrational structure is evident on both features. Chutjian et al.[10] also observed transitions at 6.0, 6.8, 7.1 - 7.9 and 7.9 eV which they have assigned on the basis of the calculations of Schwenzer et al.[6] to the transitions $\tilde{X}\ ^1\Sigma^+ \rightarrow 1\ ^3A'$, $1\ ^3A''$, $2\ ^3A'$, $X\ ^1\Sigma^+ \rightarrow 2\ ^3A''$, $\tilde{X}\ ^1\Sigma^+ \rightarrow 3\ ^3A'$ and $\tilde{X}\ ^1\Sigma^+ \rightarrow 3\ ^3A''$, respectively. No vibrational structure was observed in their spectra at their stated resolution of 80 to 100 meV. Close examination of our 25 eV, 10° spectrum reveals the presence of vibrational structure which also appears with much greater intensity in the 25 eV, 80° spectrum and may definitely be assigned to singlet → triplet transitions. Unfortunately, it is only possible at this time to state that our results are consistent with assignment of the transitions observed between 5.5 and 7.25 and between 7.5 and 8.0 eV in both optical and low-angle electron impact spectra to singlet → triplet excitations.

The first intense feature in the 10° spectrum of hydrogen cyanide appears between 8.0 and 9.63 eV. Previous investigations have identified two transitions in this region, the $\tilde{X}\ ^1\xi^+ \rightarrow \tilde{C}\ ^1A'$ and the $\tilde{X}\ ^1\xi^+ \rightarrow \tilde{D}\ ^1A'$.[3,11] The 0-0 bands of these transitions have been reported to be at 8.139 and 8.881 eV, respectively. We observe a progression in the bending mode, ν_2, of about .10 eV beginning at 8.03 eV. This is in excellent agreement with the ν_2 frequency for the $\tilde{C}$ state of 869 cm^{-1} (.108 eV) obtained by Herzberg.[3] No vibrational structure was resolved in this energy region in the previous electron impact studies of Chutjian et al.[10] and Tam and Brion.[7] Fridh and Asbrink[8] have observed and assigned the

vibronic peaks of the $\tilde{X}\ ^1\xi^+ \rightarrow \tilde{C}\ ^1A'$ and $\tilde{X}\ ^1\xi^+ \rightarrow \tilde{D}\ ^1A'$ transitions but did not obtain an absolute energy scale calibration and have therefore based their reported transition energies on the values obtained by Herzberg.[3] We therefore suggest that the true 0-0 transition for the $\tilde{X}\ ^1\xi^+ \rightarrow \tilde{C}\ ^1A'$ excitation occurs at 8.03 eV and that the previously reported value of 8.139 actually includes one quantum of the bending mode. Additional members of this progression are listed in Table 1. The long progression in the bending mode is due to the decrease in the bond angle of the $\tilde{C}\ ^1A'$ state (α = 141°) relative to that of the ground state (180). A significant enhancement of the intensities of peaks at 8.84 and 9.03 eV is due to overlap with elements of the $\tilde{X}\ ^1\xi^+ \rightarrow \tilde{D}\ ^1A''$ transition. In our spectra, the 0-0 band of the $\tilde{X} \rightarrow \tilde{D}\ ^1A'$ transition (8.881 eV) is not resolved from the $\tilde{X}\ ^1\xi^+ \rightarrow \tilde{C}\ ^1A'$ (v_2 = 8) transition which occurs at 8.84 eV. A progression in the C≡N stretching mode (v_3) is evident with additional members of the progression occurring at 9.03, 9.22, 9.42 and 9.63 eV. The peak at 9.03 also overlaps with the $\tilde{X}\ ^1\xi^+ \rightarrow \tilde{C}\ ^1A'$ (v_2 = 10) transition. The spacing of elements of this progression of about .2 eV compares well with the frequencies of the v_3 mode of the $\tilde{A}$ and $\tilde{C}$ states, 1495 cm^{-1} (.185 eV) and 1530 cm^{-1} (.190 eV), respectively.

Numerous features are observed in our spectra with excitation energies above 10 eV. All these transitions with the exceptions of those at 10.70, 10.86, 15.17 and 16.9 eV have been assigned to Rydberg series converging to the first and second ionization potentials of 13.607 and 14.011 eV, respectively.[8] Excitation energies obtained are in excellent

agreement with prevous results. The transitions at 10.70 and 10.86 eV which have been assigned by Tam and Brion[7] as vibronic components of excitations from the 5σ orbital to the 3s orbital have also been assigned by Asbrink et al.[11] as components of the $\tilde{X}\ ^1\Sigma^+ \rightarrow\ ^1\Sigma^+\ (\pi \rightarrow \pi^*)$ transition who suggest that the 5σ → 3s transition has negligible intensity. The suggestion that the 5σ → ns series has negligible intensity prohibits the assignment of transitions occurring at 12.48, 13.13, 13.45 and 13.61 eV to this series. However, these transitions are fitted quite well to a Rydberg series with a quantum defect of .98. In addition, Tam and Brion[7] observed vibrational structure in the 10.64 to 10.88 eV region with spacings which correlate well with those obtained in photoelectron spectra. We, therefore, assign the peaks in this region to the 5σ → 3s transition. The two very broad structureless features observed at 15.17 and 16.9 eV have been assigned by Fridh and Asbrink[8] to the 4σ → π^* and the 4σ → 3s transitions, respectively. A summary of the energies of features observed in hydrogen cyanide as well as assignments of those features is given in Table 1.

Acetonitrile

The spectrum of acetonitrile in the 4.6 to 9.3 eV energy loss region closely resembles that of hydrogen cyanide. In the 25 eV, 10° spectrum three weak, highly overlapped features are observed with apparent maxima at about 5.5, 6.7 and 7.7 eV. In addition, an intense feature is observed at 8.96 eV with shoulders at 8.45, 8.64, 8.72, 9.11 and 9.21 eV. The 25 eV, 80° shows a broad unresolved feature between

5.2 and 7.5 eV as well as another feature at 8.1 eV which were not observed in the 10° spectrum. The DCS's of these transitions, shown in figure 4, indicate that these features are due primarily to singlet → triplet excitations. Numerous other features are observed in the spectrum of acetonitrile above 9.3 eV which may not be readily correlated to features appearing in the hydrogen cyanide spectrum. The excitation energies for all features observed in the acetonitrile spectra are listed in table 2.

The weak features observed in our spectra at 5.5 and 6.7 eV have not been previously observed. Intense features due predominantly to singlet → triplet transitions are observed in this energy region in our higher angle spectra. It is not possible to determine whether the weak features appearing at 5.5 and 6.7 eV are also due to these same transitions or are due to the very weak singlet → singlet excitations.

In the 70 eV electron impact studies of Stradling and Loudon a fairly strong feature was observed at 6.1 eV in spectra taken at scattering angles of both 0° and 90°, which they assigned tentatively as a singlet → triplet excitation. An attempt by Fridh[16] to observe this same feature was unsuccessful in spite of the use of an identical impact energy (70 eV) and scattering angle (0°). Fridh has suggested that the feature observed by Stradling and Loudon is due to an impurity. In our high angle spectra, a broad feature is observed between 5.2 and 7.5 eV which bears no resemblence to the feature Stradling and Loudon observed. The feature we observe is probably due to the overlap of several singlet → triplet, $\pi \rightarrow \pi^*$ transitions.

Herzberg and Scheibe[12] observed a broad continuum with a maximum at 7.32 eV. Stradling and Loudon also observed a weak feature in this region, at 7.5 eV. In our spectra, a weak feature is observed with an apparent maximum at 7.7 eV. Agreement between our results and those of previous workers is poor due to our inability to resolve this feature from the intense 8.96 eV feature. This 7.7 eV feature has been suggested to correspond to an $n \rightarrow \pi^*$ transition or a forbidden component of a $\pi \rightarrow \pi^*$ transition.

An intense feature is observed in our spectra taken at both low and high scattering angles at 8.96 eV. Shoulders appear on this feature at 8.45, 8.64, 8.72, 9.11 and 9.21 eV. Stradling and Loudon[15] have also observed a transition in this region, at 9.04 eV. Okabe and Dibeler[14] measured the fluorescence yield from CN produced by photolysis of acetonitrile as a function of wavelength and observed a quasicontinuum with features at about 8.95, 9.01, 9.11, 9.22 and 9.33 eV. Fridh[16] observed diffuse bands at 8.45 and 9.0 eV. Our results are in excellent agreement with this previous work. Fridh has suggested assignment of the features at 8.45 and 9.0 eV to a $\pi \rightarrow \pi^*$ transition and an $n \rightarrow \pi^*$ transition, respectively. The similarity of the acetonitrile spectrum in this region to that of hydrogen cyanide which has been assigned to overlapping $\pi \rightarrow \pi^*$ and $n \rightarrow \pi^*$ transitions supports her assignment.

Nearly all features with excitation energies greater than 9.3 eV have been previously observed and may be assigned to Rydberg series converging to the first and second IP's of 12.20 and 13.14 eV, respectively.[21]

Stradling and Loudon have suggested assignment of the peak which they observe at 9.04 eV to the $\pi \rightarrow 3s$ excitation. The similarity between our acetonitrile and hydrogen cyanide spectra below 9.3 eV suggests that the predominant contribution to this feature results from the valence $n \rightarrow \pi^*$ transition. The absence of sharp structure for the spectrum of acetonitrile at about 9 eV comparable to that observed for the $\pi \rightarrow 3s$ transition in hydrogen cyanide suggests that the intensity of the $\pi \rightarrow ns$ series is significantly less for acetonitrile than for hydrogen cyanide. We have assigned all the peaks in the 9.3 to 13 eV region to Rydberg excitations to np_σ, np_π, nd_σ and nd_π orbitals. Quantum defects obtained are comparable to those obtained for similar orbitals of hydrogen cyanide. Table 2 lists transition energies and assignments for the acetonitrile spectrum.

Malononitrile

The electronic spectrum of malononitrile has not been reported previously. The spectrum of malononitrile in the energy loss region less than 9.5 eV is very similar to the spectra of hydrogen cyanide and acetonitrile. Weak highly overlapped features are observed at about 5.6, 6.5 and 7.9 eV in the 25 eV, 10° spectrum. Features possessing DCS's (figure 5) typical of singlet → triplet transitions are observed from 5.2 to 7.1 eV and at 7.95 eV. The rapid decrease in the DCS's for those features between 10° and 20° suggests that the singlet triplet transitions overlay weak spin allowed transitions. Two weak shoulders occurring at 9.14 and 9.33 eV are observed on the intense

feature at 8.94 eV. In accordance with our assignments for the corresponding transitions in hydrogen cyanide and acetonitrile we assign both singlet → triplet transitions to $\pi \rightarrow \pi^*$ excitations. The features observed at 5.6, 6.5 and 7.9 eV probably result from singlet → singlet $\pi \rightarrow \pi$ excitations. The feature at 8.94 is tentatively assigned to an $n \rightarrow \pi^*$ transition.

The features observed having excitation energies greater than 9.5 eV may be assigned to Rydberg series converging to the first four IP's of 12.68, 13.10, 13.41 and 13.59 eV.[22] The interaction of the two CN groups splits the CN π and n orbitals into two sets of two orbitals. Table 3 lists the transitions observed and our tentative assignments. As with acetonitrile, no evidence of excitations to ns Rydberg orbitals is found. The quantum defect we obtain for the np_σ series (about .75) agrees quite well with the values previously obtained for hydrogen cyanide and acetonitrile. Three additional series may be fitted using quantum defects of .55, .45 and .45. Such quantum defects seem low for transitions to p_π orbitals and high for transitions to d_σ orbitals. Therefore, the correct excited orbital designation is not clear.

Propionitrile

The electron impact spectrum of propionitrile resembles those of hydrogen cyanide, acetonitrile and malononitrile in the 4.6 to about 9 eV energy loss region. In the low angle spectrum, highly overlapped features are observed with apparent maxima at about 6.5 and 7.8 eV and an intense

feature is observed at 8.95 eV. At high scattering angle, additional features are observed between 5.4 and 7.5 eV and at 8.14 eV. The similarity to the spectrum of hydrogen cyanide in this region again suggests assignment of these features to valence transitions. We therefore assign the 5.4 to 7.5 eV feature as overlapping singlet → triplet $\pi \rightarrow \pi^*$ transitions. A feature was observed by Stradling and Loudon[15] at about 6.4 eV in spectra taken at scattering angles of 0° and 90° and an impact energy of 70 eV. This feature was tentatively assigned as a singlet → triplet excitation and corresponds to the feature they observed in the spectrum of acetonitrile at 6.1 eV which Fridh[16] has suggested was due to an impurity. The broad structureless transition we observe at high angle bears no resemblence to that feature observed by Stradling and Loudon.

The features observed in our spectra at about 6.5 and 7.8 eV have not been previously reported although the feature Stradling and Loudon report at 6.4 eV may correspond to the 6.5 eV feature we observe. Both of these transitions are probably due to spin-allowed, symmetry-forbidden components of a $\pi \rightarrow \pi^*$ transition.

The feature observed in our spectra at 8.14 eV is not observed in our low angle spectra. Due to the similarity of this feature to the corresponding features of hydrogn cyanide, acetonitrile and malononitrile for which DCS curves could be obtained, we assign this feature as a singlet → triplet excitation.

The intense feature observed at 8.95 eV may be assigned as an $n \rightarrow \pi^*$

transition. The 8.95 eV feature is overlapped with another feature at 9.35 eV which corresponds to the first element of a Rydberg series converging to the first vertical IP of 12.11 eV.[21] The quantum defect of .67 indicates that the upper state is probably a 3p orbital. The additional transitions observed at higher excitation energies may also be tentatively assigned as Rydberg excitations converging to the first and second IP's of 12.11 and 12.91, respectively.[21] The quantum defects calculated .67, .65, .20 and .23 suggest that only transitions to two series of upper states, probably np and nd orbitals are involved. Excitation energies we observe are in good agreement with those obtained by Stradling and Loudon[15] in this energy region. Excitation energies and assignments for these transitions are listed in table 4.

Butyronitrile

The electron impact spectrum of butyronitrile taken at an impact energy of 25 eV and a scattering angle of 10° in the energy loss region 4.6 to 11.6 eV displays a weak highly overlapped feature at about 6.4 eV and intense features at 9.12, 9.77, 10.60 and 11.30 eV. The 6.4 eV feature may correspond to a weak $\pi \rightarrow \pi^*$ transition similar to those observed in the previously discussed alkyl cyanides. The spectrum taken at 75 eV, 5° (not shown) displays two peaks at 9.18 and 9.42 eV having intensities roughly 75% of that of the 10.60 eV peak. Spectra of propionitrile at similar impact energies and scattering angles indicate that the intensity of the valence transition occurring at 8.95

is reduced by about a factor of two relative to that of the higher lying Rydberg transitions (9.35 and 10.44 eV) when the impact energy is increased from 25 to 75 eV and the scattering angle is decreased from 10° to 5°. This suggests that the feature observed at 25 eV, 10° is due to the overlap of the $n \rightarrow \pi^*$ observed in the previously discussed alkyl cyanides at about 9 eV and the first member of a Rydberg series occurring at 9.18 and 9.42 eV (the 9.42 eV peak probably includes one quantum of the C≡N stretching frequency).

The spectrum taken at 25 eV, 80° shows additional features between 5.4 and 7.6 eV and at 8.2 eV which are virtually identical to the features observed in the other alkyl cyanides and which we have assigned to singlet → triplet transitions. We therefore assign the 5.4 to >6 eV feature to the overlap of several $\pi \rightarrow \pi^*$ singlet → triplet transitions. The feature appearing in butyronitrile is also assigned to a singlet → triplet, possibly $n \rightarrow \pi^*$, transition.

Stradling and Loudon[15] have again observed a feature at about 6 eV which appears in both 0° and 90° spectra taken at an impact energy of 70 eV, which they have tentatively assigned as a singlet → triplet transition. As was the case for acetonitrile and propionitrile, the feature we observe in our high angle spectra of butyronitrile bears no resemblence to the feature which they observe.

Peaks which probably correspond to Rydberg excitations converging to the first (11.65 eV)[23] and second (not reported) IP's are observed at 9.18, 9.42, 9.80, 10.60, 11.27 and 12.03 eV. The 9.18 eV feature

may be assigned to a $\pi \rightarrow 3p$ excitation with a quantum defect of .65, which is very close to the quantum defect observed for the corresponding transition of propionitrile. We are presently unable to assign the higher lying features. Transition energies and assignments (if any) for the features we observe in butyronitrile are listed in table 5.

Conclusions

We have obtained electron impact spectra of hydrogen cyanide, acetonitrile, maloronitrile, propionitrile and butyronitrile at several different impact energies and scattering angles from 5° to 80°. Our results for hydrogen cyanide are in excellent agreement with previous ones. We have reported previously unobserved singlet → triplet transitions in acetonitrile, propionitrile and butyronitrile. In addition, we report the first study of the electronic spectrum of malononitrile. We have assigned both valence and Rydberg transitions observed in acetonitrile, malononitrile, propionitrile and butyronitrile relying heavily on the similarities of the spectra to those of hydrogen cyanide.

Table 1

Excitation Energies of Hydrogen Cyanide (in eV)

Valence Excitations

State	Excitation[a]	Theoretical[a]	Previous Experimental		This Work
$x^1\Sigma^+(^1A'')$	Ground State	0	0		0
$1^3A'$	6a' → 7a' ($\pi \rightarrow \pi^*$)	4.42			5.46,5.60,5.83[c]
$1^3A''$	1a'' → 7a' ($\pi \rightarrow \pi^*$)	5.46	6.0[b]		5.99,6.08,6.18
$2^3A'$	1a'' → 2a'' ($\pi \rightarrow \pi^*$) 6a' → 7a' ($\pi \rightarrow \pi^*$)	5.91			6.31,6.42,6.53 6.63
$1^1A''(\tilde{A})$	1a'' → 7a' ($\pi \rightarrow \pi^*$)	6.48	6.8-7.5,[b] 6.48[d]		6.45
$2^1A'$	6a' → 7a' ($\pi \rightarrow \pi^*$) 5a' → 7a' ($\sigma \rightarrow \pi^*$) 1a'' → 2a'' ($\pi \rightarrow \pi^*$)	6.78	7.1[b]		
$2^3A''$	6a' → 2a'' ($\pi \rightarrow \pi^*$) 1a'' → 7a' ($\pi \rightarrow \pi^*$)	6.85	6.8[b]		6.83,7.00,7.10[c] 7.18,7.36,7.55
$3^3A'$	5a' → 7a' ($\sigma \rightarrow \pi^*$) 1a'' → 2a'' ($\pi \rightarrow \pi^*$)	6.98	7.1-7.9[b]		7.75,7.86,7.97 8.08,8.19,8.41
$3^3A''$	5a' → 2a'' ($\sigma \rightarrow \pi^*$)	7.41	7.9[b]		
$2^1A''(\tilde{B})$	6a' → 2a'' ($\pi \rightarrow \pi^*$) 1a'' → 7a' ($\pi \rightarrow \pi^*$)	7.52	7.5[b]		
$3^1A'(\tilde{C})$ 000	5a' → 7a' ($\sigma \rightarrow \pi^*$)	7.85			8.03
010	1a'' → 2a'' ($\pi \rightarrow \pi^*$)		8.139,[e]	8.139[f]	8.13
020	6a' → 7a' ($\pi \rightarrow \pi^*$)			8.245[f]	8.23
030				8.350[f]	8.33
040				8.460[f]	8.44
050				8.565[f]	8.54
060				8.670[f]	8.64
070				8.770[f]	8.75
080				8.87 [f]	8.84
090				8.965[f]	8.94
010				9.145[f]	9.03
011					9.12
012				9.320[f]	

Table 1 (continued)

State	Excitation	Theoretical	Previous Experimental	This Work
$3^1A''(\tilde{D})$ 000	$5a' \rightarrow 2a''(\sigma \rightarrow \pi^*)$	8.97	8.93,[b] 8.881,[e] 8.881[f]	8.84
001			9.065[f]	9.03
100			9.175[f]	
002			9.250[f]	9.22
200			9.360[f]	
003			9.445[f]	9.42
300			9.515[f]	
004			9.64 [f]	9.63
	$4\sigma \rightarrow \pi^*$		15.2 [f]	15.7

Rydberg Excitations

Excitation	Previous Experimental	This Work	Calculated [h]	Quantum Defect
$1\pi \rightarrow 3s$ 000	10.18,[f] 10.20[g]	10.17	10.17	1.01
001	10.40,[f] 10.43[g]	10.41		
$5\sigma \rightarrow 3s$ 000	10.70,[f] 10.73[g]	10.70	10.68	.98
020	10.82,[f] 10.82[g]	10.86		
001	10.90,[f] 10.88[g]			
$1\pi \rightarrow 3p_\sigma$	10.93[g]			
$1\pi \rightarrow 3p_\pi$	11.036,[f] 11.06[g]	11.03	11.04	.70
$5\sigma \rightarrow 3p_\sigma$	11.345,[f] 11.32[g]	11.30	11.30	.76
$5\sigma \rightarrow 3p_\pi$	11.482,[f] 11.54[g]	11.50	11.44	
$1\pi \rightarrow 3d_\sigma$	11.80[g]	11.77	11.79	.26
$1\pi \rightarrow 3d_\pi$	11.95[g]	11.91	11.92	.16
$1\pi \rightarrow 4s$ 000	12.060,[f] 12.07[g]	12.03	12.08	
001	12.288,[f] 12.30[g]	12.25		
$5\sigma \rightarrow 4s$	12.543,[f] 12.48[g]	12.45	12.52	
$1\pi \rightarrow 4d_\sigma$	12.543,[f] 12.57[g]	12.54	12.63	

Table 1 (continued)

Excitation	Previous Experimental	This Work	Calculated	Quantum Defect
$5\sigma \rightarrow 4p\sigma$	12.77^{g}	12.74	12.71	
$5\sigma \rightarrow 4p\pi$			12.76	
$1\pi \rightarrow 5s$ 000			12.75	
$1\pi \rightarrow 5s$ 001	12.99^{g}	12.92		
$5\sigma \rightarrow 4d\sigma$			13.03	
$1\pi \rightarrow 6s$	13.09^{g}	13.06	13.06	
$5\sigma \rightarrow 4d\pi$			13.09	
$5\sigma \rightarrow 5s$	13.18^{g}	13.13	13.17	
$1\pi \rightarrow 7s$		13.25	13.23	
$5\sigma \rightarrow 6s$		13.45	13.47	
$5\sigma \rightarrow 7s$		13.61	13.64	
$4\sigma \rightarrow 3s$	16.6^{f}	16.9		

[a] Ref. 16.

[b] Ref. 10.

[c] Excitation energies listed correspond to unassigned vibronic peaks of one or more electronic transitions.

[d] Ref. 3.

[e] Ref. 4.

[f] Ref. 8.

[g] Ref. 7.

[h] Calculated according to $E = IP - \frac{R}{(n - \delta)^2}$

Table 2

Excitation Energies (in EV) of Acetonitrile

Valence Excitations

Excitation	Excited State Spin	Previous Experimental	This Work
$\pi \rightarrow \pi^*$	Triplet	6.1[a,e]	5.2 - 7.5
	Singlet ?		5.5
	Singlet ?		6.7
	Singlet ?	7.5,[a] 7.32[b]	7.7
$\pi \rightarrow \pi^*$	Triplet		8.1
$\pi \rightarrow \pi^*$	Singlet	8.45[c]	8.45
	Singlet		8.64
	Singlet		8.72
$n \rightarrow \pi^*$	Singlet	9.04,[a] 8.95,[d] 9.00[c]	8.96
	Singlet	9.11[d]	9.11
		9.22[d]	9.21

Rydberg Excitations

Excitation	Previous Experimental	This Work	Calculated[f]	Quantum Defect
$\pi \rightarrow 3p_\sigma$	9.63,[a] 9.59,[c] 9.59[e]	9.58	9.57	.73
$\pi \rightarrow 3p_\sigma + \nu_4$	9.70,[c] 9.71[e]	9.71		
$\pi \rightarrow 3p_\sigma + \nu_2$	9.82,[a] 9.84,[c] 9.83[e]	9.80		
$\pi \rightarrow 3p_\sigma + \nu_2 + \nu_4$	9.94,[c] 9.93[e]	9.95		
$\pi \rightarrow 3p_\sigma + 2\nu_2$	10.04,[a] 10.07,[e] 10.06[c]	10.03		
$\pi \rightarrow 3d_\sigma$	10.29[c]	10.29	10.29	.34
$\sigma \rightarrow 3p_\sigma$	10.52[a]	10.54	10.54	.72
$\sigma \rightarrow 3p_\pi$	10.76,[a] 10.78,[e] 10.78[c]	10.75	10.76	.62
$\pi \rightarrow 4p_\sigma$	10.95,[a] 10.92,[e] 10.92[c]	10.94	10.94	
$\pi \rightarrow 4d_\sigma$	11.34,[a] 11.26,[e] 11.22[c]	11.25	11.19	
$\sigma \rightarrow 3d_\sigma$			11.24	

Table 2 (continued)

Rydberg Excitations

Excitation	Previous Experimental		This Work	Calculated	Quantum Defect
$\pi \rightarrow 5p_\sigma$				11.46	
$\sigma \rightarrow 3d_\pi$			11.46	11.46	.17
$\sigma \rightarrow 3d_\sigma + v_2$					
$\sigma \rightarrow 3d_\sigma + 2v_2$	11.67[a]		11.68		
$\sigma \rightarrow 4p_\sigma$		11.95[c]	11.94	11.90	
$\sigma \rightarrow 4p_\pi$				11.97	
$\sigma \rightarrow 4d_\sigma$		12.18[c]	12.14	12.14	
$\sigma \rightarrow 4d_\pi$			12.24	12.23	
$\sigma \rightarrow 5d_\pi$		12.53[c]	12.57	12.58	
$\sigma \rightarrow 6d_\pi$		12.76[c]	12.75	12.76	
$\sigma \rightarrow 7d_\pi$		12.85[c]	12.85	12.87	
			13.84	13.84	
			14.51	14.51	

[a] Ref. 15.

[b] Ref. 12.

[c] Ref. 16.

[d] Ref. 14.

[e] Ref. 13

[f] $E = IP - \frac{R}{(n - \delta)^2}$

Table 3

Excitation Energies (in eV) of Malononitrile

Valence Excitations

Excitation	Excited State Spin	Observed
$\pi \rightarrow \pi^*$	Triplet	5.2 - 7.1
	Singlet ?	5.6
	Singlet ?	6.5
	Singlet ?	7.9
$n \rightarrow \pi^*$	Triplet	7.95
$n \rightarrow \pi^*$	Singlet	8.94
	Singlet	9.14
	Singlet	9.33

Rydberg Excitations

Excitation	Observed	Calculated	Quantum Defect
$\pi_1 \rightarrow 3R$	9.96	9.96	.76
$\pi_1 \rightarrow 3R + v$	10.13		
$\pi_1 \rightarrow 3R + 2v$	10.26		
$\pi_1 \rightarrow 3R'$	10.43	10.43	.54
$\sigma_1 \rightarrow 3R$	10.74	10.69	.74
$\pi_2 \rightarrow 3R''$	11.01	11.01	.45
$\sigma_1 \rightarrow 3R''$	11.32	11.32	.45
$\pi_1 \rightarrow 4R$	11.58	11.54	
$\pi_1 \rightarrow 5R$	11.98	11.92	
$\pi_1 \rightarrow 5R$		12.00	
$\pi_2 \rightarrow 4R''$		12.02	
$\pi_1 \rightarrow 6R$	12.20	12.18	
$\pi_1 \rightarrow 6R'$		12.22	
$\sigma_1 \rightarrow 4R''$	12.36	12.33	
$\pi_1 \rightarrow 7R$		12.36	
$\pi_1 \rightarrow 7R'$		12.36	
$\pi_2 \rightarrow 5R''$	12.47	12.44	
$\sigma_1 \rightarrow 5R''$	12.77	12.75	
$\sigma_1 \rightarrow 6R''$	13.03	12.97	
	13.47		
	16.34		

Table 4

Excitation Energies (in eV) of Propionitrile

Valence Excitations

Excitation	Excited State Spin	Previous Experimental[a]	This Work
$\pi \rightarrow \pi^*$	Triplet	6.4	5.4 - 7.5
	?		6.5
	?		7.8
$n \rightarrow \pi^*$	Triplet		8.14
$n \rightarrow \pi^*$	Singlet	8.74	8.95

Rydberg Excitations

Excitation	Previous Experimental	This Work	Calculated	δ
$\pi \rightarrow 3R$	9.39	9.35	9.34	.67
	9.52	9.56		
	9.68	9.74		
	9.86			
$\pi \rightarrow 3R'$	10.09	10.12	10.12	.20
	10.34			
$\sigma \rightarrow 3R$	10.50	10.44	10.45	.65
$\pi \rightarrow 4R$	10.65		10.62	
	10.87	11.01		
$\pi \rightarrow 5R$		11.09	11.12	
$\sigma \rightarrow 3R'$			11.14	.23
	11.19			
$\pi \rightarrow 6R$	11.30	11.32	11.37	
$\pi \rightarrow 5R + v$			11.38	
$\pi \rightarrow 6R'$		11.47	11.45	
$\sigma \rightarrow 4R$		11.7	11.7	
		11.8		
$\sigma \rightarrow 4R'$		11.96	11.95	
$\sigma \rightarrow 5R$		12.28	12.2	
$\sigma \rightarrow 5R'$			12.31	
$\sigma \rightarrow 6R$		12.46	12.44	
$\sigma \rightarrow 6R'$			12.50	
		12.63	12.61	
		12.94		
		13.63		

[a]Ref. 15.

Table 5

Excitation Energies (in eV) of Butyronitrile

Valence Excitations

Excitation	Excited State Spin	Previous Experimental[a]	This Work
$\pi \rightarrow \pi^*$	Triplet	5.9	5.4 - 7.6
	?		6.4
	?	7	
$n \rightarrow \pi^*$	Triplet		8.2
$n \rightarrow \pi^*$	Singlet		9.12

Rydberg Excitations

Excitation	Previous Experimental	This work
$\pi \rightarrow 3R$	9.3	9.18
$\pi \rightarrow 3R + V$		9.42
	9.85	9.80
	10.5	10.6
		11.27
		12.03
		13.65

[a]Ref. 15.

References

1. W. C. Price, Phys. Rev. 46, 529 (1934).
2. W. C. Price and A. D. Walsh, Trans. Far. Soc. 41, 381 (1945).
3. G. Herzberg and K. K. Innes, Can. J. Phys. 35, 842 (1957).
4. G. Herzberg, Electronic Spectra of Polyatomic Molecules (Van Nostrand, Princeton, N.J., 1966).
5. R. Ditchfield, J. Del Bene and J. A. Pople, J. Am. Chem. Soc. 94, 4806 (1972).
6. G. M. Schwenzer, S. V. O'Neil and H. F. Schaefer, J. Chem. Phys. 60, 2787 (1974).
7. W.-C. Tam and C. E. Brion, J. Electron Spectrosc. 3, 281 (1974).
8. C. Fridh and L. Asbrink, J. Electron Spectrosc. 7, 119 (1975).
9. M. Peric, S. D. Peyerimhoff and R. J. Buenker, Can. J. Chem. 55, 3664 (1977).
10. A. Chutjian, H. Tanaka, B. G. Wicke and S. K. Srivastava, J. Chem. Phys. 67, 4835 (1977).
11. L. Asbrink, C. Fridh and E. Lindholm, Chem. Phys. 27, 159 (1978).
12. G. Herzberg and G. Scheibe, Zeits. f. Physik Chemie, B7, 390 (1930).
13. J. A. Cutler, J. Chem. Phys. 16, 136 (1948).
14. H. Okabe and V. H. Dibeler, J. Chem. Phys. 59, 2430 (1973).
15. R. S. Stradling and A. G. Loudon, J. C. S. Faraday II 73, 623 (1977).
16. C. Fridh, J. C. S. Faraday II 74, 2193 (1978).
17. (a) A. Kuppermannn, J. K. Rice and S. Trajmar, J. Phys. Chem. 72, 3894 (1968).

(b) S. Trajmar, J. K. Rice and A. Kuppermann, Advan. Chem. Phys. 18, 15 (1970).

18. O. A. Mosher, W. M. Flicker and A. Kuppermann, J. Chem. Phys. 59, 6502 (1973).

19. O. A. Mosher, W. M. Flicker and A. Kuppermann, J. Chem. Phys. 62, 2600 (1975).

20. A. Kuppermann, W. M. Flicker and O. A. Mosher, Chem. Rev. 79, 77 (1979).

21. R. F. Lake and H. Thompson, Proc. Roy. Soc. Lond. A 317, 187 (1970).

22. H. Stafast and H. Bock, Z. Naturforsch, 28b, 746 (1973).

23. K. Watanabe, T. Nakayama and J. Mottl, J. Quant. Spectr. Radiation Trans. 2, 369 (1961).

Figure Captions

Fig. 1: Electron-impact energy-loss spectra of hydrogen cyanide at scattering angles (a) 10° and (f) 70°, acetonitrile at (b) 10° and (g) 80°, malononitrile at (c) 10° and (h) 80°, propionitrile at (d) 10° and (i) 80°, and butyronitrile at (e) 10° and (j) 80°. The impact energy was 25 eV. Typical experimental parameters for these spectra and those presented in later figures are: sample pressure ranging from 3.0 mTorr and 7.0 mTorr as measured with an uncalibrated Schulz Phelps ionization gauge, incident electron beam currents ranging from 10 namp to 50 namp, and resolution in the range 60 meV to 90 meV.

Fig. 2: Electron energy-loss spectrum of hydrogen cyanide at 25 eV impact energy and scattering angles of (a) 10° and (b) 70°. Experimental conditions as described in Fig. 1. Resolution approximately 65 meV. Spectra are repeated here to better display vibrational structure observed.

Fig. 3: Differential cross-sections of HCN as a function of scattering angle at an incident electron energy of 25 eV; for elastic scattering (+) and for excited states: T_{5-7} (O), $T_{7.86}$ (◇), $S_{8.84}$ (△), and $S_{11.03}$ (□). The elastic peak DCS was multiplied by .1 before plotting. The DCS's for $T_{7.86}$ and $S_{11.03}$ were multiplied by 10 before plotting. The letters S and T indicate singlet and triplet upper states, and the index represents the corresponding transition energy.

Fig. 4: Differential cross-sections of acetonitrile as a function of scattering angle at an incident electron energy of 25 eV; for elastic scattering (+) and for excited states $T_{5.2\text{-}7.5}$ (O), $T_{8.1}$ (◇), $S_{8.96}$ (□), and $S_{10.75}$ (△). Letter designations and indices as described for Fig. 3. The elastic peak DCS were multipled by .1 before plotting. The DCS's for $T_{8.1}$ and $S_{8.96}$ were multiplied by 10 before plotting.

Fig. 5: Differential cross-section of malononitrile as a function of scattering angle at an impact energy of 25 eV; for elastic scattering (+) and for excited states $T_{5.2\text{-}7.1}$ (O), $T_{7.95}$ (◇), $S_{8.94}$ (△) and $S_{10.74}$ (□). Letter designations and indices as in Fig. 3. The elastic peak DCS was multipled by .1 before plotting. The DCS for $T_{7.95}$ was multiplied by 10 before plotting.

Fig. 6: Energy loss spectra of (a) hydrogen cyanide, (b) acetonitrile, (c) malononitrile, (d) propionitrile, and (e) butyronitrile at an incident electron energy of 75 eV and a scattering angle of 50°. Experimental conditions as described in Fig. 1.

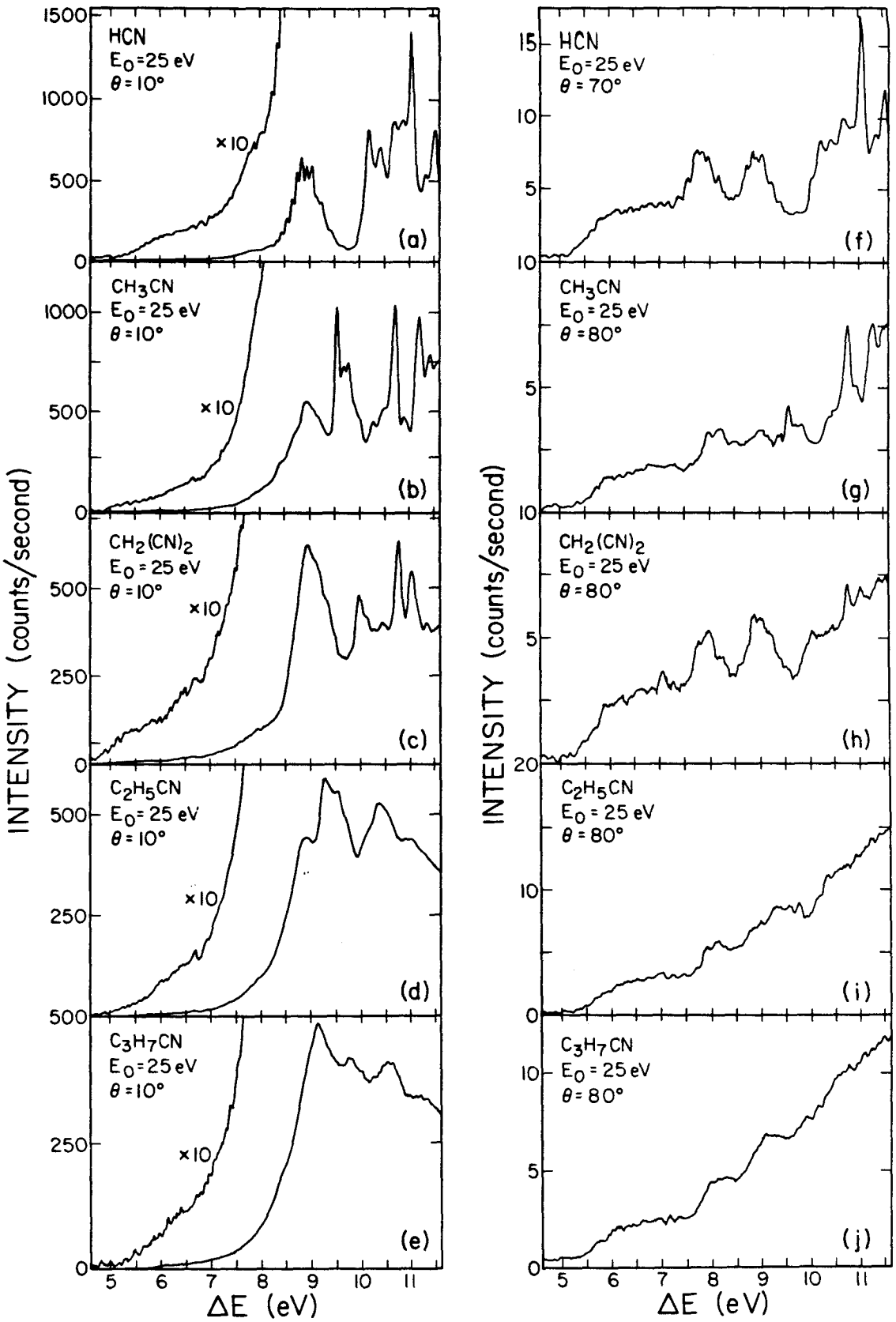
HCN
E0=25 eV
θ=10°
×10
(a)
CH3CN
E0=25 eV
θ=10°
×10
(b)
CH2(CN)2
E0=25 eV
θ=10°
×10
(c)
C2H5CN
E0=25 eV
θ=10°
×10
(d)
C3H7CN
E0=25 eV
θ=10°
×10
(e)
HCN
E0=25 eV
θ=70°
(f)
CH3CN
E0=25 eV
θ=80°
(g)
CH2(CN)2
E0=25 eV
θ=80°
(h)
C2H5CN
E0=25 eV
θ=80°
(i)
C3H7CN
E0=25 eV
θ=80°
(j)
INTENSITY (counts/second)
ΔE (eV)

Figure 1

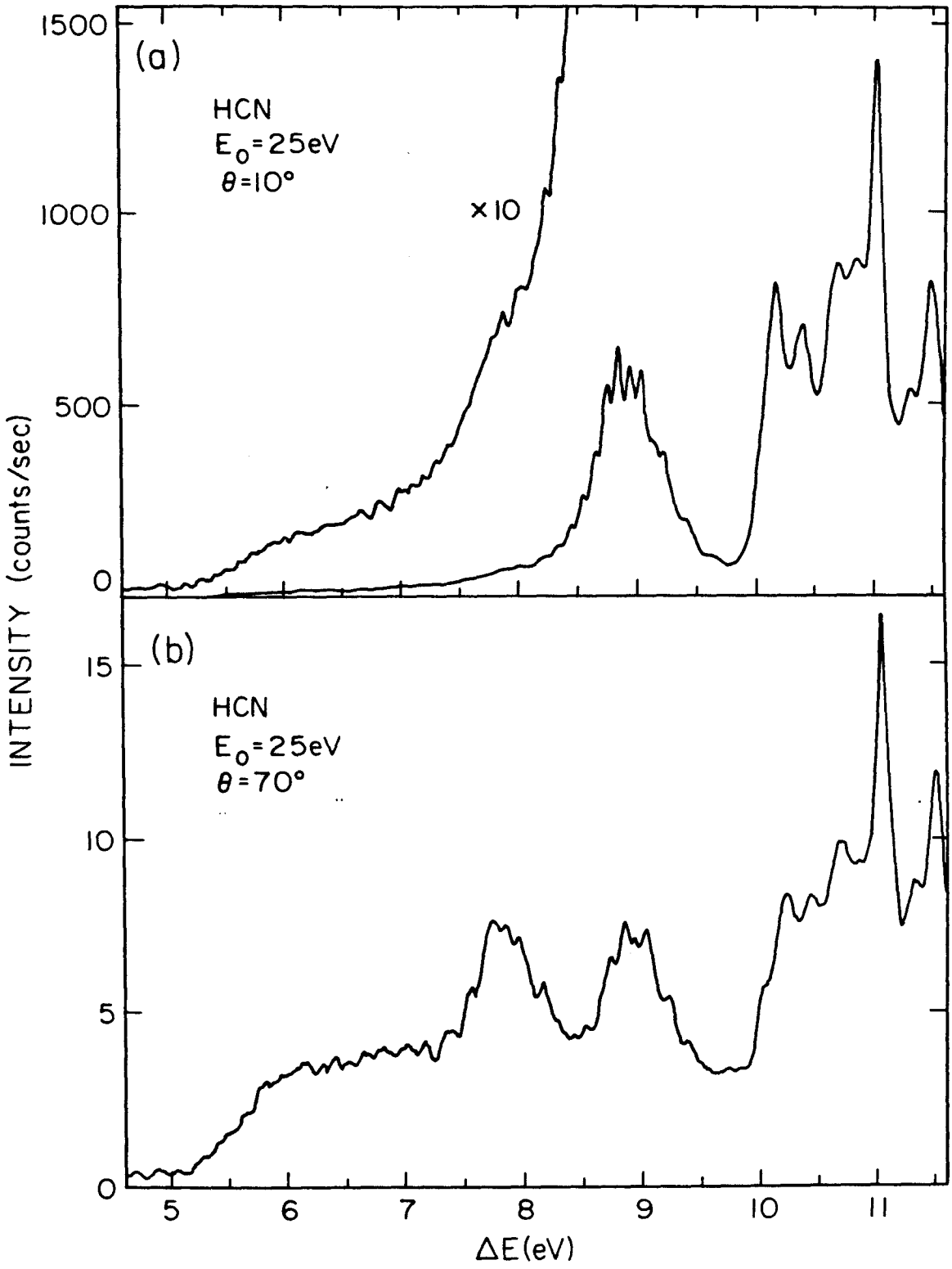
(a)
HCN
E_0=25eV
θ=10°
×10
(b)
HCN
E_0=25eV
θ=70°
INTENSITY (counts/sec)
ΔE(eV)
1500
1000
500
0
15
10
5
0
5
6
7
8
9
10
11

Figure 2

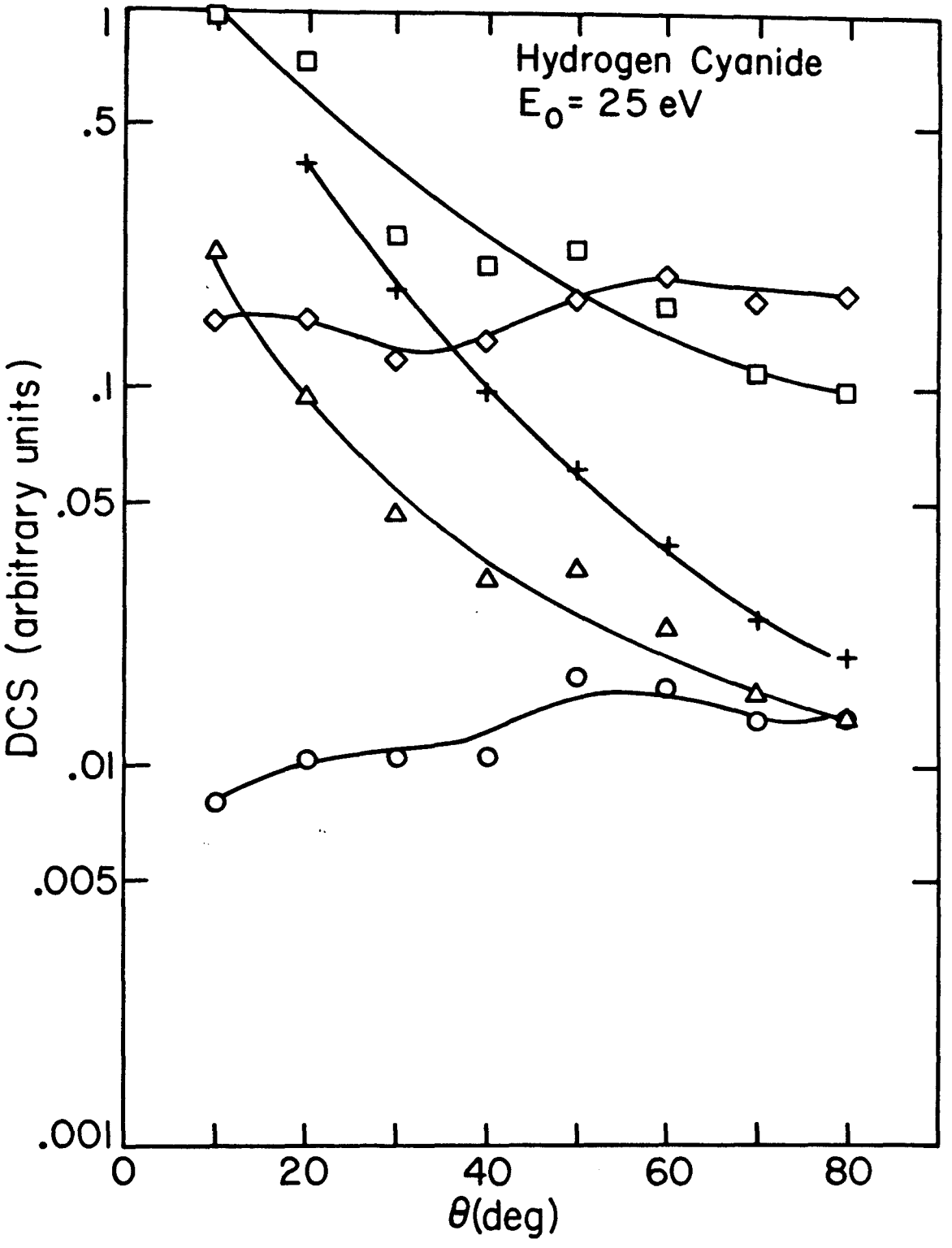
Hydrogen Cyanide
E_0 = 25 eV
DCS (arbitrary units)
1
.5
.1
.05
.01
.005
.001
0
20
40
60
80
θ(deg)

Figure 3

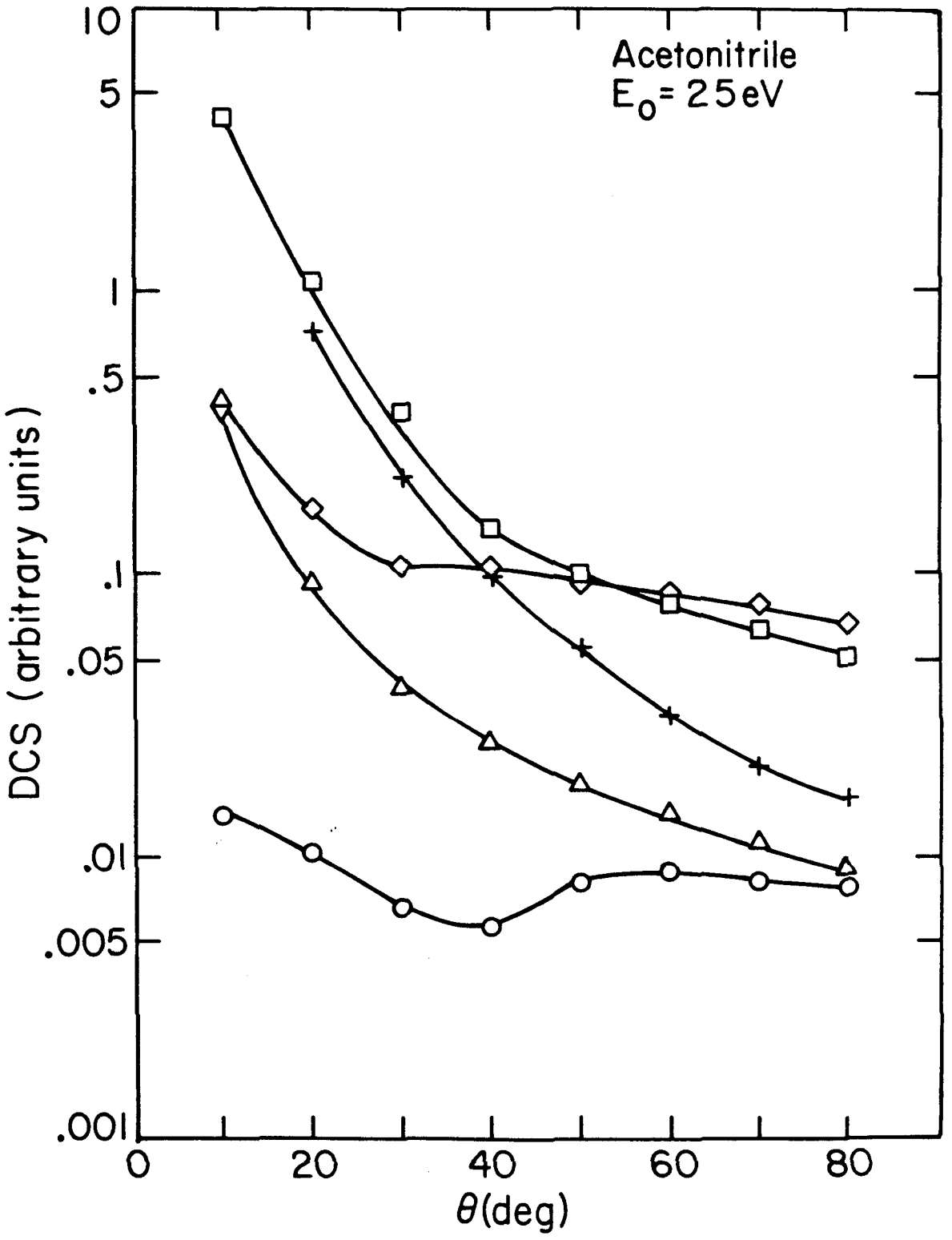
Acetonitrile
E_o= 25eV
DCS (arbitrary units)
10
5
1
.5
.1
.05
.01
.005
.001
0
20
40
60
80
θ(deg)

Figure 4

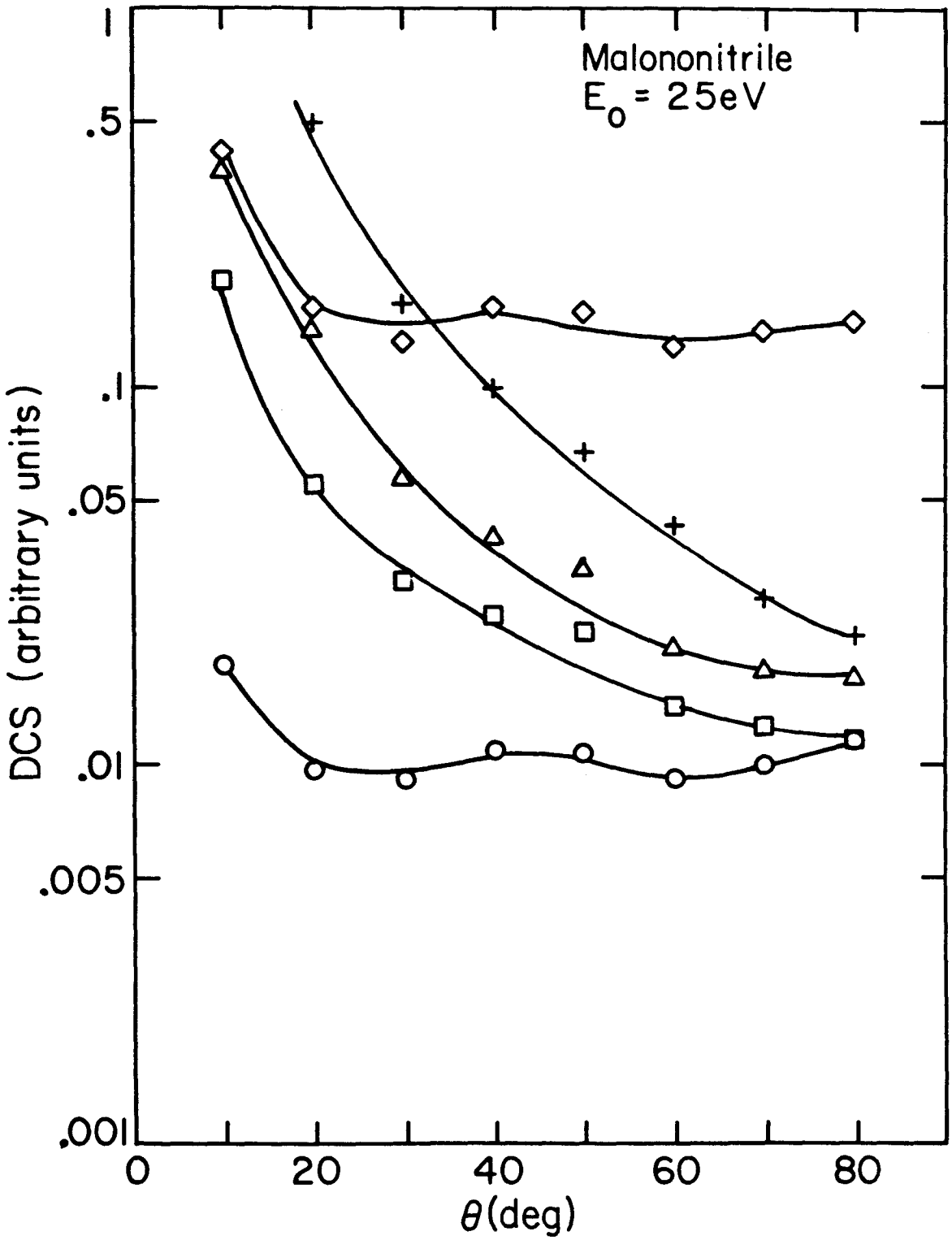
Malononitrile
E_0 = 25eV
DCS (arbitrary units)
1
.5
.1
.05
.01
.005
.001
0
20
40
60
80
θ(deg)

Figure 5

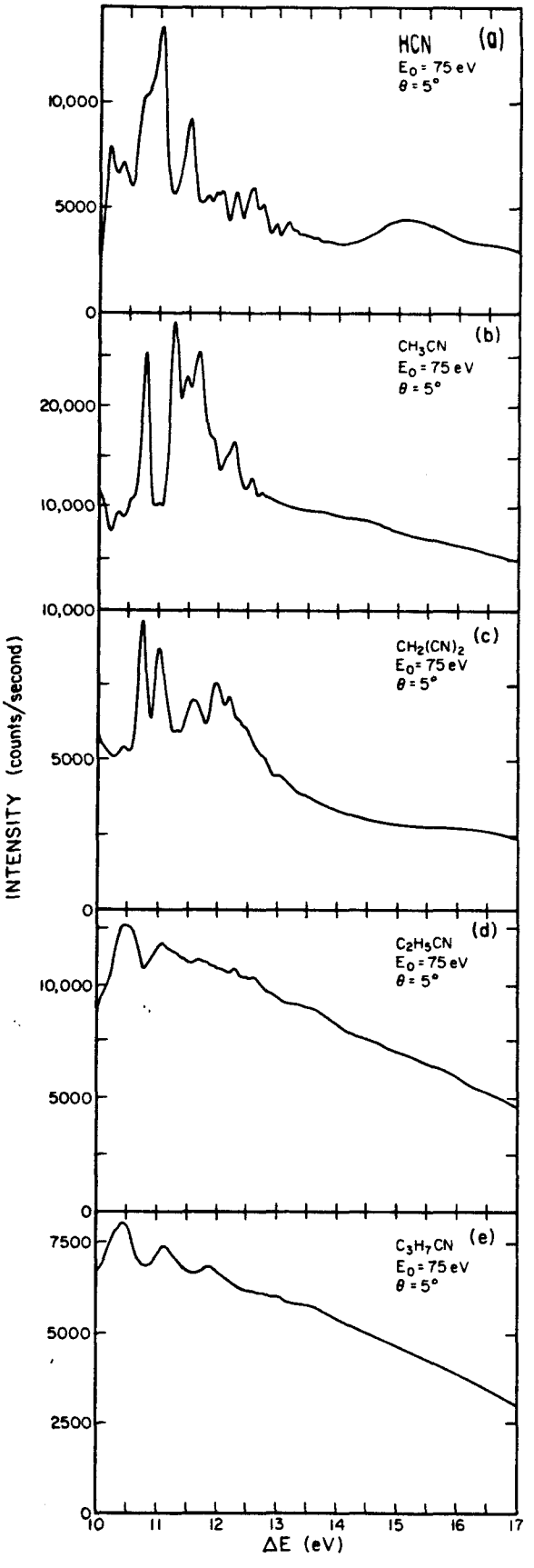
HCN (a)
E_0 = 75 eV
θ = 5°
10,000
5000
0
CH_3CN (b)
E_0 = 75 eV
θ = 5°
20,000
10,000
10,000
$CH_2(CN)_2$ (c)
E_0 = 75 eV
θ = 5°
5000
0
C_2H_5CN (d)
E_0 = 75 eV
θ = 5°
10,000
5000
0
C_3H_7CN (e)
E_0 = 75 eV
θ = 5°
7500
5000
2500
0
INTENSITY (counts/second)
10
11
12
13
14
15
16
17
ΔE (eV)

Figure 6

Appendix I: The Low Lying States of Ammonia; Generalized Valence Bond and Configuration Interaction Studies.

The Low Lying States of Ammonia; Generalized Valence Bond and Configuration Interaction Studies[1]

Ronald Rianda[2], Robert P. Frueholz[2]
and William A. Goddard III

Arthur Amos Noyes Laboratory of Chemical Physics[3]
California Institute of Technology
Pasadena, California 91125, USA

Abstract

The nine lower singlet and triplet states of ammonia were studied using *ab initio* generalized valence bond (GVB) and configuration interaction (CI) wavefunctions. The eight lowest (vertical) excited states were found to be Rydberg in nature. Vertical excitation energies were determined to be (in eV): 6.14 and 6.37 for $n \rightarrow 3s$; 7.86 and 7.88 for $n \rightarrow 3p_{x,y}$, and 7.87 and 8.15 for $n \rightarrow 3p_z$ (in each case the triplet energy is first). These results are in excellent agreement (0.06 eV average error) with the observed electron impact excitation energies (in eV), 6.39 ($A\ ^1A_2''$), 7.93 ($B\ ^1E''$) and 8.26 ($C\ ^1A_1'$). The small singlet triplet energy splittings are consistent with those expected for Rydberg-like excited states. We find no vertical transition consistent with the small peak at 4.4 eV apparently observed in threshold electron impact experiments.

1. Introduction

The lower excited states of ammonia have been the object of experimental[4-7] and theoretical[8-11] investigations. Despite these studies, the nature and location of low-lying triplet and singlet excited states are note completely understood.[6,10-13] In order to elucidate further the character of these transitions and in particular the triplet states, *ab initio* generalized valence bond (GVB) and configuration interaction (CI) calculations have been performed on the $\tilde{X}\ ^1A_1$, $\tilde{A}\ ^{3,1}A_2''$, $\tilde{B}\ ^{3,1}E''$, $\tilde{C}\ ^{3,1}A_1'$, and $\tilde{D}\ ^{3,1}A_2''$ states and vertical excitation energies were determined. The excited states were found to result from excitation of an electron from the nonbonding lobe orbital to Rydberg-like excited orbitals.

Experimentally, vertical transitions have been observed at 6.39 eV, 7.93 eV, 8,26 eV, and 9.25 eV; the first three have been assigned by Harshbarger[7] as excitations from the ground state to the $\tilde{A}\ ^1A_2''$, $\tilde{B}\ ^1E''$, and $\tilde{C}\ ^1A_1'$ states, respectively, while the fourth may be assigned as an excitation to the $\tilde{D}\ ^1A_2''$ state.[14] The corresponding triplet states have not been experimentally observed, however, Compton *et al.*,[6] using a threshold SF_6 electron scavenger technique, have reported a low-lying transition at 4.4 eV which they suggest is due to a triplet state.

Our best calculated results for vertical excitation energies (eV)[15] are 6.140 ($^3A_2''$), 6.370 ($^1A_2''$), 7.860 ($^3E''$), 7.877 ($^1E''$), 7.865 ($^3A_1'$), 8.145 ($^1A_1'$), 8.844 ($^3A_2''$), and 8.855 ($^1A_2''$). In addition, we find no evidence for the existence of the low-lying triplet state reported by Compton *et al.*[6]

2. Computational Details and Results

The experimental ground state geometry was used:[16]

$$R_{N-H} = 1.0079\ \text{Å} \qquad \text{and} \qquad HNH = 107.30^{\circ}.$$

The double zeta basis of Huzinaga[17] and Dunning[18] was used [(9s,5p/4s) primitive Gaussians contracted to (4s,2p/2s)], but with a set of 3d polarization functions[19] and a set of diffuse functions[20] [(3s,2p) to better describe Rydberg orbitals] included on the nitrogen.

2.1 GVB Calculations

2.1.1 The Ground State

The ground state Hartree-Fock wavefunction of ammonia consists of five doubly-occupied orbitals,

$$\Psi_{HF} = \{\phi_{1_{a_1}}^2 \ \phi_{2_{a_1}}^2 \ \phi_{1_{e_x}}^2 \ \phi_{1_{e_y}}^2 \ \phi_{3_{a_1}}^2 \ \alpha\beta\ldots\alpha\beta\} \ . \qquad (1)$$

The HF wavefunctions of the low-lying excited states consist of four doubly-occupied orbitals and two singly-occupied orbitals. In general, the correlation error in a closed-shell HF ground state is significantly greater than the correlation error in the open-shell excited states. This manifests itself in erroneously low HF excitation energies.

In a GVB wavefunction,[21] all orbitals are singly-occupied and the spin function is completely general. For ammonia, this would lead to ten non-orthogonal orbitals. However, in our calculations, we dealt with an intermediate case in which the nitrogen 1s-like orbital is kept doubly-occupied, while each of the bond pairs and the lobe orbital were

correlated. Each bond pair was correlated with two orbitals as usual in GVB calculations

$$\phi_i(1)\phi_i(2) \rightarrow \phi_{ia}(1)\phi_{ib}(2) + \phi_{ib}(1)\phi_{ia}(2) \tag{2}$$

and these orbitals were solved for in terms of the natural orbitals

$$\phi_{ia}\phi_{ib} + \phi_{ib}\phi_{ia} \rightarrow C_1^2\bar{\phi}_{ai}\bar{\phi}_{ai} + C_2^2\bar{\phi}_{bi}\bar{\phi}_{bi} \quad . \tag{3}$$

For the lone pair of the ground state, we included all dominant correlations (in-out and angular) leading to a pair function of the form

$$C_1^2\phi_1^2 + C_2^2\phi_2^2 + C_3^2\phi_3^2 + C_4^2\phi_4^2 \quad . \tag{4}$$

The resulting wavefunction is then the product of a doubly-occupied N1s-like orbital times three bond functions of the form (2) times a lone pair function of the for (4). This wavefunction is multiplied by an appropriate spin function and antisymmetrized, and the orbitals are then optimized self-consistently with the restriction that the orbitals in different pairs be orthogonal and that the spin function be the simple valence bond spin function. These restrictions were removed by subsequent configuration interaction (CI) calculations. This wavefunction is sometimes denoted as GVB(4) to indicate that four pairs of electrons are correlated.

The first natural orbital from (4), ϕ_{n1}, and the first natural orbital from (3), $\phi_{\sigma 1}$, for one of the bond pairs are shown in Fig. 1a.

2.1.1 Excited States

Self-consistent GVB calculations were carried out on the lowest

excited triplet and singlet states. Each state has the character of a transition from the non-bonding orbital ϕ_n to a 3s-like Rydberg orbital, ϕ_{3s}, and hence is denoted as

$$n \rightarrow 3s \ .$$

In these GVB calculations, the three bond pairs are described as in (3), however, the lone pair (4) is replaced by

$$(\phi_n\phi_{3s} \pm \phi_{3s}\phi_n) \qquad (5)$$

for the singlet and triplet states, respectively. The 3s-like orbital of the singlet state is shown in Fig. 1b.

In D_{3h} symmetry (the expected geometry for such excited states), these states give rise to $^3A_2''$ and $^1A_2''$ symmetry. The calculated vertical excitation energies (see Tables 1 and 2) are 6.008 eV for $\tilde{a}\ ^3A_2''(n \rightarrow 3s)$ and 6.129 eV for $\tilde{A}\ ^1A_2''(n \rightarrow 3s)$. The experimental vertical excitation energy for the singlet state is 6.392 eV, indicating $\sim\frac{1}{4}$ eV of differential correlation effects in the GVB description.

Due to the diffuseness of the excited orbitals, we expect that the core orbitals (1s orbital, bonding orbital and the singly-occupied lobe) would differ little between Rydberg excited states of the same spin multiplicity. Consequently, the method of improved virtual orbitals[22] (IVO) was used to obtain excited orbitals for the higher excited states, in preparation for configuration interaction calculations. The IVO technique uses core orbitals from a prior self-consistent calculation (in this case core orbitals were obtained by GVB solution of the 3s singlet and triplet excited states) and solves self-consistently for the

singly-occupied excited orbitals of a given spin multiplicity (without varying the core orbitals). The $3p_x$, $3p_y$ and $3p_z$ excited orbitals from such calculations should be well described. We also retained the 4s-like orbital, although the basis is less adequate for it. Diffuse d functions were not included and hence we cannot describe the 3d excited states expected to lie in the vicinity of the 4s excited state. Excitation energies from the IVO calculations are listed in Table 1 for comparison with subsequent results.[23] IVO singlet-triplet splittings for the A_1 states are expected to be somewhat lower than exact values because orthogonality of the excited $^1A_1$ states to the ground state is not treated rigorously (the effect is small here, $\sim$0.03 eV).

2.2 CI Calculations

The basis orbitals for the CI calculations of the ground state consisted of all the GVB natural orbitals (eleven orbitals) except the nitrogen 1s orbital (which was kept double-occupied). All configurations resulting from single excitations from the basic configuration (first configuration of Table 3) were included, where σ_i and σ_i^* refer to the bonding and antibonding NO's of bond pair i and the n_i refers to the NO's for the lone pair. To generate additional configurations, the set of natural orbitals was separated into four sets: $(\sigma_1\sigma_1^*)$, $(\sigma_2\sigma_2^*)$, $(\sigma_3\sigma_3^*)$ and (n_1,n_2,n_3,n_4) and intragroup excitations to a total order of four over this entire space were included. The principal configurations[24] are included in Table 3.

For the excited states, the CI calculation was based on the GVB orbitals of the $^1A_2''$ ($n \rightarrow 3s$) state to which we added the four (singlet) IVO orbitals (corresponding to $3p_x$, $3p_y$, $3p_z$ and 4s character) and the dominant correlating orbital (n_2) from the ground state (orthogonalized to the previous orbitals). The CI wavefunction for $^3A_2''(n \rightarrow 3s)$ was based on the corresponding GVB orbitals of the $^3A_2''(n \rightarrow 3s)$ state and the four (triplet) IVO orbitals. However, for the $n \rightarrow 3p_{x,y}$ and $n \rightarrow 4s$ states, slightly lower energies (0.02 eV) were obtained from the CI using the singlet orbitals as described above.

For the excited state, the configurations for the CI calculations were selected as follows:

(i) We included all single excitations from the dominant configuration of each of the five excited states (for the single case, the ground state configuration was also included).

(ii) Partitioning the orbitals into four subsets

$$(\sigma_1,\sigma_1^*),\ (\sigma_2,\sigma_2^*),\ (\sigma_3,\sigma_3^*),\ (n_1,n_2,3s,3p_x,3p_y,3p_z,4s),$$

we allowed all <u>intra</u>-group excitations from each dominant configuration with the restriction that not more than two groups are excited simultaneously (thus, no excitations of order greater than four).

Principal configurations for the 3s and $3p_z$ Rydberg-like excited states are given in Table 3. Principal configurations for the other excited states are identical to those of the $3p_z$ Rydberg except for occupancy of the appropriate excited state orbital.

In order to eliminate the possiblity of the existence of a low-lying valence triplet state (below 6 eV) which might not have been converged to in the prior computations, an additional GVB calculation was performed. In this calculation, a wavefunction modeling a triplet $\sigma \rightarrow \sigma^*$ transition in one of the bond pairs was calculated. The vertical excitation energy was found to be several volts above the experimental ionization potential.

Only limited calculations were performed on the ammonia ion. In addition to the Hartree-Fock result (see Table 1), a small CI calculation for the ion using GVB(4) ground-state orbitals as a basis was performed. The configurations involved correspond to ionization of an electron from the lobe orbital or from one of the three bonding orbitals. The purpose of this calculation was to determine the contribution of the configuration corresponding to ionization from the lobe orbital relative to that of configuration corresponding to ionization from the bonding orbitals. The results of this calculation indicate that the lowest ionization occurs predominantly (89%) from the lobe orbital.

3. Comparison with Other Calculations

Horsley and Flouquet[10] carried out Hartree-Fock calculations on the ground state and the lowest lying singlet and triplet excited states. They used a minimal basis set and obtained adiabatic excitation energies of 3.56 eV for the singlet and 3.95 eV for the triplet. (Note: In this calculation the triplet excitation energy was greater than that of the corresponding singlet.) These values are about 2 eV too low.

Much cruder Hartree-Fock calculations were carried out by Bishop

et al.[11] who used a single-center expansion and obtained approximate Hartree-Fock calculations for the excited states. The ground state energy and excitation energies were not reported.

Higuchi[8] carried out minimal basis Hartree-Fock calculations using approximate integrals and obtained a vertical excitation energy of 6.7 eV for the $^1A_1 \rightarrow {}^1A_2''$ transition. The agreement with the experimental value is remarkable considering the approximations and limitations of the basis set (which did not include a nitrogen 3s orbital).

The semi-empirical CNDO technique has been applied to the $\tilde{X}\ {}^1A_1 \rightarrow \tilde{A}\ {}^1A_2''$ adiabatic transition by Kroto and Santry.[9] Their calculated excitation energy was 6.80 eV compared with the 5.72 eV experimental value.[13]

4. Summary

We find that relatively simple GVB calculations including CI among the GVB orbitals leads to excellent excitation energies (average error $\sim$0.06 eV). We find that the lower excited states are of Rydberg character with very small triplet-singlet splittings. No evidence was found for a low lying (below 6 eV) triplet state (using the ground state geometry).

Table 1: Vertical excitation energies for ammonia (eV).

	HF	GVB(1)[a]	GVB(4)[b]	CI	Experimental[c]
Ground State	0	0	0	0	0
3s Triplet	5.251	5.798	5.930	6.140	
3s Singlet	5.481	6.029	6.129	6.370	6.392
$3p_x$ Triplet	6.798	7.346	7.747[d]	7.860	
$3p_x$ Singlet	6.851	7.398	7.747[d]	7.877	7.927
$3p_z$ Triplet			7.643[d]	7.865	
$3p_z$ Singlet			7.821[d]	8.145	8.258
4s Triplet			8.694[d]	8.844	
4s Singlet			8.701[d]	8.855	9.25
Ion	9.405				10.85[e]

[a]The NH bond pairs were not correlated.

[b]The wavefunction described in Section 2.1.

[c]Electron impact results of W. R. Harshbarger.[7]

[d]Obtained from IVO calculations described in Section 2.1.2.

[e]D. W. Turner, C. Baker, A. D. Baker and C. R. Brundle, "Molecular Photoelectron Spectroscopy", Wiley-Interscience, New York, 1970, p. 357.

Table 2. Calculated total energies in hartree atomic units (1h = 27.2116 eV).

	HF	GVB(1)	GVB(4)	CI
Ground State	-56.19918	-56.21932	-56.26842	-56.30105
$^3A_2''$ (n → 3s)	-56.00623		-56.05052	-56.07541
$^1A_2''$ (n → 3s)	-55.99775		-56.04317	-56.06695

Table 3. Principal configurations of the CI wavefunction for the ground state of NH_3.

Character[a]	Number of Cases	Orbital										Energy Lowering Per Case (mh)[b]
		σ_1	σ_1^*	σ_2	σ_2^*	σ_3	σ_3^*	n_1	n_2	n_3	n_3	
HF	1	2	0	2	0	2	0	2	0	0	0	-
GVB(σ)	3	2	0	0	2	2	0	2	0	0	0	15.6
GVB(n)	1	2	0	2	0	2	0	0	2	0	0	15.5
IP(σ,n)	3	2	0	1	1	2	0	1	1	0	0	9.5
IP(σ_i,σ_j)	3	1	1	2	0	1	1	2	0	0	0	3.5

[a] IP indicates an interpair correlation.

[b] 1 mh = 10^{-3}h = 0.0272116 eV = 0.62751 kcal/mole.

Table 4. Principal configurations for excited states of NH_3.

	Character	Number of Cases	σ_1	σ_1^*	σ_2	σ_2^*	σ_3	σ_3^*	n_1	n_2	3s	$3p_x$	$3p_y$	$3p_z$	4s	Energy Lowering Per Case (mh)
$\tilde{A}\ ^1A_2''$	HF	1	2	0	2	0	2	0	1	0	1	0	0	0	0	
	GVB(σ)	3	2	0	2	0	0	2	1	0	1	0	0	0	0	13.5
	IP(σ_i,σ_j)	3	2	0	1	1	1	1	1	0	1	0	0	0	0	3.1
	IP(σ,n)	3	1	1	2	0	2	0	0	1	1	0	0	0	0	2.6
$\tilde{C}\ ^1A_1'$	HF	1	2	0	2	0	2	1	1	0	0	0	0	1	0	
	GVB(σ)	3	2	0	0	2	2	1	1	0	0	0	0	1	0	13.3
	IP(σ_i,σ_j)	3	2	0	1	1	1	1	1	0	0	0	0	1	0	3.0
	IP(σ,n)	3	1	1	2	0	2	0	0	1	0	0	0	1	0	2.5

References

1. Initiated as a Chemistry 120 research project. Partial supported by a grant (CHE73-05132) from the National Science Foundation.
2. Supported by a contract [E(04-3)-767] from the Energy Research and Development Administration.
3. Contribution No. 5425.
4. A. E. Douglas, Disc. Faraday Soc. 25, 158 (1963).
5. E. N. Lassettre, A. Skerbele, M. A. Dillon and K. J. Ross, J. Chem. Phys. 48, 5066 (1968).
6. R. N, Compton, J. A. Stockdale and P. W. Reinhardt, Phys. Rev. 180, 111 (1969).
7. W. R. Harshbarger, J. Chem. Phys. 54, 2504 (1971).
8. J. Higuchi, J. Chem. Phys. 24, 535 (1956).
9. H. W. Kroto and D. P. Santry, J. Chem. Phys. 47, 792 (1967).
10. J. Horsley and F. Flouquet, Chem. Phys. Lett. 5, 165 (1970).
11. J. M. Bishop, J.-C. LeClerc and Y. Takahate, J. Mol. Spectrosc. 39, 79 (1971).
12. M. B. Robin, Higher Excited States of Polyatomic Molecules, V. 1 (Academic Press, New York, 1974) pp. 208-215.
13. G. Herzberg, Electronic Spectra of Polyatomic Molecules (Van Nostrand, Princeton, 1966) pp. 515-517.
14. A. D. Walsh and P. A. Warsop, Trans. Faraday Soc. 57, 345 (1971).
15. For the excited states, the symmetry designation used here is that appropriate for D_{3h} despite the fact that the calculations use the ground state geometry (C_{3v}).

16. Handbook of Chemistry and Physics, Chemical Rubber Co., 46th ed., p. F120 (1965).

17. S. Huzinaga, J. Chem. Phys. 52, 1243 (1965).

18. T. H. Dunning, Jr., J. Chem. Phys. 53, 2823 (1970).

19. α = 0.98 from T. H. Dunning, Jr., J. Chem. Phys. 55, 3958 (1971).

20. α_s = 0.0226, 0.0107, 0.003 and α_p = 0.0288, 0.0112. From an extrapolation of Huzinaga's exponents as suggested by Mr. Stephen P. Walch.

21. W. A. Goddard III, T. H. Dunning, Jr., W. J. Hunt and P. J. Hay, Accts. Chem. Res. 6, 368 (1973); W. J. Hunt, P. J. Hay and W. A. Goddard III, J. Chem. Phys. 57, 738 (1972); F. W. Bobrowicz and W. A. Goddard III, a chapter entitled "The Self-Consistent Field Equations for Generalized Valence Bond and Open-Shell Hartree-Fock Wavefunctions", to appear in Modern Theoretical Chemistry: Electronic Structure, H. F. Schaefer III, Ed. (Plenum Publishing Corp., New York, 1976), Vol. II.

22. W. J. Hunt and W. A. Goddard III, Chem. Phys. Lett. 3 (1969); W. J. Hunt, PhD Thesis, California Institute of Technology, 1971; W. A. Goddard III and W. J. Hunt, Chem. Phys. Lett. 24, 464 (1974).

23. The IVO excitation energy is obtained directly by comparing the orbital energy of the excited orbital with the energy of the corresponding GVB 3s orbital.

24. The energy lowering in Tables 3 and 4 is defined as the increase in energy resulting from deleting that spatial configuration from the CI wavefunction. All spatial configuration contributions of 1 mh = 10^{-3}h or more are included.

Figure Caption

Fig. 1. NH_3 orbitals. (a,b) GVB first natural orbitals for one of the bond pairs and for the lone pair of the ground state; (c) GVB excited orbital for the A $^1A_2''(n \rightarrow 3s)$ excited state; (d,e) IVO excited orbitals for the B $^1E'(n \rightarrow 3p)$ and C $^1A_2'(n \rightarrow 3p_z)$ excited states. Long dashes indicate nodal lines. Other lines are separated by equal increments of 0.05 a.u. for (a,b) and 0.01 a.u. for (c,d,e). The plot scale is in bohr = 0.529177 Å.

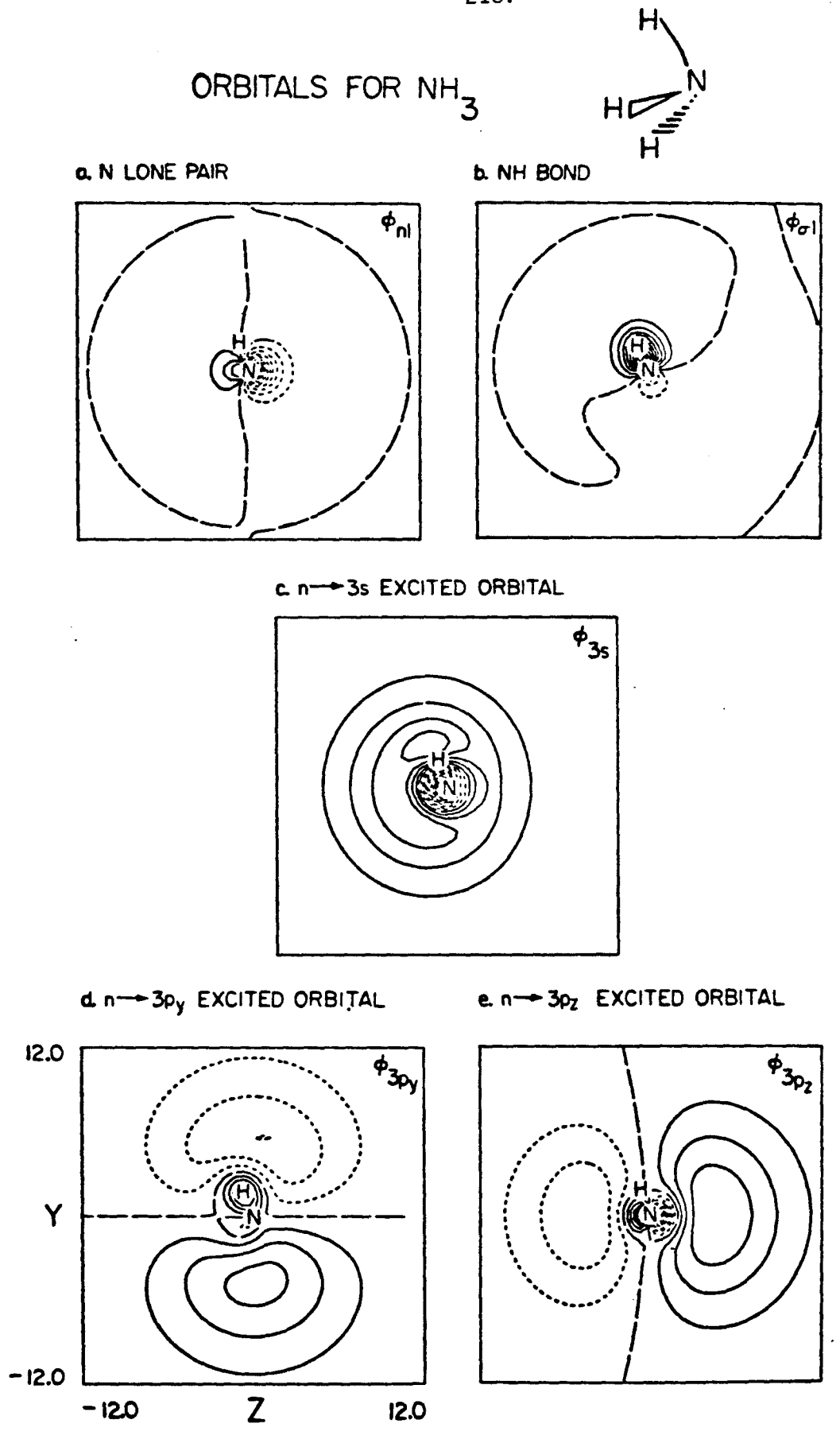
ORBITALS FOR NH_3
H
N
H
H
a. N LONE PAIR
b. NH BOND
ϕ_{nl}
$\phi_{\sigma 1}$
c. n→3s EXCITED ORBITAL
ϕ_{3s}
d. n→$3p_y$ EXCITED ORBITAL
e. n→$3p_z$ EXCITED ORBITAL
ϕ_{3p_y}
ϕ_{3p_z}
12.0
Y
-12.0
-12.0
Z
12.0

Figure 1.

Appendix II: Excited Electronic States of 1,3,5-Cycloheptatriene

EXCITED ELECTRONIC STATES OF 1,3,5-CYCLOHEPTATRIENE*

Robert P. FRUEHOLZ,† Ronald RIANDA, and Aron KUPPERMANN

Arthur Amos Noyes Laboratory of Chemical Physics,‡
California Institute of Technology,
Pasadena, California 91125, USA

(Received)

The electron-impact energy-loss spectrum of 1,3,5-cycloheptatriene has been measured at impact energies of 30, 50, and 75 eV, and scattering angles varying from 5° to 80°. Singlet→triplet transitions were observed at 3.05 eV and 3.95 eV. No evidence for the very weak transition at 2.1 eV previously reported on the basis of threshold electron-impact studies was found. Singlet→singlet transitions were observed at 4.85 eV and 6.40 eV in good agreement with the optical spectrum and semi-empirical calculations.

---

* This work was supported in part by a contract (No. EY-76-S-03-767) from the Department of Energy. Report Code: CALT-767P4-160.

† Work performed in partial fulfillment of the requirements for the Ph.D. degree in Chemistry at the California Institute of Technology.

‡ Contribution No. 5712.

The electronic spectrum of 1,3,5-cycloheptatriene (CHT) has been investigated using low-energy, variable-angle, electron-impact spectroscopy. This has been shown to be a powerful technique for studying both optically forbidden and optically allowed electronic transitions [1]. The excitation energies and band shapes of the optically forbidden singlet – triplet transitions obtained are of particular interest since CHT was found to improve dye-laser performance (e.g., 7-diethyl-amino-4-methyl-coumarin, brilliant sulphaflavine, and kiton red) via what is believed to be quenching of the lowest triplet state [2] of the dye. Marling et al. [2] have proposed that CHT quenches the lowest dye triplet state via a collisional process in which CHT in its lowest triplet state (resulting from intersystem crossing with the excited singlet CHT state populated by the flash from the UV lamp) interacts with a dye molecule also in its lowest triplet state yielding a ground state dye molecule and by spin and energy conservation a CHT molecule in an excited singlet state.

The electronic spectrum of CHT has been studied previously by Knoop et al. [3] using the threshold-electron-impact technique. The excited states of CHT have also been studied theoretically by Knoop et al. [3] and by Van Catledge and Allinger [4] who investigated only the singlet excited states. Using electron diffraction techniques, Traetteberg [5] has determined the structure of CHT in the gas phase and found that it possesses C_s symmetry.

In the present experiments, the electron-impact spectrum of CHT in the energy loss range 0 – 15 eV was studied at impact energies of 30 eV, 50 eV and 75 eV, and scattering angles from 5° to 80°. Sample pressures in the scattering chamber were typically 4 mTorr, as indicated by an uncalibrated Schulz-Phelps ionization gauge, while the electron current incident into the scattering chamber was approximately 60 nA. The energy resolution, as measured by the full width at half maximum (fwhm) of the elastically scattered peak, was set electron-optically at 100 meV in general, while some spectra were obtained with a fwhm of 70 meV. The CHT sample was obtained from the Aldrich Chemical Company Inc. with a stated purity of 97% and was subjected to several liquid nitrogen freeze-pump-thaw cycles before use.

Figure 1 shows the low energy-loss part of the electron impact spectrum of CHT at an impact energy of 30 eV and scattering angles of 30° and 80°. The figure indicates the presence of at least four transitions having maximum intensities at 3.05 eV, 3.95 eV, 4.85 eV, and 6.40 eV. In figs. 2 and 3 we display the corresponding differential cross sections (DCS's) at impact energies of 50 eV and 30 eV. These DCS's were obtained by a method described previously [6].

The most intense feature in the energy -loss region shown in fig. 1 has a maximum intensity at 6.40 eV and an apparent inflection at 6.2 eV. The optical spectrum [7] of CHT in heptane has an absorption maximum (ϵ = 17,800 $\ell\,\mathrm{mole}^{-1}\,\mathrm{cm}^{-1}$) at 6.21 eV. In the threshold electron-impact spectrum of Knoop et al. [3] this transition is observed at 6.25 eV. The DCS's of this transition at 50 eV and 30 eV decrease by factors of 90 and 68, respectively, as the scattering angle varies

from 10° to 80°. These sharply forward peaked differential cross sections are characteristic of a fully allowed singlet – singlet transition. Van Catledge and Allinger's [4] semi-empirical calculations predict a $^1\pi - {}^1\pi^*$ transition occurring at 6.60 eV. We assign the transition occurring at 6.40 eV to a singlet – singlet, $\pi - \pi^*$, excitation and designate it $S_{6.4}$.

At 4.85 eV we observe a transition which is weaker than that at 6.40 eV. This excitation energy is in excellent agreement with Van Catledge and Allinger's [4] calculated result of 4.84 eV for a $\pi - \pi^*$, singlet – singlet transition. For this transition the differential cross sections are again sharply forward-peaked, decreasing over the angular range 10° to 80° by factors of about 50 at both 50 eV and 30 eV impact energies. This angular behavior is consistent with a fully-allowed singlet – singlet excitation. In the optical spectrum [7], the absorption maximum for this transition occurs at 4.75 eV with ϵ = 3100 ℓ mole^{-1}cm^{-1}. The excitation is also observed in the threshold electron-impact spectrum at 4.60 eV. This transition is designated $S_{4.85}$. The fact that both this and the 6.40 eV singlet – singlet excitations display DCS's typical of fully-allowed transitions is consistent with CHT's belonging to the C_s point group for which all electronic transitions are symmetry allowed [8].

At excitation energies below 4.85 eV, we observe two additional transitions, with intensity maxima at 3.05 eV and 3.95 eV, which are designated $T_{3.05}$ and $T_{3.95}$. As can be seen from figs. 2 and 3, the DCS's of these transitions are relatively independent of scattering angle, varying by less than a factor of two from their mean values in

the angular range of 20° to 80°. Moreover, at each scattering angle studied these transitions were relatively more intense (with respect to the feature at 6.40 eV) at 30 eV impact energy than at 50 eV impact energy. This behavior is characteristic of a spin-forbidden process [1] and allows the assignment of these transitions to singlet→triplet excitations.

Our agreement with the threshold electron-impact spectrum of Knoop et al. [3] is not particularly good. They observe transitions, which they assign as singlet→triplet, at 3.68, 3.89, and 4.25 eV and possibly a weak excitation at 2.1 eV. In our spectra we do not observe the additional transitions at 3.68 eV, or 4.25 eV. In addition, below the 3.05 eV feature, which has an apparent onset at 2.4 eV, we find no evidence for another singlet→triplet transition. In fig. 4 the 1.5 eV to 4.5 eV energy-loss region of the CHT spectrum is displayed. Due to the weakness of the scattered signal and the relatively high noise level, this spectrum was digitally smoothed. The data in a given channel were replaced by the average of the data in adjacent channels corresponding to an energy range of 0.2 eV centered about the particular channel [9]. We cannot entirely eliminate the possibility that there exists an extremely weak singlet→triplet transition with intensity maximum at 2.1 eV. However, such a transition, if it does indeed exist, must have an excitation function which not only rises sharply near threshold but which also drops off unusually rapidly with increasing impact energy. Our experience to date indicates that this is an unlikely possibility. As a result, we believe that the lowest-lying triplet state of CHT occurs with a maximum intensity at 3.05 eV

and has an apparent onset at 2.4 eV.

Figure 5 shows the electron-impact spectrum of CHT above 6 eV energy-loss, with the first IP occuring at 8.57 eV [10], indicated by an arrow. Above 6.4 eV but below the first IP, three reproducible transitions are observed occurring at 6.93, 7.23, and 8.48 eV. Due to the fact that we can see these features at all at the relatively high 75 eV impact energy and the low 5° scattering angle, they may be assigned as singlet – singlet excitations. They may be valence excitations or transitions to Rydberg orbitals. Above 8.57 eV several previously unobserved super-excited states are detected. Their excitation energies are summarized in table 1.

In summary, we have used the method of low-energy, variable-angle, electron-impact spectroscopy to investigate the excited states of CHT. Two singlet – triplet excitations were observed at 3.05 eV and 3.95 eV, while no evidence was found for a singlet – triplet transition at 2.1 eV. Singlet – singlet transitions were observed at 4.85 and 6.40 eV in good agreement with the optical spectrum [7] and semi-empirical calculations [4]. Several previously unobserved super-excited states were observed above the first IP.

Table 1

1,3,5-Cycloheptatriene excitation energies eV (± .05 eV)

Nature of Transition	Present Results
Singlet – triplet	3.05
" "	3.95
Singlet – singlet	4.85
Singlet – singlet (shoulder)	6.2
Singlet – singlet	6.40
" "	6.93
" "	7.23
" "	8.48
Singlet – singlet (super-excited)	9.23
" "	9.98
" "	10.62
" "	11.35
" "	11.90
" "	12.47
" "	13.17
" "	14.16

References

[1] A. Kuppermann, J. K. Rice and S. Trajmar, J. Phys. Chem. 72 (1968) 3894; S. Trajmar, J. K. Rice and A. Kuppermann, Adv. Chem. Phys. 18 (1970) 15.

[2] J. B. Marling, D. W. Gregg and L. Wood, Appl. Phys. Lett. 17 (1970) 527; J. B. Marling, Ph.D Thesis, University of California, Davis (1971).

[3] F. W. E. Knoop, J. Kistemaker and L. J. Oosterhoff, Chem. Phys. Lett. 3 (1969) 73.

[4] F. A. Van-Catledge and N. L. Allinger, J. Am. Chem. Soc. 91 (1969) 2582.

[5] M. Traetteberg, Acta Chem. Scand. 86 (1964) 4265.

[6] O. A. Mosher, W. M. Flicker and A. Kuppermann, J. Chem. Phys. 62 (1975) 2600.

[7] U.V. Atlas of Organic Compounds, Vol. 4 (Butterworth Chemie Verlag, London, 1966).

[8] F. A. Cotton, Chemical Applications of Group Theory, 2nd ed. (Wiley-Interscience, New York, 1971) pp. 102-104.

[9] The spectra shown in figs. 1 and 5 were smoothed to a much lesser extent and by a different technique, using 5 to 15 point least square quadratic or cubic polynomial fits to introduce a correction at the midpoint [10].

[10] A. Savitzky and M. J. E. Golay, Anal. Chem. 36 (1964) 1627.

[11] C. Batich, P. Bischof and E. Heilbronner, J. Electron Spectrosc. 1 (1972/73) 333.

FIGURE CAPTIONS

Fig. 1. Electron energy-loss spectrum of CHT at a scattering angle of (a) 30° and (b) 80°; 30 eV incident electron energy; 5×10^{-8} A incident beam current; 4 mTorr sample pressure reading from an uncalibrated Schulz-Phelps gauge; resolution approximately 0.10 eV (fwhm). The spikes in the spectra below 4 eV energy loss are due to instrumental noise.

Fig. 2. Differential cross sections of CHT as a function of scattering angle at an incident electron energy of 50 eV; for elastic scattering (+) and for excited states: $T_{3.05}$ (○), $T_{3.95}$ (◇), $S_{4.85}$ (□), and $S_{6.4}$ (△). The elastic DCS was multiplied by 0.1 before plotting. The letters T and S stand for triplet and singlet upper states, respectively, and the index in these symbols represents the corresponding transition energies in eV.

Fig. 3. Differential cross sections of CHT as a function of scattering angle at an incident electron energy of 30 eV. The symbols for each transition are the same as in fig. 2. The elastic DCS was multiplied by 0.1 before plotting.

Fig. 4. Electron energy-loss spectrum of CHT over the 1.5 to 4.5 eV energy-loss region for the same experimental conditions as in fig. 1(b).

Fig. 5. Electron energy-loss spectrum of CHT at a scattering angle of 5°, 75 eV incident electron energy; 7×10^{-8} A incident beam current; 4 mTorr sample pressure as measured by an uncalibrated Schulz-Phelps gauge.

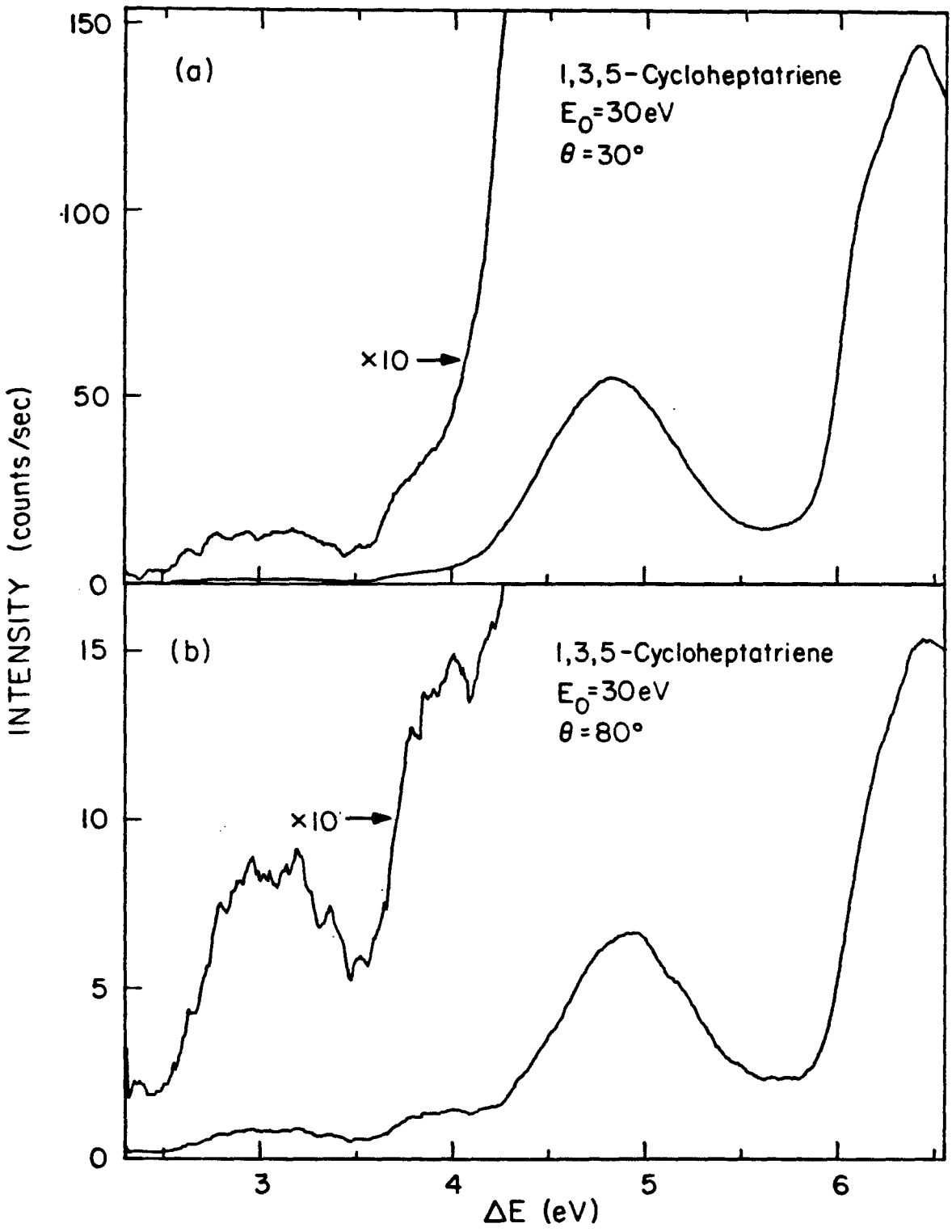
150
100
50
0
(a)
1,3,5-Cycloheptatriene
E_0=30eV
θ=30°
×10
15
10
5
0
(b)
1,3,5-Cycloheptatriene
E_0=30eV
θ=80°
×10
INTENSITY (counts/sec)
3
4
5
6
ΔE (eV)

Figure 1.

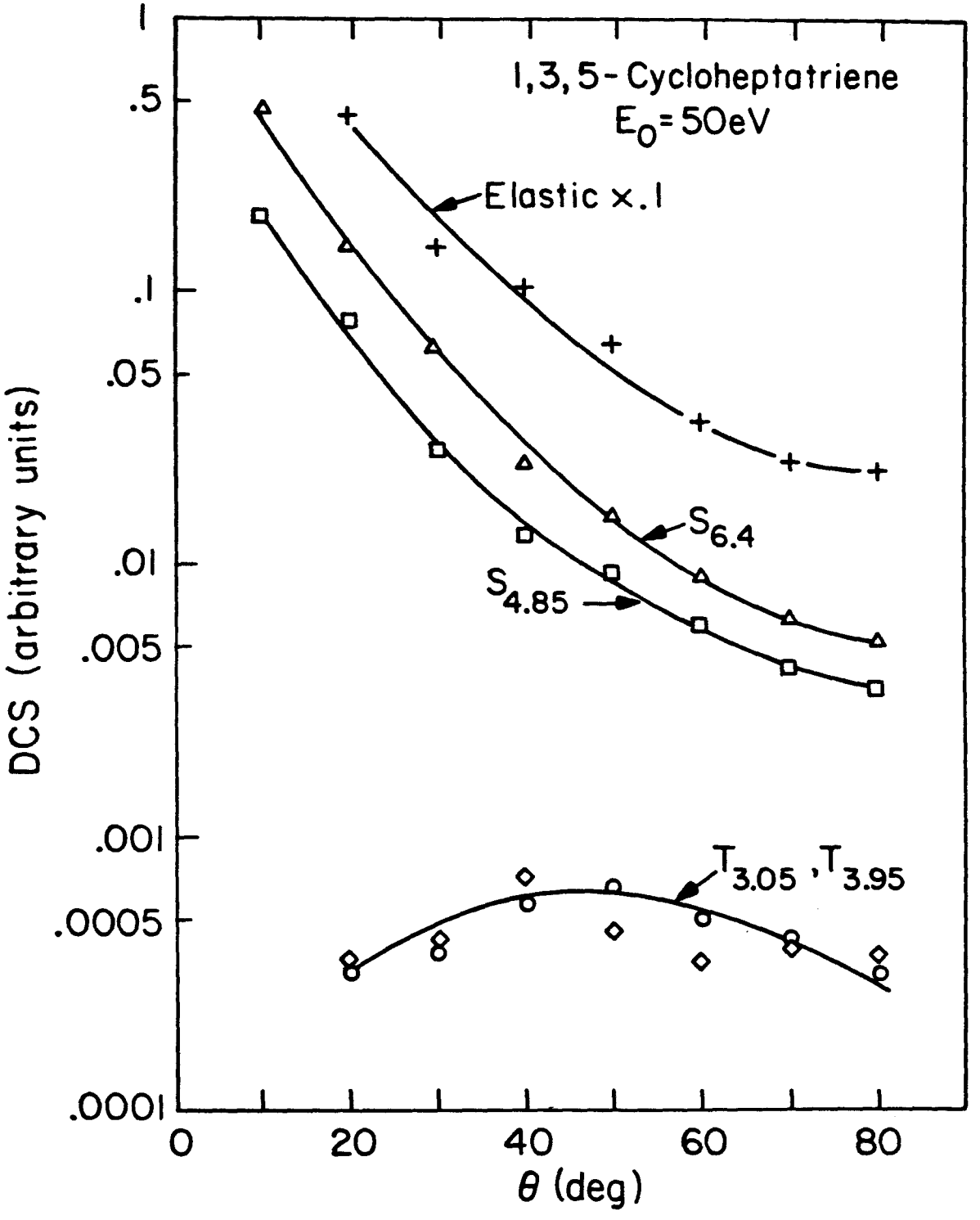
1,3,5-Cycloheptatriene
E_0=50eV
Elastic ×.1
$S_{6.4}$
$S_{4.85}$
$T_{3.05}$, $T_{3.95}$
DCS (arbitrary units)
θ (deg)
1
.5
.1
.05
.01
.005
.001
.0005
.0001
0
20
40
60
80

Figure 2.

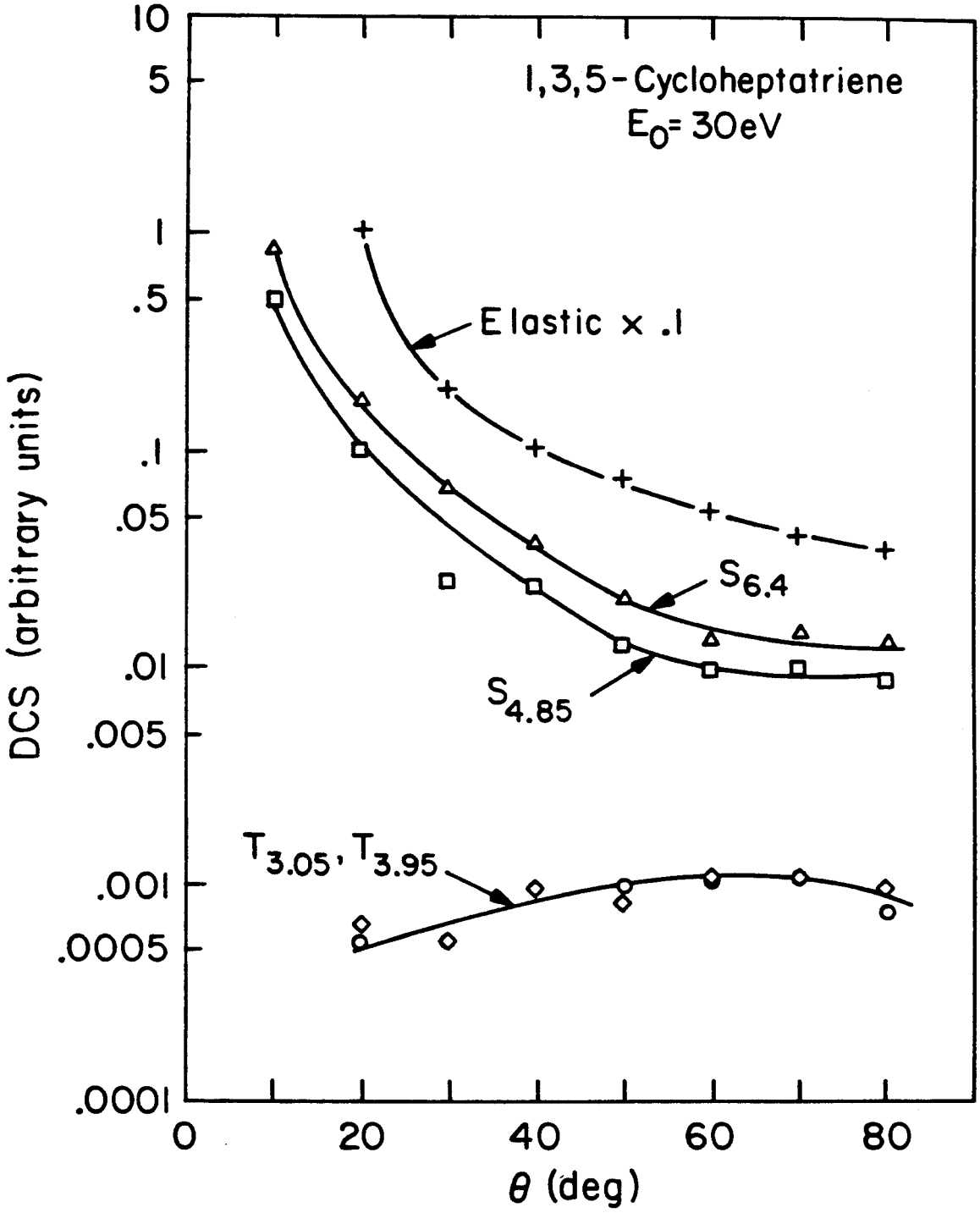
1,3,5-Cycloheptatriene
E_0= 30eV
Elastic x .1
$S_{6.4}$
$S_{4.85}$
$T_{3.05}$, $T_{3.95}$
DCS (arbitrary units)
θ (deg)
10
5
1
.5
.1
.05
.01
.005
.001
.0005
.0001
0
20
40
60
80

Figure 3.

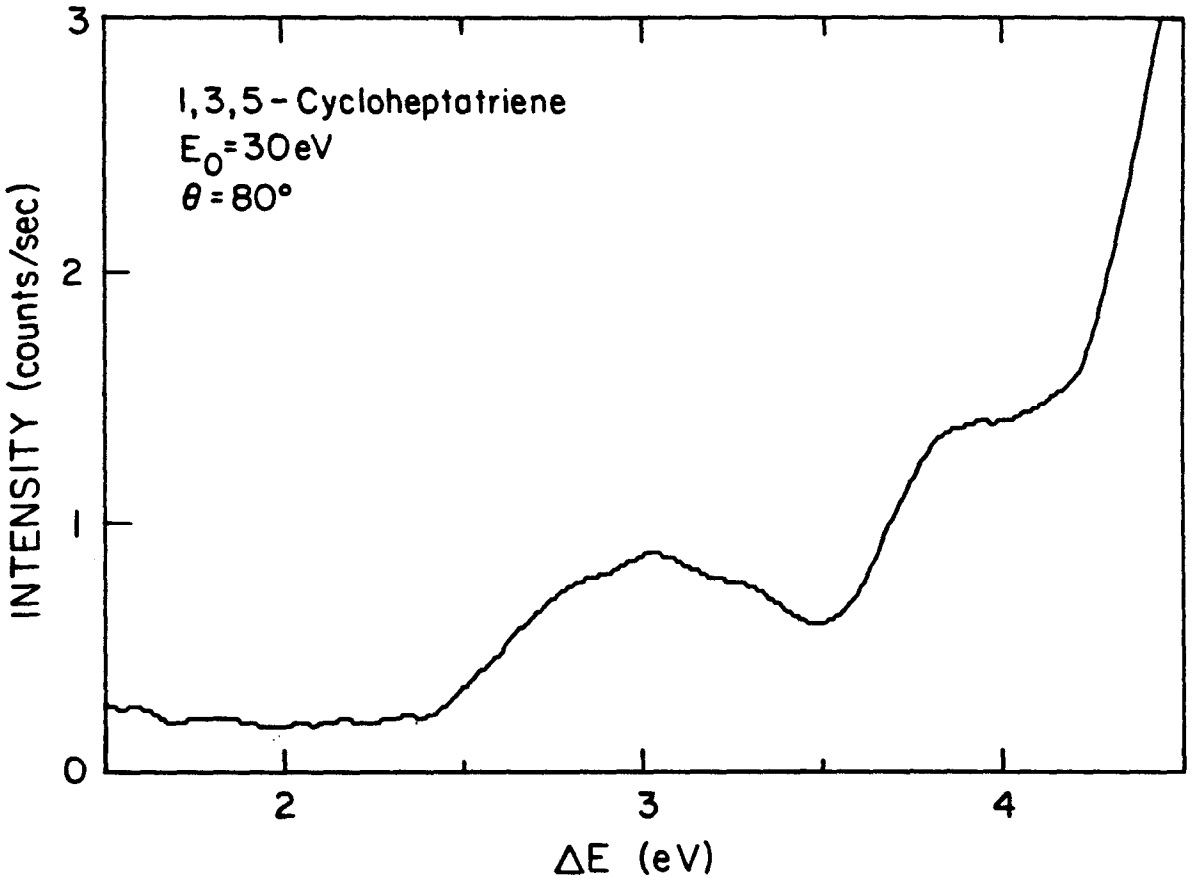
1,3,5 - Cycloheptatriene
E_0=30eV
θ=80°
INTENSITY (counts/sec)
ΔE (eV)
0
1
2
3
2
3
4

Figure 4.

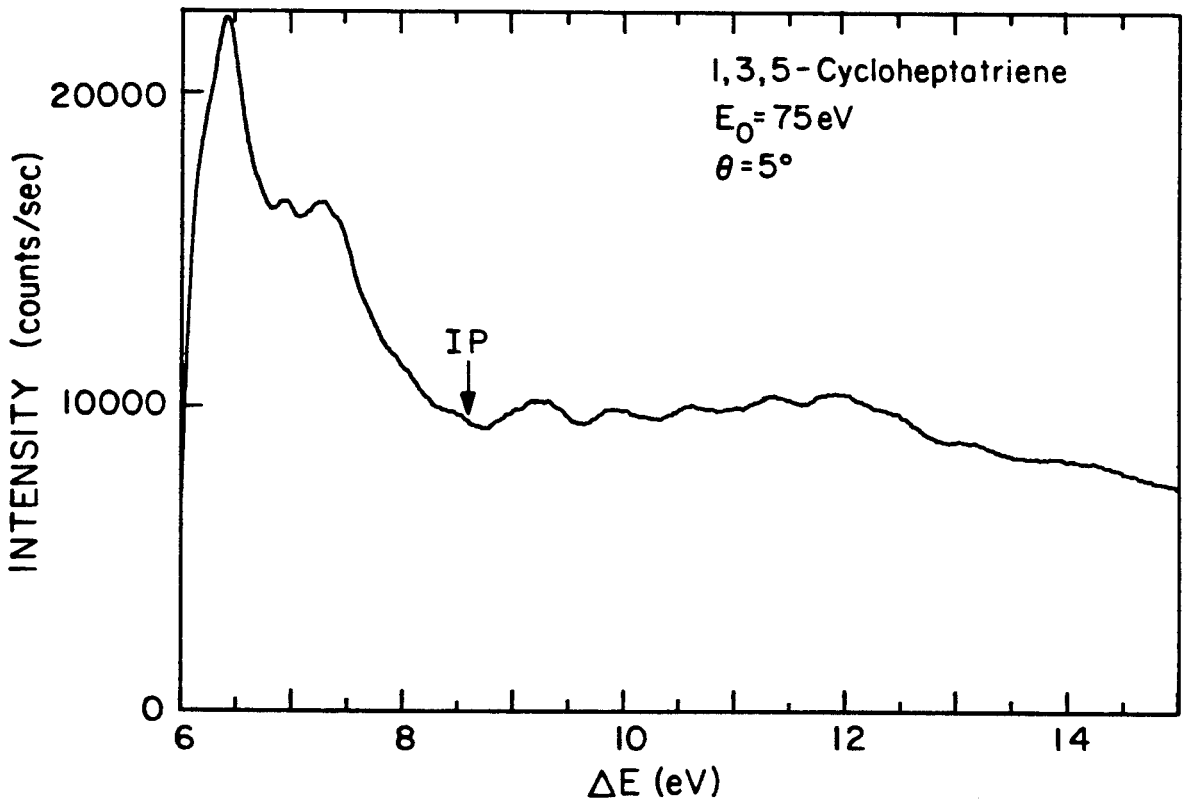
1,3,5-Cycloheptatriene
E_0=75eV
θ=5°
IP
INTENSITY (counts/sec)
20000
10000
0
6
8
10
12
14
ΔE (eV)

Figure 5.

Part II. Multiphoton Ionization Spectroscopy

4. Introduction

4. Introduction

When a very intense visible or ultraviolet photon field interacts with molecules, several processes may occur which are not observed under normal conditions of light intensity. Multiphoton processes, those in which two or more photons interact with a molecule simultaneously, become probable if the photon flux is high enough. Such multiphoton interactions may result in the excitation of the molecules to highly energetic electronic states. The molecule may lose this excess energy via ionization, decomposition, emission of a photon, or nonradiative transition. Any of these decay modes provides a means by which the existence of an excited state, produced by the multiphoton process, may be inferred. The wavelength dependence of the multiphoton transition intensity thus provides information about the electronic structure of the molecule. For many molecules the intense photon field will cause ionization of electronically excited states to be highly probable.[1] Therefore by monitoring the ionization current produced as a function of wavelength, an electronic spectrum may be produced. This technique is known as multiphoton ionization (MPI) spectroscopy.[2]

The recent availability of pulsed tunable dye lasers capable of producing focused beams of high intensity, on the order of 10^{25} photons cm^{-2} sec^{-1}, has resulted in the application of MPI spectroscopy to numerous molecular systems.[1-15] The technique has proven to be very powerful for both the detection and identification of electronically excited states of molecules.

MPI spectroscopy offers significant advantages over single photon

spectroscopy. The first is extremely sensitive detection of excited states. Ions or electrons produced may be very efficiently collected and detected so that virtually every ionization which occurs results in a signal at the detector. There are no geometrical constraints which limit the fraction of transitions detected as there are for fluorescence monitoring experiments. In addition, competitive nonradiative modes of decay may result in an immeasurable level of fluorescence. In such cases, an MPI signal may still be obtained. Background levels, due primarily to ionization of windows and to detector noise, are also quite low so experimental results are not dependent on the determination of a small difference between large signals as in absorption measurements. The technique is also readily adaptable to spectroscopic studies of gases at the low pressures typical of molecular beams.[8,13-15]

MPI spectroscopy has primarily been applied to the study of two-photon excited states.[1-14] In these cases, a state exists in the molecule of interest at an energy corresponding roughly to that of two photons. As the laser wavelength is scanned different rovibronic levels of this state come into resonance resulting in an enhancement of the ionization current relative to the nonresonant case. In general, one or two additional photons are required to ionize the two photon resonant state. However, if further transitions from this state are broad and structureless or if the probability of absorption of additional photons by molecules in this two-photon excited state is high, such that the two-photon step is rate limiting then the dependence of the ionization current on laser wavelength corresponds to the spectrum of the two-photon resonant intermediate state.[16-18]

The selection rules for absorption of even numbers of photons differ from those for absorption of odd numbers of photons.[19-21] Perhaps the most significant difference between absorption of odd and even numbers of photons is that in the case of molecules with centers of symmetry the selection rule is g↔g for even numbers of photons versus g↔u for odd numbers of photons. Thus, transitions which are forbidden to single photon spectroscopy may be allowed in two-photon spectroscopy and vice versa. Johnson took advantage of this fact and was able to identify a $^1E_{1g}$ state of benzene which had been previously remained hidden under an intense single photon allowed $^1B_{1u}$ state.[4,5]

In addition, McClain has shown that the intensity of a two-photon transition is dependent on the polarization of the laser beam (or beams) even in the case of randomly oriented molecules.[19-21] Thus by measuring the intensity of a two-photon transition using different combinations of beam polarizations, one may assign the symmetry of the excited state. No such behavior is observed in single photon spectroscopy. Under certain conditions the polarization dependence of a two-photon transition will be carried on into the multiphoton ionization through that intermediate state.[16-18] Therefore, measurement of the multiphoton ionization probability as a function of laser polarization may assist in assignment of the symmetry of the resonant intermediate state.

MPI spectroscopy has also proven to be useful for studying intermediate states produced by absorption of odd numbers of photons.[8,22,23] Since intense tunable laser radiation is obtained easily up to 217 nm, wavelengths to 72.3 nm are available for high resolution three-photon

spectroscopy. Selection rules for three-photon absorption are similar to those for single-photon absorption, however the use of longer wavelwngth radiation to probe high lying excited states generally eliminates difficulties related to window absorptions.[23] (Focusing conditions are adjusted such that laser intensities are much lower at the windows.) Recently, MPI spectroscopy was applied by this author to the detection of spin forbidden transitions of CS_2 as first photon resonances in a multiphoton ionization.[23] In this instance, as in the case of an initial two-photon process, the initial step is rate limiting and the singlet triplet absorption spectrum is generated as the laser wavelength is scanned. This technique promises to allow measurement of spin forbidden transitions with great sensitivity and high resolution.

The author initiated studies of the electronic spectroscopy of molecules using the MPI technique and was responsible for the development of the experimental apparatus used. The results of the studies on the $^3A_2$ state of CS_2 are included in section 7. In addition, preliminary results obtained for pXylene are also discussed. A detailed description of the apparatus used is contained in section 6. Section 5 contains a discussion of the theory of multiphoton ionization.

References

1. P. M. Johnson, Acc. Chem. Res. 13, 20 (1980).
2. C. B. Collins, B. W. Johnson, M. Y. Mirza, D. Popescu and I Popescu, Phys. Rev. A 10, 813 (1974).
3. P. M. Johnson, M. Berman and D. Zakheim, J. Chem. Phys. 62, 2500 (1975).
4. P. M. Johnson, J. Chem. Phys. 62, 4562 (1975).
5. P. M. Johnson, J. Chem. Phys. 64, 4143 (1976).
6. P. M. Johnson, J. Chem. Phys. 64, 4638 (1976).
7. K. Aron and P. M. Johnson, J. Chem. Phys. 67, 5099 (1977).
8. D. Zakheim and P. M. Johnson, J. Chem. Phys. 68, 3644 (1978).
9. G. Petty, C. Tai and F. W. Dalby, Phys. Rev. Lett. 34, 1207 (1975).
10. D. H. Parker, S. J. Sheng and M. A. El Sayed, J. Chem. Phys. 65, 5534 (1976).
11. D. H. Parker and P. Avouris, Chem. Phys. Lett. 53, 515 (1978).
12. D. H. Parker and P. Avouris, J. Chem. Phys. 71, 1241 (1979).
13. L. Zandee and R. B. Bernstein, J. Chem. Phys. 70, 2574 (1979).
14. L. Zandee and R. B. Bernstein, J. Chem. Phys. 71, 1359 (1979).
15. M. A. Duncan, T. G. Dietz and R. E. Smalley, Chem. Phys. 44, 415 (1979).
16. D. H. Parker, J. O. Berg and M. A. El Sayed, in: Advances in Laser Chemistry, ed. A. H. Zewail (Springer-Verlag, New York,1978) pp. 320-335.
17. J. O. Berg, D. H. Parker and M. A. El Sayed, J. Chem. Phys. 68, 5661 (1978).
18. B. A. Heath, G. J. Fisanick, M. B. Robin and T. S. Eichelberger IV, J. Chem. Phys. 72, 5991 (1980).

19. W. M. McClain, J. Chem. Phys. 55, 2789 (1971).

20. W. M. McClain, J. Chem. Phys. 58, 324 (1973).

21. W. M. McClain, Acc. Chem. Res. 7, 129 (1974).

22. V. S. Letokhov, Opt. and Laser Tech., 249 (1978).

23. R. Rianda, D. J. Moll and A. Kuppermann, Chem. Phys. Lett. 73, 469 (1980).

5. Theoretical

5. Theory of Multiphoton Ionization

5.1 Introduction

The theory of multiphoton ionization has received renewed attention in recent years due to advances in tunable, narrow bandwidth, high powered lasers which have led to a great deal of experimental work in this field. Most theoretical work prior to this time had utilized perturbation theory to calculate transition rates and paid little or no attention to the effects of resonant intermediate steps.[1-4] The more recent theoretical investigators have attempted to develop a formalism for treating resonant multiphoton ionization and have made significant strides in the development of a rigorous formalism for the description of the case in which only a single intermediate state is in resonance with the photon field.[5-12] No such formalism exists for treatment of multiphoton ionization when more than one resonant intermediate state exists although a kinetic approach has been developed which can aid in the interpretation of experimental results.[13]

This theoretical section contains three parts in addition to the introduction. The second subsection describes the treatment of non-resonant multiphoton ionization using a perturbation theory approach. A discussion of the theory of resonant multiphoton ionization for a single resonant intermediate state is contained in subsection 3. The remaining subsection contains a description of the kinetic approach to multiphoton ionization.

5.2 Nonresonant Multiphoton Ionization

The process of multiphoton ionization is a nonresonant one if no intermediate excited state exists with an excitation energy from the ground state close to the energy of one or more quanta of the external field. The formal perturbation theory for nonresonant multiphoton ionization has been presented by Bebb and Gold.[1] Their development is summarized here. The Hamiltonian for a bound electron interacting with the radiation field may be written in the interaction representation using quantum-electrodynamic formalism as

$$H = H_o + H_I$$

where

$$H_I = -e\underset{\sim}{\varepsilon}(\underset{\sim}{r},t)\cdot\underset{\sim}{r}$$

$$H_o = H_e + H_r$$

and

$$H_e = \frac{\underset{\sim}{p}^2}{2m} + V(\underset{\sim}{r})$$

$$H_r + \frac{1}{8\pi}\int (|\underset{\sim}{\varepsilon}|^2 + |\underset{\sim}{H}|^2)dV = \sum_\lambda n_\lambda \hbar w_\lambda$$

$\underset{\sim}{\varepsilon}(\underset{\sim}{r},t)$ is the transverse part of the electric field in the Coulomb gauge and n_λ is the occupation number for mode λ of the quantized radiation field.

The electric field operator may be defined in terms of the creation and annihilation operators, q_λ^+ and q_λ, respectively,

$$\underset{\sim}{\varepsilon} = \left(\frac{i}{c}\right)\sum_\lambda w_\lambda(q_\lambda \underset{\sim}{A}_\lambda - q_\lambda^* \underset{\sim}{A}_\lambda^*)$$

where the vector potential

$$\underset{\sim}{A}_\lambda = (4\pi c^2)^{\frac{1}{2}} e^{i\underset{\sim}{k}_\lambda \cdot \underset{\sim}{r}} \underset{\sim}{e}_\lambda \quad .$$

The raising and lowering operators, q_λ^* and q_λ are defined as

$$q_\lambda |n_\lambda> = [(\hbar/2w_\lambda)n_\lambda]^{\frac{1}{2}} |n_\lambda - 1>$$

$$q_\lambda^* |n_\lambda> = \left[\left(\frac{\hbar}{2w_\lambda}\right)(n_\lambda + 1)\right]^{\frac{1}{2}} |n_\lambda + 1> \quad .$$

The number operator H_r may now be defined in terms of these ladder operators,

$$H_r = \sum_\lambda [(2w_\lambda/\hbar) q_\lambda^* q_\lambda] \hbar w_\lambda$$

The theory of multiphoton ionization may then be developed by application of time dependent perturbation theory. In the interaction representation, the time evolution of the system arises from the interaction part of the Hamiltonian, H_I. If at time t = 0, the system is in an eigenstate $|g>$ of the unperturbed Hamiltonian, H_0 then at time t, the system is in state $|\psi(t)>$. The evolution operator $U_I(t)$ is postulated to exist such that $|\psi(t)> = U_I(t)|g>$. The probability that the system has undergone a transition from state $|g>$ to state $|n>$ of the unperturbed Hamiltonian in time t is

$$W_{n,g}(t) = |<n|U_I(t)|g>|^2 \quad .$$

The evolution operator also satisfies Schroedinger's equation, thus

$$U_I(t) = 1 + (ih)^{-1} \int H_I'(t')U_I(t')dt', \qquad (1)$$

where

$$H_I'(t) = e^{iH_o t/\hbar} H_I e^{-iH_o t/\hbar} .$$

By successively substituting the right-hand side of (1) back in for $U_I(t')$, Bebb and Gold obtained

$$U_I(t) = 1 + \sum_{n=1}^{\infty} U_I^{(n)}(t)$$

where

$$U_I^{(n)}(t) = (i\hbar)^{-n} \int_o^t dt_n \int^{t_n} dt_{n-1} \cdots \int^{t_2} dt_1 H_I'(t_n) H_I'(t_{n-1}) \cdots H_I'(t_1)$$

$$= (i\hbar)^{-n} \int^t d^n t \; H_I'(t_n) H_I'(t_{n-1}) \cdots H_I'(t_1) \quad .$$

The Nth-order contribution to the transition rate between the ground state $|g\rangle$ and a final state $|f\rangle$ is given by the matrix element of $U_I^{(N)}(t)$

$$\langle f|U_I^{(N)}(t)|g\rangle = (i\hbar)^{-N} \int_o^t d^N t \langle f|H_I'(t_N) H_I'(t_{N-1}) \cdots H_I'(t_2) H_I'(t_1)|g\rangle \; .$$

Following integration over time, the rate becomes

$$\langle f|U_I^{(N)}(t)|g\rangle = (-\hbar)^{-N} \frac{e^{iw_{fg}t} - 1}{w_{f,g}} M_{f,g}^{(N)}$$

where

$$M_{f,g}^{(N)} = \sum_{m_{N-1}} \sum_{m_{N-2}} \cdots \sum_{m_2} \sum_{m_1} \langle f|H_I|m_{N-1}\rangle \frac{\langle m_{N-1}|H_I|m_{N-2}\rangle}{w_{m_{N-1},g}} \; X$$

$$\frac{m_{N-2}|H_I|m_{N-3}\rangle}{w_{m_{N-2},g}} \; X \cdots X \; \frac{\langle m_1|H_I|g\rangle}{w_{m_1,g}} \quad ,$$

and $w_{k,l} = (E_k - E_l)/\hbar$ where E_k and E_l are energy eigenvalues of H_o. The sums over m_v are extended over the complete set of eigenstates of H_o.

The formulas presented thus far are applicable to a large class of multiphoton effects. For the case of multiphoton ionization, the first-order contribution to the transition rate involves only the annihilation of photons from the radiation field. Therefore, for the case of a monochromatic radiation field of occupation number n the interaction Hamiltonian H_I is given by

$$H_I = -e\underset{\sim}{\varepsilon}\cdot\underset{\sim}{r} = -iewq(4\pi)^{\frac{1}{2}} e^{i\underset{\sim}{k}\cdot\underset{\sim}{r}} \underset{\sim}{e}\cdot\underset{\sim}{r} \quad .$$

The ground state $|q\rangle$ may be denoted $|a_q;n\rangle$ where a_q specifies the molecule quantum numbers and n specifies the occupation number for the monochromatic radiation field. The states $|m_v\rangle$ are similarly represented as $|a_v;n'\rangle$. Since for each successive matrix element the occupation number of the radiation field is decreased by one (i.e. one photon has been absorbed), the N^{th}-order matrix element becomes

$$M^{(N)}_{f,g} = [-ie(2\pi\hbar w)^{\frac{1}{2}}]^N\{[n - (N - 1)][n - (N - 2)]X \cdots X (n - 1)n\}^{\frac{1}{2}}K^{(N)}_{a_f,a_g}$$

where

$$K_{a_f,a_g} = \sum_{a_{N-1}} \sum_{a_{N-2}} \cdots \sum_{a_1} \langle a_f|R|a_{N-1}\rangle \frac{\langle a_{N-1}|R|a_{N-2}\rangle}{w_{a_{N-1},a_g} - (N - 1)w} X\cdots$$

$$X \frac{\langle a_1|R|a_g\rangle}{w_{a_1,a_g} - w}$$

$$R = \underset{\sim}{e}\cdot\underset{\sim}{r}\, e^{i\underset{\sim}{k}\cdot\underset{\sim}{r}} \quad .$$

The transition probability $W^{(N)}_{f,g}(t)$ is therefore given by

$$W^{(N)}_{f,g}(t) = \left[2\pi w n \frac{e^2}{\hbar}\right]^N |e^{iw_{f,g}t} - 1 \big/ w_{f,g}|^2 |K^{(N)}_{a_f,a_g}|^2$$

The depletion of the radiation field has been neglected in obtaining this last equation since for the case of a laser source, the occupation number is typically greater than 10^{15}. Replacing n by F/c where F is the photon flux, $|(e^{iw_{f,g}t} - 1)/w_{f,g}|^2$ by its asymptotic value $2\pi t\delta(w_{f,g})$ since we are interested in times which are long with respect to $\frac{1}{w_{f,g}}$, and $\frac{e^2}{\hbar c}$, the fine structure constant, by α we obtain the transition rate per atom

$$\left(\frac{d}{dt}\right) W^{(N)}_{f,g}(t) = [2\pi\alpha w F]^N \, 2\pi\delta(w_{f,g}) |K^{(N)}_{a_f,a_g}|^2 \quad . \tag{2}$$

This equation is applicable for transitions between discrete states. Note that the dependence of the transition probability on the photon flux is given by the first term of this expression.

When considering transitions to continuum states, as is the case for multiphoton ionization, it is necessary to include a group of states within an energy range $d\varepsilon_{f,g}$ instead of a single discrete level. After integrating (2) over $\varepsilon_{f,g}$, Bebb and Gold[7] obtain

$$w^{(N)}_{f,g} = 2\pi\hbar(2\pi\alpha F w)^N |K^{(N)}_{a_f,a_g}|^2 \rho(\varepsilon) \quad . \tag{3}$$

The density of states $\rho(\varepsilon)$ is given by

$$\rho(\varepsilon) = \frac{(m/\hbar^2)k}{(2\pi)^3} \, d\Omega_k$$

where k is the wave number of the electron and the energy is defined as

$$\varepsilon_{f,g} = \varepsilon_I - Nhw + \hbar^2 k^2/2m = 0$$

where ε_I is the ionization energy. Substituting this density of states into (3) gives

$$W^{(N)}_{f,g}(\theta_k,\phi_k) = \frac{mk}{(2\pi)^2\hbar} (2\pi\alpha Fw)^N \, |K_{a_f,a_g}|^2 \, k \quad .$$

The angular distribution of the emitted electrons is thus given by this equation. The total transition rate per atom may be obtained by integrating over solid angle $d\Omega_k$.

The preceding discussion of multiphoton ionization has omitted consideration of damping and level shifts. Phenomenological damping may be included in the perturbation theory of multiphoton ionization following the work of Heitler[14] and Weisskopf and Wigner[15] by introducting a damping constant γ_a related to the combined widths of the initial and final states such that the time dependence is given by

$$|\psi(t)> = e^{-iw_a t - \gamma_a t/2} |a> \, .$$

The addition of the damping term introduces the term $\frac{i\gamma}{2}$ into the energy denominators of all previous equations. A more detailed treatment utilizing a complex flux-dependent damping parameter which would

account for both shifts and broadenings of resonance lines was suggested by Bebb and Gold, but was not included in their work.

Bebb and Gold[1] have applied their perturbation treatment to the multiphoton ionization of hydrogen and the rare gases He, Ne, Ar, Kr and Xe. Their calculated results for Xe are in excellent agreement with the experimentally measured cross-section obtained by Voronov and Delone.[16] Cremaschi, Johnson and Whitten[17] have also applied this technique to the resonant four photon ionization (resonance occurs on absorption of either the second or third photon) of NO obtaining relative cross-sections which were in good agreement with experimental measurements for most resonant states. Deviations of their calculated relative cross-sections from experimental values are attributed to inadequacy of the basis set used. The results of Cremaschi et al. are particularly interesting considering the fact that the theory presented by Bebb and Gold is not expected to describe adequately the resonant process.

5.3 Resonant Multiphoton Ionization

The process of multiphoton ionization is a resonant one if there exists an intermediate state with energy E_p such that

$$E_p = E_g + nh\nu$$

where E_g is the energy of the ground state, ν is the frequency of the photon field and n is an integer. Beers and Armstrong[6] have developed the effective Hamiltonian method to describe the case of resonant multiphoton ionization through a single resonant intermediate state. Their

application of this technique to a resonant two photon ionization will be described here.

The resolvant method is used to evaluate the probability that the atom or molecule originally in the ground state $|g\rangle$ at time $t = 0$ is in some continuum eigenstate at a later time having absorbed two photons. The following assumptions are made:

(a) The photon field is monochromatic and single mode.

(b) The nonresonant two photon ionization is treated by using an effective Hamiltonian $H_{eff}^{(2)}$ which connects the ground state directly to the continuum of ionized states $|\alpha E\rangle$ of energy E where α is a label which removes degeneracies. It is assumed that the matrix elements of $H_{eff}^{(2)}$ are given by second-order perturbation theory where the sum over intermediate states excludes the resonant intermediate state.

(c) Integrations over continuum states are evaluated at roughly the resonant energy, $E_g + n\omega$.

(d) Spontaneous decay of the intermediate resonant state $|a\rangle$ is ignored.

(e) Only a single continuum is considered.

(f) The rotating wave approximation is made.

The equation for the resolvant, G, takes the form

$$(Z - H_A - H_F - H_{AF} - H_{eff}^{(2)})G(Z) = 1$$

where H_A is the atomic Hamiltonian, H_F is the photon field Hamiltonian, and H_{AF} is the interaction Hamiltonian. The resolvant, G(Z), is a

a function of the complex variable Z whose singularities are the eigenvalues of the Hamiltonian.[18] The states $|g,nw\rangle$, $|a,(n-1)w\rangle$, and $|\alpha E,(n-2)w\rangle$ are coupled to each other via this relation. Taking matrix elements with respect to these states yields a set of equations which may be solved. Beers and Armstrong found that

$$G_{gg} \equiv \langle g,nw|G|g,nw\rangle$$

is given by

$$G_{gg}(Z) = \frac{Z - E_a^1 + \frac{1}{2} i\gamma_a}{(Z - Z_+)(Z - Z_-)}$$

where

$$Z_\pm = \frac{1}{2}\{E_a' + E_g' - \frac{1}{2} i\Gamma \pm [(\delta - \frac{1}{2} i\rho)^2 + \gamma_a\gamma_g(q - i)^2]^{\frac{1}{2}}\}$$

and the ionization decay widths of the $|g\rangle$ and $|a\rangle$ states γ_g and γ_a are given by

$$\gamma_g = 2\pi|\langle g,nw|H_{eff}^{(2)}|\alpha E,(n-2)w\rangle|^2 \quad ,$$

$$\gamma_a = 2\pi|\langle a,(n-1)w|H_{AF}|\alpha E,(n-2)w\rangle|^2 \quad .$$

In the equations $E \simeq E_g + 2w$, $\Gamma = \gamma_a + \gamma_g$, $\rho = \gamma_g - \gamma_a$, and E_a' and E_g', the shifted energies of states $|a\rangle$ and $|g\rangle$, respectively, are given by

$$E_g' = E_g + nw + \Delta E_g$$

$$E_a' = E_a + (n-1)w + \Delta E_a$$

where

$$\Delta E_g = P \int \frac{|\langle g,nw|H^{(2)}_{eff}|\alpha E,(n-2)w\rangle|^2 dE}{Z - E - (n-2)w}$$

$$\Delta E_a = P \int \frac{|\langle a,(n-1)w|H_{AF}|\alpha E,(n-2)w\rangle|^2 dE}{Z - E - (n-2)w}$$

the principal part integrals being evaluated at $Z = E_g + nw$. In addition, the quantity q given by

$$q = \frac{\langle g,nw|\left(H_{AF} + P\int dE \frac{H^{(2)}_{eff}|\alpha E_1(n-2)w\rangle\langle\alpha E\ (n_1-2)w|H_{AF}}{Z - E - (n-2)w}\right)|\ a,(n-1)w\rangle}{\pi\langle g,nw|H^{(2)}_{eff}|\alpha E_1(n-2)w\rangle\langle\alpha E_1(n-2)w|H_{AF}|a,(n-1)w\rangle}$$

$$= \frac{2H_{ga}}{(\gamma_a\gamma_g)^{\frac{1}{2}}}$$

The remaining variable δ is defined by

$$\delta = E'_g - E'_a \ .$$

In the same terms G_{ag} is given by

$$G_{ag} = \frac{(\gamma_a\gamma_g)^{\frac{1}{2}}(q - i)}{2(Z - Z_+)(Z - Z_-)} \ .$$

The evolution operator U(t) is the Fourier transform of G(Z). The probability of ionization P(t) is

$$P(t) = 1 - |U_{gg}(t)|^2 - |U_{ag}(t)|^2$$

$$= 1 - \left\{\left(\frac{w^2}{4} + \frac{\Gamma^2}{16} + \frac{a^2}{4} + \frac{\delta a\cos\phi}{2} - \frac{\rho a\sin\phi}{4}\right)e^{-\Gamma_1 t}\right.$$

$$+\left(\frac{w^2}{4}+\frac{\Gamma^2}{16}+\frac{a^2}{4}-\frac{\delta a\cos\phi}{2}+\frac{\rho a\sin\phi}{4}\right)e^{-\Gamma_2 t}$$

$$-2\left[\frac{w^2}{2}+\frac{\Gamma^2}{16}-\frac{a^2}{4}\cos(ta\cos\phi)\right.$$

$$\left.+\left(\frac{\delta a\sin\phi}{2}+\frac{a\rho\cos\phi}{4}\right)\sin(ta\cos\phi)\right]e^{-\Gamma t/2}\Bigg\}\ a^2 \qquad (1)$$

where

$$W=(\delta^2+q^2\gamma_a\gamma_g)^{\frac{1}{2}}$$

$$a^2=\left[\left(w^2-\frac{\Gamma^2}{4}\right)^2+(\delta\rho+2q\gamma_a\gamma_g)^2\right]^{\frac{1}{2}}$$

$$\tan 2\phi=-(\delta\rho+2q\gamma_a\gamma_g)/\left(w^2-\frac{\Gamma^2}{4}\right)$$

$$\Gamma_1=\frac{\Gamma}{2}-a\sin\phi$$

$$\Gamma_2=\frac{\Gamma}{2}+a\sin\phi \quad .$$

This expression is exact to within the limits of the initial assumptions The result may be generalized to any m + n photon ionization having an m-photon resonant state by replacing H_{AF} by the m- and n-photon effective Hamiltonians.

The expression for P(t) is applicable for all combinations of molecular parameters and photon fluxes and no simpler expression will describe the ionization process adequately in all cases. However, simpler expressions may be obtained which are applicable over limited ranges of parameters and fluxes. These simpler expressions may provide a more useful form for qualitative understanding of power dependence and cross sections observed.

The first three simplifications all require that $\gamma_g << \gamma_a$ (i.e. the ionization decay width of the intermediate state is much greater than that of the ground state). For photon fluxes used in a multiphoton ionization experiments this is generally the case.

Case 1: $2|H_{ga}| << \frac{1}{2}\gamma_a$.

In this region, the probability for ionization from the intermediate state is much higher than the probability for excitation to the intermediate state from the ground state. Therefore, virtually all molecules which reach the intermediate state are immediately ionized. The expression for P(t) may be reduced to

$$P(t) = 1 - (1 + \alpha)e^{-\gamma_1 t}$$

where

$$\gamma_1 = \gamma_g \left(\frac{(2\delta + q\gamma_a)^2}{2\delta^2 + \gamma_a^2} \right)$$

and

$$\alpha = \frac{3|H_{ga}|^2\gamma_a^2}{4(\delta^2 + \frac{1}{4}\gamma_a^2)^2}$$

In the limit of long times, $t > \frac{3}{\gamma_a}$, this expression for P(t) is very nearly equal to that obtained using perturbation theory.

Case 2: $2|H_{ga}| >> \frac{1}{2}\gamma_a$, $2|H_{ga}| \gtrsim \delta$

In this case, the strong driving field can roughly equilibrate the

populations of the ground and intermediate states and ionization only perturbs this process. A simpler expression for P(t) may now be obtained,

$$P(t) = 1 - e^{-\gamma_2 t}$$

where

$$\gamma_2 = \frac{\gamma_g}{2}\left(1 + \frac{(\delta + \gamma_a q)^2}{\delta^2 + 4|H_{ga}|^2}\right)$$

This expression has also been obtained previously using perturbation theory. In the limit of long time, this simpler expression for P(t) is nearly equivalent to Eq. (1).

Case 3: $2|H_{ag}| \sim \frac{1}{2}\gamma_a$

In this region ionization and stimulated emission from the intermediate state are equally probable. There are now no approximations to Eq. (1) which are appropriate on any time scale.

A fourth case is possible if $\gamma_a \approx \gamma_g$. In this case, there are combinations of H_{ag}, γ_a, γ_g and δ for which

$$P(t = \infty) = \frac{\gamma_g}{\gamma_g + \gamma_a} \quad .$$

This implies that the transition probability is less than unity in the limit of infinite time of interaction.

No perturbation treatment or simplification describes this region

adequately and the full expression for P(t) must be used. Another consequence of $\gamma_a \simeq \gamma_g$ is that the effect of a resonant process would be unobservable in an experiment which did not run to saturation ($t = 2 - 3(1/\gamma_g)$).

The remaining case $\gamma_g >> \gamma_a$ yields the expression for P(t)

$$P(t) = 1 - e^{-\gamma_3 t}$$

where

$$\gamma_3 = \gamma_g\left[1 + \gamma_a \frac{4\delta q - \gamma_g(q^2 - 1)}{4\delta^2 + \gamma_g^2}\right] = \gamma_g$$

In this case the ionization would be dominated by the direct process and little or no effect of the resonance would be observed.

5.4 Rate Equation Approach to Resonant Multiphoton Ionization

A model for resonant multiphoton ionization has been developed recently which utilizes kinetic rate equations to describe the ionization process.[13] This approach provides a qualitative description of MPI which may be extended to multiply resonant MPI (i.e. when more than one intermediate state is in resonance with the photon field).

As an example of this approach, consider the three photon ionization of a molecule for which there exists a two photon resonant intermediate state. The ground state, the resonant intermediate state and the ionization continuum are denoted by g, r and f, respectively. The intermediate state is populated by the two photon absorption process $\sigma_2 I^2$ and is depopulated by a single photon ionization process $\sigma_1 I$ and by a nonradiative decay at rate γ, assuming a monochromatic radiation field with a linewidth which is greater than the resonance width. In addition, no repopulation of the ground state is included. The time dependence of the system is found from

$$\frac{dN_g}{dt} = - N_g(t)\sigma_2 I^2$$

$$\frac{dN_r}{dt} = N_g(t)\sigma_2 I^2 - N_r(t)(\sigma, I + \gamma)$$

$$\frac{dN_f}{dt} = N_r(t)\sigma_1 I$$

where the populations of the ground, resonant intermediate and ion states are given by N_g, N_r and N_f, respectively. Approximating the laser pulse

as a step function of height I between 0 and 10 nsec and zero otherwise one obtains

$$N_r(t) = \frac{N'_g \sigma_2 I^2}{\sigma_1 I + \gamma - \sigma_2 I^2} \left(e^{-\sigma_2 I^2 t} - e^{-(\sigma_1 I + \gamma)t} \right) \qquad (1)$$

using as initial conditions $N_r = 0$ and $N_g = N'_g$ at $t = 0$. The resulting ion current is

$$\frac{dN_f}{dt} = \frac{N'_g \sigma_1 \sigma_2 I^3}{\sigma_1 I + \gamma - \sigma_2 I^2} \left(e^{-\sigma_2 I^2 t} - e^{-(\sigma_1 I + \gamma)t} \right) . \qquad (2)$$

For typical values of cross-sections, nonradiative decay rate and photon flux of $\sigma_1 = 10^{-18}$ cm^2, $\sigma_2 = 10^{49}$ cm^4 sec,[13] $\gamma = 10^{10}$ sec^{-1} and $I = 10^{28}$ cm^{-2} sec^{-1} (5mj in a 10 nsec pulse at 400 nm). The ion current is seen to rise rapidly to a maximum value and decays very slowly as the ground state is depleted. Similarly, for these typical parameters the population of the intermediate state is shown to increase rapidly and remain fairly constant for the duration of the pulse, suggesting that the steady state approximation for $N_2(t)$ may be used. This approximation yields the following expression for the ion current $\frac{dN_f}{dt}$

$$\frac{dN_f}{dt} = \frac{N'_g \sigma_1 \sigma_2 I^3}{\sigma_1 I + \gamma} . \qquad (3)$$

The validity of expression (3) is limited to systems for which the two photon cross-sections are not so large that depletion of the ground state population results in the decay of the intermediate state population.

If the ionization cross-section is smaller than 10^{-15} cm^2 and $\gamma < \sigma_1 I$ then a slow rise of N_r results and the steady state approximation is not valid. However, radiationless decay rates for such highly excited states as the resonant intermediate state will still result due to nonradiative decay.

Under conditions where a steady state approximation for the population of the resonant intermediate state is valid (i.e. when the two photon absorption process is rate limiting) the ionization rate may be given by the rate of two photon excitation, $N_g^1 \sigma_2 I^2$, times the fraction of molecules which are ionized from the intermediate state, $\sigma_1 I/(\sigma_1 I + \gamma)$. Thus, if the fraction of molecules which are ionized varies slowly as a function of wavelength relative to the variation of the two photon absorption with wavelength, then measurement of the ion current yields the two photon absorption spectrum. Information as to the symmetry of the resonant intermediate state may also be obtained through the use of polarized light for the MPI measurements under such conditions. For single photon absorption there is no dependence on photon polarization for randomly oriented molecules. This is not the case for simultaneous absorption of multple photons. In the case of multiple photon absorption a polarization dependence remains for each symmetry type.[13,19,20] Thus, by measurements of the ionization rate using differently polarized photons, information regarding the symmetry of the intermediate state may be obtained providing that either $\sigma_1 I >> \gamma$ such that equation (3) reduces to

$$\frac{dN_f}{dt} \approx N_g^1 \sigma_2 I^2$$

or the rotational relaxation rate is faster than the ionization rate. Heath et al. have shown recently that these conditions are not always met and that useful polarization ratios may be obtained only at very high added gas pressures and low laser fluxes.[21]

This kinetic approach may also be applied to similar multiphoton ionization processes for which there exists a rate limiting first step followed by much more probable succeeding steps leading finally to ionization. However, the validity of polarization ratios obtained if the rate limiting step is a two photon process, for example, will be much more limited.

References

1. H. B. Bebb and A. Gold, Phys. Rev. 143, 1 (1966).
2. W. L. Peticolas, Ann. Rev. Phys. Chem. 18, 233 (1967).
3. P. Lambropoulos, Phys. Rev. Lett. 28, 585 (1972).
4. P. Lambropoulos, Phys. Rev. A 9, 1992 (1974).
5. L. Armstrong, Jr., B. L. Beers and S. Feneuille, Phys. Rev. A 12, 1903 (1975).
6. B. L. Beers and L. Armstrong, Jr., Phys. Rev. A 12, 2447 (1975).
7. Y. Gontier, N. K. Rahman and M. Trahin, Phys. Rev. A 14, 2109 (1976).
8. M. Crance and S. Feneuille, Phys. Rev. A 16, 1587 (1977).
9. A. Valli and S. Stenholm, Phys. Lett. 64A, 447 (1978).
10. B. Ritchie, Phys. Rev. A 17, 659 (1978).
11. B. Ritchie, Phys. Rev. A 20, 1734 (1979).
12. S. Stenholm, Contemp. Phys. 20, 37 (1979).
13. D. H. Parker, J. O. Berg and M. A. El-Sayed, Advances in Laser Chemistry, ed. A. H. Zewail (Springer-Verlag, New York, 1978) pp. 320-335.
14. W. Heitler, The Quantum Theory of Radiation (Oxford U.P., London, 1954).
15. V. F. Weisskopf and E. P. Wigner, Z. Physik 63, 54 (1930).
16. G. S. Voronov and N. B. Delone, Sov. Phys. JETP Lett. 1, 66 (1965).
17. P. Cremaschi, P. M. Johnson and J. L. Whitten, J. Chem. Phys. 69, 4341 (1978).
18. A. Messiah, Quantum Mechanics (John Wiley & Sons, Inc., New York, 1962) Vol II.

19. J. O. Berg, D. H. Parker and M. A. El-Sayed, J. Chem. Phys. 68, 5661 (1978).

20. W. M. McClain, J. Chem. Phys. 55, 2789 (1971).

21. B. A. Heath, G. J. Fisanick, M. B. Robin and T. S. Eichelberger IV, J. Chem. Phys. 72, 5991 (1980).

6. Experimental

6. Experimental

6.1 Introduction

The multiphoton ionization spectrometer used to obtain the results presented in this thesis is shown in Figure 1. The laser system used is the Molectron UV400/DL200 nitrogen laser pumped dye laser. A description of this system is contained in Subsection 2 of this experimental section. Subsection 3 contains a description of the detection apparatus, including detectors, preamplifiers, amplifiers and integrators. Subsections 4 and 5 describe the digital data acquisition system hardware and assembler coded software. The remaining section describes the FORTRAN coded data analysis programs I have written.

6.2 Description of the Laser System

All the multiphoton ionization spectra reported in this thesis were obtained using a superradiant nitrogen laser to transversely pump a tunable dye laser. This provides an intense monochromatic (bandwidth approximately 0.4 cm^{-1}) light source. The pump laser, Molectron model UV 400, is a pulsed molecular nitrogen second positive laser operating at 337.1 nm and producing a peak output power of approximately 450 kilowatts in a 10 nanosecond (nominal) pulse at pulse rates up to 100 pulses per second.[1] Direct electron impact excitation is utilized to overpopulate the upper laser level, the $C^3\pi_u$ state at 11.03 eV, relative to the lower laser level, the $B^3\pi_g$ state at 7.35 eV.[2,3] The radiative lifetime of the $C^3\pi_u$ and $B^3\pi_g$ levels are approximately 40 nanoseconds and 10 microseconds, respectively.[2] Therefore, in order to achieve a population inversion, it

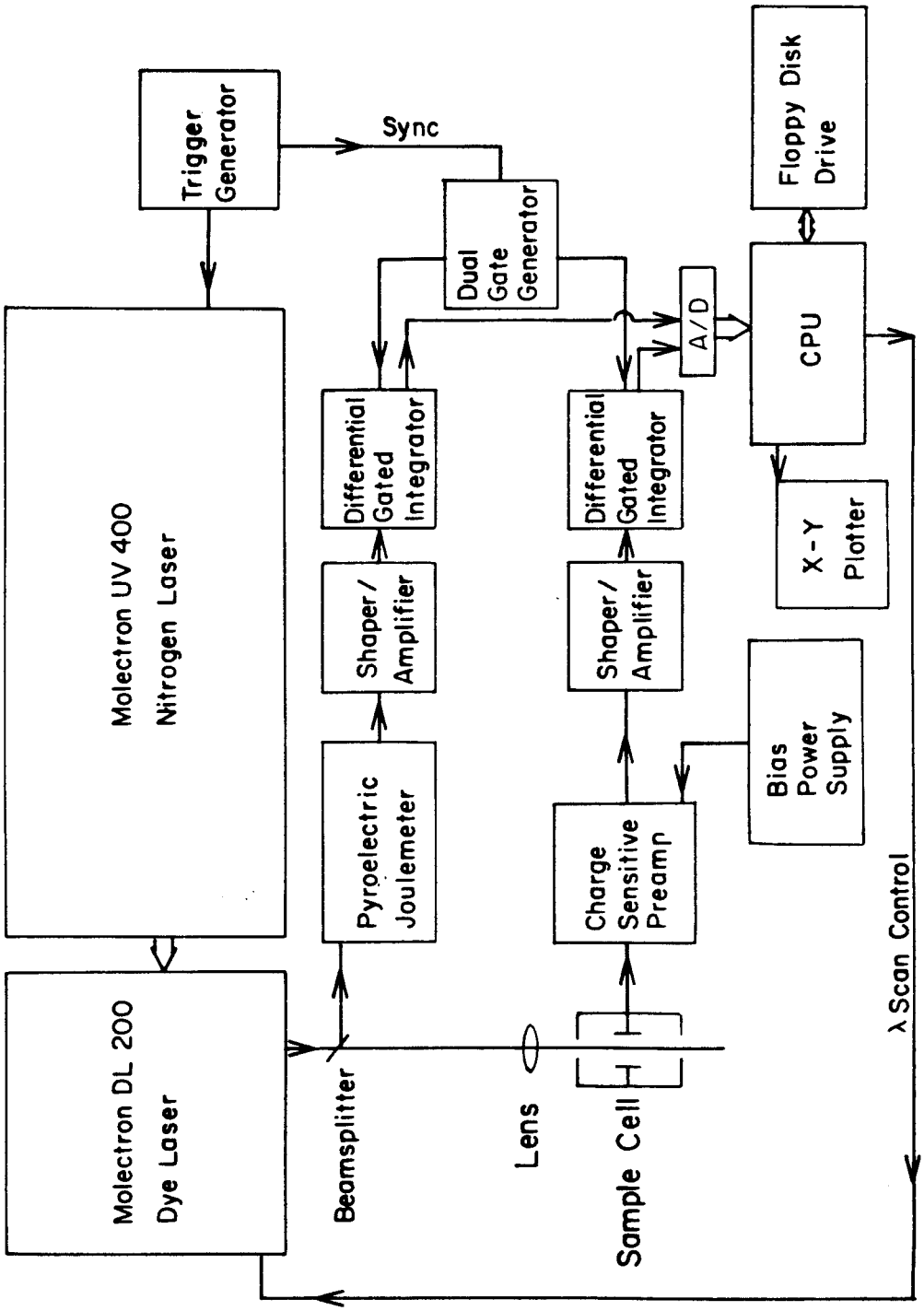

MULTIPHOTON IONIZATION SPECTROMETER

Figure 1

is necessary to populate the $C^3\pi_u$ state in a time which is short relative to the radiative lifetime of the state, requiring a very large excitation current.

The current necessary to achieve lasing is obtained by charging a primary capacitor (15.15 nf) to approximately 30,000 volts by a high voltage power supply. A pulse from the trigger generator is then applied to the high voltage thyratron pulser causing it to conduct, bringing the +30 kv plate of the primary capacitor to ground and the opposite plate to -30 kv. Charge is thereby transferred to 24 secondary capacitors at the discharge channel until breakdown of the nitrogen gas occurs and the gas conducts current. Lasing occurs during this breakdown stage. Since the breakdown voltage of the nitrogen is a function of the rate of voltage rise, it is necessary to minimize circuit inductance so that maximum charge is stored in the secondary capacitors prior to breakdown. Therefore the peak power from the laser increases with the value of the breakdown voltage.[4]

In order to obtain high output power, it is necessary to flow nitrogen through the laser tube so that metastable species (the $A^3\Sigma_u^+$ state, for example) are removed from the system. This is accomplished by feeding nitrogen into the laser from the gas outlet of a liquid nitrogen dewar and by exhausting gas by means of an Alcatel rotary vacuum pump. The input gas is flowed through a few feet of copper tubing so the gas will be warmed to nearly room temperature before entering the laser as it was feared that condensation might form on the laser tube and windows if the cold nitrogen was input directly. At the low flow rates used (less than

18 cubic feet per hour), this simple heat exchange is sufficient to prevent condensation on laser components.

The gain in the nitrogen laser is sufficiently large that only one mirror is used to achieve maximum output power (as opposed to most lasers which use two mirrors to produce a resonant cavity). This absence of a resonant cavity results in a larger beam divergence and bandwidth than are typical of gas lasers. Bandwidths are large in superradiant lasers (still less than 1 $\mathring{A}$ in the nitrogen laser) due to the absence of cavity modes which have bandwidths which are small relative to the lasing transition bandwidth.

The output of the nitrogen laser is then directed into the dye laser (Molectron model DL200) and is focused into a line in a magnetically stirred quartz curvette containing about 2cc of an approximately 10^{-3} M solution of an organic dye exciting dye molecules to an excited singlet state. The dyes are conjugated polyenes and can therefore, to surprisingly good approximation, be treated as a square well of length L where L is the length of the chain plus one band length beyond the terminal atoms. The longest wavelength absorption band then corresponds to

$$\lambda_{max} = \frac{8mc}{h} \frac{L^2}{N+1}$$

where N is the number of π electrons. This free electron model gives reasonably good agreement with experimental values for large dye molecules.[5]

The absorption bandwidths of typical dye molecules are very wide, on the order of 10 - 20 nm. This is due to the fact that dye molecules possess a very large number of vibrational modes for each electronically

excited state. For each vibronic level there are also numerous rotational sublevels. The collision frequency in dye solutions is very high, resulting in rapid thermalization of vibrations following an electronic transition ($\tau \sim 1$ picosecond).[5] This results in the broadening of transition lines, yielding essentially continuous absorption and emission throughout an absorption or emission band. Another consequence of the rapid thermalization of vibrations is the red shifting of emission bands from the corresponding absorption band.

There are many pathways by which the excited state of the dye can decay to the ground state. These include radiationless transitions such as internal conversion, intersystem crossing and collisional deactivation as well as the process used in dye lasers, radiative transitions generally from the first excited singlet state to the ground state.

Internal conversion results from tunneling from an electronically excited state to a highly excited vibrational level of a lower electronic state. Internal conversion from higher excited singlet states to the first excited singlet state is usually extremely fast, on the order of 10 picoseconds.[5] In some cases, internal conversion from the first excited state to the ground state is so rapid that fluorescence between the states is extremely difficult to detect. In the case of dyes commonly used in lasers, this is not the case and the intersystem crossing rate to the ground state is slow relative to the radiative transition rate.

Excited singlet states may also undergo radiationless transition to a lower lying triplet state by means of spin orbit coupling within the molecule or by collisions with paramagnetic molecules or with molecules containing large atoms. This process is known as intersystem crossing.

It is for this reason that dyes used in lasers do not contain metal atoms since transition to a triplet state reduces lasing efficiency not only due to depletion of the upper lasing level but also because these excited triplet states have relatively long lifetimes, thus depleting the ground state population and allowing absorptive transition to higher lying triplet states from which dissociation is more probable. The use of a nitrogen laser as a pump source instead of a flashlamp reduces the relative importance of intersystem crossing since the pulse width, 10 nanoseconds, is very short compared to the intersystem crossing time, 100 nanoseconds.[5]

Following excitation by the pump source to an excited singlet state, the dye molecule will be rapidly deactivated to the lowest vibronic level of the first excited singlet state. Fluorescent emission then occurs to the various vibronic levels of the ground state. If the dye solution is placed in a resonant cavity consisting of two parallel end windows with reflectivity R, lasing will occur providing the gain of the system is greater than one, when the gain from stimulated emission exceeds cavity losses including transmission of mirrors, absorption of fluorescence by ground state molecules, and diffraction and scattering losses (which can be accounted for in the oscillator condition equation

$$R \exp(-\sigma_a cL) \exp(\sigma_f cL) \geq 1$$

by replacing R with an effective reflectivity where σ_a and σ_f are the absorption and stimulated fluorescence cross-sections at wavelength λ respectively, L is the dye cell length, and c_0 and c_1 are the concentrations of the ground state and the excited state, respectively). The addition of a dispersive element (grating, etc.) within the cavity allows tuning

of the laser output across the fluorescence band, since cavity losses are very large for all frequencies except that which is selected.

The design utilized in the Molectron DL-200 is that developed by Hänsch.[6] In this design the nitrogen laser pulse is focused into a line just inside the near side of an antireflection coated quartz cuvette. An optical schematic of the DL-200 is shown in Figure 2. The cuvette has parallel windows which are offset from the cavity axis in order to avoid etalon effects. The dye is placed inside a cavity having a diffraction grating as one end mirror (actually a quartz flat or lens with one antireflection coated surface). The output mirror need have only a small reflectivity since the gain in the laser is very high.

It is important that the grating used in the laser has a high dispersion so that high resolution may be obtained. The optical path in the cavity is limited by the fact that in order to achieve lasing, feedback from the grating must return to the dye cell before the end of the pump pulse (10 n sec). Since the optical path cannot be increased beyond about 0.5 meter to improve resolution, the resolution of the laser is determined by the dispersion of the grating.[7]

Constructive interference occurs only for wavelength such that $N\lambda = 2d \sin\theta$, where N is the grating order, d is the distance between lines on the grating (600 lines per millimeter in the DL-200), and θ is the angle of incidence. Since the obtainable resolution is proportional to the number of illuminated grooves ($\Delta\lambda = \lambda^2/2\pi w_2 \tan\theta$, where w_2 is the waist size of the beam incident on the grating),[6] an anchromatic beam expanding telescope is employed in order to enlarge the area of the grating

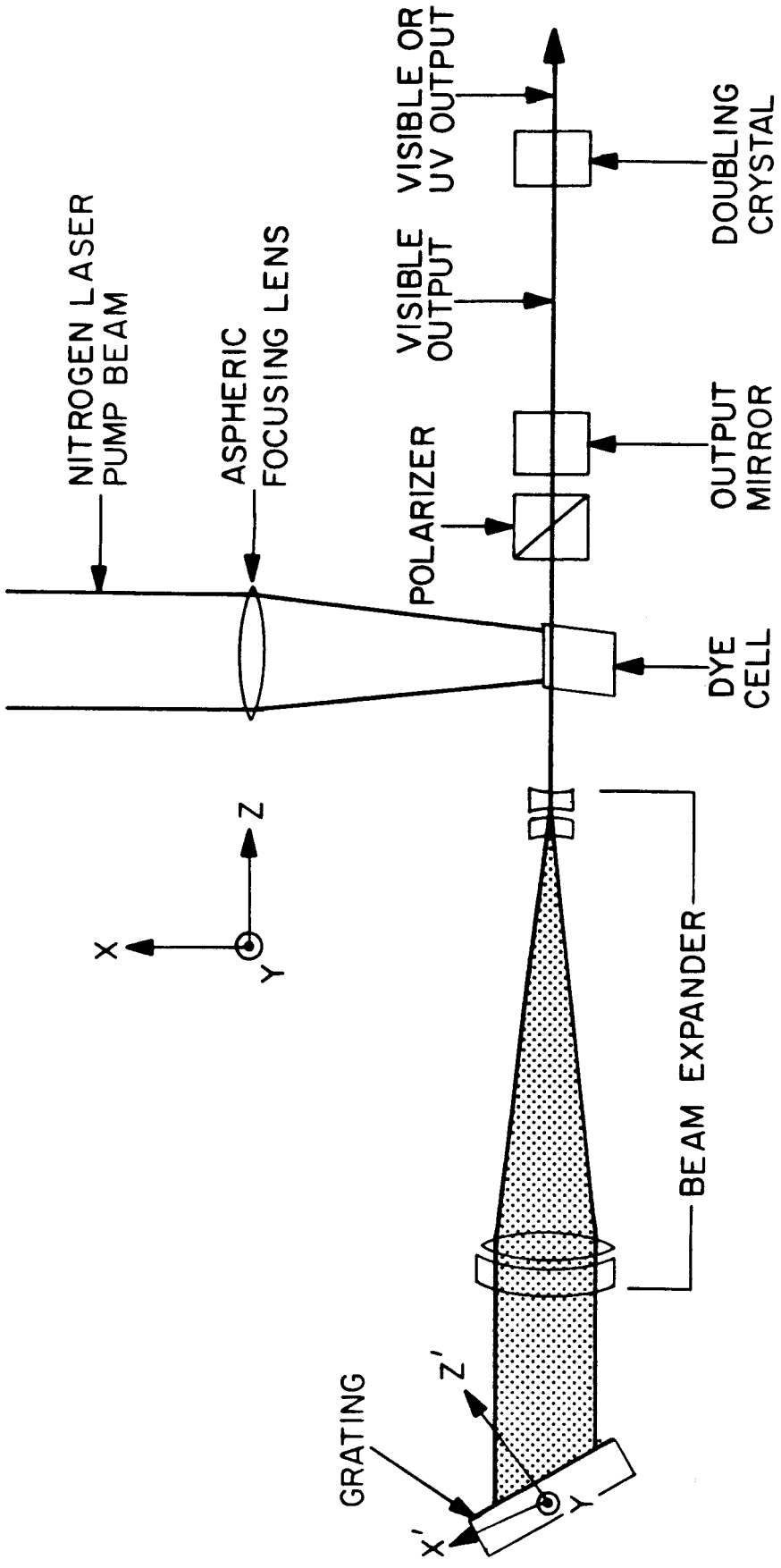

OPTICAL SCHEMATIC OF DL200 LASER

Figure 2

illuminated and thereby improve the resolution (stated by the manufacturer to be 0.01 nm at 600 nm). The grating is driven by means of a sine drive mechanism enabling linear wavelength scanning. By scanning the grating in the appropriate order (fourth, fifth, sixth and seventh orders) and using the different dyes available, continuous tunability is achieved from 360 to 750 nm with a pulse energy on the order of 400 μjoules in a 6 nanosecond (nominal) pulse. Other dyes are available which would extend the tuning range to longer wavelengths, but these dyes are not available from Molectron at present and the use of any dyes from sources other than Molectron voids the dye cell warranty.

In order to extend the laser's tunability farther into the ultraviolet, extracavity frequency doubling crystals such as KDP (potassium dihydrogen phosphate) and ADP (ammonium dihydrogen phosphate) are employed. Second harmonic generation is made possible by second order nonlinear electric susceptibilities of the crystals.[8] Phase matching requires different crystal orientations for different wavelengths having an acceptance bandwidth of approximately 1 nm.[9] The power conversion efficiency has a maximum of about 10% for incident power above 10 kw and decreases linearly as the peak input power decreases below 10 kw. The pulse length of the doubled beam is half that of the fundamental, therefore energy conversion is 5%.

In the DL-200, five KDP crystals, each cut at a different angle, are mounted in a turret wheel assembly just outside the laser cavity. The turret can then be rotated to allow phase matching throughout the wavelength coverage of a given crystal. In order to maximize doubled power,

a focusing mirror replaces the front laser mirror and an intracavity polarizer is installed to horizontally polarize the fundamental beam since only the horizontal component is doubled.

6.3 Detection Apparatus

The output of the dye laser is focused using a lens (focal lengths used were 25 mm and 50 mm) into the sample cell. The sample cell consists of a stainless steel cylinder approximately 2.5" inside diameter, 3.0" long, and 0.5" wall thickness. The cell contains two parallel stainless steel plates approximately .75" square with rounded corners separated by .75". One plate is attached to the wall of the cell via a stainless steel rod. The remaining plate is attached to a high voltage feedthrough. A voltage bias of between +600 V and +1500 V is applied by connection to the charge sensitive preamplifier through an MHV connector. The perimeter of the plate is covered with a teflon jacket in order to prevent arcing to the walls of the cell.

The charge sensitive preamplifier used is the Canberra spectroscopy preamplifier model 2001A. The preamplifier converts the ionization charge developed in the detector into a pulse output whose amplitude is proportional (jumper selectable to either 2V/picocoulomb or 10V/picocoulomb) to the total charge accumulated in that event.[10] The output pulse decays exponentially with a time constant of 50 microseconds. The high voltage bias (0 to ±2000 V; arcing may occur within the sample cell at higher potentials) for the sample cell is connected to the model 2001A where it is filtered with a 10-second time constant before being connected to the

sample cell. The 2001A is capacitor coupled between the detector and preamplifier. A higher signal-to-noise ratio is obtained using a positive bias (hence, electrons are detected) than with a negative bias due apparently to components of the preamplifier. Power for the 2001A (±12 VDC and ±24VDC) is obtained from the NIMBIN power supply which houses the amplifiers and integrators.

A fraction (<10%) of the dye laser beam is split off using a quartz flat and directed into a pyroelectric joulemeter in order that the laser output may be monitored. The joulemeter consists of the Laser Precision RkP-335 pyroelectric energy probe and the Laser Precision Rk-3230 pyroelectric energy meter. The RkP-335 consists of a slice of ferroelectric material possessing a permanent electric polarization which is highly temperature dependent. This material is then coated with a black absorbing layer with a high absorptivity over the range 0.25 to 16 microns. In order to ensure 100% absorption of the incoming optical radiation, the detector is designed as a light trap so that any light entering the detector along its axis will strike the absorbing layer at an angle such that any radiation not absorbed during this first interaction will be reflected so as to strike another segment of the detector.

As radiation is absorbed by the detector coating, a current is generated which is proportional to the time rate of change of the element temperature. The time integral of this current is proportional to the total temperature increase, and therefore to the energy of the light pulse. The RkP-335 possesses an internal preamplifier in order to improve signal-to-noise and eliminate the dependence of responsivity on

cable length. The response of the probe is either 10 or 10000 volts per joule, selectable by switching an internal reed relay, and is stated to be flat to ±2% from 0.25 to 16 microns.[11]

The Rk 3230 provides signal processing and display electronics as well as power for the probe. Seven full scale display ranges from 2 μJ to 200 mJ (in decade steps) and 1 J are provided. On the 2 mj through 1J ranges, the reed relay within the RkP335 is energized reducing the responsivity of the probe by 1000. The Rk 3230 will accept pulses up to 1 millisecond long at repetition rates to 100/second. The energy meter displays pulse energies averaged over 1, 10 or 100 pulses. However, the signal processing capabilities of the joulemeter are not utilized during data acquisition. Pulses from the detector are made available through the DIRECT output after amplification only within the energy meter. The necessary signal processing is accomplished through our Molectron dual channel gated integrator system which provides all the processing employed by the joulemeter but which also allows pulse shaping, amplification and integration with a time constant equal to that employed for integration of the MPI signal. This eliminates the possibility that a mismatch in integration time constants might lead to false structure.

The outputs of the charge sensitive preamp and the joulemeter are each input into the first stage of the Molectron dual channel gated differential integrator system (Laser Spectroscopy Detection System), the model 131 Amplifier Shaper. The amplifier-shaper is a high-gain bandpass amplifier whose bandpass is controlled by the differentiator and integrator settings. The amplifier gain is continuously adjustable

from .3 to 1000. The differentiator sets the low pass cutoff from 160 Hz to 160 kHz. The integrators control the high pass cutoff from 1.6 kHz to 1.6 MHz. The combination of integrators and differentiators allows for shaping of pulses. This is necessary since the signals from the charge sensitive preamp and the energy meter differ significantly in rise and fall times. In contrast to the 50 μsec decay time of the charge sensitive preamp, the joulemeter signal decay is about 30 msec. The use of the pulse shaping capability of the model 131 allows the alteration of the joulemeter signal such that the resulting signal possesses rise and fall times that allow integration using the same gate generator for each channel.

Integration of the amplified pulses is accomplished using two Molectron model 112 differential gated integrators (one for each channel). The model 112 is an RC integrator which is active only during an externally supplied gate window. Two gates are supplied to the integrator. The first gate is adjusted to measure the signal pulse while the second is adjusted to measure the signal baseline. The output of the integrator is the difference between the signals obtained during the gates. This feature minimizes the effect of amplifier DC drift as well as eliminating any detector DC components due to current leakage (of the sample cell) or temperature drift (of the pyroelectric detector). The effective integration time constant (t_{eff}) is given by

$$t_{eff} = RC(\frac{T}{tg})$$

where R is the value of the integration resistor in ohms, C is the

integration capacitance in farads, T is the gate repetition period, and t_g is the gate width.[12] The integration resistance may be set to 300Ω, 1KΩ, 3KΩ, 10KΩ, 30KΩ, 100KΩ, 300KΩ, 1MΩ or 3MΩ and the integration capacitance may be set from 100 pF to 1μf in decade steps. The effective integration time constant is usually set to 1 to 5 seconds so that a weighted average over 30 to 150 laser pulses is obtained. Additional filtering of the integrator output, which is helpful when short integrator RC time constants are used, may be obtained by selecting a suitable output time constant setting. However, when two channel ratio measurements are being taken (as is always the case for MPI experiments), the output time constant selected must be less than the effective integration time constant. This is necessary because the integrator time constants are matched to 0.5% while the output time constants are only matched to 5%.

The gates necessary for operation of the integrators are provided by the Molectron model 122 dual gate generator. Upon receipt by the model 122 of a trigger pulse, two gates of equal width separated in time are generated. The trigger pulse is generally obtained from the laser trigger generator. The delay of the leading edge of the first gate from the trigger pulse is continuously variable from 100 nsec to 150 msec. Gate widths and separation are continuously variable from 30 nsec to 150 msec.

6.4 Digital Data Acquisition System

6.4.1 Introduction

Digital data acquisition and experimental control capabilities are provided by the 8080A based microcomputer system I have designed. This system consists of an Intel SBC 80/20 single board computer, an Intel SBC 116 combination memory and I/O expansion board, an Intel SBC 310 high speed mathematics board, an Analog Devices RTI 1200 real time interface board, an iCOM FD3712 dual floppy disk drive and controller board, an Intel SBC 660 card cage and power supply, and a memory expansion and interface board which I have designed. All these boards interface with the CPU board (the SBC 80/20) via the Intel Multibus. The commercially available boards are described briefly in Section 6.4.2., since additional information is available from manuals published by the manufacturers. The prototyped board which I designed is described in detail in Section 6.4.3.

6.4.2 Commercial Hardware

The SBC 80/20 is an Intel Multibus (see Table 3, Section 2.4.1 for Multibus pin assignments) compatible single board computer utilizing the 8-bit Intel 8080A-2 processor. The board includes 2K bytes of static random access memory (RAM), sockets for 4K bytes of EPROM, two 8255 parallel peripheral interfaces, an RS232C serial port, an 8253 programmable interval timer, and an 8259 programmable interrupt controller.

The 8080A microprocessor operates on a 2.15 MHz clock, yielding an instruction cycle of about 1.8 μsec. The 8080A contains six 8-bit

general purpose registers, an accumulator, and two 16-bit registers. The six 8-bit registers may be used individually or in pairs as 16-bit registers. In addition, five single-bit flags are provided. The user accessible register configuration is shown in Figure 3.

The 8080A utilizes a 16-bit address bus. The address bus provides the address for memory (up to 64K bytes) data exchanges and for I/O data exchanges. I/O addressing uses only eight address bits to select up to 256 input and 256 output ports. A system memory map is shown in Table 1. Table 2 shows the system I/O address map. Data transfers occur through an 8-bit bidirectional data bus.

The SBC 80/20 includes four PROM sockets which are configured to occupy memory space from 0000H to 0FFFH. All four sockets are currently occupied. The first two hold 2708 EPROMS which contain the Intel SBC 925 monitor. Only the first 06AFH bytes of the SBC 925 are used since the remaining section contains a floppy disk diagnostic which is incompatible with our system. The remaining PROM sockets contain machine language code which I have written providing floating point input and output routines and other general utility routines. The SBC 80/20 also includes 2K bytes of RAM which are jumper selected to occupy addresses 3800H to 3FFFH. This RAM section is available only to the 80/20 board.

Six 8-bit programmable parallel I/O ports based on a pair of 8255 programmable peripheral interfaces are included on the SBC 80/20. Currently, these ports are configured for output, however, none of the 48 bits available are used.

An RS232C serial port is provided on the SBC 80/20 board by an 8251

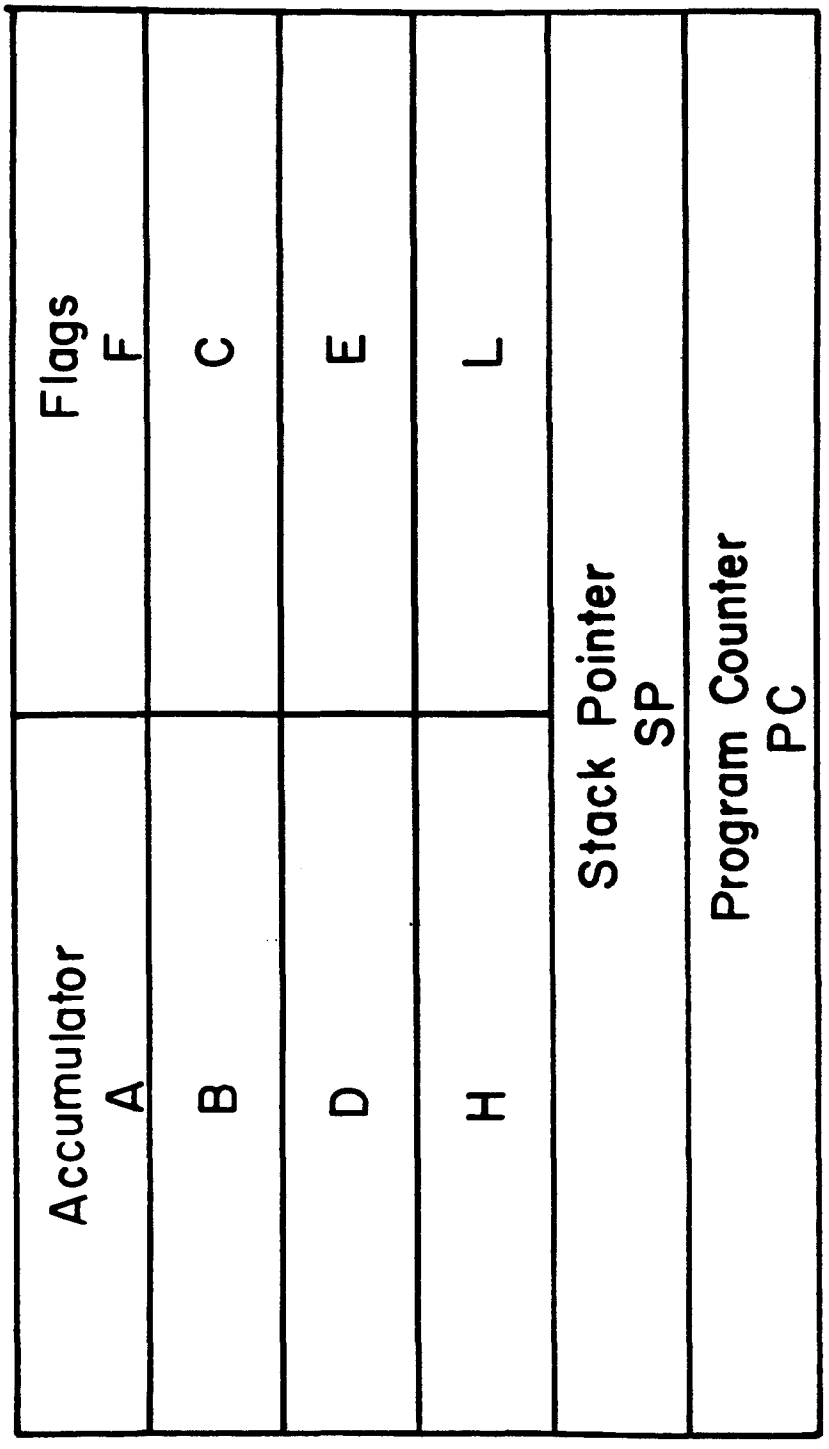

8080A CPU REGISTER CONFIGURATION

Figure 3

Table 1

Memory Map for MPI Computer System

0000-0FFF	SBC 80/20	PROM (2708's)
	0000-03FF	SBC 925 monitor PROM No. 1
	0400-07FF	SBC 925 monitor PROM No. 2
	0800-0BFF	Math and general purpose routines
	0C00-0FFF	Math and general purpose routines (continued)
1000-FFF	SBC 116	
	1000-13FF	PROM (2708) socket No. 1 (unused)
	1400-17FF	PROM socket No. 2 (unused)
	1800-1BFF	PROM socket No. 3 (unused)
	1C00-1FFF	PROM socket No. 4 (unused)
2000-2FFF	Prototyped Board	
	2000-23FF	PROM (2708) socket No. 1 (unused)
	2400-27FF	PROM socket No. 2 (unused)
	2800-2BFF	PROM socket No. 3 (unused)
	2C00-2FDF	PROM socket No. 4 (unused)
	2FE0-2FE3	Counter Timer Circuit (8253) No. 1
		2FE0 counter 0
		2FE1 counter 1
		2FE2 counter 2
		2FE3 mode control
	2FE4-2FE7	Counter Timer Circuit (8253) No. 2
		2FE4 counter 0
		2FE5 counter 1
		2FE6 counter 2
		2FE7 mode control

Table 1 (continued)

	2FE8-2FEB	Programmable Peripheral Interface (8255)
		2FE8 Port A
		2FE9 Port B
		2FEA Port C
		2FEB Control
	2FEC-2FFF	Decoded but unused
3800-3FFF	SBC 80/20 RAM 2K	
4000-7FFF	SBC 116 RAM 16K	
8000-BFFF	Prototyped Board RAM 16K	
E800-EBFF	FDOS Resident PROM	
FC00-FFFF	RTI 1200	
	FC00-FFEF	PROM socket
	FFF0	Setup Byte
	FFF1-FFF2	Not used
	FFF3	Drivers
	FFF4-FFF5	DAC2 data (12-bit LSB, MSB)
	FFF6-FFF7	DAC1 data (12-bit LSB, MSB)
	FFF8	ADC data (8-bit,MSB only)
	FFF9	Gain select
	FFFA	Multiplexer Address
	FFFB	Convert Command
	FFFC	Status Byte
	FFFD-FFFE	ADC data (12-bit LSB, MSB)
	FFFF	Card Select

Table 2

I/O Map for MPI Computer System

00-05	Unused
06-07	FD3712 Control Board
	06 Control Port
	07 Data Port
08-BF	Unused
C0-C7	SBC 310
	C0 Op Code
	C1 Low memory address and status byte
	C2 High memory address
	C3 Reserved
	C4 Reserved
	C5 Reserved
	C6 Reserved
	C7 Flag Byte
D4-DF	SBC 80/20
	D4 Power fail status
	D5 Bus override control
	D6 LED diagnostic indicator
	D7 Not used
	D8-DB Programmable Interrupt Controller (8259) command registers
	DC-DF Counter Timer Circuit (8253)
	DC counter 0
	DD counter 1
	DE counter 2
	DF mode control

Table 2 (continued)

E0-E3	Unused	
E4-EF	SBC 80/20	
	E4-E7	Programmable Peripheral Interface (8255) #1
		E4 Port A
		E5 Port B
		E6 Port C
		E7 Control
	E8-EB	Programmable Peripheral Interface (8255) #2
		E8 Port A
		E9 Port B
		EA Port C
		EB Control
	EC-EF	USART (8251)
		EC+EE Data port
		ED+EF Control and status port
F0-FF	SBC 116	
	F0	Interrupt status register
	F1	Interrupt mask register
	F2	Reset timer interrupt
	F3	Reserved
	F4-F7	Programmable Peripheral Interface (8255) #1
	F8-FB	Programmable Peripheral Interface (8255) #2
	FC-FF	USART (8251)
		FC+FE Data port
		FD+FF Control and status port

universal synchronous/asynchronous receiver/transmitter (USART). The functions of the USART have been described previously (Section 2.4.1). The transmitter and receiver clocks are connected to the output of counter 2 of the on-board 8253. Baud rates are therefore software programmable by reprogramming the 8253. The SBC 925 system monitor provides all the software necessary for operation of this serial port which is used as the console port. Upon initialization, the monitor software will begin a search for the correct baud rate. The user need only enter 'u' from the console until the computer responds with a sign-on message.

The 8253 programmable interval timer (or counter-timer circuit) has also been described in Section 2.4.1. Counters 0 and 1 are not currently used. Counter 2 is used to provide the baud rate clock for the serial port. The clock to counter 2 is the 1.0753 MHz ϕ_2(TTL) output of the 8224, the chip which provides the clocks for the 8080A. Upon system initialization or reset, counter 2 is programmed to mode 3, square wave rate generator, and is loaded with a count of 7. The counter then divides the input frequency by 7, yielding an output of about 153.6 kHz. This rate is then divided by 16 within the USART, yielding a baud rate of 9600. The count loaded into counter 2 is doubled (thereby halving the baud rate) following entry of each character from the console until the correct baud rate is determined (i.e. no errors are detected by the 8251).

Interrupt control is provided by Intel's 8259 Programmable Interrupt Controller. The 8259 manages eight levels of interrupt requests and may be cascaded to handle up to 64 levels. The 8259 may be

programmed to operate in one of four different interrupt modes:

1) Fully nested mode
2) Rotating priority mode
3) Special mask mode
4) Polled mode

When the interrupt controller receives an interrupt request (one or more of the 8 input lines is raised high), the controller resolves the priorities and, if no higher priority interrupt is being currently serviced, issues an interrupt to the CPU. The CPU acknowledges the interrupt (if interrupts are enabled) and responds with an $\overline{\text{INTA}}$ pulse. Upon receiving this pulse, the 8259 will release a CALL instruction code onto the data bus. The CALL instruction will in turn cause two more $\overline{\text{INTA}}$ pulses to be sent by the CPU. Upon receipt of these pulses, the 8259 will place a preprogrammed subroutine address onto the data bus (least significant byte first). The 8 interrupting devices have eight subroutine addresses equally spaced in memory. The spacing may be programmed to be either 4 or 8 bytes. When the 8259 is initialized, the high order bits of the subroutine addresses (A15-A6 if the interval is 8 bytes or A15-A5 if the interval is 4 bytes) are programmed into the controller. The remaining subroutine address bits are automatically generated by the 8259.

The 8259 in this application is initialized by the system monitor to the fully nested mode with a spacing of 4 bytes between service routines. The base address of the subroutines is set to 3FE0H. The monitor then places jump instructions to a general purpose interrupt

servicing routine into each of the interrupt servicing subroutine addresses. In order to use the interrupt controller, it is therefore only necessary to alter the appropriate jump address stored by the monitor to the address of a subroutine designed to service a particular interrupt.

Interrupt level 2 is reserved for use by the monitor for operation of the single step command. Interrupts 3 and 4 are connected to the memory expansion and interface board and are used to signal the computer when particular numbers of pulses have been sent to the dye laser wavelength scanning stepping motor.

The SBC 116 provides the computer system with an expanded memory and I/O capability. The SBC 116 contains 16K of dynamic RAM. The base address for the RAM may be jumper and switch selected to any 16K byte boundary. In this case, the RAM is set to occupy address space from 4000H to 7FFFH. This is accomplished by connecting a jumper between pins 89 and 90 and by opening switch numbers 5, 6, 7 and 8 at S3. (Note: The manual is written for the SBC 104 which has only 4K bytes of RAM. Therefore, four switches must be opened at S3 not just one as the manual indicates.)

The SBC 116 also provides sockets for 4K of PROM's. Additional I/O capability is provided by two 8255 parallel peripheral interfaces and by an 8251 USART. The two 8255's provide a total of 48 I/O lines, none of which are currently used. The USART is used to provide a 1200 baud RS232C printer port. The 8251 is configured to operate as a data set. This required removal of jumpers between pins 15 and 16, 17 and

18, 19 and 20, and 21 and 22. Additional jumper connections between pins 15 and 18, 16 and 17, 19 and 22, and 20 and 21 were made. Also, the TXD and RXD lines were reversed between the edge connector to the board and the 25 pin D connector to the printer. Jumpers between pins 83 and 84 and between pins 79 and 82 disable interrupts from the USART (it is used in polled mode only). A jumper between pins 1 and 7 provides a 19.2 kHz transmitter and receiver clock. Thus, by programming the USART to divide this rate by 16, a baud rate of 1200 may be generated. The SBC 116 also provides an eight-level maskable interrupt feature and a 1 msec interval timer. Neither of these features is used currently.

High speed mathematics capability is provided by the Intel SBC 310 high-speed mathematics unit. The SBC 310 performs arithmetic functions an order of magnitude faster than is possible using software. The SBC 310 is interfaced to the CPU as eight I/O ports. It is through these ports that operation codes and argument addresses are passed to the SBC 310 and status and flag bytes are sent to the CPU. The SBC 310 operates on arguments stored in RAM. The arguments, each four bytes long, must occupy consecutive addresses beginning on a 16-byte boundary. The SBC 310 performs operations on both 16-bit and 32-bit fixed point integers as well as 32-bit floating point numbers. Floating point numbers are stored as a 23-bit fraction (the fraction is always normalized so a 1 is assumed to be the highest bit, yielding an effective 24-bit fraction), an eight-bit exponent (bias by 7FH), and a sign bit. The argument is expressed as:

$$(-1)^{S} \cdot 2^{(exp-bias)} \cdot (1.F) \ ,$$

where S is the sign bit and F is the 23-bit fraction. The range of numbers which can be expressed is therefore 1.17×10^{-38} to $3.4 \times 10^{+38}$.

The floating point operations provided by the SBC 310 include multiplication, division, addition, subtraction, squaring, square root, and conversion to fixed point format. The fixed point operations provided are multiplication, division, extended division (32-bit result plus a 32-bit remainder), and conversion to floating point. The routines which provide for entry of decimal numbers from the console as well as those which provide for output to the console of decimal numbers stored in memory in binary floating point format make extensive use of this board.

In order for the computer system to acquire data from the boxcar integrator system discussed in Section 6.3, it is necessary to convert the analog signals obtained from each of the two integrators into digital data which can be utilized by the computer. It is also desirable to provide digital-to-analog (D/A) conversion capability so the computer may drive an X-Y recorder or other display devices. Both analog-to-digital (A/D) and D/A conversion capabilities are provided by the Analog Devices RTI 1200 real time interface. The RTI 1200 provides 32 analog input channels (multiplexed), a software programmable gain amplifier, 12-bit A/D conversion, an on-board PROM socket, two 12-bit D/A converters, and two logic driver outputs.

The RTI 1200 interfaces to the computer as a 1K byte block of memory (see Table 1, Section 6.4.1). Data and command information are

transmitted to the RTI 1200 via memory write instructions, and data and status information is retrieved from the RTI 1200 via memory read instructions.

The RTI 1200 is currently configured for 32 single-ended inputs. The input voltage range (0 to 10 VDC) is established by connection of jumpers between pins 24 and 25, 30 and 31, and 33 and 34. The output of the A/D is natural binary (12 bits). The RTI 1200 also contains a programmable gain amplifier which may be used to increase the input sensitivity. Gain factors of 1, 2, 4 or 8 may be selected in order to improve measurement precision for small signals. For example, since the 12-bit A/D is set to operate over a 10 V range, a 9.9951 V signal yields a digital result of 0FFFH. This result is precise to one part in 2^{12}. However, if the input signal is 1.247 V, the result is 01FFH, which is precise to only one part in 2^{9}. By amplifying this input by a factor of eight using the programmable gain amplifier, a digital value that is precise to about one part in 2^{12} is obtained.

In order to digitize an analog input, the CPU must output the following to the RTI 1200:

1) Amplifier gain factor (1, 2, 4 or 8).
2) Input channel number (0 - 31).
3) Convert command.

Once the convert command has been issued, the A/D will begin conversion of the analog data to digital format. The CPI may poll the RTI 1200 status to determine when the conversion has been completed. The digital data may then be read from addresses FFFD and FFFE. Since the CPU has

set the gain factor, it is possible to obtain the actual input voltage by conversion of the input data into floating point format, dividing by the gain factor, and multiplying by 10 V/4096.

The 12-bit D/A converters are currently used to drive an X-Y recorder and a storage oscilloscope. The D/A's are configured to accept natural binary and output 0 - 10 VDC. This is accomplished by making jumper connections between pins 38 and 39, 41 and 42, 46 and 47, and 49 and 50.

The RTI 1200 is also equipped with two software controllable logic drivers. Writing a '1' to the appropriate bit in the 'DRIVERS' byte (see Table 1, Section 6.4.2) turns the driver output on. (The driver is simply an NPN transistor with the emitter grounded. The ouptut is the collector of the transistor. This output is then effectively shorted to ground when the driver is on.) The logic drivers are each currently connected to one side of the coil of a reel relay. The other side of the coil is connected to 5 volts. Thus, when the driver is on, current flows through the relay coil closing the contacts. The relay for driver 0 is currently used to switch 5 volts to the storage oscilloscope Z-axis, thereby causing a point to appear on the screen. Connections to the logic drivers as well as to all analog inputs and outputs are made to the RTI 1200 through three edge connectors. Pin definitions for these connectors are given in the RTI 1200 User's Guide.

6.4.3 Memory Expansion and Interface Board

Capabilities of the computer system in addition to those possessed

by the commercial boards described previously were necessary to complete the laser scan control and data acquisition system. A facility for pulse generation for driving the stepping motor, for counting the generated pulses, and for scan direction control was also required. Although the system did already possess enough memory to acquire data from a 30 nm scan, some dyes may be usable up to 40 - 50 nm, therefore it was considered desirable to increase both RAM and PROM capability. In order to meet these requirements, I designed a memory expansion and interface board. This board is very similar to that designed for the electron inpact spectrometer which has been described previously in Section 2.4.2. A diagram of the overall board layout is shown in Figure 4. Table 3 lists the components utilized. Detailed schematics of those sections of the board which differ substantially from those of the electron spectrometer board are shown in Figures 5 and 6.

The prototyping board used is the Monolithic Systems MSC 8204 Universal Card. The MSC 8204 provides buffering of the Multibus address and data lines as well as transfer acknowledge logic. As was also the case for the electron spectrometer board, this board is configured as a slave, not a bus master.

The prototyped board circuitry I have designed may be divided into four sections:

1) Address decoding (Figure 5)
2) Pulse generator and parallel interface (Figure 6)
3) 16K - 32K RAM
4) 4K PROM

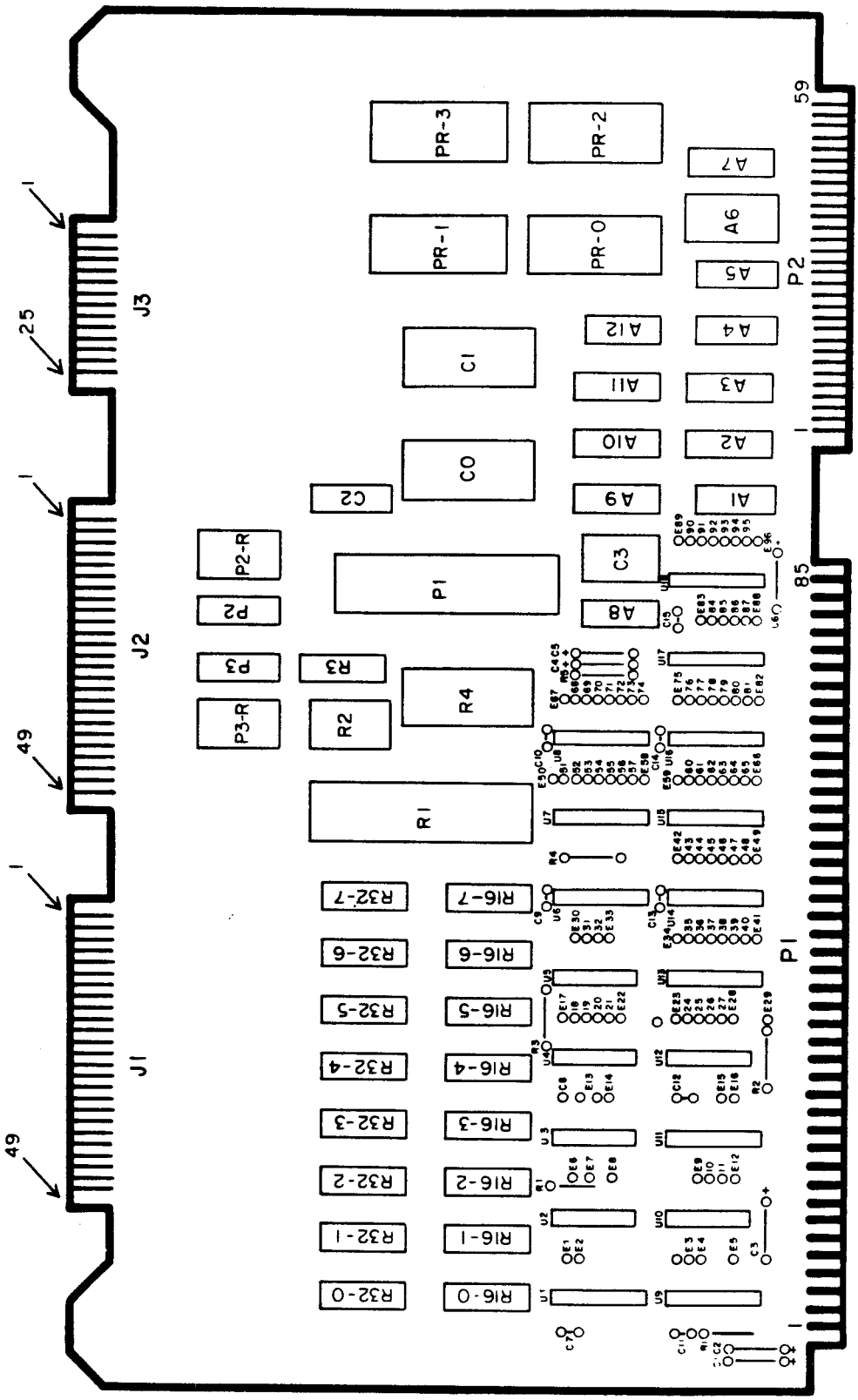

MEMORY EXPANSION AND INTERFACE BOARD

Figure 4

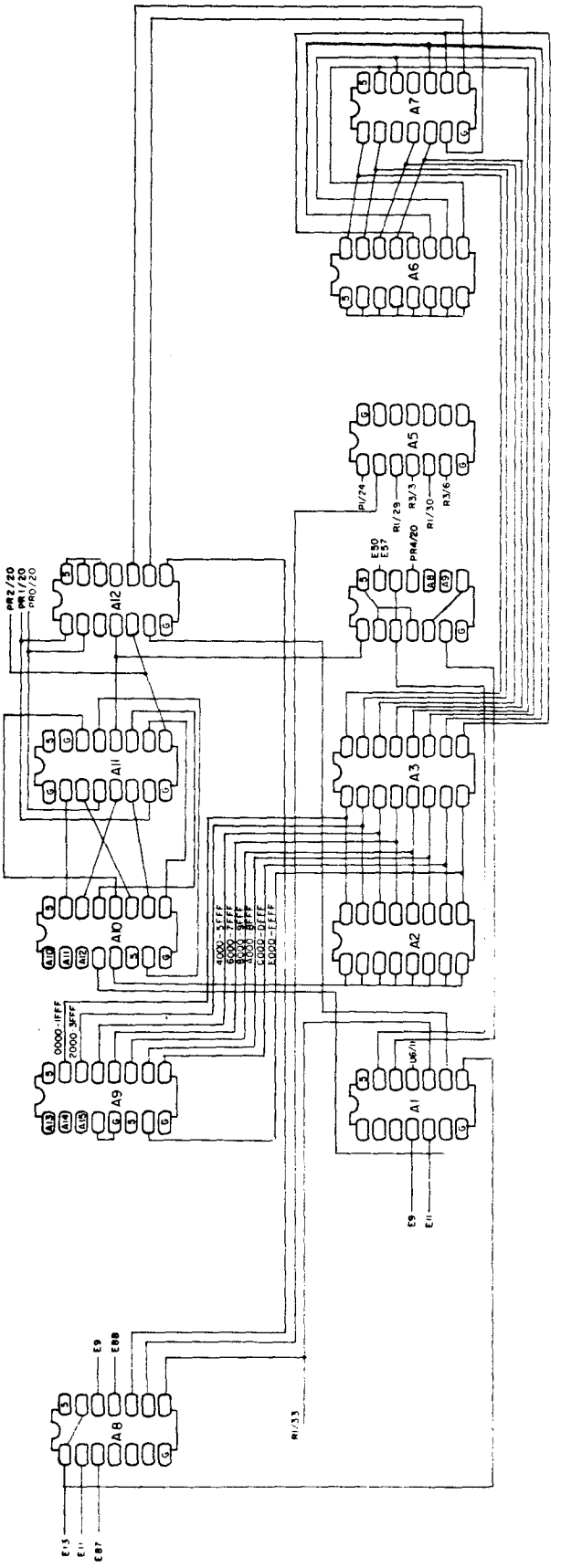

ADDRESS DECODING

Figure 5

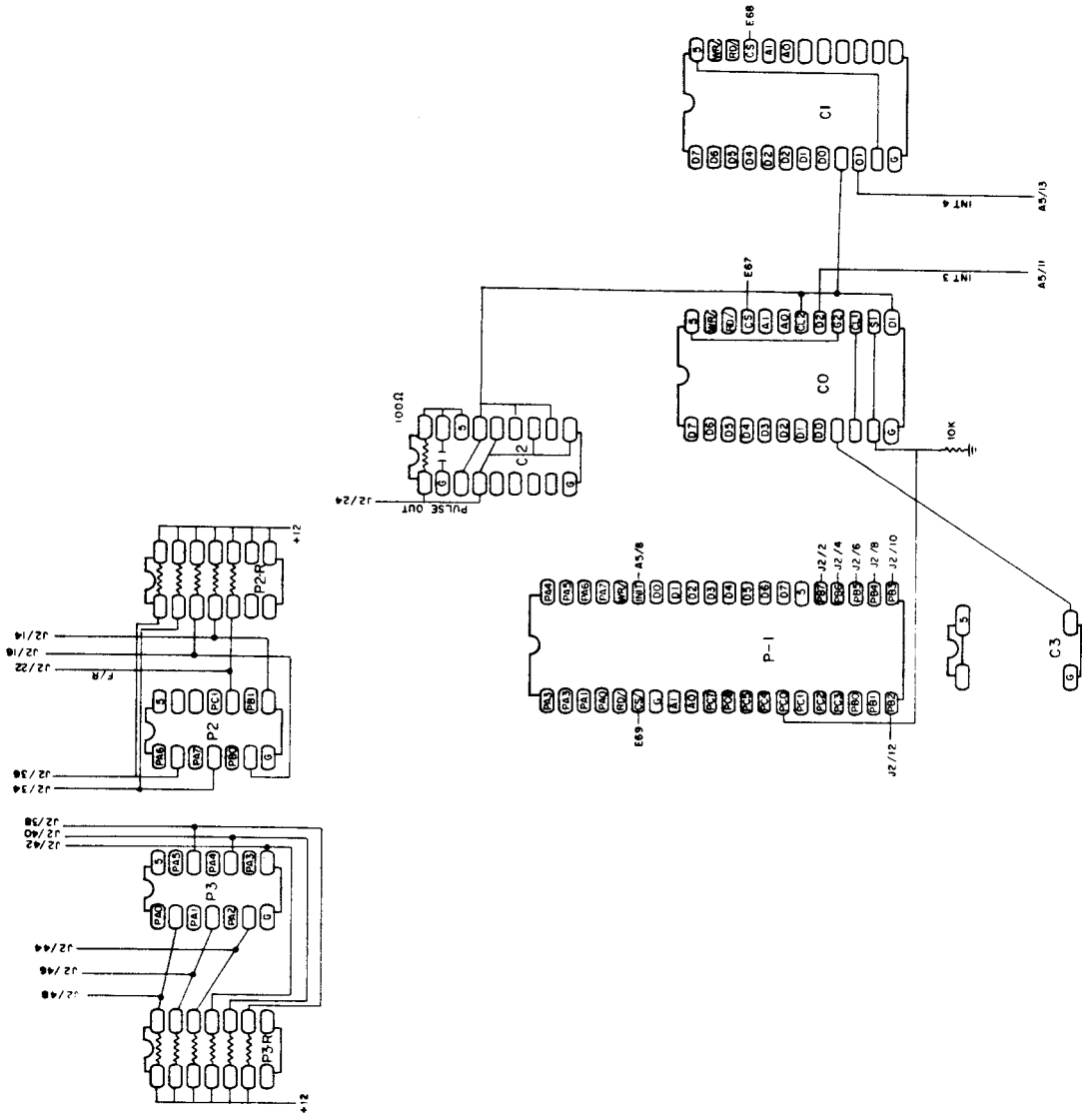

PULSE GENERATOR AND PARALLEL INTERFACE

Figure 6

Sections 3 and 4 are virtually identical to the comparable sections of the electron spectrometer computer system so only deviations from the circuitry already described in Section 2.4.2 will be included in this section.

The MSC 8204 provides address decoding circuitry. Unfortunately, this circuitry is designed for use with 74S287 PROM's for which we have no programming capability. Although Monolithic Systems will (I believe) program these PROM's to meet the user's requirements, it would make the system inflexible since any alteration of addressing would require ordering a new PROM which would lead to unreasonable down times. Due to these difficulties, I decided to bypass the Monolithic Systems decoding circuitry (which does not eliminate the need for additional decoding) and design circuitry using readily available chips which would meet current requirements as well as provide the flexibility to meet future needs.

The three high order bits of the 16-bit address are connected to an Intel 8205 high speed 1 of 8 binary decoder (A9). The enable inputs (pins 4, 5 and 6) are tied to the appropriate levels such that the chip is always enabled. One output of the 8205 will be logic level 0 while all others will be logic level 1 depending on the levels of the input address lines. Thus, A9 decodes the address into 8K blocks. The outputs of A9 are connected to DIP switches A2 and A3 which allow selection of 8K blocks of memory to be occupied by the PROM and memory mapped I/O (A2) and by the RAM (A3). Only one switch of A2 is connected at a time. The 4K block of memory occupied by the PROM and I/O will then lie in

either the upper or lower half of the 8K block selected. The output of A2 is connected to the gate input of another 8205 (A10). The other active low gate of A10 is connected to the output of a 7408 which AND's the board memory read and write (BMWTC/and BMRDC/) lines. Both BMWTC/ and BMRDC/ are active low signals obtained from the MSC 8204 circuitry. Thus, A10 is enabled only when the address lies within the 8K block selected and a memory read or write operation is requested. The 8205 (A10) is also connected to address lines A12, A11 and A10. It therfore decodes further the 8K block selected into eight 1K sections. These 8 device selects are then connected to 74157 (A11) quadruple 2-line-to-1-line multiplexers. The 4 outputs of A10 corresponding to the 4 lower 1K blocks of the selected 8K block of memory are connected to the A inputs of A11. The remaining four outputs of A10 are connected to the B inputs of A11. The outputs of A11 may be selected to correspond to either the A or B inputs depending on the state of the select input (pin 1). If select is low then the levels of the A inputs are transmitted to the outputs. Thus by only changing the connection to pin 1 of A11, one may position the PROM and I/O in either the upper or lower 4K of the 8K block of memory switch selected using A2. The select line is grounded currently and only switch 2 of A2 is closed therby positioning the PROM's and memory mapped I/O between 2000H and 2FFFH. Three of the outputs of A11 provide the device selects for PROM sockets PR-0, PR-1 and PR-3. The remaining output of A11 which is low for addresses 2C00H to 2FFFH requires further decoding so the memory mapped I/O will overlay the last 32 of these addresses. All four outputs of A11 are

ANDed together by A12. The associated output of A12 is therefore low whenever a memory read or write to addresses 2000H-2FFFH occurs. This signal is later used to generate the BRDSEL/ signal.

The fourth output of A11 is inverted by a 7400 (A4) (NANDed with 5 volts). This signal and the inverted result of NANDing address lines A8 and A9 are ANDed together by a 7408 (A1). This output of A1 is then connected to pin 11 of U6 (which is in turn connected to pin 6 of U7). This line is the active high gate input of U7. Thus, U7 becomes active only when a memory read or write occurs to addresses 2F00H to 2FFFH. U7 is a 74S138 (which is equivalent to an 8205) which decodes address lines A5, A6 and A7. Output 7 of U7 is low whenever a memory operation occurs between adresses 2FE0H and 2FFFH. This output is connected to the DAXEN/ line [the active low gate input of another 74S138 (U8)] and pin 13 of A4. U8 decodes address lines A4, A3 and A2, yielding the device selects for I/O circuits. These circuits decode A1 and A0 internally. The DAXEN/ line and the previously inverted fourth output of A11 are then NANDed together by A4. This output is then low only when a memory read or write occurs to an address between 2F00H and 2FDFH, and thus provides the chip select for PROM socket PR-3.

The DIP switch A3 allows selection of RAM addresses. Since RAM is provided in 16K blocks in this design, two switches must be closed for each block of 16K. The outputs of A3 are ANDed together in groups of four by a 74H21 (A7). Pull up resistors (A6) serve to hold lines connected to open switches of A3 high. The outputs of A7 are further ANDed with 5 volts by A12, yielding a low output from A12 when any address

within the selected region is requested. This signal is then ORed (A8) with the inverted active low RAM inhibit line from the bus. This output of A8 is then connected to the chip select of the 8202 (R1) and is also connected to pin 1 of a 74157 (R3) and is ANDed (A1) with the PROM and I/O select line to yield the BRDSEL/ signal. The 8202 then provides additional decoding to select the appropriate 16K block of RAM whenever it is selected. In addition, R1 provides advanced acknowledge ($\overline{AACK}$) and transfer acknowledge ($\overline{XACK}$) signals to inform the CPU that the data has been successfully transferred to or from the bus, whenever it is selected.

The transfer acknowledge signals must be provided by any devices accessed by the CPU. Devices in the PROM and I/O section do not generate transfer acknowledge signals. The MSC 8204 provides a means of generating these acknowledge signals at a selectable number of bus clock (9.216 MHz) cycles after BRDSEL/ goes low. Since there are two different sources of these acknowledge signals, a multiplexer (R3) selects the appropriate levels to be connected to the bus. (Note: R3 is equivalent to A10 of the electron spectrometer board not to the R3 of that board.) R3 is connected so as to route the acknowledges from R1 to the bus whenever R1 has been selected (RAM operation) and to route the timed acknowledges to the bus whenever a BRDSEL/ occurs without R1 being selected.

The second section is the pulse generator and parallel interface section. This section provides the interface to the dye laser stepping motors (both the Nd:YAG pumped laser and the nitrogen pumped laser) and to the doubling and mixing crystal positioning circuit of the Nd:YAG

pumped dye laser. (A discussion of the Nd:YAG system will appear in the thesis of David J. Moll.) The pulse generator circuitry consists of two 8253 programmable interval timers (C0 and C1), a TTL oscillator circuit (C3) and a driver (C2). Programmable pulse generation is actually accomplished using counters 0 and 1 of C0. Counter 0 of C0 is programmed to operate in mode 4, square wave rate generator, and is loaded with a count of 15. The input frequency to counter 0 is the 1.26 MHz produced by C3. Thus, the output of counter 0 is 84 kHz. This is then input as the clock to counter 1 of C0. Counter 1 of C0 is operated in mode 3 as a rate generator. The count to be loaded into counter 1 depends on the scan rate desired. The stepping motor drive systems used on both dye lasers produce a wavelength change of 1 nm in first order for each 400 pulses. Therefore, the count to be programmed into counter 1 is obtained from the equation:

$$C = \frac{12600}{GR}$$

where C is the count, G is the grating order, and R is the desired rate in nm/min. The maximum count for any counter of an 8253 is $2^{16} - 1$ (65535); therefore if C is greater than 65535, then C is divided by 10 and the count for counter 0 is changed to 150 from 15.

The output of counter 1 of C0 is connected to the clock inputs of counter 2 of C0 and counter 0 of C1 and also to the driver C2. The output of C2 is then connected to the pulse input of the stepping motor drivers. Counter 2 of C0 serves simply to count the number of pulses output to the stepping motor. The CPU may read this count and determine the current grating position. The output of counter 2 is connected to

interrupt line 3 so that if the maximum count of 65535 is reached, the computer is interrupted and may reprogram the counter. Counter 0 of C1 is programmed with a count corresponding to (2*Grating order -1)*2. When this count is reached, counter 0 generates an interrupt on line 4 indicating to the computer that the wavelength has been incremented by .01 nm so data from the integrators may be read. The remaining counters of C1 are not currently used. (Note: The counters of an 8253 are down counters so a count is reached when the actual count reaches zero. Also, it is due to a peculiarity of the counters that counter 0 of C1 must be programmed with (2*Grating order -1)*2 instead of the obvious 4* grating order.)

The parallel interface necessary to provide crystal positioning information for the Nd:YAG pumped dye laser as well as to provide the gate for the pulse generating circuitry is based on the 8255 programmable peripheral interface (P-1). Output 0 of port C of P1 (PC0) provides the gate for counter 0 of Cϕ. Output PC1 is connected to driver P2 and provides wavelength scan direction control. Outputs PB0, PB1 and PA0-PA7 are also connected to drivers P2 and P3 providing control of the crystal position. All outputs from the pulse generator and interface section are routed to the edge connector J2.

The third and fourth sections of the prototyped board, the 16K - 32K RAM section and the 4K PROM section, are virtually identical to the equivalent sections of the board used with the electron spectrometer. As those sections of the electron spectrometer board have already been described (Section 2.4.2), only differences between the boards will be detailed here.

The 16K - 32K RAM section is identical to that shown in Figure 6 of Section 2.4.2 with the following exceptions: (1) Component R3 of this board is not equivalent to R3 of the EIS board. R3 of the MPI board is equivalent to A10 of Figure 5 of Section 2.4.2. The RAS/ inputs of R16-0,7 are connected directly to the RAS3/ output of R1. The RAS/ inputs of R32-0,7 are connected to the RAS4/ output of R1. (2) Sockets R32-0,7 are currently wired for Intel 2117-4's on the MPI board. Since 2117-4's are no longer available, these sockets must be rewired for 2118's as was done on the EIS board.

The 4K PROM section is identical to that of the equivalent section of the EIS board shown in Figure 7 of Section 2.4.2. There is of course no serial interface on the MPI board. The only difference between the two PROM sections is in the positioning on the board of the chips occupying particular memory addresses. In both cases, the lowest numbered PROM occupies the lowest 1K block of address space utilized.

6.5 MPI Computer System Software

Software for the MPI computer system consists of the Intel SBC 925 monitor, the iCOM Floppy Disk Operating System (FDOS III), and the numerous assembler language routines I have written. The SBC 925, the resident module of FDOS III, and many assembler language subroutines reside in PROM. The bulk of FDOS III and the laser scan routine are diskette resident and are loaded into RAM for execution.

6.5.1 Intel SBC 925 Monitor

The SBC 925 consists of two sections: a command controlled monitor for the SBC 80/20 and an exerciser/diagnostic for the SBC Flexible Diskette Controller and Diskette Drives. The SBC 925 resides on four 2708 PROM's and is designed to occupy memory space from 0000H-0FFFH. Since the MPI computer system uses an iCOM Floppy Disk System instead of the Intel system, the second part of SBC 925 is not used. The instructions belonging to the diskette diagnostic have been deleted, by simply not installing the second two 2708's and by copying bytes 0 through 06ABH from the first two PROM's onto new PROM's. This results in a substantial savings (2K + bytes) in occupied memory space.

The monitor provides commands enabling display and alteration of memory and processor registers, initiation of execution of programs, and execution of single program steps. The monitor also provides routines for console operation through the serial port of the SBC 80/20 board including baud rate searching capability. The monitor also initializes the interrupt controller and provides a routine for servicing any interrupt which is not serviced by a user written routine. I have added two subroutines to the monitor which provide for initialization and operation of the serial port (the printer port) on the SBC 116. Detailed documentation of the SBC 925, including a listing of the program, may be found in the SBC 925 User's Guide.

6.5.2 iCOM Software

The iCOM software, the Floppy Disk Operating System (FDOS III) and

the Basic interpreter (DEBBI), have been previously discussed in Section 2.5.1. Only the input/output routine vectors stored on the resident module PROM differ between the EIS computer system and the MPI computer system, due to the use of different monitors. The correct I/O vectors for the MPI system are:

Keyboard Input Vector: 02F4H

Console Output Vector: 0307H

Reader Input Vector: 02F4H

List Output Vector: 06CAH

Punch Output Vector: 0307H

Neither a reader nor punch device exists currently on the system so the appropriate console input or output vector is used.

6.5.3 PROM Resident General Purpose Subroutines

I have written a large number of frequently used assembler language subroutines which provide for floating point arithmetic using the SBC 310 high-speed math board, floating point number input and display, and plotting using an X-Y recorder or oscilloscope. These routines reside in two 2708 PROM's in sockets 3 and 4 on the SBC 80/20 board and occupy memory from 0800H to 0FE9H. Numerous other short routines are also included. The addresses of these subroutines are shown in Table 4.

Subroutines MATH1 and FPMATH perform arithmetic operations using the SBC 310. Subroutine MATH1 initializes the high-speed math board, passes the operation code in register B to the SBC 310, and awaits completion of the operation, returning to calling routine if the operation

Table 4

Starting Addresses for General Purpose Subroutines

Subroutine	Starting Address
AUTORG	0FB9
AXIS	0EE0
BUFFERIN	0C3D
CLRMEM	0CB5
CMPHD	0CC2
CNVERT	086B
COMPLM	0CDB
DISEC	0C99
DSMSEC	0CAB
FIX	0882
FLOAT	087C
FPIN	0A4C
FPMATH	0831
FPOUT	0888
HXTODC	0A0D
INTMSK	0D31
MATH1	0800
OUTSTR	0C8D
PLOT	0F64
PLSCAL	0F2A
POWER	0C00
PTPLT	0F21
RTICAL	0DC5
SCALE	0EBF
SHIFTL	0851
SHIFTR	085E
TRANSFER	0C80
UNMASK	0D3F
VALDEC	0CCA

was successfully completed or exiting to the monitor if an error has occurred. The SBC 310 is instructed to use RAM from 7FF0H to 7FFFH for its computations. The first argument must be placed in locations 7FF0H-7FF3H and the second argument must be placed in locations 7FF4H-7FF7H before MATH1 is called. (Note: All routines dealing with the SBC 310 were written before the available memory was expanded by the memory expansion and interface board. At that time, 7FFFH was the highest RAM address available. The expansion RAM extends RAM addresses to BFFFH. Thus, the SBC 310 uses locations in the middle of available RAM which prohibits continuous data storage from 4000H to BFFFH if the SBC 310 is used since data in locations 7FFF0H to 7FFFH may be destroyed. The routines should be eventually changed to instruct the SBC 310 to use locations BFF0H-BFFFH.) Subroutine FPMATH performs arithmetic operations on arguments pointed to by the HL register pair (the first argument) and the DE register pair (second argument). The arguments are moved to locations 7FF0H to 7FF7H then MATH1 is called, thus performing the requested operation. The result is then placed in the location originally specified by the HL register pair.

The subroutine FPOUT may be called to output a number stored in binary floating point format to the console in decimal floating point format. The base address of the stored number must be stored in register pair HL before calling FPOUT. The decimal number is output to the console at the current cursor position.

Subroutine FPIN enables input of a number from the console. The number is input in decimal (fixed or floating point) and is converted to

binary floating point by FPIN. The resulting number is stored in memory at the base address specified by register pair HL when the routine was called.

Subroutine POWER raises a binary floating point number stored at base address 7FF0H to an integral power stored in register C. Care must be exercised when calling this routine since if an overflow or underflow occurs, the routine will exit to the monitor.

Other subroutines provide for input of characters from the console into memory (BUFFERIN), transfer of blocks of memory to new locations (TRANSFER), output of character strings to the console (OUTSTR), delays of 1 second (D1SEC) and 5 milliseconds (D5MSEC), loading a section of memory with zeroes (CLRMEM), and comparing the value contained in the HL register pair with that in the DE register pair (CMPHD). A program which aids in calibration of the RTI 1200 is included as is a subroutine for automatic gain ranging for inputs to the RTI 1200 (AUTORG).

Additional subroutines provide for XY plotting using an XY recorder or oscilloscope and the two DAC outputs of the RTI 1200. Subroutine AXIS may be called to draw X and Y axes each 4000 points long with tick marks every 400th point. Subroutine SCALE outputs 0 or 4000 to both DAC's, enabling setting of the plotter vertical and horizontal ranges.

A set of subroutines which were designed to function with a previous interface board is contained in locations 0CEEH to 0D30H and 0D4EH to 0DC4H. These routines are not compatible with the current memory expansion and interface board and may be deleted.

6.5.4 Diskette Resident Software

Most of the larger and more sophisticated programs are designed to operate in RAM since locations within the program may be altered during run time enabling increased program flexibility. These programs are stored on diskettes and are loaded into RAM immediately prior to execution. The diskette resident software consists of all the programs described in Section 2.5.5 and two programs STPRS and MTD2S which are used only on the MPI comptuer system.

The program STPRS sets the laser wavelength scan rate and acquires data from the integrators, displays the normalized signal on the XY recorder and storage oscilloscope, and stores both the signal and intensity values obtained at each wavelength increment on a diskette. This program has also been modified slightly by David Moll to calculate the doubling or mixing crystal position that is appropriate for the current dye laser wavelength using parameters determined by a BASIC routine also written by Mr. Moll. The calculated positions are output to the Molectron crystal positioning drive unit each .01 nm during a scan. STPRS occupies RAM from 4000H to 4B48H and uses locations from 5000H for storage of signal data and from 6800H for storage of laser intensity data. Locations from 3800H to 384EH are used for storage of data input to the program. Additional locations from 3DF0H to 3FFFH are also altered by the program. Table 5 lists the locations in RAM used by STPRS.

Immediately following initiation of execution of the program, interrupts are disabled and the interrupt controller is reset. The 8255 P1 is then initialized. The computer then inquires 'SCALE PLOTTER?'.

Table 5

STPRS Memory Usage Table

3800-3802	Counter 0 of C0 (Mode, LSB, MSB)
3803-3805	Counter 1 of C0
3806-3808	Counter 2 of C0
3809-380A	Counter 0 of C1
380B-3824	Unused
3825-3828	Starting Laser Counter Position
3829-382C	Present Wavelength
382D-3830	Final Laser Counter Position
3831-3834	Grating Order
3835-3838	Scan Rate
3839-383C	Present Laser Counter Position
383D-3840	Vertical Scale Factor
3841	Horizontal Scale Factor
3842	Normalization Exponent
3843-3846	Temporary Storage
3847-3848	Number of Pulses Output
3849-384A	Number of Data Points Recorded
384B-384C	Current Address of Signal Data
384D-384E	Current Address of Intensity Data
384F-3CDF	Unused
3CB0-3CEF	Used by FDOS Resident
3CF0-3DEF	Unused
3DF0-3DFF	Output Buffer
3E00-3EFF	Input Buffer
3F00-3F80	May Be Used for Processor Stack
3F81-3FDF	Unused
3FE0-3FFF	Interrupt Jump Table
4000-4B48	Program
5000-67EF	Available for Signal Data Storage
6800-7FEF	Available for Intensity Data Storage
7FF0-7FFF	Reserved for SBC 310 Operation
BF70-BF9F	Crystal Position Parameters

If a 'Y' is entered, the plotter scaling routine is executed allowing the operator to set the range and zero of the plotter. If any other character is entered or after exiting from the scaling routine, then the computer will request the current laser counter position to be entered. Following input of the counter position, the computer will calculate the doubling or mixing crystal position. (If no crystal is being used, then the polynomial coefficients should be set to zero to avoid overflow.) Next, the computer will type 'R/S' inquiring whether running or slewing is requested. (No data may be taken in the slew mode. This is simply used to position the laser wavelength quickly.) If an 'S' is entered, the computer will request the desired final counter position. The CPU will wait until another character is entered before beginning slewing. Once slewing has begun, entry of any character will immediately stop the slew.

If any character besides 'S' was entered, the program operates in the run mode. The CPU will request the grating order to be used and the desired scan rate (nm/min). Once the scan rate has been input. The CPU calculates the values to be programmed into the counters 0 or 1 of 8253 C0. The algorithm used was discussed in Section 6.4.3. The value to be used for counter 2 of Cϕ is then calculated (4*Grating Order -2). This yields an interrupt 3 every .01 nm during a scan. The scan length in nanometers is then requested. If a positive value is entered, the laser wavelength will be increased during the scan. If a negative scan length is entered, the wavelength will be decreased. (Note: The maximum scan length is about 30 nanometers if data are to be taken, due to memory allocation limitations.)

The computer will then type 'DATA?'. If a 'N' is entered, no data will be taken. (This mode is used to simply move the laser wavelength to another position.) If a 'Y' is entered then the vertical and horizontal display scale factors will be requested. The vertical scale factor should be chosen such that the scale factor times the maximum signal divided by the intensity raised to the normalization exponent equals about 4000. The horizontal scale factor should equal 40 nm ÷ (scan length) and must be an integral value. Next, the normalization exponent will be requested. This exponent must be an integral value.

After all the parameters have been specified, the computer will type the current laser counter position and the corresponding wavelength. The counters will then be programmed with the appropriate values. Counter 0 of C1 is programmed with FFFEH and is simply used to count the number of pulses output to the stepping motor. An interrupt 4 is issued by the counter if more than 65535 pulses are received. The starting laser counter position is then updated and the counter is reprogrammed. The computer will await the entry of a character from the keyboard before initiating the scan. Data points will be taken every .01 nm at which time the displayed counter position and wavelength will be incremented. The new point will also be displayed on the XY recorder and the storage oscilloscope. Scanning and data acquisition will continue until either the final counter position is reached (determined using the input scan length) or a character is entered from the console.

Following completion of a scan or slew, the computer will disable interrupts and shut off the gates to the pulse generating counters. If

a slew has been completed, the computer will ask 'MNTR OR STPRS?'. Entry of an 'M' will cause the CPU to exit to the monitor program. Entry of any other character will restart STPRS. If a scan has been completed, the computer will inquire whether the operator wishes to restart STPRS, exit to the monitor or FDOS, or draw axes on the XY recorder. After axes are drawn, the CPU will ask whether the data are to be written to disk. If any character but 'Y' is entered, STPRS is restarted. If 'Y' is entered, the CPU will type the number of data points taken. A continuous block in memory will be formed which consists of two bytes for the number of data points, followed by data. Intensity data immediately follow the last signal data point taken during the scan. The address of the end of the data set will then be typed. The computer will request an FDOS filename for the data set. After an acceptable filename is received, the data set is written to the diskette. The computer will then inquire whether the operator wishes to exit to the monitor or FDOS or to restart STPRS.

The program MTD2S is designed to write data contained in memory between specified limits to diskette or to read a file previously written on a diskette into memory. This program is very similar to MDESS (Section 2.5.5) except that MTD2S stores data on disk in binary not the hex ASCII format which is used by MDESS. Also, no checksum bytes, record lengths, or memory addresses are stored. Therefore, MTD2S makes more efficient use of diskette space.

Following loading of MTD2S, the CPU will request an FDOS compatible filename. This filename should be either the name of an existing file to be read or the name of a new file to be created. After an acceptable

filename has been received the computer will type 'READ OR WRITE?'. If any character other than 'W' is entered, the CPU will attempt to open the diskette file specified for reading. If the file is not found, the CPU will request another filename. If the file is found, the computer will type 'MEMLO'. The starting memory address (in hexadecimal) of the block into which the file is to be written should then be entered. If an acceptable address has been received, the diskette file will be copied into RAM starting at MEMLO. (Note: The file length must not exceed the available memory space.) The computer will then type 'FDOS OR MNTR?'. If 'F' is entered, the CPU will load FDOS, overwriting MTD2S. If any other character is entered, the CPU will exit to the monitor. The monitor may then be used to examine or alter the file now stored in RAM.

IF 'W' was entered, the computer enters the write mode. The computer will then ask the low address and the high address of the block of memory to be written to the diskette file specified previously. The final sector of the diskette file will be padded with zeroes, if necessary, since 128 bytes must be written to a sector. As in the read mode, the program ends when the CPU types 'FDOS OR MNTR?'. For read or modify operations involving a single sector 'EXAMS' is much easier to use; however, for multiple sector operations MTD2S is more efficient. Also, since no memory addresses are stored by MTD2S, the operator need not specify an offset from the stored starting address as is necessary for use with MTESS. Also, although there are no checksum bytes used by MTD2S, no errors in data transfer have occurred when using this program.

6.6 Data Handling

Data obtained using the MPI computer system is stored on diskettes so that data analysis and plotting may be accomplished with the computer center's IBM 370/3032 system using programs written in FORTRAN. As was mentioned previously in Section 2.6, the IBM 370/3032 system possesses no facility for retrieval of data directly from diskettes. It is necessary to transfer the contents of a diskette to an IBM compatible magnetic tape, to reorder the data on the magnetic tape to its correct sequence, and to translate the binary data to EBCDIC before additional FORTRAN programs may be utilized to analyze the data. The computer center possesses hardware which will copy the data contained on user specified tracks (all tracks excepting track 0, which contains directory information, are requested to be copied in this case) onto a magnetic tape. The resulting tape contains an image of the contents of the diskette. The tape format is 9-track, 1600 bpi, with a blocksize of 3328 bytes (one block contains one diskette track of data), and record format F. The data now contained on the tape are written in binary and must be translated to a FORTRAN compatible format before they may be accessed by data analysis programs. Also, the data on the magnetic tape are not in the proper sequence due to differences between the floppy disk drive controller used by the computer center and that used by the MPI computer system. I have written a FORTRAN program FLOPPY which performs the necessary translation and reordering of the data.

FLOPPY is very similar to the program ESTOMT (FLOPPY actually

predates ESTOMT) which performs the translation and reordering of data for electron impact spectra and was described in Section 2.6. Unlike EIS data, the data produced by the MPI computer system consist entirely of binary numbers each of which is 2 bytes long. The format of the data on the diskette was described in Section 6.5.4.

A data card is entered for each spectrum on the diskette giving the spectrum number, the spectrum name, the date, the starting laser counter position, the final laser counter position, and the grating order used. One complete data set will be returned for each data card entered. (Note: The data cards must be in the same order that data sets appear on the diskette.)

One entire track of data (one block on the magnetic tape) is read at a time using the system subroutine READSP. READSP converts each 8-bit byte in the 3328 byte block into a 16-bit word of the form ZOOFF (Z indicates hexadecimal in IBM FORTRAN) by filling the 8 most significant bits of the 16-bit word with zeroes and the 8 least significant bits with the data byte read from the magnetic tape. In this manner, READSP fills the integer *2 array TDATA with the data contained in one magnetic tape block. The data on one block of the magnetic tape consist of 1664 two-byte words written with the least significant byte first. The 1664 data words are formed by shifting the second integer *2 numbers in TDATA 8 bits to the left and then adding the resulting number to the other member of the pair by the subroutine which calls READSP,TRKRD. The array resulting, NDATA, now contains the 1664 data words which were originally written onto one track of the data storage diskette. The numbers in

NDATA are not properly sequenced, however due to the differences between the diskette driver controllers (see Section 2.4.1). The unidimensional array NDATA is then transferred into a bidimensional array IA(26,64) which effectively redivides the data into 26 sectors of 64 integer *4 numbers. (Actually, only the least significant 16 bits of each number are used.) These 'sectors' of data are then reordered as they are copied into another 26x64 array IDATA. [The matrix IDATA is organized like a diskette, the first 64 data words are IDATA (1,1-64) and the last 64 data words are IDATA (26,1-64).] IDATA now contains the data in the correct sequence. The first datum of IDATA [IDATA (1,1)] is the number of data points in the spectrum (NPTS). Subroutine MATFIL then copies the next NPTS numbers of IDATA into a unidimensional array ISIGNL (the set of MPI signal data). Another call to MATFIL fills the intensity array INTENS. When MATFIL reaches the last element of IDATA, another track of data is read and filling of the intensity or signal array is continued. This operation is continued until the entire NPTS of the array is copied.

The spectrum heading (input on a data card) and the data are then printed and written onto an IBM disk file. The first dimension of IDATA will be incremented by one and the second dimension will be set to one unless the last number of the intensity matrix corresponded to the 64th element of a row of IDATA. This positions a pointer effectively to the first datum of the next sector. The next card is then read (if there is no additional heading card the program terminates) and processing of the next data set begins at the pointer position. The number at this position is the number of data points in the next spectrum, since files on diskettes do not share sectors.

The disk file produced by FLOPPY thus contains all the data sets which were originally stored on the diskette along with the spectrum headings associated with each data set. This disk file may then be accessed by the data analysis programs, RSPLOT and DATAPL, which I have written.

RSPLOT is a program designed to plot both raw signal and raw laser intensity data on the same sheet, in order that the contribution of laser intensity fluctuations to the measured MPI signal may be more readily observed. The 10" x 14" plot area is divided into two 5" x 14" sections such that the MPI signal curve is plotted above the laser intensity curve. The vertical scale factor for each curve is chosen so that each curve spans the entire vertical scale available in its 5" x 14" section. (Since the amplifier gain is adjustable, intensity values recorded are not absolute.) The abscissa corresponds to the actual dye laser wavelength if a calibration point (the actual wavelength in nanometers corresponding to a specific data channel) is input or if no calibration point is given, the nominal wavelength scale will be used. (The nominal wavelength scale is given by using as a calibration point the starting laser counter position (from the heading) divided by the grating order times 10, yielding the nominal wavelength in nm, and channel number 1 as the reference channel.) The plot may also be scaled to thesis size (5" x 7") instead of 10" x 14", if desired.

Datapl is a FORTRAN program which is designed to calculate the intensity dependence of an MPI spectrum. Two spectra taken over the same wavelength range and at identical amplifier settings are input into

the program. (Only spectrum numbers need to be given since the spectra are already stored on disk by FLOPPY.) The laser intensities used when the spectra were run should differ by 5 - 10%. Since the intensity dependence is not constant, it is important that the intensities used differ enough that signal noise is not an important contributor to the apparent dependence but not so great as to be causing different levels of saturation. Datapl then performs a least squares fit of the data to

$$S_\lambda = \sigma_\lambda I_\lambda^{**FNORM}$$

where S_λ is the observed MPI signal at a particular wavelength, I_λ is the corresponding laser intensity, FNORM is the intensity dependence, and σ_λ is proportional to the transition cross-section. (This fit is valid only if a small fraction of the molecules is excited. This is generally the case for the very weak two-photon or spin-forbidden transitions studied.) Each spectrum is then normalized and plotted. (This is essentially plotting σ_λ.)

DATAPL is also used for plotting spectra for publication. (If only one spectrum number is given, no fitting is performed.) A calibrated wavelength scale is obtained through the use of a calibration point as with RSPLOT. (The dye laser wavelength drive is very nearly linear so only one calibration point is necessary to obtain an absolute calibration for the entire spectrum.)

Both DATAPL and RSPLOT have been recently modified by David Moll such that a correct laser wavelength scale is plotted for spectra taken using a frequency doubling or mixing crystal. Since in cases in which a mixing crystal has been used to mix an Nd:YAG beam with the dye laser

beam, the output wavelength is not linearly related to the laser counter position (or dye laser wavelength) a new set of interpolated data is formed in a subroutine before plotting or curve fitting is done. The resulting data set thus contains points which are now equally spaced in wavelength. For cases in which a doubling crystal has been used, the labels on the wavelength axis are simply halved.

References

1. Model UV 400 Pulsed Nitrogen Laser Manual, Molectron Corporation.
2. E. T. Gerry, Applied Physics Letters 7, 6 (1965).
3. J. K. Rice, PhD Thesis, California Institute of Technology, 1969.
4. N. Gellar, D. E. Altmann and T. A. DeTemple, Applied Optics 7, 2232 (1968).
5. F. P. Schafer, "Dye Lasers", (Springer-Verlag, New York, 1973).
6. T. W. Hansch, Applied Optics 11, 895 (1972).
7. G. Capelle and D. Phillips, Applied Optics 9, 2742 (1970).
8. C. F. Dewey, W. R. Cork, R. T. Hodgsin and J. J. Wynne, Applied Physics Letters 26, 714 (1975).
9. DL-Series Tunable Dye Laser manual, Molectron Corporation.
10. Spectroscopy Preamplifier Model 2001/2001A Instruction Manual, Canberra Industries, Inc.
11. Rk 3200 Series Pyroelectric Energy Meter Operating Instructions, Laser Precision Corporation.
12. Molectron Laser Spectroscopy Detector System Instruction Manual, Molectron Corporation.

7. Results and Discussion

7.1 Paper 1: Detection of the $^3A_2$ State of CS_2 by Multiphoton Ionization.

DETECTION OF THE $^3A_2$ STATE OF CS_2 BY MULTIPHOTON IONIZATION

Ronald RIANDA,* David J. MOLL, and Aron KUPPERMANN

Arthur Amos Noyes Laboratory of Chemical Physics,**
California Institute of Technology, Pasadena, California 91125, USA

Received

The application of the technique of resonance-enhanced multiphoton ionization (REMPI) spectroscopy to the detection of triplet states via a first photon resonance is examined. It is shown to work well for the $\tilde{a}\,^3A_2$ state of CS_2. This technique promises to permit the detection of spin-forbidden transitions at high resolution and with great sensitivity.

---

* Work performed in partial fulfillment of the requirements for a Ph. D. in Chemistry at the California Institute of Technology.

** Contribution No. 6082.

The REMPI technique [1-10] has been extensively utilized for the detection of two-photon excitations. However, it has not been employed for the investigation of weak one-photon absorptions, such as singlet → triplet transitions [10]. Such an application could lead to a useful method of studying these kinds of processes, and it is examined in the present paper.

The near-ultraviolet absorption bands of CS_2 extending from 390 to 330 nm have been the subject of extensive experimental and theoretical investigation [11-18]. The vibrational and rotational structure of the bands indicates that the spectrum results from transitions from a linear ground state ($^1\Sigma_g^+$) to a bent excited state of B_2 symmetry [13]. Douglas and Milton [14] and Hougen [15] have studied the pronounced Zeeman effect of the bands and have shown that it can only be understood if the observed B_2 state is a component of a $^3A_2$ state with substantial triplet splitting. Differential cross section measurements performed by Flicker et al. [18] using low-energy, variable-angle electron-impact spectroscopy are also consistent with assignment of the transition as singlet → triplet in nature.

REMPI spectroscopy has proven to be a very sensitive technique for studying two-photon electronic transitions [1-10]. Parker et al. [19] have shown that when the transitions from the two-photon excited state to the continuum are saturated, which is generally the case at the intensities normally used for such experiments, the weak two-photon process is rate-determining, and the ion current is proportional to the rate of the two-photon resonance excitation. In the present case the initial one-photon singlet → triplet transition is strongly forbidden

($f < 5 \times 10^{-7}$ in the spectral region studied)[16], and subsequent excitations within the triplet manifold are expected to be many orders of magnitude faster. Therefore, the initial step is the rate-limiting process, and the spectrum of the singlet→triplet transition is generated as the laser wavelength is scanned.

The experimental apparatus used differs somewhat from that reported by other researchers. The laser system consisted of a Molectron DL 200 dye laser pumped by a UV400 nitrogen laser. Output power in the spectral region studied, 375 to 360 nm, varied monotonically from 30 kW to 5 kW using the dye PBD at 20 Hz. The laser beam was focused with a quartz lens (f = 50 mm) into a gas cell containing two parallel plates 0.75 in. square separated by 0.75 in. The charge pulse is detected by a Canberra 2001A charge-sensitive preamplifier with a nominal sensitivity of 10 V/picocoulomb. The preamplifier output and the output from the pyroelectric joulemeter, which monitored the laser-pulse energy, were directed into a dual-channel, gated differential integrator system. A microcomputer system digitized and stored the data and controlled the laser wavelength scan. The sample pressure was 5 torr.

A typical REMPI spectrum of CS_2 is shown in fig. 1. The spectrum displays the sharp structure characteristic of transitions to the $^3A_2$ state superimposed on a broad, intense doublet. The peaks assigned by Kleman [13] and Douglas and Milton [14] using absorption techniques appear in our spectra with positions agreeing within our wavenumber calibration accuracy of 4 cm^{-1}. Representative results for the Σ and Π bands are summarized in Table I. The band oscillator strengths

measured by Barrow and Dixon [16] are also listed to give an indication of the sensitivity of the REMPI technique. We detect vibronic transitions having oscillator strengths as low as 2.7×10^{-8}.

An intense doublet has been observed at 55,002 and 55,197 cm^{-1} by Price and Simpson [20]. Rabalais et al. [21] reported a broad, unresolved feature at 54,963 cm^{-1}. Both groups assigned this transition as a π_g orbital to sulfur 4s Rydberg excitation. This transition is forbidden ($^1\Sigma_g^+ \rightarrow {}^1\Pi_g$) for single photon excitation but can acquire intensity through vibronic coupling with either the $\nu_2(\pi_u)$ or $\nu_3(\sigma_u^+)$ vibrational modes. The transition is allowed for two-photon excitations, however. It is likely that the two-photon singlet $\rightarrow$ singlet transition accounts for the doublet observed in our spectra at about 367.2 and 365.5 nm, corresponding to two-photon transition energies of 54,466 and 54,720 cm^{-1}, respectively. The accuracy of these values is affected by the presence of the superimposed one-photon bands. The differences between the average of our doublets and those obtained by Price and Simpson [20] and Rabalais et al. [21] are 506 and 370 cm^{-1}, respectively. The latter correlates well with the ν_2 vibrational frequency of 397 cm^{-1} for the ground electronic state.

Several peaks are observed between 368 and 369 nm that, because of their positions and intensities, cannot be assigned to the $\tilde{X}\,^1\Sigma_g^+ - \tilde{a}\,^3A_2$ excitation. This structure may also result from the two-photon $\tilde{X}\,^1\Sigma_g^+ - \tilde{B}\,^1\Pi_g$ transition. The peaks are separated by approximately 36 cm^{-1}, suggesting that they are due to rotational structure arising from a slightly bent configuration in the excited state. Such an explanation has been offered by Price and Simpson [20] for the 40 cm^{-1} spacing between band heads in the 208 nm band.

In summary, we have shown that REMPI spectroscopy is a very sensitive technique for studying spin-forbidden single-photon transitions. The current availability of far more intense pulsed dye lasers promises applicability of this technique to other molecular systems for which the spin-orbit coupling is much weaker than for CS_2. At sufficiently high intensities, however, the nonresonant MPI process will dominate the signal and limit this technique [22]. Below such intensities and under saturation conditions, the different power dependencies of the initially spin-forbidden process vis-a-vis that of any energetically coincident spin-allowed two-photon processes should allow deconvolution of the spectra, yielding both the single-photon spin-forbidden spectrum as well as the two-photon spin-allowed spectrum. Our measurements indicate that in our experimental arrangement over the pulse energy range 3 to 24 μJ/pulse the 06-Π1 spin-forbidden transition signal varies as laser intensity to the 3/2 power. Such dependence, under saturation conditions, for a first photon resonance multiphoton process has been previously observed [23, 24] and attributed to features of the focusing geometry [23-25]. The two-photon spin-allowed transition signal, measured at 366.9 nm where the spin-forbidden transition contribution is assumed to be small (since there is only little sharp structure characteristic of the $\tilde{a}\ ^3A_2$ state at this wavelength), varies approximately as the laser intensity squared. Furthermore, comparison of the resulting intensities of the one-photon spin-forbidden transitions with those of a pulsed ultraviolet laser photoacoustic spectroscopy technique recently developed in our laboratory may furnish information about the dynamics of energy relaxation from these electronically excited states.

Acknowledgements

This research was supported in part by the U. S. Department of Energy Grant No. EX-76-G-03-1305. However, any opinions, findings, conclusions, or recommendations expressed herein are those of the authors and do not necessarily reflect the view of DOE. Partial support was also provided by the U. S. Department of Energy Contract No. DE-AS03-76SF00767, Project Agreement No. DE-AT03-76ER72004. Report Code: CALT-767P4-181.

TABLE I. Transition wavenumbers (in cm^{-1}) and oscillator strengths for the $\tilde{X}\,^1\Sigma_g^+ - \tilde{a}\,^3A_2$ Σ and Π bands of CS_2.

	Present Work	Kleman[a]	Douglas[b]	$10^7 f_{v'v''}$ Barrow[c]
Σ Bands				
05-02	26,898	26,894.9	26,901.25	0.99
06-02	27,188	27,183.7	27,190.06	2.88
07-02	27,469	27,467.1	27,471.96	4.54
03-00		27,101.8		0.002
04-00		27,402.5		0.007
05-00	27,689	27,698.0	27,703.29	0.029
13-02	26,986	26,981.8	26,990.39	0.27
14-02	27,281	27,278.6	27,285.22	1.01
15-02	27,567	27,564.9		1.98
Π Bands				
06-03	26,790	26788.0		
07-03	27,074	27,068.9		
08-03	27,346	27,342.9		
04-01	27,014	27,013.8		
05-01	27,313	27,309.9	27,314.46	
06-01	27,601	27,599.6		
14-03	26,884	26,882.1	26,886.66	
15.03	27,168	27,166.5		
16-03	27,432	27,430.1		
17-03	27,676	27,675.0		
13-01		27,397.3		
14-01	27,694	27,693.4	27,697.59	

[a] Reference [13].

[b] Reference [14].

[c] Reference [16].

REFERENCES

[1] M. Lambropoulos, S. E. Moody, W. C. Lineberger, and S. J. Smith, Bull. Am. Phys. Soc. 18 (1973) 1514.

[2] M. Lambropoulos, S. E. Moody, S. J. Smith, and W. C. Lineberger, Phys. Rev. Lett. 35 (1975) 159.

[3] G. Petty, C. Tai, and F. W. Dalby, Phys. Rev. Lett. 34 (1975) 1207.

[4] P. M. Johnson, M. R. Berman, and D. Zakheim, J. Chem. Phys. 62 (1975) 2500.

[5] P. M. Johnson, J. Chem. Phys. 62 (1975) 4562.

[6] P. M. Johnson, J. Chem. Phys. 64 (1976) 4143.

[7] P. M. Johnson, J. Chem. Phys. 64 (1976) 4638.

[8] D. H. Parker, S. J. Sheng, and M. A. El-Sayed, J. Chem. Phys. 65 (1976) 5534.

[9] D. H. Parker and P. Avouris, Chem. Phys. Lett. 53 (1978) 515.

[10] R. E. Turner, V. Vaida, C. A. Molini, J. O. Berg, and D. H. Parker, Chem. Phys. 28 (1978) 47. In this work, a triplet state of pyrazine was detected during the course of a REMPI search for the analog of the E_g state observed in benzene by Johnson [7] via a two-photon resonance.

[11] L. N. Liebermann, Phys. Rev. 60 (1941) 496.

[12] A. E. Douglas, Can. J. Phys. 36 (1958) 147.

[13] B. Kleman, Can. J. Phys. 41 (1963) 2034.

[14] A. E. Douglas and E. R. V. Milton, J. Chem. Phys. 41 (1964) 357.

[15] J. T. Hougen, J. Chem. Phys. 41 (1964) 363.

[16] T. Barrow and R. N. Dixon, Mol. Phys. 25 (1973) 137.

[17] M.-J. Hubin-Franskin and J. E. Collin, J. Electron Spectrosc. 7 (1975) 139.

[18] W. M. Flicker, O. A. Mosher, and A. Kuppermann, J. Chem. Phys. 69 (1978) 3910.

[19] D. H. Parker, J. O. Berg, and M. A. El-Sayed, in: Advances in laser chemistry, ed. A. H. Zewail (Springer-Verlag, New York, 1978), pp. 320-335.

[20] W. C. Price and D. M. Simpson, Proc. R. Soc. London, Ser. A: 165 (1938) 272.

[21] J. W. Rabalais, J. M. McDonald, V. Scheer, and S. P. McGlynn, Chem. Rev. 71 (1971) 73.

[22] L. Zandee and R. B. Bernstein, J. Chem. Phys. 71 (1979) 1359

[23] G. Hancock, J. D. Campbell and K. H. Welge, Opt. Commun. 16 (1976) 177.

[24] T. P. Cotter and W. Fuss, Opt. Commun. 18 (1976) 31.

[25] S. Speiser and J. Jortner, Chem. Phys. Lett. 44 (1976) 399.

FIGURE CAPTION

FIG. 1. Multiphoton ionization spectrum of the single-photon $\tilde{X}\,^1\Sigma_g^+ - \tilde{a}\,^3A_2$ transition of CS_2 superimposed on the two-photon $\tilde{X}\,^1\Sigma_g^+ - B\,^1\Pi_g$ transition. The ordinate is corrected for the variation of laser pulse energy with wavelength. The sample pressure was 5 Torr. The band assignments at the top of the figure are for the $\tilde{X}\,^1\Sigma_g^+ - \tilde{a}\,^3A_2$ transition from Kleman [13] where Σ, Π, Δ, ..., correspond to $k' = \ell'' = 0, 1, 2, 3, \ldots$, and the symbol $12\text{-}\Sigma 3$ implies $v_1' = 1$, $v_2' = 2$, $v_2'' = 3$, and $v_3' = v_3'' = v_1'' = 0$. k is the symmetric top quantum number and ℓ is the quantum number describing the vibrational angular momentum. Vibrational modes 1, 2, and 3 correspond to the symmetric stretch, bend, and antisymmetric stretch, respectively, with double prime and single prime corresponding to ground and excited electronic states, respectively.

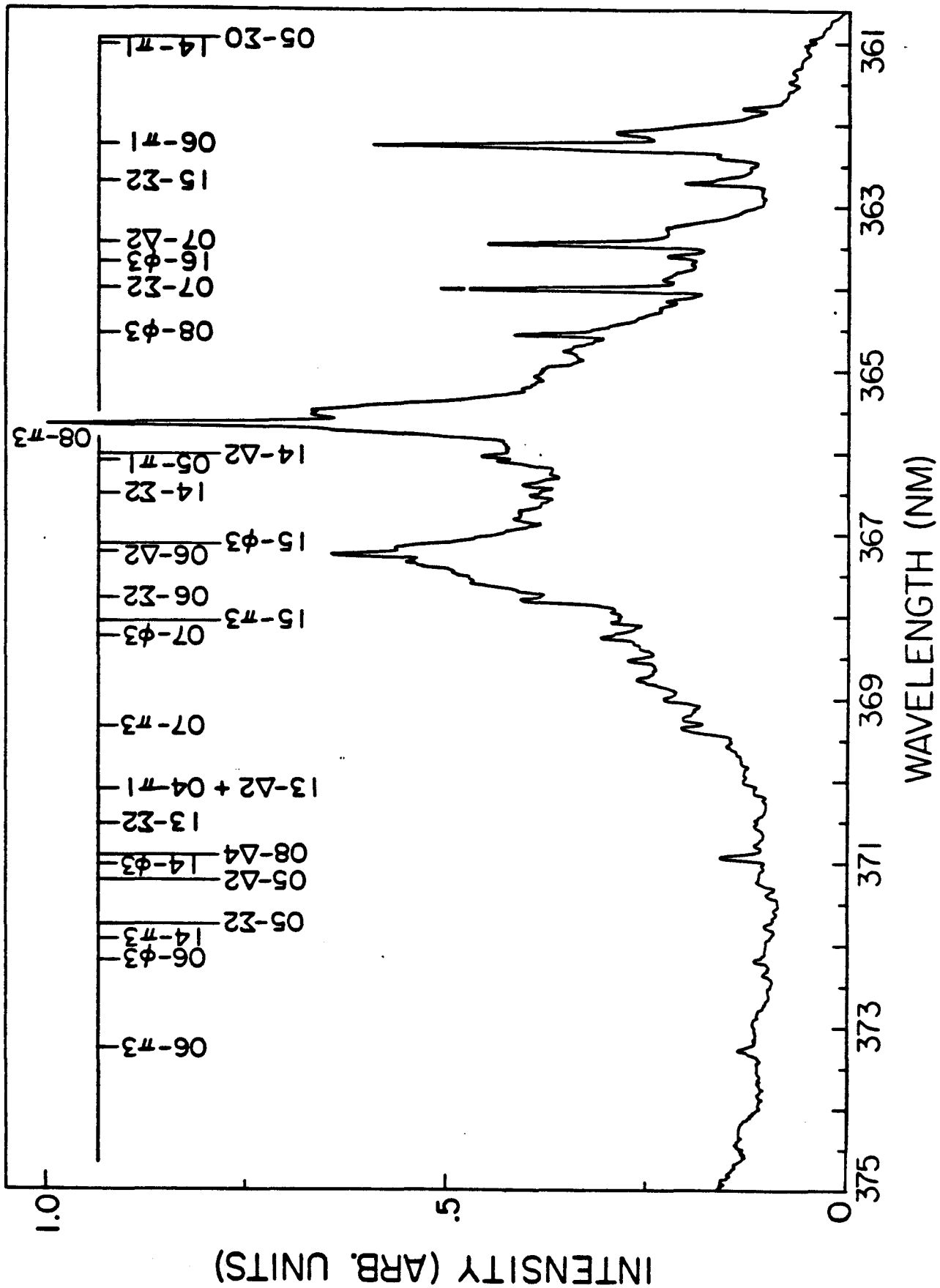
INTENSITY (ARB. UNITS)
1.0
.5
0
WAVELENGTH (NM)
361
363
365
367
369
371
373
375
05-Σ0
14-π1
06-π1
15-Σ2
07-Δ2
16-φ3
07-Σ2
08-φ3
08-π3
14-Δ2
05-π1
14-Σ2
15-φ3
06-Δ2
06-Σ2
15-π3
07-φ3
07-π3
13-Δ2 + 04-π1
13-Σ2
08-Δ4
14-φ3
05-Δ2
05-Σ2
14-π3
06-φ3
06-π3

7.2 Preliminary Investigation: The Multiphoton Ionization Spectrum of p-Xylene.

An investigation of the two photon resonance enhanced multiphoton ionization spectrum of p-xylene was undertaken in the spectral region 530.0 nm to 460.0 nm in order to determine the position of the $^1B_{2u}$ state, the analog to those observed previously in benzene[1-7] and p-difluorobenzene.[8] No previous study of the two-photon spectrum of p-xylene has been reported, and in fact no report of the single photon spectrum of p-xylene in the gas phase has appeared in the literature in English.

The point group to which p-xylene belongs has been reported to be both C_{2h}[9] and D_2,[10] however, use of the point group D_{2h} has yielded good results for the analysis of the vibrational spectrum of p-xylene.[9] It is therefore expected that the two-photon spectrum of p-xylene will resemble that of p-difluorobenzene although the number of vibrational modes is expected to increase the number of observed transitions.

The experimental apparatus was that reported by Rianda et al.[11] The p-xylene sample was obtained from Matheson Coleman and Bell and was subjected to several freeze pump thaw cycles prior to use. Sample pressures in the ionization cell were 5 torr. The sample cell was evacuated and refilled after each scan in order to reduce the buildup of photofragments.

The spectra obtained, normalized to the laser intensity, are shown in figures 1 through 3. Several broad bands are observed which increase in intensity to a sharp peak as wavelength decreases. The positions of the band maxima are 521.60, 511.25, 505.90, 501.08, 496.2, 491, 487, 482, 478 and 473.5 nm, corresponding to two-photon transition energies of 38344, 39120, 39534, 39914, 40306, 40700, 41100, 41500, 41800 and 42240 cm^{-1}.

Superimposed on most bands are numerous very sharp bands having a nearly constant spacing. Similar fluctuations are observed in the laser intensity at exactly the same wavelengths, however, the laser intensity fluctuations are only about 5-10%. The overall intensity dependence of the spectrum is about unity, measured by comparing signal strengths at a given wavelength different laser powers, and cannot account for the large fluctuations in the photoionization signal. Since the peak-to-peak spacing of the fluctuations is nearly constant, some etalon effect may be suspected. The spacing of .2 nm would correspond to interference from reflecting surfaces about .12 cm apart. Also since the joulemeter measure the energy of the beam before it enters the sample cell if the parallel surfaces exist within the cell then some feedback into the laser must occur to cause laser intensity fluctuations. The source of these fluctuations is currently unknown, however, it is unlikely that these sharper peaks correspond to real p-xylene structure.

The general features of the spectra are very similar to those of p difluorobenzene which have been analyzed by Robey and Schlag.[8] Spectra of p-difluorobenzene which I have obtained are shown in figures 4 and 5. As is the case for p-difluorobenzene the dominant active vibration is expected to be the b_{2u} mode ν_{14} (benzene notation). The strong vibronic origin at 38344 cm^{-1} may be assigned as the $14'_0$ band of the $^1A_g \rightarrow {}^1B_{2u}$ transition. The second band at 39120 cm^{-1} separated from the origin by 776 cm^{-1} probably indicates taht it is the $14^1_0 1^1_0$ band. The ν_1 frequency is very close to the value of 809 cm^{-1} observed in p difluorobenzene. The second element of this progression may account for the band at

39914 cm^{-1} although the energy spacing is greater than would be expected. A progression in another vibration of 1190 cm^{-1} would seem to account for bands at 39534 and 40700 cm^{-1}. The analogous mode in p-difluorobenzene is the 7z mode at about 1250 cm^{-1}.[8] The remaining bands may not be currently assigned due to the paucity of information regarding p-xylene's excited state vibrational frequencies. A complete polarization analysis should allow assignment of these additional bands. Additional study of p-xylene in this spectral region may also help to clarify the source of the enormous ionization signal changes with relatively small laser intensity fluctuations.

References

1. R. M. Hochstrasser, J. E. Wessel and H. N. Sung, J. Chem. Phys. 60, 317 (1974).
2. L. Wunsch, H. J. Neusser and E. W. Schlag, Chem. Phys. Lett. 32, 210 (1975).
3. D. M. Friedrich and W. M. McClain, Chem. Phys. Lett. 32, 541 (1975).
4. J. R. Lombardi, R. Wallenstein, T. W. Hansch and D. M. Friedrich, J. Chem. Phys. 65, 2357 (1976).
5. L. Wunsch, F. Metz, H. J. Neusser and E. W. Schlag, J. Chem. Phys. 66, 386 (1977).
6. L. Zandee and R. B. Bernstein, J. Chem. Phys. 71, 1359 (1979).
7. U. Boesl, H. J. Neusser and E. W. Schlag, J. Chem. Phys. 72, 4327 (1980).
8. M. J. Robey and E. W. Schlag, Chem. Phys. 30, 9 (1978).
9. M. V. Priyutov, Optics and Spectr 32, 32 (1972).
10. N. O. Lipari and C. B. Duke, J. Chem. Phys. 63, 1748 (1975).
11. R. Rianda, D. J. Moll and A. Kuppermann, Chem. Phys. Lett. 73, 469 (1980).

Figure Captions

Fig. 1: Multiphoton ionization (MPI) spectrum of the two-photon $^1A_g \rightarrow {}^1B_{2u}$ transition of p-xylene. The ordinate has been corrected for the variation of the laser pulse energy with wavelength. The laser wavelength is given along the abscissa. The sample pressure was 5 torr.

Fig. 2: MPI spectrum of the $^1A_g \rightarrow {}^1B_{2u}$ transition of p-xylene at laser wavelengths from 510 to 480 nm. All other conditions as for Fig. 1.

Fig. 3: MPI spectrum of the $^1A_g \rightarrow {}^1B_{2u}$ transition of p-xylene at laser wavelengths from 489.6 to 459.6 nm. All other conditions as for Fig. 1.

Fig. 4: MPI spectrum of the $^1A_g \rightarrow {}^1B_{2u}$ transition of p-difluorobenzene at laser wavelengths from 529.8 to 499.8 nm. The ordinate has been corrected for the laser pulse energy variation. The sample pressure was 5 torr.

Fig. 5: MPI spectrum of the $^1A_g \rightarrow {}^1B_{2u}$ transition of p-difluorobenzene at laser wavelengths from 510 to 480 nm. All other conditions as for Fig. 4.

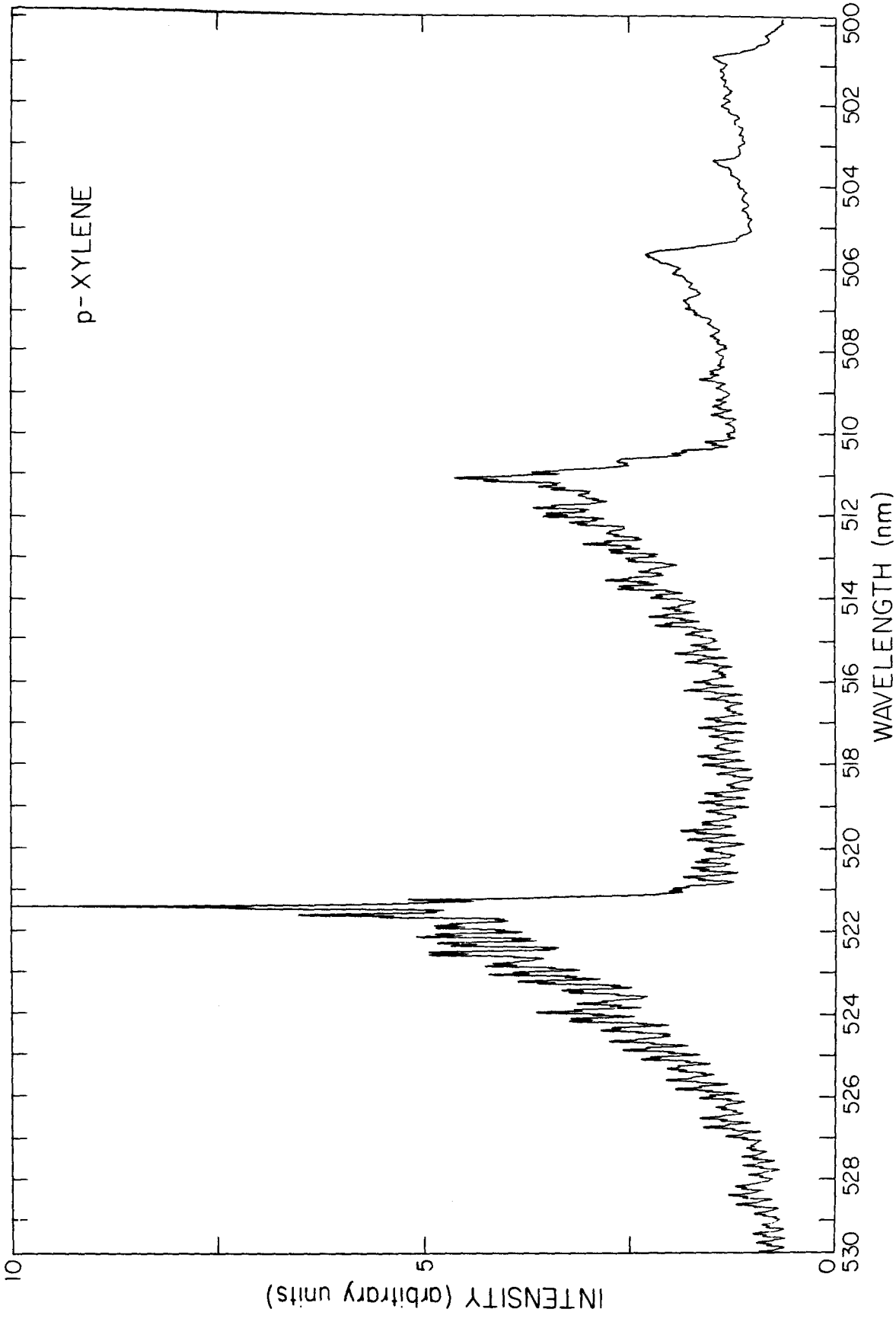
p-XYLENE
INTENSITY (arbitrary units)
WAVELENGTH (nm)
0
5
10
500
502
504
506
508
510
512
514
516
518
520
522
524
526
528
530

Figure 1

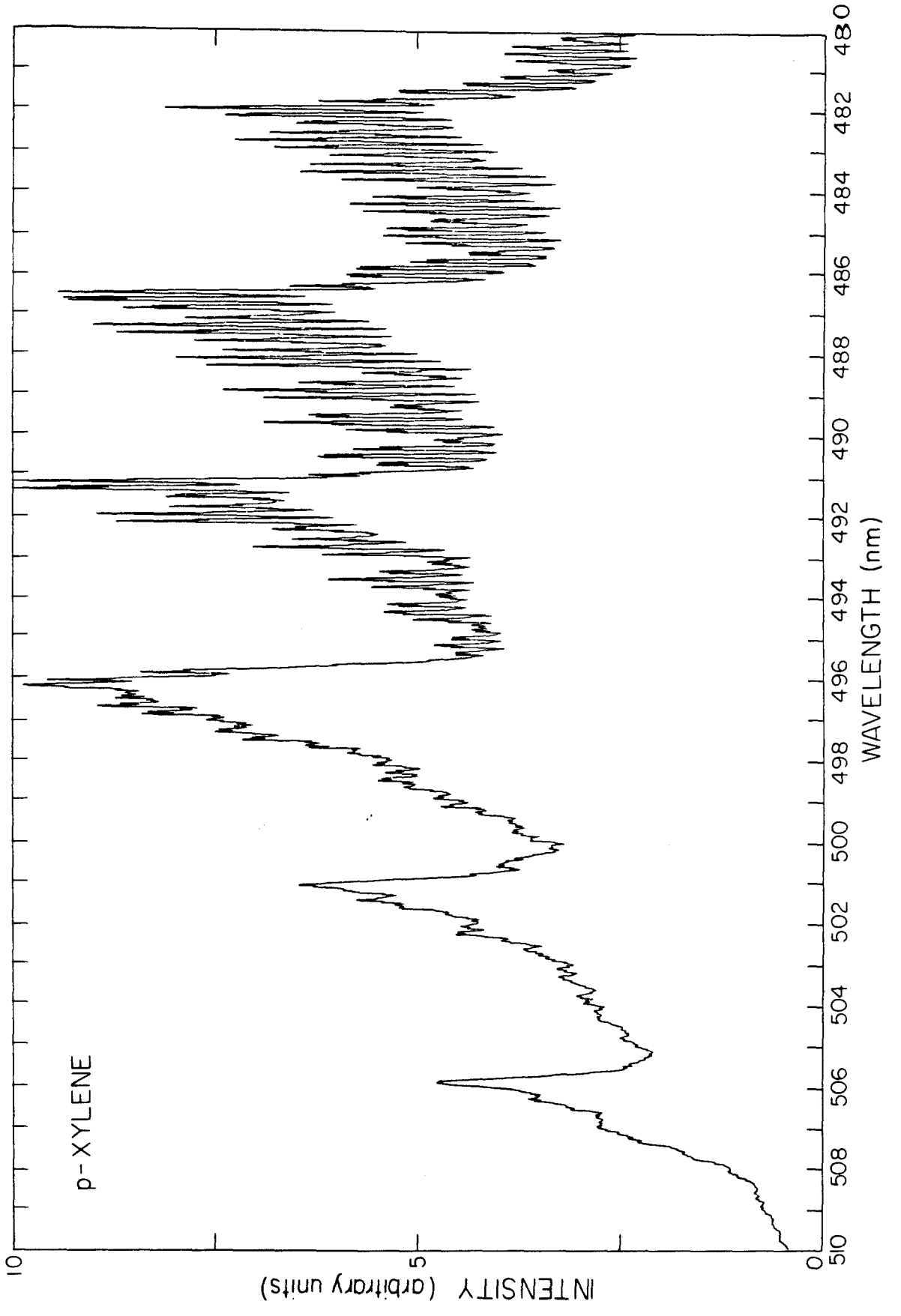
p-XYLENE
INTENSITY (arbitrary units)
WAVELENGTH (nm)
0
5
10
480
482
484
486
488
490
492
494
496
498
500
502
504
506
508
510

Figure 2

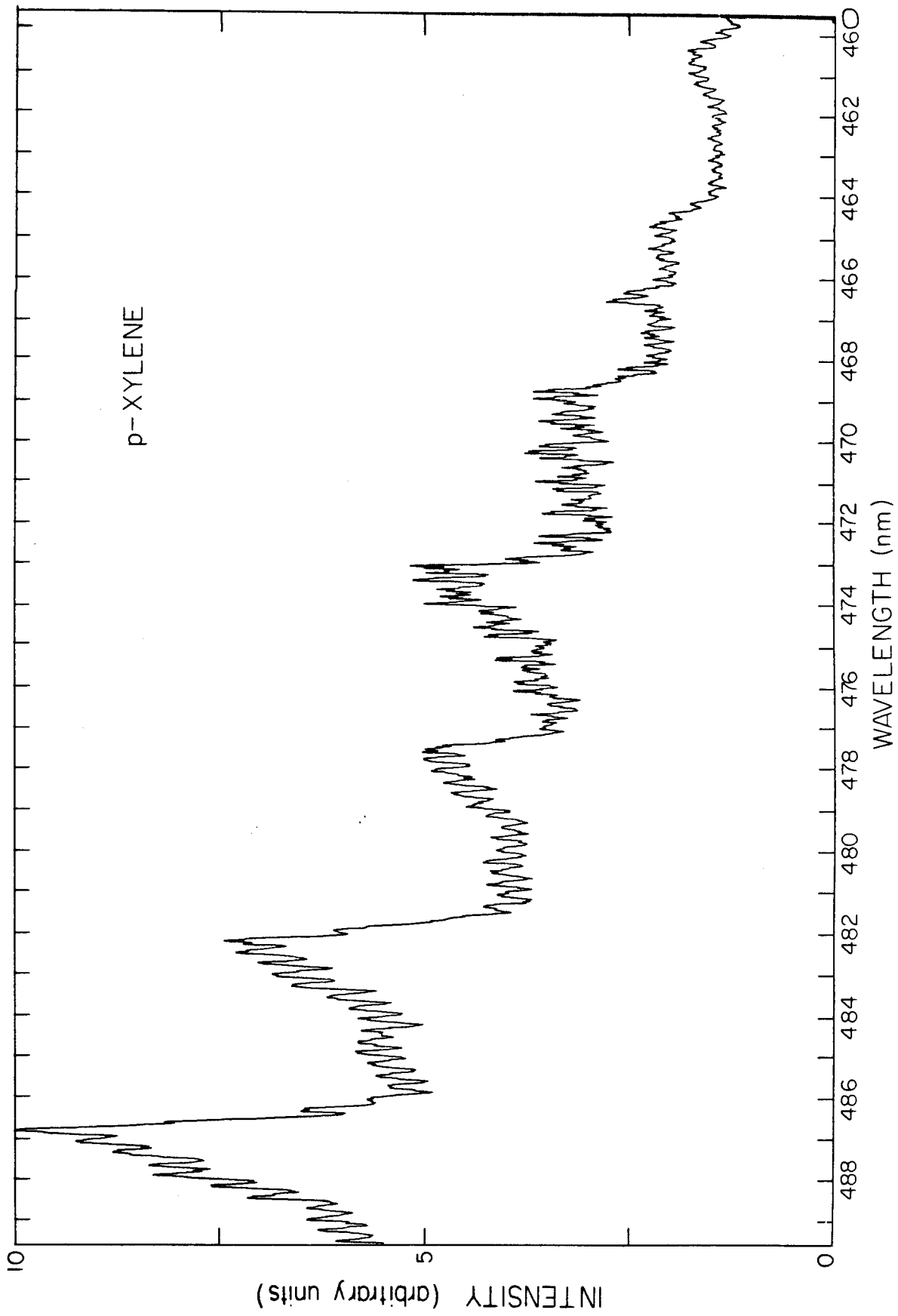
p-XYLENE
INTENSITY (arbitrary units)
0
5
10
WAVELENGTH (nm)
460
462
464
466
468
470
472
474
476
478
480
482
484
486
488

Figure 3

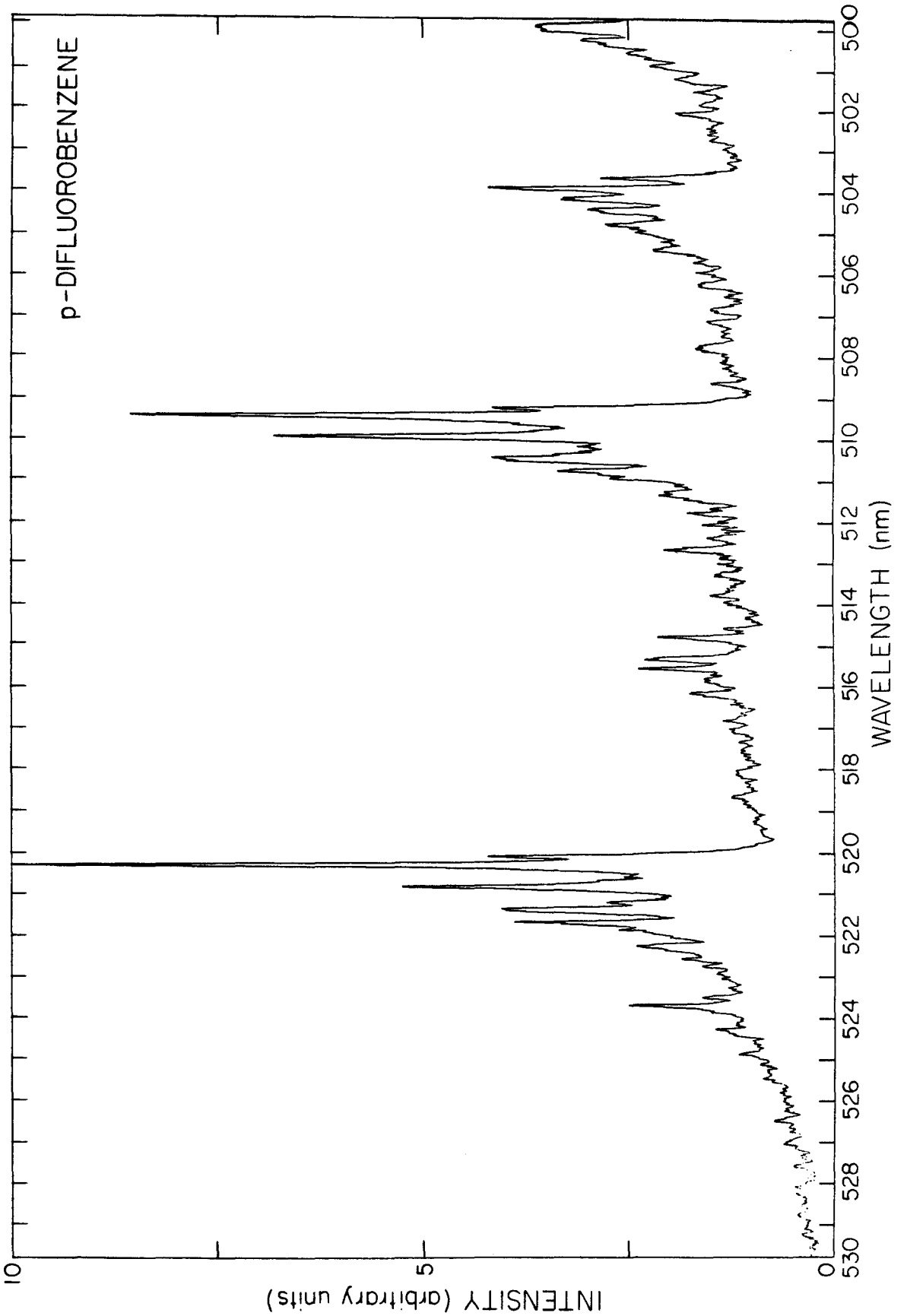
p-DIFLUOROBENZENE
INTENSITY (arbitrary units)
0
5
10
WAVELENGTH (nm)
500
502
504
506
508
510
512
514
516
518
520
522
524
526
528
530

Figure 4

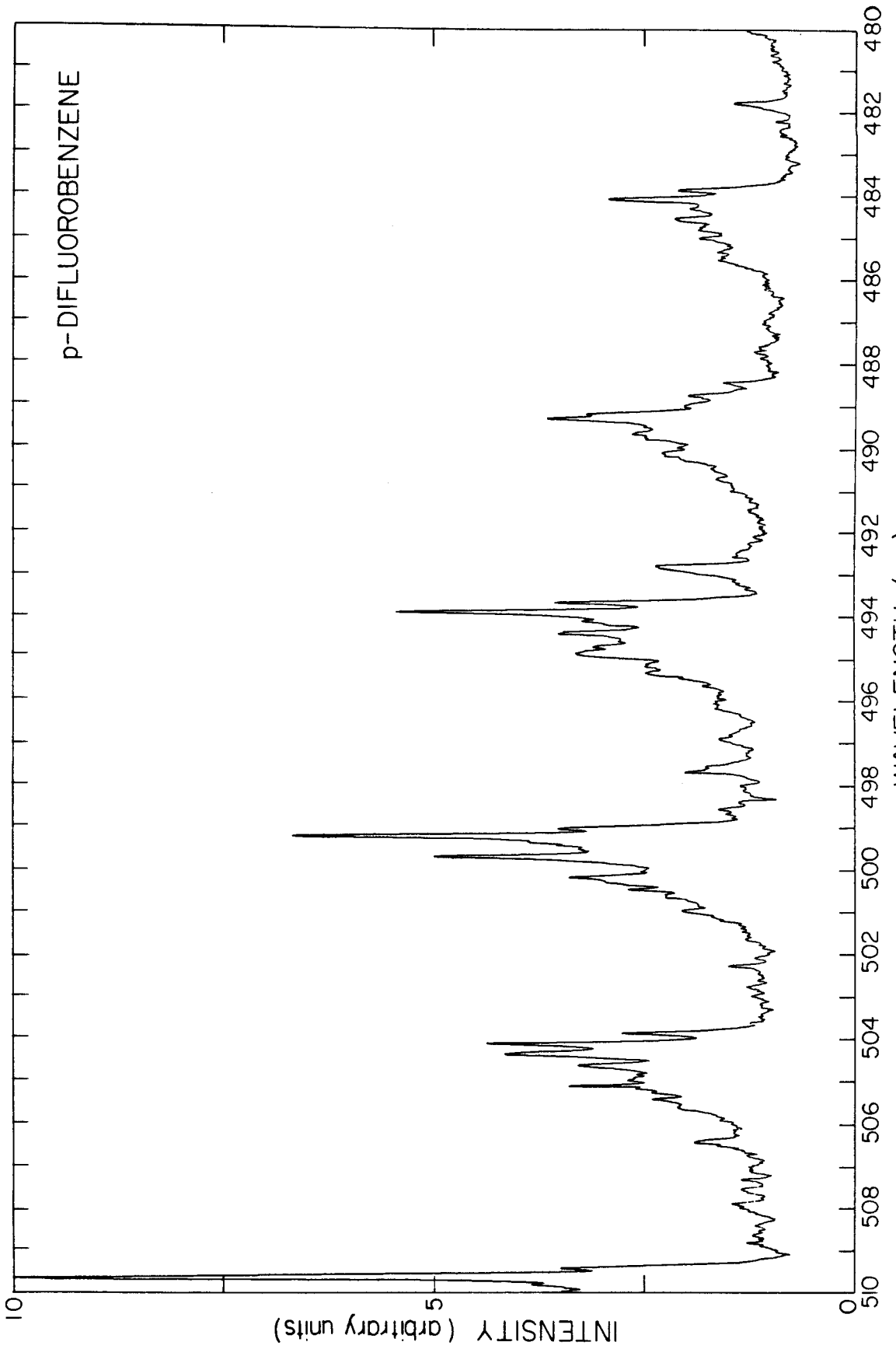
p-DIFLUOROBENZENE
INTENSITY (arbitrary units)
10
5
0
510
508
506
504
502
500
498
496
494
492
490
488
486
484
482
480
WAVELENGTH (nm)

Figure 5

Propositions

Proposition 1: Study of the Quantum yield of $O(^1D_2)$ in Ozone Photolysis between 280 and 320 nm.

Abstract: It is proposed that the quantum yield of $O(^1D_2)$ from ozone photolysis be determined in a flow tube using a pulsed tunable dye laser and a mass spectrometer as a detector. The accurate determination of this quantum yield as a function of wavelength would be valuable to atmospheric modeling studies.

Metastable oxygen, $O(^1D)$, which is formed by the photolysis of ozone in the Hartley continuum and the Huggins bands, is the driving force behind the photochemistry of the troposphere[1] and the most important source of nitrogen oxide (NO) in the stratosphere.[2] Due to the greater reactivity of excited atomic oxygen relative to ground state oxygen, $O(^3P)$, an accurate determination of the quantum yield for $O(^1D)$ formation resulting from ozone photolysis would provide a valuable piece of information for atmospheric modeling studies. The major source of radicals in the troposphere is the reaction of $O(^1D) + H_2O \rightarrow 2OH$, yielding hydroxyl radicals which are converted to peroxyl radicals by subsequent reactions.[1] Of particular importance in stratospheric chemistry is the reaction of excited oxygen with nitrous oxide (from bacterial action in soil or from jet exhaust) resulting in the production of nitric oxide which catalyzes the decomposition of ozone by the following sequence of reactions:[3]

A. $O_3 + h\nu \rightarrow O_2 + O(^1D)$

B. $O(^1D) + N_2O \rightarrow 2NO$

C. $O(^1D) + N_2O \rightarrow N_2 + O_2$

D. $NO + O_3 \rightarrow NO_2 + O_2$

E. $NO_2 + O_3 \rightarrow NO_3 + O_2$

F. $NO_3 + h\nu \rightarrow NO + O_2$ _(day)

net of reactions D through F is: $2O_3 + h\nu \rightarrow 3O_2$.

A similar catalytic cycle for the destruction of ozone involving hydroxyl radicals also exists. The result of both these cycles is the rapid destruction of ozone following the production of metasable oxygen by ozone photolysis. Any decrease in atomspheric ozone will result in a concomitant increase in ultraviolet radiation reaching the Earth's surface. However, in order for recommendations to be made for legislation restricting the production of compounds which have damaging effects on the ozone layer (including freons as well as nitrogen oxides), it will be necessary to accurately model atmospheric chemistry, requiring detailed and accurate data on reactions involved, including the $O(^1D)$ quantum yield.

The electronic configuration of the ground state of ozone is $(\pi_c)^2(1_a)^2(1_b)^2(\pi_a)^1(\pi_b)^1$, yielding the symmetry designation $^1A_1$.[4-6] The low lying excitations from the ground state have been shown to result from excitations of the form $1_a \rightarrow \pi_a$ or $1_b \rightarrow \pi_b$.[6] The Hartley continuum and the Huggins bands have been theoretically determined to be the vertical and nonvertical components of the same electronic transition, the $X^1A_1 \rightarrow 1^1B_2$.[4] The large difference between the vertical and adiabatic excitation energies ($\sim$1.3 eV) is due to the increase of the bond length in the excited state relative to the ground state of about .1 Å.[6]

The experimental dissociation energy of ozone to ground state products $O_3(^1A_1) \rightarrow O_2(^3\Sigma_g^-) + O(^3P)$ is 1.05 eV. The electronic excitation energies of $O(^1D_2)$ and $O_2(^1A_g)$ are 1.97 and .98 eV, respectively. (The spin forbidden dissociation of ozone to $O(^1D)$ and $O_2(^3\Sigma_g^-)$ has been shown to be unimportant.) The threshhold for production of excited oxygen atoms is therefore 4.00eV corresponding to a wavelength of 310 nm.

Several investigations of the ozone photolysis quantum yield of $O(^1D)$ have been conducted, however agreement between different studies is very poor. In a review article by Welge,[7] unpublished results obtained by Lin and Demore for the quantum yield as a function of wavelength from 275 to 334 nm at -40°C were reported. They stated that the quantum yield from $\lambda \leq 305$ was a constant (presumably $\phi = 1$), one-half as great a yield at 808 nm and 0.1 times as great at 313 nm as 305 nm, reaching a quantum yield of zero at 334 nm. Simonaitus et al. reported the quantum yield for $O(^1D)$ formation to be 0.5 at 313 nm.[8] Jones and Wayne reported a room temperature quantum yield of 0.1 at 313 nm.[7] Demore and Raper reported a low temperature quantum yield of 0.27 at 313 nm.[9] Other authors have reported a quantum yield of 1 at 313 nm.[10] More recently, several groups have determined relative quantum yields for the production of $O(^1D)$ using NO_2^* chemluminescence as a monitor.[11-13] The relative quantum yields obtained were then normalized to an assumed value of the $O(^1D)$ quantum yield of unity at 300 nm. The agreement among these three studies is only fair and a long wavelength tail observed in the most recent work is not in agreement with the results of the previous two studies.[11,12] In addition, recent studies indicate that the quantum yield at 300 nm is not unity but is actually closer to .9.[14-17] Thus there is still a great deal of uncertainty in the value of a quantum yield which is believed to be crucial to the photochemistry of the atmosphere.

I suggest the quantum yield for formation of $O(^1D)$ from ozone photolysis by means of the mass spectrometric measurement of NO_2 resulting from photodissociation of ozone by a frequency doubled pulsed tunable dye laser. This would involve photolyzing a mixture of ozone and nitrous

oxide (N_2O) in a flow tube at wavelengths from 320 nm to 280 nm at temperatures ranging from approximately 200 to 300 K (the range of atmospheric temperature[3]).

The photolysis of ozone in this wavelength range yields oxygen atoms in either the ground state, (^3P), or the state of interest (the ^1D). No reaction between ground state oxygen atoms and N_2O occurs. However, reaction between excited oxygen atoms and N_2O is quite rapid, yielding euqally probably N_2 and O_2 or 2NO molecules.[18] This provides a convenient means of determining the state of product oxygen atoms. The important reactions are:

$$O_3 + h\nu \rightarrow O(^1D_2) + O_2(^1\Delta_g)^{18-21}$$

1.	$O(^1D) + N_2O \rightarrow 2NO$	$k_1 = 1.1 \times 10^{-10}$
2.	$O(^1D) + N_2O \rightarrow N_2 + O_2$	$k_2 = k_1$
3.	$NO + O_3 \rightarrow NO_2^* + O_2$	$k_3 = 1.3 \times 10^{-12} e^{-4.18 \text{ kcal/RT}}$
4.	$NO + O_3 \rightarrow NO_2 + O_2$	$k_4 = 7.2 \times 10^{-12} e^{-2.33 \text{ kcal/RT}}$
5.	$NO_2^* \rightarrow NO_2 + h\nu$	$k_5 = 1.1 \times 10^4 \text{sec}^{-1}$
6.	$NO_2^* + N_2O \rightarrow NO_2 + N_2O$	$k_6 = ?$
7.	$O(^1D) + O_3 \rightarrow 2O_2$	$k_7 = 2.5 \times 10^{-10}$
8.	$O_2 + NO_2 \rightarrow NO_3 + O_2$	$k_8 = 1.1 \times 10^{-13} \exp(-2450/T)$
9.	$NO_3 + NO_2 \rightarrow N_2O_5 + (n)$	$k_9 = 3.8 \times 10^{-12} \text{cm}^3/\text{mol. sec.}$
10.	$N_2O_5 \rightarrow NO_2 + NO_3$	$k_{10} = 5.7 \times 10^{14} \exp(-10600/T)$
11.	$NO_2 + NO_3 \rightarrow NO_2 + O_2 + NO$	$k_{11} = 2.3 \times 10^{-13} \exp(-1000/T)$

Reactions 1 through 7 are extremely fast (k_6 = ?), therefore the effective volume to be considered for determining the concentration of NO_2 is essentially the volume of gas illuminated by the incident laser beam, since excited oxygen atoms and the subsequently formed NO_2 will not diffuse from this region before reaction occurs.

The experimental apparatus to be used for these studies would be a modified version of the discharge flow apparatus reported by Leck, Cook and Birks.[22] This apparatus consists of a temperature controlled reaction tube having several fixed inlets and one movable inlet which is coaxial with the reaction tube. Reactants and products are sampled at the end of the reaction tube via a .7 mm orifice into a differential pumping chamber followed by a 2.8 mm orifice into another chamber which contains a quadrupole mass spectrometer. A pressure of 1 torr in the reaction tube results in a pressure of 7×10^{-7} torr at the mass spectrometer. The linear velocity through the 2.5 cm. id. reaction tube is 12.04 m/sec.

Since no reaction occurs between ozone and nitrous oxide, the reactants may be mixed prior to introduction to the flow tube, which eliminates the need for several fixed inlet tubes. The concentration of ozone in the initial mixture may be monitored photometrically as the experiment progresses. The movable inlet tube may now provide a menas of introducing the laser beam along the flow axis into the reaction tube in the region immediately prior to the sampling orifice. Thermal equilibrium between the gas and the apparatus will have been attained by the time the reactants reach this point. The orifice used in the apparatus by Leck *et al.*[22], would be replaced with a cone-shaped orifice with a comparable aperture. This will prevent reflection of the light beam back through the region of

interest.

The laser beam would be expanded so that the beam diameter would be nearly that of the beam inlet tube, probably about 1 cm. The light path between the window at the end of the beam inlet tube and the orifice would be limited to about 1 cm so that little diffusion of the product species from the central millimeter of the flow tube (the fraction that will be sampled) will occur.

The total pressure in the reaction tube would be about 10 torr although improved pumping speeds may allow higher pressures to be used. The ratio of N_2O to O_3 would be 9:1.

The absorption cross sections for ozone from 320 to 280 nm are well known, monotonically increasing as wavelength decreases.[23,24] The absorption of N_2O is negligible in this region.[25] Therefore, the minimum signal would be expected at 320 nm since both the $O(^1D)$ quantum yield and the absorption cross section are at minima. Assuming a quantum yield of 0.1 and a pulse energy of 15 mj., 2.5×10^{12} excited oxygen atoms would be formed in a volume of .79 cc. The concentration of $O(^1D)$ would thus be 3.2×10^{12}/cc. Due to competing reactions, this will result in the formation of 2.5×10^{12} molecules of NO_2 per cc. The concentration of NO_2 at the mass spectrometer due to this concentration in the flow tube would be 1.75×10^{6}/cc for about 1 msec (due to pumping of the flow tube). A product concentration of this magnitude will yield a readily detectable signal. The other resulting mixture components N_2, N_2O, O_2 and O_3 do not yield peaks at m/e = 46, whereas NO_2 does give a strong parent peak (about 30% of the total ion signal).[26] Calibration mixtures of NO_2 in air may be

used to provide a means of relating the ion signal measured to the actual concentration in the flow tube.

Scanning the laser wavelength while plotting the calibrated m/e = 46 ion signal normalized to the laser intensity and ozone concentration will yield the dependence of the $O(^1D)$ quantum yield absolutely as a function of wavelength.

This experiment should allow an accurate determination of the $O(^1D_2)$ quantum yield from ozone photolysis. It would be expected that this information would aid in providing a more thorough understanding of atmospheric processes.

References

1. H. Levy II, Advances in Photochemistry, 9, (1973).
2. P. Crutzer, Can. J. Chem. 52, 1571 (1974).
3. H. S. Johnston and G. Whitten, "Reaction of Ozone with Nitrogen Oxides at High Altitudes".
4. P . J. Hay and W. A. Goddard III, Chem. Phys. Lett. 14, 46 (1972).
5. P. J. Hay, T. H. Dunning, Jr. and W. A. Goddard III, Chem. Phys. Lett. 23, 457 (1973).
6. P. J. Hay, T. H. Dunning, Jr. and W. A. Goddard III, J. Chem. Phys. 62, 3912 (1975).
7. K. H. Welge, Can. J. Chem. 52, 1424 (1974).
8. R. Simonaitus, S. Braslavsky, J. Heicklin and M. Nicolet, Chem. Phys. Lett. 19, 601 (1973).
9. W. B. Demore and O. F. Raper, J. Chem. Phys. 44, 1780 (1966).
10. E. Castellano and H. J. Schumacher, Z. Phys. Chem. NF 65, 62 (1969).
11. D. L. Philen, R. T. Watson and D. D. Davis, J. Chem. Phys. 67, 3316 (1977).
12. I. Arnold, F. J. Comes and G. K. Moortzat, Chem. Phys. 24, 211 (1977).
13. J. C. Brock and R. T. Watson, Chem. Phys. 46, 477 (1980).
14. P. W. Fairchild and E. K. C. Lee, Chem. Phys. Lett. 60, 36 (1978).
15. C. E. Fairchild, E. J. Stone and G. M. Lawrence, J. Chem. Phys. 69, 3632 (1978).
16. R. K. Sparks, L. R. Carlson, K. Shobatake, M. L. Kowalczyk and Y. T. Lee, J. Chem. Phys. 72, 1401 (1980).

17. J. C. Brock and R. T. Watson, Chem. Phys. Lett. 71, 371 (1980).

18. D. Garvin and R. F. Hampson, CIAP monograph #1, "Tables of Rate and Photochemical Data" (1973).

19. H. Niki, Can. J. Chem. 52, 1397 (1974).

20. J. London and J. H. Park, Can. J. Chem. 52, 1599 (1974).

21. S. E. Schwartz and H. S. Johnston, J. Chem. Phys. 51, 1286 (1969).

22. T. J. Leck, J. L. Cook and J. W. Birks, J. Chem. Phys. 72, 2364 (1980).

23. E. C. Y. Inn and Y. Tanaka, J. Opt. Soc. Amer. 43, 870 (1953).

24. M. Griggs, J. Chem. Phys. 49, 857 (1968).

25. H. S. Johnston and R. Graham, Can. J. Chem. 52, 1415 (1974).

26. S. R. Hiller and G. W. A. Milne, EPA and NIH Mass Spectral Data Base, NSRDS-NBS63 (U.S. Government Printing Office, 1978).

Proposition 2: Isotopically Selective Photochemistry of Nitric Oxide.

Abstract: It is proposed that potential enrichment of ^{15}N, ^{17}O and ^{18}O isotopes via isotopically selective electronic excitation of NO followed by reaction with CO_2 be investigated. This method may provide a very effective means of enrichment.

The electronic spectroscopy of nitric oxide (NO) has been the subject of numerous investigations for more than 50 years.[1-13] These studies have been stimulated by both the inherent interest in the simplest stable molecule with an odd number of electrons and the important role nitric oxide has been found to play in atmospheric chemistry.[14,15]

The electronic configuration of the $X^2\pi$ ground state of NO is $(KK)^4(\sigma_{2s})^2(\sigma^*_{2s})^2(\sigma_{2p})^2(\pi_{2p})^4(\pi^*_{2p})$.[16] The lowest lying spin allowed excitation is the $\pi^*_{2p} \rightarrow 3s$ transition yielding a $^2\Sigma^+$ excited state. The spectrum of this band is characterized by very sharp structure with readily observed rotational lines.[2,8,11,13] The spectrum of the $X^2\pi \rightarrow A^2\Sigma^+$ transition (γ bands) was found to show a significant self-induced pressure broadening effect.[2-10] Further experiments have shown that this self-induced broadening caused by very rapid quenching of the excited state is due to the following reactions:[17]

$$NO(A^2\Sigma^+) + NO \rightarrow N_2 + O_2 \quad \text{or} \quad N + NO_2 \qquad (a)$$

$$NO(A^2\Sigma^+) + NO \rightarrow 2NO \qquad (b)$$

$$NO(A^2\Sigma^+) + NO \rightarrow N_2O + O \quad . \qquad (c)$$

The two possibilities for reaction (a) are indistinguishable due to additional reactions:

$$O_2 + 2NO \rightarrow 2NO_2$$

$$N + NO \rightarrow N_2 + O$$

$$O + NO + M \rightarrow NO_2 + M \quad .$$

McGee and Heicklen[17] have estimated the ratio of the rates of reactions (a) to that of reaction (b) to be .61.

Studies of the quenching of NO($A^2\Sigma^+$) fluorescence in the presence of buffer gases have shown that carbon dioxide is a particularly effective quencher of NO emission.[18,19] The two possible mechanisms are

$$NO^* + CO_2 \rightarrow NO_2 + CO \qquad (d)$$

$$NO^* + CO_2 \rightarrow NO + CO_2 \quad . \qquad (e)$$

Kleinberg and Terenin[18] suggested that the quenching is primarily due to reaction (d). Their suggestion has been confirmed by other workers.[19] Cohen and Heicklen[19] have determined that

$$(k_a + k_b + k_c)/(k_d + k_e) = .29 \quad .$$

The reaction of CO_2 with excited NO suggests that if ^{15}NO may be selectively excited to the $A^2\Sigma^+$ state then reaction with CO_2 will yield isotopically pure $^{15}NO_2$. In addition, $N^{17}O^{16}O$ and $N^{18}O^{16}O$ (predominately) may also be obtained by selectively exciting NO molecules containing ^{17}O or ^{16}O.

Isotopically selective absorption by rovibronic levels of NO has been previously demonstrated.[2,10,11,13] In fact, the first evidence of the existence of ^{15}N was the observation by Naudé of vibronic peaks in the ultraviolet spectrum which corresponded to molecules having the reduced mass of $^{15}N^{16}O$.[2] The isotopic shifts measured for some band heads of elements of the γ bands are given in Table 1. These absorption bands were observed by Naudé at 20 torr using a 92 cm path.[2] More recently, Zacharias

Table 1

Isotopic Shifts of Some Band Heads in the γ-Bands of NO[a]

Band	λ(Å) for $^{14}N^{16}O$	Isotopic Species	λ(Å)	Δλ(Å)
0,0 P_1	2269.40	$^{15}N^{16}O$	2269.56	.16
		$^{14}N^{18}O$	2269.69	.29
1,0 Q_1	2153.63	$^{14}N^{17}O$	2155.23	1.60
		$^{15}N^{16}O$	2155.73	2.10
		$^{14}N^{18}O$	2156.75	3.12
P_1	2154.90	$^{14}N^{17}O$	2156.49	1.59
		$^{15}N^{16}O$	2156.98	2.08
		$^{14}N^{18}O$	2157.98	3.08
2,0 Q_1	2051.01	$^{14}N^{17}O$	2054.02	3.01
		$^{15}N^{16}O$	2054.82	3.81
		$^{14}N^{18}O$	2056.54	5.53
P_1	2052.43	$^{14}N^{17}O$	2055.15	2.72
		$^{15}N^{16}O$	2055.97	3.54
		$^{14}N^{18}O$	2057.66	5.23

[a]Ref. 2.

et al. measured the charge transfer $^{15}NO^+ + {}^{14}NO \rightarrow {}^{15}NO + {}^{14}NO^+$ by means of isotopically selective two-step photoionization of NO.[13] The intermediate state in their studies was the $A^2\Sigma^+$, v = 0.

Since the product of reaction (d), NO_2, absorbs photons in the same wavelength region as is necessary to excite NO to the $A^2\Sigma^+$ state, it will be necessary to remove NO_2 from the reaction vessel as it is formed.[20] This would be accomplished by cooling the photolysis cell to $\sim -120^oC$. The vapor pressure of CO_2 is still 10 torr at this temperature whereas the vapor pressure of NO_2 is on the order of 10^{-6} torr.[21] Operation at reduced temperature will also provide several other advantages. Collision rates are reduced relative to that at room temperature for the same gas density therefore higher gas densities may be used, yielding greater absorption for a particular amount of collisional broadening. Doppler widths are also reduced. In addition, the occupation of higher rotational levels of the ground state will be reduced. This will not only reduce the width of the vibronic levels of the A state but will also increase the probability for transitions from each of the ground state rotational levels.

The important reaction steps to enrichment of ^{15}N are summarized as follows:[22]

$$^{15}N^{16}O + h\nu \rightarrow {}^{15}N^{16}O^* \quad (1)$$

$$^{14}N^{16}O + h\nu \rightarrow {}^{14}N^{16}O^* \quad (A^2\Sigma^+) \quad (2)$$

$$^{15}N^{16}O^* + {}^{14}N^{16}O \rightarrow {}^{15}N^{16}O + {}^{14}N^{16}O^* \quad (3)$$

$$NO^* \rightarrow NO + h\nu \quad (4)$$

$$NO^* + NO \rightarrow N_2 + O_2 \quad \text{or} \quad N + NO_2 \tag{5}$$

$$NO^* + NO \rightarrow 2NO \tag{6}$$

$$NO^* + NO \rightarrow N_2O + O \tag{7}$$

$$NO^* + CO_2 \rightarrow NO_2 + CO \tag{8}$$

$$NO^* + CO_2 \rightarrow NO + CO_2 \tag{9}$$

Reactions 1-3 and 5 affect the isotopic selectivity. Based on the work of Naudé[2] and Zacharias et al.[13] it would seem possible to selectively excite only $^{15}N^{16}O$ at certain temperature and pressure conditions. In that case reaction (2) may be ignored. However, if pressure broadening results in spectral overlap at pressures high enough to yield a reasonable absorption then the ratio of the probabilities of steps (1) and (2) will limit the ultimate enrichment level. The energy transfer reaction (3) will also reduce the isotopic selectivity of this process. The rate of step (3) is not known, however, McGee and Heicklen[17] have suggested that deactivation of NO^* by NO occurs on nearly every collision. Since the rate of removal of NO^* by CO_2 is greater than by NO, the use of a significant excess of CO_2 should result in a high probability of reaction with CO_2 before energy transfer can occur.

Reaction steps (4-9) affect the overall quantum yield of the process. The total rate of removal of NO^* is given by

$$-\frac{1}{[^{15}NO^*]}\frac{d[^{15}NO^*]}{dt} = k_4 + (k_3 + k_5 + k_6 + k_7)[NO] + (k_8 + k_9)[CO_2] .$$

Thus the probability (P) of one excited ^{15}NO molecule producing one $^{15}NO_2$ is

$$P = \frac{k_8[CO_2]}{k_4 + (k_3 + k_5 + k_6 + k_7)[NO] + (k_8 + k_9)[CO_2]} \quad .$$

Neglecting reaction (3) and using the results of Cohen and Heicklen and Kleinberg and Terenin[18] this reduces to

$$P = \frac{k_8[CO_2]}{k_4 + (k_8)\ [CO_2]\left(1 + .29\ \frac{[NO]}{[CO_2]}\right)} \quad .$$

The rates k_4 and k_8 at room temperature are approximately 4.5×10^6 sec^{-1} and 27×10^{10} M^{-1} sec^{-1}, respectively.[22] Thus, for a mixture consisting of 10 torr CO_2 and 1 torr NO, the quantum yield of NO_2 from NO^* would be .94. Assuming the rates are temperature independent, using a temperaure of -120^oC and the absorption cross section of 2.9×10^{-19} cm^2 [6] (measured for the entire $\gamma_{o,o}$ band at room temperature), only 7×10^{-5} of the incoming photons are absorbed by ^{15}NO per centimeter of path. Thus, even for a 1 meter path, only .7% of the photons will yield an enriched NO_2 molecule. This indicates the importance of a spectroscopic study to determine the maximum pressures which can be used for a particular level of enrichment (the number of excited molecules produced depends nearly linearly on the density).

The first phase of this research would therefore involve study of the spectroscopy of NO-CO_2 mixtures as a function of temperature and partial pressures of the components. No such information is currently available. This study would be conducted using a cooled 1 meter cell containing the gas mixture with a frequency doubled pulsed tunable dye laser as the

excitation source. Currently, only the pulsed laser source provides sufficient tunability and flux with the required narrow bandwidth ($<.1\ cm^{-1}$). Ideally, isotopically enriched samples of NO would be obtained in order that high quality spectra of all the isotopic components may be obtained. This study is necessary since it is desireable to use the maximum NO pressure possible such that virtually all the laser photons are absorbed while simultaneously ensuring that only one isotopic species is excited (this is limited by pressure broadening) and that nearly all excited NO molecules react with CO_2.

Once the spectral study has been completed, analysis of the data should indicate which combinations of excitation wavelength, temperature, and pressure will yield the best compromise between selectivity and quantum efficiency. Irradiations of the sample cell for longer periods of time such that a significant fraction of the selected isotopic nitric oxide is destroyed would then be conducted for several of the previously determined experimental conditions. The cell may be evacuated following irradiation to remove excess NO, CO_2 and CO. The NO_2 produced will remain frozen on the cell walls. Mass spectrometric analysis of this NO_2 would then allow accurate measurement of the isotopic composition.

It would be expected that this research would lead to an effective scheme for production of NO_2 which is enriched in one of the nitrogen or oxygen isotopes. The NO_2 so produced may then be incorporated into other compounds for biological tracer studies. The light source to be utilized in this study is not very energy efficient, however, development of other laser sources might make such an isotope separation scheme very

attractive. In addition, the spectral studies may indicate coincidental overlap with an atomic line source which may also allow more cost efficient separation.

References

1. S. Leifson, Astrophy. J. 63, 73 (1926).
2. S. M. Naude, Phys. Rev. 36, 333 (1930).
3. O. R. Wulf, Phys. Rev. 46, 316 (1934).
4. A. G. Gaydon, Proc. Phys. Soc. (London) 56, 96, 160 (1944).
5. L. Gerö and R. Schmid, Proc. Phys. Soc. (London) 60, 533 (1948).
6. F. F. Marmo, J. Opt. Soc. Am. 43, 1186 (1959).
7. G. W. Bethke, J. Chem. Phys. 31, 662 (1959).
8. N. Basco and R. G. W. Norrish, Proc. Roy. Soc. (London) 268A, 291 (1962).
9. K. P. Miescher, Helv. Phys. Acta, 36, 257 (1963).
10. R. B. Bray, R. M. Hochstrasser and J. E. Wessel, Chem. Phys. Lett. 27, 167 (1974).
11. D. Zakheim and P. Johnson, J. Chem. Phys. 68, 3644 (1978).
12. R. P. Frueholz, R. Rianda and A. Kuppermann, Chem. Phys. 31, 315 (1978).
13. H. Zacharias, R. Schmiedl, K. H. Welge, Appl. Phys. 21, 127 (1980).
14. H. S. Johnston, Acta Astronautica 1, 135 (1974).
15. J. London and J. H. Park, Can. J. Chem. 52, 1599 (1974).
16. G. Herzberg, Spectra of Diatomic Molecules (Van Nostrand, Princeton, 1950) p. 343.
17. J. J. McGee and J. Heicklen, J. Chem. Phys. 41, 2974 (1964).
18. A. V. Kleinberg and A. N. Terenin, Dokl. Akad. Nauk. SSSR 101, 1031 (1955).
19. N. Cohen and J. Heicklen, J. Phys. Chem. 52, 1415 (1974).

20. H. S. Johnston and R. Graham, Can. J. Chem. 52, 1415 (1974).

21. Handbook of Chemistry and Physics (Chemical Rubber Co., Cleveland, 1968) p. D140.

22. J. Heicklen and N. Cohen, Advan. Photochem. 5, 157 (1968).

Proposition 3: Determination of Angular Distributions and Kinetic Energies of Fragments Produced by Multiphoton Ionization.

Abstract: It is proposed that the angular distributions and kinetic energies of neutral fragments produced in multiphoton ionization be investigated as a function of wavelength and laser peak power. This investigation should provide additional information about both the dynamics of the multiphoton ionization process as well as information on the nature of highly excited states of the molecules investigated.

Multiphoton ionization (MPI) spectroscopy has proven to be a very powerful technique for studying the electronic spectroscopy of molecules.[1-8] Perhaps the most useful application of MPI is to the observation of transitions that are forbidden by electric dipole selection rules to single photon spectroscopy. Due to the broad applicability of the technique a great deal of research has been performed using the MPI technique simply as a tool for spectroscopic investigations. More recently investigations of the dynamic processes involved in MPI have been undertaken. At this time however only the mass distributions of ion fragments produced have been determined.[6-8] No information is currently available regarding the kinetic energies or angular distributions of the neutral or ionic fragments. This information would assist in the identification of states which dissociate to the observed fragments and would therefore provide information on the dynamics of the MPI process. It is therefore proposed that the kinetic energies and angular distributions of fragments produced by multiphoton ionization[8] be investigated.

This proposed study is a variation on the techniques of photofragment spectroscopy developed since the late 1960's by several researchers including R. N. Zare,[9] K. R. Wilson[10,11] and R. Bersohn.[12,13] Zare has suggested that the angular distributions of photofragments produced by the polarized photodecomposition of a molecule yield invaluable information concerning the photodecomposition pathways, excited state symmetries and lifetimes.[9] When polarized light is absorbed by a gas molecule, it excites the molecule with a probability

proportional to $|\underset{\sim}{\mu}\cdot\underset{\sim}{\varepsilon}|^2$ thus yielding a relatively higher probability of excitation for those molecules whose transition dipoles, $\underset{\sim}{\mu}$, are alighed with the polarization vector of the light beams. If dissociation fragments separate with large kinetic energy, as is normally the case, then the fragment trajectories will be along the direction of the vibrational motion of the broken bond. Thus, if dissociation occurs within a time which is shorter than or comparable to the rotational period of the molecule then the distribution of fragment trajectories is an isotropic. Measurement of this anisotropy may yield information regarding the symmetry of the dissociating state. In addition, in the case of single photon absorption measurement of the anisotropy parameter, β, for the distribution $F(\theta) = \frac{1}{4\pi}[1 + \beta P_2(\cos\theta)]$ will also provide information on the lifetime of the excited state.[13] In the case of multiphoton absorption, a more complicated distribution function will be observed due to the differing "memories" of excited intermediate states and the mode of preparation. Thus the angular distribution observed may also yield information regarding the number of photons absorbed since the last orientational randomization.

Determination of fragment kinetic energies yields information regarding energy partitioning in excited states. If the kinetic energies of all fragments produced are known and if the number of photons absorbed is known then the amount of internal excitation of the fragments may be calculated.

The experimental apparatus to be used for these studies would consist of a supersonic molecular beam crossed perpendicularly with a

pulsed dye laser (Nd:YAG-pumped) beam at the scattering center. The axis of the neutral fragment mass spectrometer would then intersect the plane defined by the laser and molecular beams at the scattering center in a 90^{o} angle. The axis of the ion extraction and mass spectrometer system would then be placed opposite the neutral fragment spectrometer axes.

Neutral fragments passing through the entrance aperture of the mass spectrometer would be ionized by electron impact and accelerated in the usual manner. Since the distance between the ionizer and the scattering center is well known and since the light pulse is extremely short ($\sim$10 nsec) the arrival measurement of times of molecules at the ionizer of the mass spectrometer yields the fragment kinetic energies. (The flight times within the mass spectrometer after ionization may be readily calculated.) Measurement of intensities of ion peaks due to different neutral fragments as a function of the angle between the polarization vector of the laser and the line defined by the scattering center and the mass spectrometer aperature will yield the angular distributions of the various fragments. Fitting of these distributions to those calculated for n-photon processes may yield information regarding the number of photons absorbed, the lifetime of the excited state, and the symmetry of that state. This is expected to be a very difficult deconvolution for high laser fluxes where numerous photons may be absorbed, however.

The second mass spectrometer, used for ion fragment analysis will be operated simultaneously such that for each pulse data on both ion and neutral fragments will be obtained. This mass spectrometer might be

operated in two different modes. A grounded aperture could be installed at the entrance to the MS which would shield the ions at the scattering center from potentials within the MS. Ions which pass through the aperture may then be accelerated and mass analyzed. As with the neutral fragments the arrival times of ions at the detector are related to the initial kinetic energies. Angular distributions would also be obtained by rotating the laser polarization. It is expected that this mode of operation would only be useful in cases of low molecular beam density, low laser fluxes, or low ionization cross sections, such that the density of the plasma produced by the laser is small enough that space charge effects are not important.

A second mode of operation would simply involve removal of the field shielding entrance aperture and application of an extracting potential. In this case nearly all ions of a given mass produced may be detected yielding much higher signal-to-noise.

Typically quadrapole or time of flight mass spectrometers are used for mass analysis for photofragment and MPI spectroscopy. For this experiment, however, I propose the use of twin focal plane spectrometers (given unlimited funding) of the Mattauch-Herzog design.[14] An electro-optical ion detector (EOID) consisting of a microchannel plate, phosphor coated fiber optic coupler and Reticon diode array would be used with the ion fragment mass spectrometer when an extraction potential is used in order to provide measurement of all mass peaks from a single laser pulse at high resolution (>1000).[15,16]

The electro-optical ion detectors which have been developed are not fast enough to provide the flight time information necessary for fragment kinetic energy determinations, so it is not possible to make full use of the focal plane mass spectrometer. However, several high-speed multipliers may be installed with apertures at selected points on the focal plane such that several masses may be monitored simultaneously. The EOID may be used however when making angular distribution measurements.

Interpretation of data obtained in these experiments may be very difficult in the cases of molecules which have a high probability of dissociation from states which are intermediate in the ionization process. However if the dissociation of the parent ion or neutral yields the same fragment the angular distribution or energy distribution may be double valued allowing separation of the two pathways. Also dissociation in the neutral fragment mass spectrometer ionizer may also complicate interpretation of data. However, dissociation in the ionizer will yield fragments with arrival times which differ from those of photofragments. Thus it is expected that this apparatus might be best applied to relatively simple molecular systems such as I_2 or CS_2 where the fragments observed are known to result from the photolysis.

The benzene molecule has been of great interest to MPI/MS investigators. Application of the technique I propose may assist in the assignment of the symmetries of the ion states which dissociate to the ion fragments observed. (Boesl, Neusser ahd Schlag have shown that fragmentation occurs after ionization in this case.[8])

In addition to providing information on the properties of highly excited states of molecules and on the dynamics of MPI this apparatus may prove to be a very powerful analytical tool. This system provides the selectivity of multiphoton ionization with mass spectrometric ion analysis along with the additional dimensions of neutral fragment detection and kinetic energy analysis and fragment angular distributions. The combination of all these dimensions should allow the unique identification of compounds with nonzero vapor pressures.

References

1. P. M. Johnson, M. Berman and D. Zakheim, J. Chem. Phys. 62, 2500 (1975).
2. P. M. Johnson, J. Chem. Phys. 64, 4143 (1976).
3. P. M. Johnson, J. Chem. Phys. 64, 4638 (1976).
4. P. M. Johnson, Acc. Chem. Res. 13, 20 (1980).
5. V. S. Antonov and V. S. Letokhov, Appl. Phys. 24, 89 (1981).
6. L. Zandee and R. B. Bernstein, J. Chem. Phys. 70, 2574 (1979).
7. L. Zandee and R. B. Bernstein, J. Chem. Phys. 71, 1359 (1979).
8. U. Boesl, H. J. Neusser and E. W. Schlag, J. Chem. Phys. 72, 4327 (1980).
9. R. N. Zare, Mol. Photochem. 4, 1 (1972).
10. G. Busch, J. R. Cornelius, R. T. Mahoney, R. I. Morse, D. W. Scholsser and K. Wilson, Rev. Sci. Inst. 41, 1066 (1970).
11. G. Busch, R. T. Mahoney, R. I. Morse and K. Wilson, J. Chem. Phys. 51, 837 (1967).
12. C. Jonah, P. Chandra and R. Bersohn, J. Chem. Phys. 55, 1903 (1971).
13. M. Dzvonik, S. Yang and R. Bersohn, J. Chem. Phys. 61, 4408 (1974).
14. J. Mattauch and R. F. K. Herzog, Z. Phys. 89, 789 (1934).
15. J. H. Beynon, D. O. Jones and R. G. Cooks, Anal. Chem. 47, 1734 (1975).
16. C. E. Giffin, H. G. Boettger and D. D. Norris, Int. J. Mass. Spectr. and Ion Phys. 15, 437 (1974).

Proposition 4: Determination of the Lifetime of the 2p Excited State of Solvated Electrons.

Abstract: It is proposed that the lifetimes of the first excited states of solvated electrons in amines be determined. It is expected that these lifetime measurements may assist in the determination of the mechanism of relaxation of these excited states.

The formation of the solvated electron by the action of ionizing radiation on polar liquids and by dissolving alkali metals in polar solvents is well established.[1] There has been considerable work on the absorption spectra and reaction kinetics of solvated electrons, particularly in water and ammonia solutions. The physical and chemical properties of excess electrons in polar solvents have been found to be independent of the nature of the positive ion, indicating that at low concentrations electron-cation interaction is negligible. The electron is localized by a solvation mechanism similar to that of an ion in an electrolyte solution. The electric field of the electron polarizes the solvent molecules, resulting in the orientation of the nearest neighbor shell while the solution beyond this shell is subjected to a long-range polarization potential.[2] Both chemically stable solutions (metal-ammonia or ether solution)[3-9] and metasable excess electron solutions (electrons in water or alcohol solution)[10-15] have been studied extensively.

Excess electron states can be described in two different models, the quasifree and the localized electron models.[2] In the quasifree electron model, the excess electron is treated as a plane wave which is scattered by the solvent molecules. Under these circumstances it is not expected that the structure of the liquid would be perturbed by the electron. This model is characteristic of excess electron solutions consisting of atoms and molecules having low polarizability (He, Ne, O_2) and results in a positive ground state energy for the excess electron state. For heavier species the effect of attractive polarization is

greater than that of short-range repulsions, giving negative energy excess electron states.

In the localized excess electron model the wavefunction for the excess electron goes to zero for large distances from the localization center. Due to the presence of the localized electron the liquid structure is perturbed, forming a cavity in which the excess electron is localized. The relative energies of the quasifree state and the localized electron state determine the properties of the solvated electrons. It has been shown experimentally that excess electrons in polar solvents fit the localized, or cavity, model. The energy levels for the excess electron in the cavity model are then determined by the nature of the cavity; e.g. the size of the cavity, electrostatic interactions with molecules in the first coordination layer, and the relatively weaker interactions with molecules beyond the first layer. The potential acting upon the excess electron inside the cavity has the form $V(v) = -\beta e^2/R$ thus the solutions to the Schroedinger equation are hydrogenic.[2] The ground state is therefore the 1s state and the lowest energy excitation is the $1s \rightarrow 2p$. It has been predicted that the energy of the first excited state is more sensitive to short-range repulsive interactions than the ground state, thus observed excitation energies should be strongly dependent on the shape of the molecules forming the cavity wall. Due to the sensitivity of the excitation energy to the nature of the cavity, bandwidths are very large (500 nm) and bands lack structure. (Vannikov and Marevtsev[13] reported observation of structure in the spectrum of solvated electrons in ethanol, however their spectrum shows significant disagreement with

the results of other authors which are reasonably consistent,[10,14] therefore it seems likely that the structure observed is due to experimental error.)

In contrast to the large amount of information regarding the ground state and optical properties of the solvated electron, very little is known of the dynamics of the electronically excited states.[9] Questions remain in even the most heavily studied systems, the solvated electron in water and ammonia. The breadths of the absorption bands are a factor of two greater that are theoretically calculated. In addition, the experimental band shape is assymmetrical in contrast to the symmetric theoretical curve. Huppert et al. have shown that in the case of the solvated electron in ammonia that the absorption is homogeneously broadened and that the lifetime of the excited state is 2×10^{-13} seconds.[9] Their work has suggested that the theory of phonon type broadening of the $1s \rightarrow 2p$ transition must be refined.

Several nonradiative relaxation phenomena may be possible. If the observed absorption band results from a bound-bound transition in the nuclear ground state configuration then the nuclear configuration in the excited state may relax to the equilibrium 2p configuration which then crosses to the ground state. This motion on the potential surfaces corresponds to multiphonon nonradiative relaxation of the trapping cavity. A second possibility is that the $1s \rightarrow 2p$ transition is followed by thermal ionization of the excited state. This ionization results in a quasifree electron which is subsequently trapped to the localized

ground state. A third possibility is that the transition is a bound-continuum one and the quasifree electron which is directly produced is trapped to the localized ground state. On the basis of their work, Huppert et al. have not been able to ascertain which of the first two mechanisms is responsible in ammonia solution.[9]

I propose to study the relaxation of the 2p state of the electron solvated in several different amines on the picosecond time scale. It is hoped that this additional information regarding relaxation rates in these solvents may assist in the understanding of relaxation pathways. In addition, relaxation rates in these solvents (methylamine, dimethylamine and aniline) will be slower than for ammonia if reorientation of the trapping cavity is involved. This may allow measurement of the spectrum while relaxation is occurring.

The experimental investigation would be accomplished in two phases. The first phase would consist of measurement of the absorption spectrum of the solvated electron in each of the solvents. The technique of pulsed radiolysis would be used to provide the solvated electrons. An accelerator like that reported by Perkey and Farhataziz[7] which produced 5-10 nsec pulses of electrons would be utilized. This electron beam would be directed into a quartz cell in a visible and infrared absorption spectrometer ionizing the solvent molecules and yielding solvated electrons. (The yield of solvated electrons in ethanol is 1 per 100 eV adsorbed.) The spectrometer would be designed so that a particular frequency which will be absorbed by the solvated electrons is continually monitored in order to provide normalization of the spectrum to the number

of solvated electrons produced. A second beam would be scanned across the absorption band (only one wavelength per pulse). The absorption spectrum is then determined point by point relative to the absorption at the reference wavelength. An extinction coefficient measured by means of a dosimeter to determine the yield of electrons absolutely at the reference wavelength can then be used to obtain absolute extinction coefficients from the relative absorptions determined previously. The absorption spectrometer could consist of a continuum source which is split into a probe beam and a reference beam with a beam splitter and then passed through two monochromators (or a filter (ref.) and a monochromator depending on the bandwidth desired), through the absorption cell, and into a suitable detection system.

Previous studies of the spectra of solvated electrons have indicated that a stable absorption spectrum decaying slowly in time will result in a period on the order of a few hundred nsec.[7,10] These long time (100 nsec) measurements will then provide the absorption cross sections needed for the second phase of the experiment. This second phase would involve excitation in the measured absorption band by an intense light pulse about 100 nsec following the accelerator pulse (to be determined in phase 1) resulting in the bleaching of the absorption band. Following this first bleaching pulse would be a string of broadband pulses separated by a few picoseconds which would allow "snapshots" of the absorption spectrum at particular times to be taken.

A mode locked Nd:Glass laser would be used to generate 1.06 pulse trains with widths on the order of 10 psec.[9,15] A single pulse would be extracted roughly 100 nsec following the accelerator pulse

through the use of a Pockels cell. The selected pulse may then be amplified by additional laser rods. Pulse energies obtainable by this method are about 75 mj.[9] A beam splitter would then be used to separate the pulse into two components, one which will be used to bleach the absorption band and another which will provide the probe pulses. (Note: If the solvated electrons in the suggested solvents do not absorb the 1.06 μ radiation, then doubling, tripling or stimulated Raman scattering should allow shifting of the pulse wavelength into the absorption band.)

The probe pulses will be generated by focusing the probe beam into a cell containing CCl_4 or H_2O where a broad band continuum pulse of duration comparable to the original pulse will be formed due to self phase modulation.[9,15] This "white" pulse would then be split into a train of pulses using a transmission echelon. The geometry of the echelon determines the separation in time of the resulting pulses. Pulse separations between 5 and 25 psec should be useable for this study. These probe pulses which are separated in both time and space may then be focused into a point intersecting each other and the bleacking pulse. After exiting the sample cell1 the probe pulses, which are again separated in space; may be passed through a monochromator and imaged onto a vidicon or a Reticon detector array. The result is then dispersion of wavelengths along one axis and dispersion in time along the other. (Of course the temporal dispersion is stepped, not continuous.) Computer analysis of this data will then yield the absorption spectrum as a function of time after the bleaching pulse. Thus, the relaxation of the excited state produced by the bleaching

pulse is monitored.

It is expected that the relaxation information provided by this experiment will yield new insight into the mode of relaxation of excited states of solvated electrons. Also it is hoped that the relaxation rates are slow enough that spectra of the relaxing system may be obtained which may indicate whether intermediate states are slow enough that spectra of the relaxing system may be obtained which may indicate whether intermediate states are involved.

References

1. S. Arai and M. C. Sauer, J. Chem. Phys. 44, 2297 (1966).
2. D. A. Copeland, N. R. Kestner and J. Jortner, J. Chem. Phys. 53, 1189 (1970).
3. G. Lapoutre and M. J. Sienko, "Metal Ammonia Solutions" (Benjamin, New York, 1964).
4. F. Cafasso and B. R. Sundheim, J. Chem. Phys. 31, 809 (1959).
5. R. Lugo and P. Delahey, J. Chem. Phys. 57, 2122 (1972).
6. F. Y. Jou and L. M. Dorfman, J. Chem. Phys. 58, 4715 (1973).
7. L. M. Perkey and Farhataziz, Int. J. Radiat. Phys. Chem. 7, 719 (1975).
8. Farhataziz and L. M. Perkey, J. Phys. Chem. 80, 122 (1976).
9. D. Huppert, W. S. Struve, P. M. Rentzepis, J. Jortner, J. Chem. Phys. 63, 1205 (1975).
10. I. A. Taub, D. A. Harter, M. C. Sauer and L. M. Dorfman, J. Chem. Phys. 41, 979 (1964).
11. M. C. Sauer, S. Arai and L. M. Dorfman, J. Chem. Phys. 42, 708 (1965).
12. S. Arai and M. C. Sauer, J. Chem. Phys. 44, 2297 (1966).
13. A. V. Vannikov and V. S. Marevtsev, Int. J. Radiat. Phys. Chem. 5, 453 (1973).
14. J. F. Gavlas and L. M. Dorfman, Int. J. Radiat. Phys. Chem. 7, 227 (1975).
15. P. M. Rentzepis, R. P. Jones and J. Jortner, J. Chem. Phys. 59, 766 (1973).

Proposition 5: Analysis of Impurities in Uranium Reactor Fuels by Saturated Optical Non-Resonant Emission Spectroscopy (SONRES).

Abstract: It is proposed that the applicability of SONRES to analysis of impurities in uranium reactor fuels be investigated. It is expected that this technique will provide a significant improvement in the limit of detection for impurities of interest.

Thermal reactors consume only 1-40% of the fissionable uranium present in the fuel element mass.[1] Inefficient consumption requires a larger critical mass to maintain the chain reaction. Trace contaminants have been found to affect the useable lifetime of the fuel. Such impurities can (1) alter the chemical and physical properties of uranium alloys and ceramics used making them more susceptible to radiation damage; (2) act as "neutron absorbing" poisons decreasing reactor efficiency; and (3) unnecessarily increase the level of radioactivity in reactor waste materials making disposal even more difficult.[1] In addition, elements which form non-volatile fluoride are also of concern to uranium processors since residues will result in the production and volatilization of uranium hexafluoride used in the gaseous diffusion isotope separation process.[2] Accurate determinations of impurity concentrations in the parts per million range and lower are required to assess conformance to specifications for uranium used.[3]

The high density of uranium atomic and ionic lines makes analyses of impurities by atomic absorption extremely difficult since uranium at concentrations greater than 1 mg/ml absorbs radiation at the wavelengths used for analysis of most elements.[2] Colorimetric procedures are time-consuming, since separate determinations must be made for each element, and are subject to elemental interferences. Emission spectrographic techniques lack accuracy.[1,2,3]

In order to overcome the uranium interferences several techniques have been developed. Among these are carrier distillation, solvent extraction and evaporation techniques.[4] The carrier distillation method involves the

addition of a carrier to the matrix in the concentration range 1-10%. The carrier serves two purposes: (1) the plasma temperature is lowered, thus lowering the number of matrix spectral lines on the photographic plate, and (2) it tends to carry impurities from the matrix into the plasma. Solvent extraction is frequently used to separate uranium from the impurities.[2,3,5,6,7] The use of tributylphosphate to extract uranium from a dissolved sample has been reasonably successful.[2,7] The evaporation technique simply makes use of the physical properties of impurities and matrix for separation. Part of the impurities are evaporated in a high frequency furnace and are captured on an electrode. The electrode is later arced enabling analysis. All these techniques have significant disadvantages. Manipulations of the sample increase the possibilities of loss of impurities and contamination. In addition, a large number of carriers may be necessary for determination of a large number of impurities.

It is therefore desireable to develop an analytical technique which would effectively reject interferences from the uranium matrix and would allow detection of impurities at the part per billion levels in a solution of the U_3O_8 matrix at the 1000 parts per million level.

The saturated nonresonant emission spectroscopy (SONRES) technique has proven to be in extremely sensitive analytical technique.[8,9] It has, in fact, yielded the detection of a single sodium atom in 1 atmosphere of argon.[9] The SONRES technique involves the use of a CW laser (or a pulsed laser with a long pulse width) to saturate an atomic transition. Collisions with ambient gases are exploited to promote excitation or deexcitation of atoms from the excited state produced by absorption of a photon to another

excited state. Fluoroescence from this new excited state is then monitored. The collisionally excited state may fluoresce to the ground state or to another excited state which may nonradiatively decay to the ground state.

Since the detected radiation differs in wavelength from that of the exciting line, interference due to Rayleigh or Mie scattering and to scatterming from components in the optical path are eliminated. In addition, selection of both the exciting and monitoring wavelengths virtually eliminates the possibility of interferences due to the presence of other atomic species. Therefore the SONRES technique offers attributes which are desireable for analysis of impurities in uranium reactor fuels.

The limit of detection for current methods of direct analysis in the uranium matrix exceeds the typical concentration found in high purity U_3O_8 for several impurities including Ba, Co, Cu, Li, Mn, MO, Pb, Sr, Ti and V.[1,4] In addition, typical concentrations found for Cr and Ni are only twice the limit of detection. SONRES may prove to be a very sensitive means of detection for many of these impurities. Examples of SONRES detection schemes for Co and V will be discussed here. This is not intended to be a complete list. Similar schemes may be obtained for many of the other likely impurities.

Cobalt atoms may be excited from the $a^4F_{9/2}$ ground state to the $y^4F^o_{9/2}$ state by radiation at 32841.99 cm^{-1}. The degeneracy-oscillator strength product, gf, for this transition, which is related to the transition, intensity, is .44. For comparison, gf for the D_1 line of sodium is .47. Another state, the $y^4G^o_{11/2}$, exists at 32430.59 cm^{-1} above the ground state. The energy difference, 411.40 cm^{-1}, is rapidly lost by collisions with

other atoms in the high temperature furnace or flame necessary to atomize the sample. This state may now decay radiatively to the $b^4F_{9/2}$ state at 3482.82 cm^{-1}. The gf value for this transition is 4.6. Radiation may also occur due to transitions between the $y^4F^o_{9/2}$ and the $b^4F_{9/2}$. The gf value for this transition is 2.7. Thus, the transition at 304.400 nm may be saturated by focusing a laser beam into the sample. Emission may then be monitored at 345.350 nm or 340.502 nm. Uranium possesses two nearby absorption lines, at 304.379 and 304.416 nm. The widths of these competing lines may be estimated to be about .002 nm assuming 10 MHz per torr collisional broadening.[13] The Doppler width even at 2000 K is only about 6×10^{-4} nm. (Calculated from $\Delta w_D = 7.163 \times 10^{-7} \sqrt{\frac{T}{A}}\, w_o$.[14]) Thus, absorption of the pumping laser line by uranium will be small providing the laser linewidth is narrow. If for example a frequency doubled ring dye laser is used as the pumping source, the linewidth would be about 1×10^{-5} nm.

The significant advantage of SONRES is that in order for uranium atoms to interfere with detection of Co not only must some of the laser line be absorbed but fluorescence must also occur at the detection wavelength. In this case the competing uranium fluorescence lines are at 345.357 nm and 340.575 nm. The proximity of the 345.357 nm line of uranium and the 345.350 nm line of cobalt will allow sufficient overlap to reduce the detection sensitivity. Therefore, monitoring the 340.512 nm fluorescence will provide the superior limit of detection.

Vanadium atoms may be excited from the $a^4F_{3/2}$ state 323 cm^{-1} above the ground state to the $x^4G^o_{9/2}$ state by 318.398 nm photons. The gf value

for this transition is 5.3. Two neighboring states, the $^4G^o_{7/2}$ and $^4G^o_{11/2}$, may then be collisionally populated. Radiation to components of the a^4F may then occur at 318.341 and 318.540 nm. The gf values for these transitions are 3.0 and 4.0, respectively.

The only competing uranium absorption lines are at 318.255, 318.283 and 318.514 nm. The gf values for these transitions are all less than .17. The probability for exciting a vanadium atom is thus approximately $.5 \times 10^6$ times as great for a uranium atom.

Uranium possesses an additional line at 318.571 nm which is a potential source of fluorescence interference. If fluorescence is monitored at 318.341 nm, an additional selectivity factor of about 5000 will be achieved. This suggests that SONRES may provide extremely selective detection of vanadium atoms. In addition, due to the large pumping transition intensity extremely sensitive detection may also be predicted.

Similar schemes may be obtained for the detection of other atomic species. An additional element of selectivity may also be found due to the high density of atomic uranium states and the small emission oscillator strengths. The probability for collisional excitation to a state followed by competing fluorescence will probably be small thus reducing the uranium background signals. In addition, if the competing fluorescence lines result from uranium ion states (the interfering lines for cobalt and vanadium detection are unassigned), the addition of an alkali metal to the matrix will reduce the interference.

The experimental techniques to be used would be very similar to those used for atomic absorption spectroscopy. Standards for each element to be

analyzed would be prepared by dissolution of the element in nitric acid. These standards would then be aspirated into a flame where most solute molecules will be atomized. The laser (a frequency doubled CW ring dye laser or a frequency doubled flashlamp pumped dye laser if sufficient power is not available at the wavelength of interest from the CW laser) would be focused into the flame. The focus region would be imaged onto the entrance slit of a monochromator having resolution better than .01 nm. A photomultiplier would detect photons which pass through the monochromator. A photon counting system would then acquire the data. The laser and monochromator wavelengths would be fine-tuned in order to maximize the detected signal. A calibration for each element would be thus obtained in terms of parts per million in the solution vs. count rate.

Once calibrations have been performed, analysis of doped U_3O_8 samples may be undertaken in order to determine the limits of detection for the elements studied. It is expected that the SONRES technique will yield significantly improved detection limits for many contaminants in the matrix.

References

1. J. P. Maney, V. Luciano, A. F. Ward, Proc. FACSS Confernece, 1978.
2. C. R. Walker and O. A. Vita, Anal. Chim. Acta 43, 27 (1968).
3. C. R. Walker, O. A. Vita and R. W. Sparks, Anal. Chim. Acta 47, 1 (1969).
4. R. Avni, Spectrochim Acta 23B, 619 (1968).
5. R. W. Sparks, O. A. Vita and C. R. Walker, Anal. Chim. Acta 60, 222 (1972).
6. S. de Moraes and A. Abrao, Anal. Chem. 46, 1812 (1974).
7. Z. P. Moseeva, G. P. Pinchuk, A. B. Sokolov, A. G. Karabash and Sh. I. Peizulaev, J. Anal. Chem. of USSR 29, 1373 (1974).
8. J. A. Gelbwachs, C. F. Klein and J. E. Wessel, Appl. Phys. Lett. 30, 489 (1977).
9. J. A. Gelbwachs, C. F. Klein and J. E. Wessel, IEEE, J. Quantum Electron QE14, 121 (1978).
10a. C. E. Moore, Atomic Energy Levels, Vol. I (U.S. Government Printing Office, Washington, D.C., 1949).
b. C. E. Moore, Atomic Energy Levels, Vol. II (U.S. Government Printing Office, Washington, D.C., 1952).
11. C. H. Corliss and W. R. Bozman, Experimental Transition Probabilities for Spectral Lines of Seventy Elements (U.S. Government Printing Office, Washington, D.C., 1962).
12. W. F. Meggers, C. H. Corliss and B. F. Scribneg, Tables of Spectral Line Intensities, Part I (USGPO, Washington, D.C., 1961).

13. J. I. Steinfeld, Molecules and Radiation (Harper & Row, San Francisco, 1974) p. 229.

14. V. S. Letokhov and V. P. Chebotayev, Nonlinear Laser Spectroscopy (Springer-Verlag, New York, 1977).